The seismogenic potential of subducting sediments

Hannah Sarah Rabinowitz

Submitted in partial fulfillment of the

requirements for the degree of

Doctor of Philosophy

in the Graduate School of Arts and Sciences

COLUMBIA UNIVERSITY

2018

Abstract

The seismogenic potential of subducting sediments

Hannah Sarah Rabinowitz

This thesis examines the seismic behavior of sediments in shallow subduction zones. In the traditional view of the seismogenic zone, the upper stability limit is controlled by a transition to velocity-strengthening (frictionally stable) clay-rich sediments at shallow depths in the accretionary prism. However, recent observations have emphasized that these shallow sediments can host a wide range of seismic behaviors. On one end of the seismic spectrum, the March 2011 M_w9.1 Tohoku-oki earthquake demonstrated that peak slip in a megathrust rupture can be hosted at the shallowest depths. At the other end of the spectrum, observations at the Hikurangi trench off the North Island of New Zealand have revealed that spontaneous, periodic slow slip events (SSEs) can nucleate in the shallowest portions of a subduction zone.

The Japan Fast Trench Drilling Project (JFAST, IODP Expedition 343) drilled through the plate boundary faults in the Japan Trench to investigate the structure that hosted the Tohoku-oki earthquake. In Chapter 2, I use a trace element-based stratigraphy to identify several large displacement faults within the bottom ∼15 m of the JFAST core. This work highlights that there are multiple candidate structures that could host a megathrust rupture and that not all displacement is accommodated along a weak pelagic clay layer recovered in the JFAST core. However, this method is incapable of determining which of these faults experienced significant seismic slip. In Chapter 3, I develop a novel paleoseismic indicator appropriate for faults hosted in seafloor sediments. This tool takes advantage of the fact

that organic material (molecular biomarkers) in sediments degrades as a function of time and temperature. In this study, I determine the kinetics of thermal maturation for alkenones (coccolithophore-derived molecules) and n-alkanes (plant leaf wax-derived molecules) found in western Pacific sediments. In Chapter 4, I apply these kinetics to measured biomarker anomalies in JFAST samples to determine which faults recovered in the JFAST core could have hosted a megathrust event such as the Tohoku-oki earthquake. This approach reveals that multiple faults in the plate boundary region have likely hosted megathrust events and that the occurrence of seismic slip is not confined to a particular lithology. This implies that small differences in frictional behavior in subducting sedimentary lithologies are not the primary control on the occurrence of shallow seismic slip.

In Chapter 5, I turn to a different type of shallow seismic behavior and focus on SSEs in the shallowest portion of the Hikurangi trench. In this study, I measure friction and velocity-dependence of the input sediments for this subduction zone at a range of pressures and temperatures relevant to the shallow portion of the slab where SSEs have been observed. These experiments demonstrate that the sediment here becomes frictionally weak at effective stresses expected deeper than $\sim$2 km. At the same effective stresses, the sediment becomes less velocity strengthening, and under some conditions exhibits velocity neutral behavior. A plate-rate experiment exhibits velocity-weakening behavior and two spontaneous SSEs, indicating that at slow velocities, the sediment subducting at the Hikurangi trench is capable of unstable frictional behavior required to promote shallow SSEs. These results demonstrate that subducting sediments can exhibit a variety of frictional properties that can support unstable behavior in the shallowest reaches of the subduction zone.

Contents

List of Figures

List of Tables

Acknowledgements

Getting through a Ph.D. really does take a village, and as such, there are many people without whom I wouldn't be the scientist I am today. Firstly, I would like to thank my advisor, Heather Savage. Your guidance and mentorship from day one have been the scaffold upon which I have grown as a scientist. I appreciate so much your willingness to talk through even my most harebrained ideas and your honesty and patience in helping me to develop projects. I would also like to thank the rest of my committee—Ben Holtzman, Chris Scholz, Pratigya Polissar, and Demian Saffer—for taking the time to read and comment on this dissertation. I particularly would like to acknowledge Ben and Chris for being available to discuss any rock deformation questions that came up along the way and Pratigya for always being available to provide me with a crash course in organic geochemistry.

This dissertation uses several different approaches to investigate questions about shallow fault behavior, and benefited from the support of some great lab groups. Firstly, the Rock Mechanics Group at the Lamont-Doherty Earth Observatory has been my jumping off point throughout my Ph.D. In addition to Heather and Ben, Christine McCarthy has been an amazing unofficial mentor. Thank you to Ted Koczynski for teaching me how to design and maintain everything needed for rock mechanics experiments. Thank you also to the other lab members during my time here—Nicholas van der Elst, Mandy Duda, Mike Nielsen, Rob Skarbek, and Genevieve Coffey—both for the amazing range of advice and help in the lab as well as your friendship during the last five and a half years. I would also like to thank Terry Plank for being a great resource to discuss geochemical questions and being instrumental to the development of our JFAST stratigraphy. Much of this dissertation centers on the

development and implementation of biomarker thermal maturity proxies, and all of this work was done in the Organic Geochemistry Lab at LDEO. I'd like to thank Billy D'Andrea, Kevin Uno, and Nicole deRoberts for helping to teach me lab techniques that were essential to this work and for creating a fun and productive lab environment. I'd also like to thank my collaborators from other universities—Christie Rowe, Jamie Kirkpatrick, Brett Carpenter, Matt Ikari, Cristiano Collettini, and Giulio di Toro—for taking me to amazing faults and opening your labs to me as well as helpful advice along the way. Thank you to Phil Skemer for introducing me to rock deformation and for continuing to be an amazing mentor so many years after I graduated from WashU.

One of the amazing parts of doing a Ph.D. at Lamont has been the breadth and depth of my education in geophysics, and this would have been impossible without the amazing group of faculty and students in the SGT Division. Thank you for making Lamont such an intellectually stimulating place to learn and for helping me to develop confidence as a scientist throughout the last few years. I particularly want to thank Natalie Accardo, Celia Eddy, and Helen Janiszewski. I was lucky to start grad school with such a great SGT cohort and through years of trials and successes in graduate school, you have become both my colleagues and some of my closest friends.

Last, but certainly not least, I would like to thank my family. Helen, Steven, Johanna and Charlie, thank you for adopting me as the third child in your family and becoming my home away from home in New York. Chris, Carol, Katie, and Jill, thank you for opening your family to me. To my parents and Josh, thank you for always being there to support and encourage me. We have always been there for each other through challenges and to celebrate successes and I will always be grateful to have you. Finally, I would like to thank Martin who has the unnatural ability to make me laugh even at my most stressed out moments. I feel incredibly lucky to have you by my side.

To Marina, Ian, and Josh

1 Introduction

Subduction zones are known to host the largest and most devastating earthquakes on Earth. Understanding seismic processes in these regions is an essential goal of earthquake mechanics research. Earthquakes generally occur within a specific depth range known as the seismogenic zone, where material properties of the rocks promote unstable, brittle behavior [Blanpied et al., 1991, Scholz, 1988, Sibson, 1982]. The limits of the seismogenic zone are defined by transitions in deformation behavior: to plastic flow at the down-dip limit and to stable slip at the up-dip limit. These transitions are thought to be controlled by changes in the mechanical behavior of the subducting material with lithology, temperature, and effective stress [Marone and Scholz, 1988, Oleskevich et al., 1999, Sibson, 1982]. Specifically, the stable behavior in the shallowest portion of subduction zones is thought to be controlled by weak, velocity strengthening clays that make up the majority of subducting sediments in combination with low effective stresses [Hyndman et al., 1997, Moore and Saffer, 2001].

However, earthquake slip can sometimes extend to significantly shallower depths. For example, the 2011 M_w9.1 Tohoku-oki earthquake exhibited peak slip in the shallowest portions of the fault, a feature that enhanced the devastating tsunami associated with this earthquake [Fujii et al., 2011, Fujiwara et al., 2011, Ide et al., 2011, Sun et al., 2017]. This implies that under certain conditions, rupture propagation can be enhanced in the shallowest regions of faults. Observations of slow slip at depths ranging from below the seismogenic zone to the trench highlight that complex seismic behaviors cannot be described by a simple depth-zoned friction model. Shallow slow slip at several subduction zones around the world [Brown et al., 2005, Outerbridge et al., 2010, Wallace and Beavan, 2010] suggests that unstable frictional

behavior can be supported in these shallowest sediments even without the effects of dynamic slip propagation from further down-dip. Shallow slow slip preceded the Tohoku-oki earthquake [Ito et al., 2013], and understanding the mechanisms of this behavior is important to improving seismic hazard estimates. At the Hikurangi trench, offshore of the North Island of New Zealand, shallow slow slip events (SSEs) have been observed extending almost to the seafloor [Wallace et al., 2016].

This dissertation uses samples from ocean drill cores to examine the shallow seismic behavior of the Japan trench and the Hikurangi trench. In Chapters 2–4, core samples from the Japan trench are analyzed using geochemical methods to identify faults in the shallowest portion of the subduction zone that have slipped seismically. In Chapter 5, deformation experiments conducted on core samples from the Hikurangi trench interrogate the frictional behavior of subducting sediment at depths relevant to shallow SSEs.

Chapter 2 (now published: *Rabinowitz et al*, 2015) focuses on characterizing the shallow fault structure of the accretionary wedge at the Japan trench where the March 11, 2011 M_w9.1 Tohoku earthquake exhibited about 50 m of slip to the trench, with the peak slip in the shallowest portion of the subduction interface [Ammon et al., 2011, Fujii et al., 2011, Fujiwara et al., 2011, Ide et al., 2011, Kodaira et al., 2012, Koper et al., 2011, Simons et al., 2011, Sun et al., 2017]. A year after the earthquake, IODP Expedition 343 (JFAST) drilled through the décollement that hosted peak slip to sample fault rocks in the subduction zone and installed an observatory to capture the temperature decay from the earthquake. Initial observations of the JFAST core identified a thin (<5 m thick) weak, foliated pelagic clay layer. The strong fabric and frictional weakness of the clay, as well as the structural changes between sediments above and below this layer, imply that this is a significant tectonic boundary [Chester et al., 2013, Ikari et al., 2015b, Keren and Kirkpatrick, 2016a, Kirkpatrick et al., 2015, Ujiie et al., 2013, Yang et al., 2013]. If seismic deformation is indeed confined to this weak layer, hazard estimates for subduction zones should consider the presence or lack of a pelagic clay unit within the subducting sediment package [Moore

et al., 2015]. This study uses trace element geochemistry to fingerprint each individual sedimentary unit in two reference cores drilled through the incoming Pacific plate, and develops a detailed chemostratigraphy of the JFAST core to determine whether deformation is indeed predominantly localized on this weak lithology. Using this stratigraphic approach, multiple large displacement faults are identified in a ∼15 m thick region recovered at the bottom of the JFAST core, indicating that deformation is distributed across multiple lithologies in the Japan trench. However, this stratigraphic approach is unable to determine whether the interpreted faults have experienced seismic slip.

The typical approach to determining whether a fault has experienced seismic slip is by using a signature of frictional heating in the rock record. Pseudotachylyte is the most commonly used paleoseismic indicator and occurs when a fault reaches temperatures high enough enough to melt the host rock during coseismic slip [Shand, 1916, Sibson, 1975]. This feature is rarely observed in sedimentary rocks, as heating is often buffered by effects such as pore fluid pressurization [Sibson and Toy, 2006]. Recently, there have been significant efforts to develop sub-solidus paleoseismic indicators that can be applied to sedimentary rocks [Barker and Pawlewicz, 1986, D'Alessio et al., 2003, Hirono et al., 2007, Rowe and Griffith, 2015, Schleicher et al., 2015, Sheppard et al., 2015, Yang et al., 2016]. In Chapter 3 (now published: *Rabinowitz et al*, 2017), I develop a new set of paleoseismic indicators, which quantify the degradation of organic molecules (biomarkers) found in seafloor sediments. Biomarkers have long been known to thermally mature due to burial heating over geologic time [Peters et al., 2004]. During earthquakes, frictional heating can cause temperature rise significantly above that experienced due to burial heating, but over a shorter timescale of seconds to minutes [Lachenbruch, 1986]. Because biomarker degradation is a function of both time and temperature, these elevated coseismic temperatures can generate anomalies in measured biomarker concentrations which can be used to identify seismic faults [Polissar et al., 2011, Savage et al., 2014]. In this study, I determine the kinetics of biomarker thermal maturity for alkenones (long-chain carbon molecules sourced from coccolithophore algae) and

n-alkanes (long-chain carbon molecules sourced from terrestrial plant leaf waxes) at seismic timescales.

In Chapter 4, I apply the kinetics of thermal maturity defined in Chapter 3 to samples from the JFAST core. Implementing the trace element stratigraphy from Chapter 2, biomarker values measured in individual JFAST samples can be compared to their initial values as measured in a reference core through the incoming Pacific plate sediments. Samples that exhibit anomalous biomarker values are interpreted as having experienced frictional heating. I use forward models of temperature rise on faults [Lachenbruch, 1986] coupled with the reaction kinetics of biomarkers to constrain the temperature rise necessary to create the biomarker anomalies. This provides estimates of the minimum slip magnitude and minimum number of earthquakes that could have generated the observed biomarker anomalies. These models confirm that megathrust earthquakes regularly propagate to the trench and that shallow coseismic slip in the Japan trench is not confined to any particular lithology. Rather, coseismic slip can be accommodated in lithologies with a range of frictional properties.

While Chapters 2–4 emphasize the frequency with which large-magnitude earthquakes propagate to shallow depths, seismic and geodetic observations have demonstrated that shallow deformation in subduction zones is accommodated by a wide range of slip behaviors. Most notably, recent advances in seafloor instrumentation have shown that slow slip events (SSEs), which have previously been observed at the down-dip limit of the seismogenic zone, extend to within $<\sim$2 km of the seafloor at the Hikurangi trench offshore North Island, New Zealand [Wallace et al., 2016, Wallace and Beavan, 2010]. In Chapter 5, I use rate-and-state friction experiments to explore the frictional stability of sediment subducting at the Hikurangi trench at a range of pressure and temperature conditions relevant to the shallow subduction zone [McCaffrey et al., 2008]. These experiments demonstrate that the subducting sediment becomes frictionally weaker, and less velocity strengthening, at conditions of increasing pressure within the upper 10 km of the subduction zone where shallow slow slip is observed. Plate-rate experiments exhibit velocity-weakening behavior and SSEs at low

effective stress conditions. These results suggest that at slow sliding velocities, the sediment subducting at the Hikurangi trench is frictionally unstable and capable of nucleating slow slip at shallow depths.

Taken together, this thesis addresses the range of seismic behaviors that occur in shallow subduction zone environments. The distribution of seismic faults through multiple lithologies suggests that subtle variations in steady-state frictional strength and stability are not the primary control on megathrust rupture propagation to the trench. On the other hand, at slow slip velocities, shallow subduction zone sediments can support unstable frictional behavior as observed at the Hikurangi trench. These observations imply that, while determination of steady-state friction parameters can help to understand the mechanisms that control slow seismic behavior (e.g. SSEs), the most effective method to determine seismic hazard from dynamic ruptures (e.g. shallow megathrust rupture) is through establishing detailed earthquake histories in seismically active regions.

2 Multiple major faults at the Japan Trench: Chemostratigraphy of the plate boundary at IODP Exp. 343: JFAST

Co-authors: Heather M. Savage, Terry Plank, Pratigya J. Polissar, James D. Kirkpatrick, Christie D. Rowe

This chapter has been published: *Rabinowitz, H. S., Savage, H. M., Plank, T., Polissar, P. J., Kirkpatrick, J. D., & Rowe, C. D. (2015). Multiple major faults at the Japan Trench: Chemostratigraphy of the plate boundary at IODP Exp. 343: JFAST. Earth and Planetary Science Letters, 423, 57-66.*

We determine the trace element stratigraphy of Site C0019, drilled during the Japan Fast Trench Drilling Project (JFAST) International Ocean Discovery Program (IODP) Expedition 343, to illuminate the structure of the plate boundary following the Tohoku-Oki earthquake of 2011. The stratigraphic units at the JFAST site are compared to undeformed Western Pacific sediments from two reference sites (Ocean Drilling Program (ODP) Site 1149 and Deep Sea Drilling Project (DSDP) Site 436). The trace element fingerprints in these reference sedimentary units can be correlated to individual JFAST samples. At the JFAST site, we find that the accretionary wedge and downgoing plate sediments in the core are composed primarily of Holocene to Eocene sediments. There are several age reversals and gaps within the sequence, consistent with multiple faults in the bottom 15 m of the JFAST core. Our

results point to several candidate faults that could have slipped during the 2011 Tohoku-Oki earthquake, in addition to the pelagic clay layer that has been proposed as the main décollement fault.

Keywords: Tohoku earthquake, Pacific plate stratigraphy, shallow subduction structure, ODP Site 1149, DSDP Site 436, IODP Expedition 343

2.1 Introduction

The 2011 M_w 9.1 Tohoku-Oki earthquake was a societally devastating event, and was unusual in that peak slip ($>$ 50 m) occurred near the seafloor [Fujiwara et al., 2011, Ide et al., 2011, Ito et al., 2011]. Although the Tohoku earthquake is the largest earthquake that has been observed on this section of the Japan Trench, tsunami records indicate previous great earthquakes with a recurrence time of approximately 1100 years [Minoura et al., 2001] and possibly as short as $\sim$500 years [Sawai et al., 2012, Simons et al., 2011]. These large tsunami deposits suggest that the previous great earthquakes may have also caused significant shallow co-seismic slip. Active source seismic surveys indicate that the shallow portion of the accretionary prism at the site of the Tohoku earthquake has experienced significant deformation [Kodaira et al., 2012, Nakamura et al., 2013]. Approximately 3 km of displacement has occurred across the plate-boundary at the JFAST site [Chester et al., 2013], and could have resulted from many large earthquakes with shallow slip propagating through the accretionary wedge cored here.

IODP Expedition 343 (JFAST) drilled through the accretionary wedge at the Japan Trench to investigate shallow, tsunamigenic earthquake slip [Chester et al., 2012]. Several holes were drilled at the site; one hole was cored (C0019E) and has been studied extensively [Chester et al., 2013, Kirkpatrick et al., 2015, Lin et al., 2014, Rowe et al., 2013, Sawai et al., 2014, Tanikawa et al., 2013, Ujiie et al., 2013, Yang et al., 2013]. Samples for this study come from core C0019E, which is hereafter referred to as the "JFAST core". The JFAST core shows many structural features that provide insight into how deformation was

accommodated. For instance, there is a change in structural domain with depth. In the top part of the core, above ∼820 meters below sea floor (mbsf), sediments dip at ∼20–80^o [Chester et al., 2013, Kirkpatrick et al., 2015] and faults have an average dip of 67^o [Chester et al., 2012]. At 820 mbsf, a 1-meter thick layer of pelagic clay with high smectite content [Kameda et al., 2015] was recovered that showed pervasive shear fabric. Below this layer the bedding has a much shallower dip [∼10^o; Chester et al., 2013, Kirkpatrick et al., 2015] and there is a change in the anisotropy of magnetic susceptibility [Yang et al., 2013]. Temperature measurements at the JFAST site are consistent with the pelagic clay layer accommodating the slip of the Tohoku-Oki earthquake [Fulton et al., 2013, Lin et al., 2014]. These observations suggest that the pelagic clay is the boundary between the off-scraped sediments and the subducting material, and has hosted a significant amount of slip, perhaps including the Tohoku earthquake [Chester et al., 2013, Kirkpatrick et al., 2015, Ujiie et al., 2013].

However, multiple faults above and below the pelagic clay layer have been noted and could be important in the slip history of the plate boundary [Chester et al., 2012, Kirkpatrick et al., 2015]. It has been difficult to develop a detailed stratigraphy and clear picture of the plate boundary structure at the JFAST site due to significant amounts of missing drillcore (57 m were recovered out of the 831 m drill hole, and there was <50% recovery within the cored sections), lack of reliable strain markers in many observed faults, and the large amount of similar mudstone lithology throughout the JFAST core [Chester et al., 2013, 2012, Kirkpatrick et al., 2015].

Here, we develop a more detailed stratigraphy of the JFAST core based on the trace element chemical compositions of the sediments. Previous studies of the core used a nearby site in the Western Pacific (DSDP Site 436) as a reference site for the incoming plate stratigraphy [Chester et al., 2013, Moore et al., 2015]. The correlation between the two ocean drilling sites has been based largely on radiolarian biostratigraphic ages and lithologic characteristics of sediments [Chester et al., 2012]. While these age-based methods of correlating stratigraphic

units between ocean drill cores are robust for undisturbed Western Pacific stratigraphy (with the exception of the pelagic clays that contain no radiolarians), the sampling for radiolarian analysis in the JFAST core may be too coarse to capture the stratigraphic complexity of the plate boundary. In this paper, we demonstrate a coherent chemostratigraphy in the lithologically equivalent units at Pacific DSDP Site 436 and ODP Site 1149, which allows for a more detailed reconstruction of the stratigraphy of the accretionary wedge at the JFAST site. Our analysis locates intervals of missing section and inverted stratigraphy that indicate the presence of major faults. Some of these faults were previously identified, but their total displacement was unconstrained. Other faults were previously unrecognized in the JFAST core because of the coarseness of radiolarian sampling or because they are within unrecovered sections of the JFAST core. These faults may have accommodated a significant portion of the total displacement along the plate boundary and, therefore, may have accommodated earthquake slip near the trench.

2.2 Background

Establishing the primary stratigraphic relationships within fault zones is essential to identifying inversions, missing and repeated sections, and other disruptions that can help identify faults. Such data are particularly useful in drillcores where coring gaps and the lack of lateral exposure can obscure important structural features. Sediment ages from biostratigraphy are typically used to date continuously deposited deep ocean sediments that contain flat lying, "layer-cake" units where the law of superposition can be applied as a relative age constraint. However, in tectonically disrupted cores, such as were recovered during the drilling of the accretionary wedge at the JFAST site, it cannot be assumed that the layers have remained in order or intact and superposition does not hold. This creates a challenge in developing a stratigraphy for JFAST sediments. In the JFAST core, radiolarian biostratigraphic data were used to correlate sediments to the nearby DSDP Site 436 site on the incoming plate. While this analysis identified significant structural features, the relatively broad spacing of the biostratigraphic samples increased the likelihood that

important stratigraphic offsets were missed.

Here we use trace element analysis to place the JFAST samples within the stratigraphic context of the incoming Western Pacific Plate stratigraphy from the closest available core record in the Japan Trench (DSDP Site 436), corroborated with the more distant core record from Izu-Bonin (ODP Site 1149). Trace element concentrations in marine sediments are controlled by factors including sedimentation rate, biological productivity in the overlying ocean, and the provenance of sedimentary detritus [Plank and Langmuir, 1998, Plank, 2014]. When regions of the Pacific Plate passed through similar depositional regimes concurrently, sedimentary layers with similar ages and similar trace element compositions were deposited [Moore et al., 2015]. Therefore, trace elements can be used to develop a geochemical stratigraphy linking widely spaced Pacific Ocean drilling cores. This consistent stratigraphy also indicates that similar lithologies make up the incoming plate at the JFAST site, and that much of the plate boundary stratigraphy consists of disrupted Western Pacific sediments [Chester et al., 2012]. Trace element patterns in Western Pacific sediments can therefore be used to correlate the tectonically disrupted stratigraphy of the JFAST site with incoming sediment profiles in nearby cores.

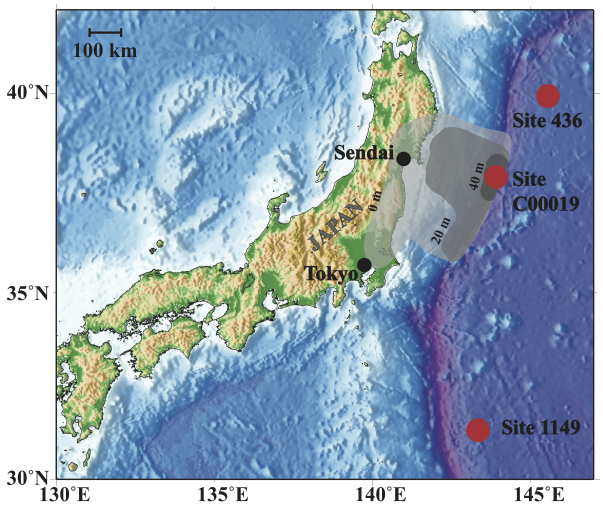

Figure 2.1: Bathymetry and topography of the Japan Trench plate boundary. Slip along the plate boundary during the 2011 Tohoku earthquake is shown in gray and contoured in meters [Ammon et al., 2011, Chester et al., 2013, Fujii et al., 2011, Koper et al., 2011]. We compare sediments in the JFAST core to stratigraphy at DSDP Site 436 and ODP Site 1149 (labeled red dots).

2.2.1 DSDP Site 436 Stratigraphy

DSDP Site 436 is ∼200 km NNE of the JFAST site and is comprised of undeformed Western Pacific Plate pelagic sediments (Figure 2.1). This site exhibits a 380 m thick, "layer-cake" stratigraphic package from Holocene through Cretaceous sediments [Figure 2.2a; Langseth et al., 1977]. The sequence was divided into three units based on age and lithology. Unit 1 is composed of diatomaceous silty clay and claystone and is subdivided into two subunits. Subunit 1A is composed of Holocene to Pliocene greenish vitric (ash-rich) diatomaceous silty clay. Subunit 1B differs gradationally from Subunit 1A in that it shows a higher degree of lithification and is predominantly composed of Late Miocene claystone. There is also a decrease in the average sedimentation rate of Units 1A (∼50 m/my) compared with the older Unit 1B (∼10 m/my; Table 2.1). Unit 2 is a darker radiolarian diatomaceous claystone from the Middle to Upper Miocene. The top of Unit 3 is composed of dark brown to nearly black early Miocene to Eocene pelagic clay underlain by Cretaceous chert, sampled as chert cobbles in the two lowermost cores [Langseth et al., 1977]. The Miocene/Eocene pelagic clays are devoid of radiolaria but were dated using fish teeth fossils [Doyle and Riedel, 1980]. Drilling at DSDP Site 436 ended in the chert layer and did not penetrate to basaltic basement.

2.2.2 ODP Site 1149 Stratigraphy

ODP Site 1149 is located ∼1000 km S of the JFAST site (Figure 2.1) and ∼100 km seaward of the Izu trench. Like DSDP Site 436, this site exhibits a "layer-cake" stratigraphy consisting of similar units [Figure 2.2c; Plank et al., 2000]. Unit I is composed of late Miocene to late Pleistocene ash and diatomaceous clay with abundant radiolarians. Unit II contains dark brown pelagic clay that is devoid of radiolarians. Due to the lack of siliceous microfossils, Unit II brown clays were not dated (although they also contain fish teeth), but are constrained to have been deposited between 6.5 and 105 Ma based on biostratigraphic designations within the adjacent units [Bartolini, 2003, Plank et al., 2000]. Unit III of ODP Site 1149 exhibits alternating Cretaceous chert and clay layers. Unit IV contains Cretaceous radiolarian chert and chalk [Plank et al., 2000], extending to the Late Valaginian (134 Ma)

on top of mid-ocean-ridge type basaltic basement. This carbonate layer is not observed in either of the other cores discussed in this paper (presumably due to the greater age of ODP Site 1149 sediments and basement, variations in local seafloor depth, or lack of penetration past the chert layer in the DSDP Site 436 and JFAST cores).

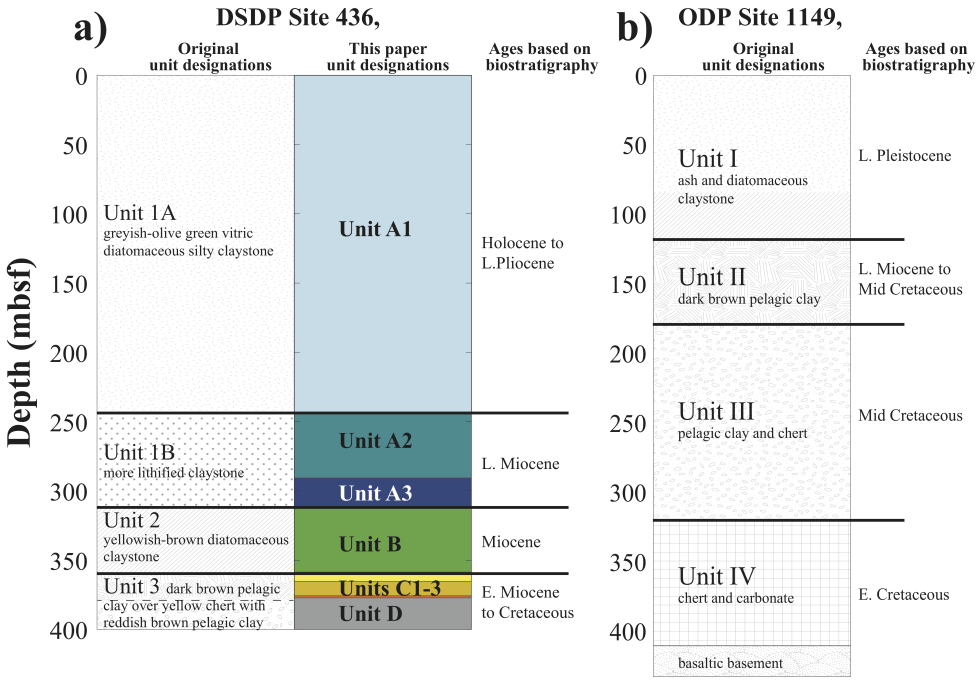

Figure 2.2: Stratigraphy and age of Western Pacific reference cores DSDP Site 436 [a, Langseth et al., 1977] and ODP Site 1149 [b, Plank et al., 2000]. Both cores show similar stratigraphy with corresponding lithologic units deposited at approximately the same time. The original unit names from DSDP 436 are shown along with the unit names used in this paper (with the unit colors that are also used in Figures 3–7.)

Table 2.1: Unit designations for the new chemostratigraphy of the JFAST core.

436-JFAST	Site 436 Unit	Lithological Description	Age	Sed rate (m/my)	Unit base depths (mbsf)	Cores at DSDP 436	Ce, ppm	Zn, ppm	Co/TiO_2	Th, ppm	Ce/Ce*	Zn/Ce
Unit A1	1A	vitric diatomaceous clay	Plio-Pleisto	50	245.5	cores 1–26	<52	>86	<40	<9	1.1–1.15	>1.7
Unit A2	1B	vitric diatomaceous claystone	Late Mio	10	293	cores 27–31	<52	<86	<40	<9	1.1–1.15	1.5–1.7
Unit A3	1B	vitric diatomaceous claystone	Late Mio	11	312	cores 31–33	55–70	<90	<40	>9	1.2–1.35	1.31.5
Unit B	2	radiolarian diatomaceous claystone	Mid Miocene	12	359.5	cores 34–38	70–100	>86	35–60	11–14	1.2–1.35	1.1–1.3
Unit C1	3	brown pelagic clay	Early Mio	1	365	core 39	100–125	130–150	85–100	14–17	1.4–1.5	1.2–1.3
Unit C2	3	brown pelagic clay	Oligocene	1	377	cores 39–40	180–210	150–170	250–450	19–22	1.2–2.0	<1
Unit C3	3	brown pelagic clay	Eocene	0.1	378	core 40	180–210	170–190	<150	19–22	<1	<1
Unit D	3	chert and clay	Late Cret.	–	>397.5	cores 41–42	<175	<175	<135	<20	<<1	13

Original DSDP Site 436 unit designations are indicated in addition to the unit designations used in this paper. Unit depths refer to the depths of the incoming stratigraphy at DSDP Site 436. Outlined boxes indicate the most diagnostic trace element indicators for fingerprinting each unit and subunit. Unit D designation is also based on the geochemical characteristics of ODP Site 1149 [Plank et al., 2007].

2.2.3 Correlation between Sites 436 and 1149

The generalized stratigraphic succession at both DSDP Site 436 and ODP Site 1149, seaward of the Japan and Izu trenches respectively, is identical, with diatom- and ash-rich greenish silty clay overlying dark brown pelagic clay, overlying Cretaceous chert. This succession characterizes most of the western North Pacific, from the Izu, to the Japan, Kurile and Kamchatka trenches [Plank, 2014]. The Cretaceous chert was first deposited as biosiliceous ooze when the sites crossed beneath equatorial regions of high productivity. Based on backtracked plate motions, the Western Pacific sites originated in the equatorial Eastern Pacific [Moore et al., 2015]. The distinctive brown-to-black, slick pelagic clay, barren of siliceous or carbonate microfossils, was deposited during the northwestward passage of sites beneath the central gyre of the Pacific [Moore et al., 2015]. Far from terrestrial sources and in a region of low biological productivity, the sedimentation rate dropped to < 1 m/m.y. during this time. At various times in the Miocene (depending upon location) these sites exited the gyre and entered a region of higher biological productivity (as in the modern Kuroshio Current) and entered the Asian dust belt, both factors leading to more rapid accumulation (> 10 m/m.y.) of biosiliceous silty clays [Moore et al., 2015]. Although this same succession characterizes the Western Pacific trenches from 35–55 ^{o}N, the thickness of the units varies latitudinally, with the thickening of the top diatomaceous silty clays correlated to the thinning of the lower brown clay and chert units from south to north.

2.2.4 JFAST Stratigraphy

IODP Site C0019 is composed of similar lithologies to those discussed above, although the sediments are highly deformed and the original succession disrupted. Due to time constraints, the JFAST expedition sampled 4 discrete depth ranges (176.5–186, 648–660.5, 770–772.35, and 780.5–837 mbsf) and therefore significant sections of the stratigraphy are missing from the core record. The JFAST science party reports seven different sedimentary units, based on lithology and depth. They provide a first-order correlation with the stratigraphy at DSDP Site 436 based on lithology, but are unable to distinguish between lithologically similar units

[Chester et al., 2012].

As described in Chester et al. [2012] the first sampled section, 176.5–186 mbsf, is composed of Pliocene green-grey siliceous mudstone (all ages are based on radiolarian dating). The next sampled section, 648–660.5 mbsf, is composed of reddish and bluish, Miocene mudstones. This section is heavily brecciated (possibly during drilling) and could not be used for structural analysis. Below this, between 688.5–821.5 mbsf, several mudstone layers are observed, including greenish-brownish-grey, dark grey with black layers, clay-rich, and dark grey pyritic mudstones. These sediments are mostly Pleistocene with the exception of a Pliocene section at 816.5–818 mbsf. From 821.5–822.5 mbsf, sediments are predominantly intensely sheared black, scaly clay (with the exception of a less sheared tan mudstone sliver tectonically emplaced within this section). This section of the core has been identified as the décollement [Chester et al., 2013]. Surrounding the 1 m-thick recovered pelagic clay layer is about 3 m of unrecovered section (820–821.5 and 822.5–824 mbsf). Therefore, the dark pelagic clay layer has a thickness of < 5 m. Below the pelagic clay, there is a yellow- to grey-brown mudstone that overlies orange-pink to buff to dark brown Miocene clays. The final lithology recovered at JFAST is a chert and clay layer beginning at around 831 mbsf [Chester et al., 2012].

Radiolarian ages in the JFAST core are primarily determined from core catcher samples and are taken to be representative of the corresponding core section above [Chester et al., 2012]. However, when the number of faults is larger than the number of cores in a segment of the hole, this standard sampling frequency is insufficient to capture multiple age reversals and gaps that could be contained within a single core. Due to the frequency of faulting in the JFAST core, especially close to the plate boundary, it is possible that the ages of the sediments in core catcher samples are not representative of the entire core. It is also probable that several more faults are contained within the unsampled sections at the JFAST site. Furthermore, Pacific radiolarian zones have age ranges that do not always allow for accurate fingerprinting of the sample to the reference core depth. The trace element method

described below allows for more precise correlations between the JFAST core and reference cores.

2.3 Methods

Samples from DSDP Site 436 and JFAST were first extracted with organic solvents for lipid biomarker analyses, and a small amount of the extracted sample (∼1 g) was used for trace element analyses. Digestion and analytical procedures generally follow those in Plank et al. [2007]. Sediments were dried at 110^{o}C before weighing 50 mg into Teflon screw-top vials, to which 3 mL of 8N HNO_3 and 1 mL of HF were added. Samples were digested overnight in sealed capsules on a hot plate ($< 100^o$C), then uncapped and evaporated to dryness. Dried samples were re-wetted with DI water and hydrogen peroxide to digest any residual organic matter. Solutions were then acidified with HNO_3, transferred to 250 mL HDPE bottles, diluted with DI water to 3000x the original dry powder weight, and sonicated for 30 minutes. A procedural blank as well as standard reference materials (IOBC, IORC, JA-2, W2) were prepared in the same manner with each batch of ten unknowns and analyzed on a PQ ExCell ICP-MS at LDEO. Data were reduced by blank subtraction, external drift correction, and standard calibration. Calibrations were strongly linear ($R^2 > 0.999$), and internal precision based on replicate analyses of each unknown solution is on the order of $< 3\%$ relative standard deviation (RSD). External precision is generally $< 5\%$ RSD for separately digested aliquots of PP829 and IORC (Supplementary Table A.1). The same solutions were then analyzed on an Agilent 700-series ICP-ES for major elements, except SiO_2, which is volatilized by the HF treatment. Prior tests, however, have demonstrated that SiO_2 can be calculated by difference from a 100 wt% sum within 0.5 wt% absolute [Wade et al., 2005], provided the total volatile content has also been measured by loss on ignition (LOI). Trace elements, major elements, SiO_2-by-difference and LOI concentrations are provided in Supplementary Table A.1.

2.4 Results

2.4.1 Trace element signatures at DSDP Site 436 and ODP Site 1149

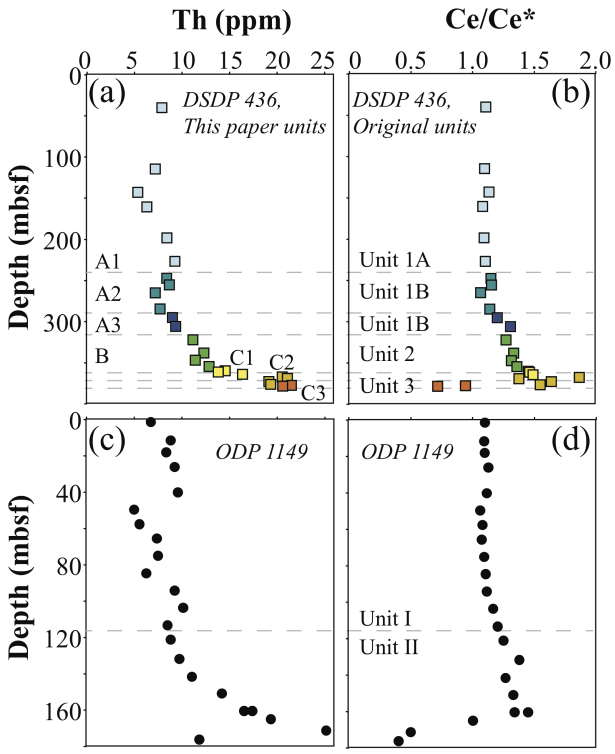

Figure 2.3: Key trace element ratios and concentrations demonstrate changing signatures with depth in both reference cores, DSDP Site 436 (a and b) and ODP Site 1149 (c and d). These signatures are consistent across wide ranges of the Western Pacific as seen by the similar signatures in corresponding sedimentary units in both reference cores. Here, we show two examples of trace element signatures — Th (a and c) and Ce/Ce* (b and d). Original DSDP 436 unit designations are shown in b) and unit designation from this paper are shown in a). Site 436 data is color-coded according to the unit colors introduced in Figure 2. Original ODP 1149 unit designations are shown in d).

We compared trace element concentrations in the diatomaceous ashy-clay and pelagic clay units above the Cretaceous cherts (at different depths, but similar time horizons at the two sites) for both DSDP Site 436 and ODP Site 1149 (Figure 2.3). The concentration of Th increases downcore in both sites, as does the Ce anomaly (Ce/Ce*), which is the deviation of Ce from the adjacent rare earth elements, La and Pr, due to its ability to partially speciate in the ocean with a different oxidation state (4+ as opposed to the other

3+ REE) [De Baar et al., 1983]. Moreover, the absolute values of these tracers in the upper units are nearly identical (5–9 ppm Th and 1.1 Ce/Ce*) despite the fact that the two sites are > 1000 km apart (Figure 2.3). At both sites, Th increases dramatically to 20–25 ppm in the brown-black pelagic clay that is barren of microfossils (except fish teeth). The Ce anomaly also increases significantly in the upper pelagic clay before decreasing near the contact with the chert [where it continues to be low, based upon ODP Site 1149 data; Plank et al., 2007]. Thorium and Ce/Ce* are both tracers strongly linked to sedimentation rate and the proportion of iron-manganese (FeMn) oxyhydroxides in marine sediments, which form by authigenic precipitation in the water column [Plank and Langmuir, 1998]. At low sedimentation rates, FeMn oxyhydroxides predominate as the proportion of detrital and biogenic sediments diminishes to very low values, as occurs in the central gyre of the Pacific. Thorium and Ce^{4+} are both highly particle-reactive, and strongly scavenged by FeMn oxyhydroxides [Anderson et al., 1983, Bau and Koschinsky, 2009]. The increases in both tracers downcore reflect the decreasing sedimentation rates as both sites track back to the central gyre. The sharp decrease in Ce/Ce* near the base of the brown pelagic clay (and cherts below) results from higher proportion of fish debris phosphate [which inherits the negative Ce anomaly of seawater; Plank and Langmuir, 1998] and biogenic productivity in general, on the far side of the gyre. Thus, there is a coherent chemostratigraphy at both sites [and indeed much of the Western Pacific; Plank, 2014] that marks the journey through different sedimentation zones across the Pacific.

Although a similar chemostratigraphy characterizes most of the sediments now entering Western Pacific trenches, from the Marianas to the Kuriles, we use the section at DSDP Site 436 as the best template for the original JFAST stratigraphy due to its proximity. The chemical variations at DSDP Site 436 presented here define finer unit boundaries than those originally designated in the initial reports volume [Langseth et al., 1977], and to avoid confusion with the DSDP Site 436 unit boundaries (1–3) and those at ODP Site 1149 (I–IV), we have used different names for the chemostratigraphic boundaries at DSDP Site 436

(Units A–D). DSDP Site 436 Unit 1A corresponds to our Unit A1 and DSDP Site 436 Unit 2 corresponds to our Unit B. We subdivide DSDP Site 436 Unit 1B into two units, Units A2 and A3, and likewise subdivide DSDP Site 436 Unit 3 into four units, Units C1–3 and D (Figure 2.2). These subdivisions are notable in that they occur in parts of the core where sedimentation rate decreases downcore. In these locations, the diatom-radiolarian biostratigraphy loses resolution (or ceases to exist entirely) and large chemical gradients form. Thus, the very processes that challenge biostratigraphy improve chemostratigraphy, and the two methods are highly complimentary.

Younger sedimentary units at the reference sites are most difficult to distinguish lithologically and we demonstrate their unique geochemical signatures through several trace element plots (Figure 2.4). Classical trace element plots are used to identify sediments with significantly different provenance. However, in the Western Pacific sediments studied here, the units have similar provenance and we use non-standard plots to highlight more subtle differences that can be used to distinguish the subunits. Figure 2.4 illustrates the basis for the new chemostratigraphy at DSDP Site 436, and Table 2.1 provides the criteria for unit designations. Unit C (brown-black pelagic clay) is clearly distinguished from Units A and B by high Th and Ce concentrations, and high Co/TiO_2 (another sedimentation rate proxy), although subunits within Unit C have different proportions of these three tracers (e.g., C3 has intermediate Co/TiO_2). Unit B is also readily distinguished from Unit A based on Th and Ce concentrations, and has a Zn/Ce ratio < 1.3. Unit A subdivisions are more subtle and can be most easily identified by variations in Ce and Zn (Figure 2.4). Unit A3 has higher Ce/Ce* (> 1.2) than Units A1 or A2; Unit A1 has higher Zn/Ce (> 1.7) than Units A2 or A3. Unit A2 occupies an intermediate position in Zn/Ce, with a lower Ce/Ce* than A3 and lower Zn concentration than A1. The Zn/Ce ratio may be a measure of biological productivity, and it is one of the few tracers that varies systematically throughout Unit A. The geochemical distinction between Unit A1 and Unit A2 is more subtle than others that we discuss here, but these subunit designations are consistent with the biostratigraphy.

Namely, sediments that are geochemically designated as Unit A1 are late Pliocene to Pleistocene while Unit A2 sediments are Miocene to Pliocene in age. Some of these tracers may be more susceptible to diagenesis or fluid-reactions (Ce/Ce*, Zn/Ce) than others (Th, Ce concentrations and Co/TiO_2). We emphasize that no single tracer, but rather an ensemble of attributes, is diagnostic of any particular subunit (Table 2.1).

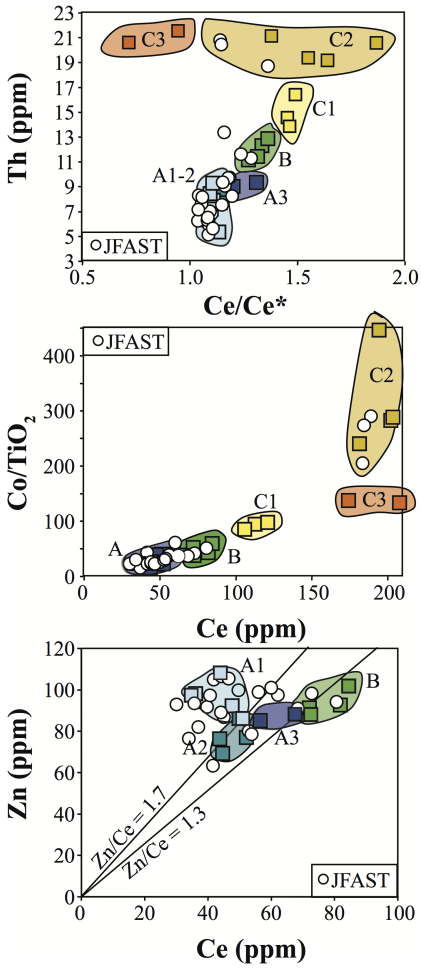

Figure 2.4: Scatterplots of key trace element parameters that differentiate between sedimentary units in Western Pacific cores. Colored squares are DSDP Site 436 samples (color-coded by sedimentary unit as introduced in Figure 2.2) and white circles are JFAST samples. In these examples, we see that Unit C is distinguishable from Units A and B and can be subdivided into Units C1–3 based on Th, Ce/Ce*, Ce, and Co/TiO_2. Unit B can be distinguished from Unit A based on higher Th and Ce concentrations and lower Zn/Ce (<1.3) values. The bottom plot demonstrates how Unit A can be subdivided into Units A1–3 based on Zn/Ce values as well as higher Ce/Ce* values for Unit A3 than Units A1–2. A more comprehensive list of trace elements used for fingerprinting these sedimentary units can be found in Table 2.1.

2.4.2 Trace element signatures at JFAST

We use the above template at DSDP Site 436 to assign JFAST samples to each unit. Figure 2.4 shows that the JFAST sediments overlap almost completely with the trace element variations in DSDP Site 436, further supporting a common original chemostratigraphy at both sites. Some of the JFAST sediments have slightly lower Ce/Ce* for the same Th concentration as DSDP Site 436 sediments, and it is possible this is a secondary (diagenetic or fault-fluid reaction) effect due to reduction of Ce^{4+} to Ce^{3+}. Likewise, the Zn concentrations in the youngest JFAST sediments are more varied than those at DSDP Site 436, and this could be due to original or secondary differences in the diatomaceous ashy-clays. We expect Ce and Th concentrations, as well as Co/TiO_2, to be more impervious to secondary processes.

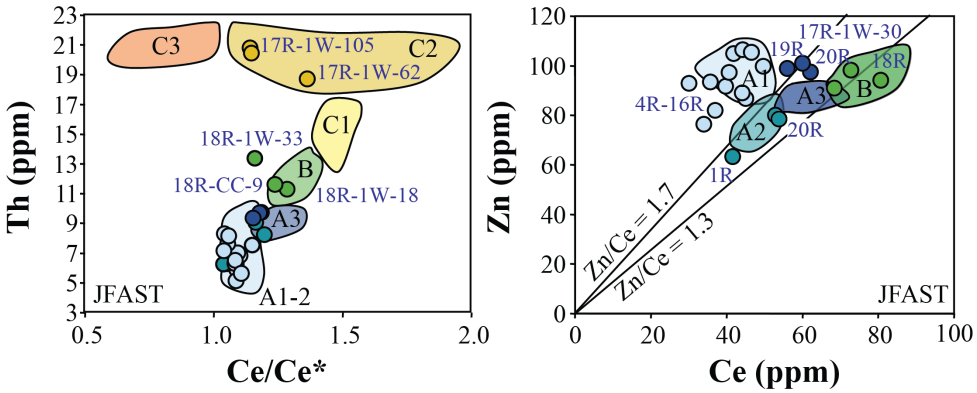

Figure 2.5: Assignment of JFAST samples to Western Pacific sedimentary units using the trace element fields from DSDP Site 436 developed in Figure 2.4. JFAST samples (circles) are colored according to the sedimentary unit to which they are assigned. Labels indicate core number and depth of the JFAST samples using standard IODP format (core number, tool, section and depth in core).

Figure 2.5 shows the unit designation for the JFAST sediments, superimposed on the field boundaries defined by DSDP Site 436 sediments. The brown-black pelagic clays of Core 17R clearly correspond to Unit C2. Core 18R sediments are best ascribed to Unit B, while Cores 19R-20R most resemble Unit A2 and A3 sediments, as does Core 1R. The long section of sediment in Cores 4R–16R is assigned to Unit A1. From these designations, it is clear that the stratigraphic sequence is re-ordered in the JFAST core, with older sediments (1R) over younger sediment (4R–16R), and younger sediments (19R–20R) below older sediments

(17R).

2.4.3 Trace element stratigraphy at JFAST

Using the fingerprinted samples from the JFAST core, we present a trace element-based stratigraphy of the subducted Pacific Plate at the JFAST site (Figure 2.6). From this analysis, we see that the top of the JFAST core (1R, ∼180 mbsf) is composed of Unit A2. This is consistent with radiolarian age dates in this section of the JFAST core of ∼4.4 Ma. Below this, there is a large break in core recovery until ∼650 mbsf. Based on radiolarian age dating, the top two cores from the second interval of recovery (2R-3R, ∼650-660 mbsf) are ∼10–11 Ma. Therefore, we assume that these cores can also be designated as Unit A2, although we did not sample this interval for the current study. It is worth noting that because the radiolarian ages of Core 1R are much younger than those of 2R–3R, this could also represent a faulted section. However, with limited core recovery in this shallowest section, no definitive conclusions are possible at this time. From a depth of ∼690 mbsf and below, most of the JFAST core is composed of Unit A1, consistent with radiolarian ages of 0.3–3 Ma (Figure 2.6). In this section, several faults are described from structural observations of the core. Notably, faults or brecciated regions are observed at ∼700, 720, and 817 mbsf [Chester et al., 2013, 2012, Kirkpatrick et al., 2015]. All of these faults occur within Unit A1 material where we do not have good chemostratigraphic resolution and cannot identify within-subunit age gaps or inversions.

Near the plate boundary, the structure becomes more complicated and contains several age gaps and inversions. At the identified décollement (17R, ∼820 mbsf), Holocene to Late Pliocene Unit A1 overlies the Unit C2 Early Miocene to Eocene pelagic clays. Assuming the Unit A1 samples are from the bottom of the Unit A1 sequence, we give a conservative estimate of ∼15 Ma of missing section between the Unit A1 mudstone and Unit C pelagic clays at 820 mbsf. This corresponds with 114 m of missing section assuming unit thicknesses of DSDP Site 436. Within the décollement pelagic clay layer, a mudstone sliver from Unit A3 indicates another significant fault with Unit C2 above and below the sliver. At ∼822

mbsf there is a major fault based upon the sharp contacts within Core 17R and the scaly microstructure of the pelagic clay layer that is indicative of shear [Labaume et al., 1997, Moore et al., 1986, Vannucchi et al., 2003].

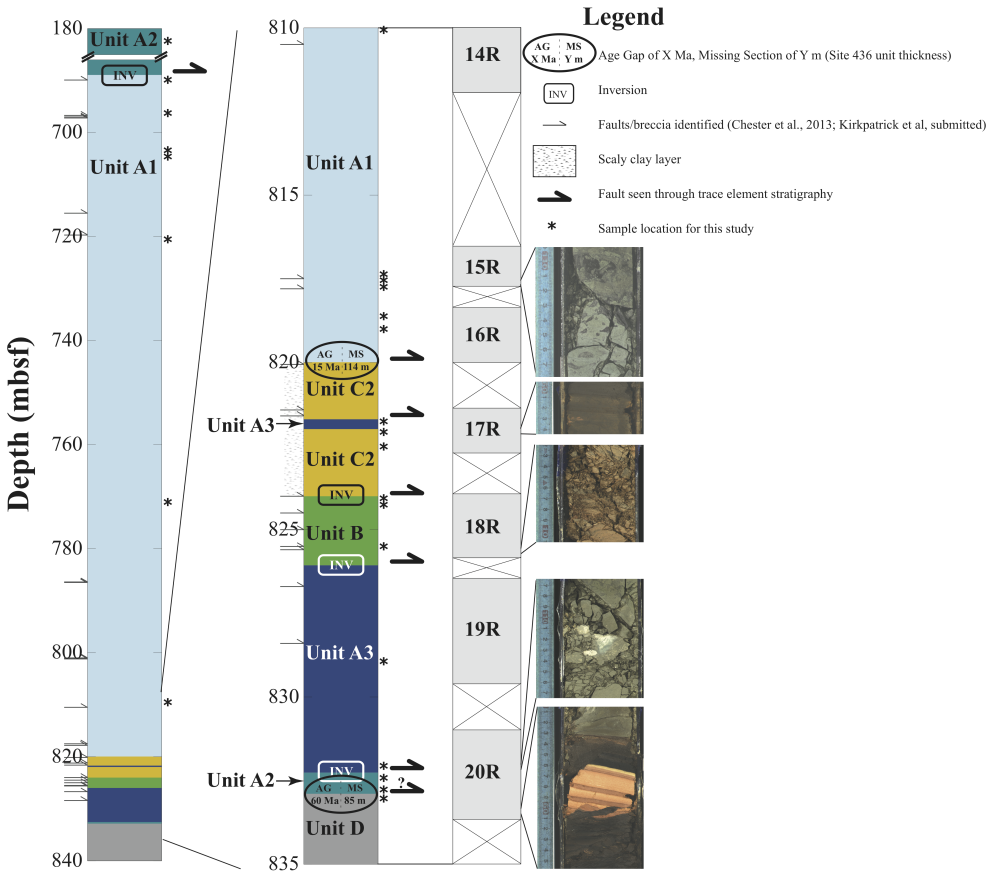

Figure 2.6: Stratigraphy of the JFAST site based upon trace element correlations to DSDP 436. Deformation features (i.e. faults, breccia, deformation fabrics) identified in the science party report are indicated with arrows to the left of each stratigraphic column [Chester et al., 2012, Kirkpatrick et al., 2015] and samples from this study are indicated with asterisks on the right. Faults inferred from the trace element stratigraphy are indicated by large arrows to the right of each column. The Japan Trench accretionary wedge at the JFAST site is composed primarily of Unit A material (note the scale break in the left stratigraphic column). There is more stratigraphic complexity approaching the décollement including a significant inversion with Unit C overlaying Units A and B and two age gaps of 15 and 60 Ma, respectively.

Below the Unit C2 pelagic clay is Unit B claystone indicating another inversion. Within the Unit B claystone are two faults observed in the JFAST core at 824.4 and 825.1 mbsf [Kirkpatrick et al., 2015], which do not appear in the stratigraphy as inversions or age gaps. Unit B in turn overlies Unit A3. This constitutes another significant age inversion below

the pelagic clay, possibly representing a fault within unrecovered section between Cores 18R and 19R. The Unit A3 mudstone overlies an interval of Unit A2 sediment (Figure 2.6) at approximately 832 mbsf (Core 20R), another possible stratigraphic inversion. Although no faults have been previously identified at this depth, the inversion of Unit A3 over A2 is marked by a change in mudstone color (with mottling over a distance of ∼30 cm) as well as a zone of brecciation. We note here that this sequence of Unit B overlying Unit A3, which, in turn, overlies Unit A2, could represent an overturned section, however, the unit thicknesses are significantly smaller than those at DSDP Site 436. Finally, near the bottom of the JFAST core (within Core 20R) at ∼833 mbsf, Unit A2 directly overlies Unit D Cretaceous partially silicified clay. This requires a ∼60 Ma stratigraphic age gap (∼85 m assuming DSDP Site 436 unit thicknesses) above the partially silicified clay layer. This age gap corresponds with deformation features observed in Core 20 such as a dark seam between the Unit A3 mudstone and the finely layered Unit D clay [Figure 2.6; Kirkpatrick et al., 2015].

2.5 Discussion

The trace element approach allows for additional relative age constraints that improve on the stratigraphy at JFAST, especially below the pelagic clay layer. Although several faults were previously identified bounding the pelagic clay layer [Chester et al., 2012, Kirkpatrick et al., 2015], the trace element stratigraphy presented here suggests that several additional large displacement faults exist between the pelagic clay layer at ∼822 mbsf and the Cretaceous partially silicified clay at 833 mbsf. These faults are identifiable based on our ability to fingerprint the Quaternary to Miocene mudstones in this interval (Figure 2.6). For example, we identify the topmost mudstone in the 824–832 mbsf interval as Unit B. Below this, we see the younger mudstone unit (Unit A3) underlain by Unit A2 mudstone. The stratigraphic inversions present here imply a significant fault at a depth of ∼826 mbsf and another at ∼832 msbf. One of the most significant age gaps is observed at ∼833 mbsf. Based on trace element measurements, we see Unit A2 material overlying Unit D chertified clay. This section is characterized by an extremely thin mm-scale transition from Unit A mudstone to

Unit D partially silicified clay. The presence of a potential gouge layer (see core images in Figure 2.6) as well as slight misorientation of bedding in the pelagic clay below this contact suggest that the ∼60 Ma of missing stratigraphy here could imply a major fault.

Notably, the bedding below Core 17R is much more shallowly dipping (∼10^o rather than ∼67^o above the pelagic clay layer). The absence of observed bedding cutoffs in the deeper JFAST cores suggests that any faults in this section are sub-parallel to bedding and likely highly localized. The localized shear strain accommodated by the faults would not have been captured by the anisotropy of magnetic susceptibility (AMS) results (due to sample spacing), which suggest vertical shortening in the deeper part of the section [Yang et al., 2013]. It follows that even though the faults we document would have accommodated little flattening, our observations are not inconsistent with the AMS results. Significant amounts of displacement would be required to explain the stratigraphic reversals and gaps on low dip structures. This may imply that the dip is not regionally constant on individual fault strands, consistent with a duplex or fault ramp model (Figure 2.7).

Chester et al. [2013] estimated that the plate boundary at the JFAST site has hosted ∼3.2 km of displacement based on balancing a two-dimensional cross-section. Because the pelagic clay layer showed the most pervasive deformation, the largest age gap in the biostratigraphy, and a low frictional strength at both slow and fast velocities [Ikari et al., 2015b], most of the 3.2 km of displacement was thought to occur within it. We have shown here that the faults we identify at the JFAST site may have accommodated a significant amount of the inferred plate boundary slip, implying that cumulative displacement at the plate boundary was not localized exclusively in the pelagic clay layer but rather distributed among several major faults. Adding together the faults inferred from the chemostratigraphy, along with the distances between them [c.f. Rowe et al., 2013] yields a plate boundary thickness ∼15 m which is consistent with the maximum décollement thickness proposed by Kirkpatrick et al. [2015]. We also note that because the JFAST core did not penetrate to basement, significant faults could have been missed below the bottom of the recovered JFAST section.

A thicker décollement (at least 10 m) would be more in keeping with observations in other subduction zone settings such as Barbados [Maltman et al., 1997], although estimates from Nankai suggest a décollement more on the order of tens to hundreds of meters [Moore et al., 1990, Rowe et al., 2013, Ujiie and Kimura, 2014]. Our results imply that structures with insignificant appearance in the core, such as thin shear surfaces with little notable damage surrounding them, may be responsible for significant displacement.

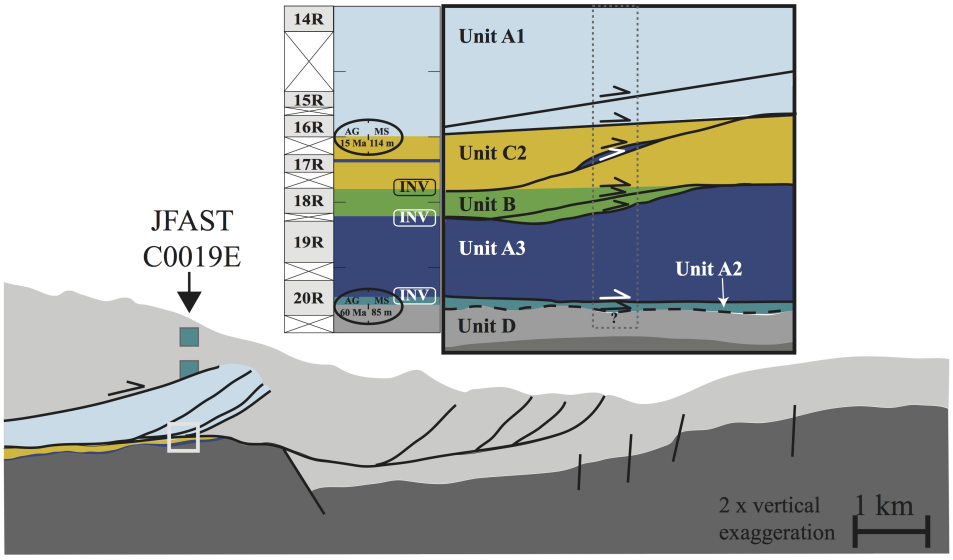

Figure 2.7: Structural interpretation of the accretionary wedge in the Japan Trench based on our trace element stratigraphy at Site C0019E. Light gray sediments in the accretionary wedge are undifferentiated frontal prism sediments that are unconstrained by our data. Dark grey at the bottom is basement. Inset is a blow-up of the region boxed in white from the larger cross section. The stratigraphic section developed in this paper and the core recovery are shown to the left of the blow-up. The section inferred to have been drilled at JFAST is indicated by the dark grey dotted line in the structure blow-up. After Kirkpatrick et al. [2015].

The pelagic clay layer in the JFAST core, like most smectite-rich clays, is frictionally weak and extremely velocity weakening at high slip rates, indicating that both aseismic and seismic slip could occur within this layer [Faulkner et al., 2011, Ikari et al., 2015b,a, Sawai et al., 2014, Ujiie and Tsutsumi, 2010]. However, the presence of multiple, large-displacement faults in the surrounding sediments implies that shallow slip was not exclusively localized within the pelagic clay. This could suggest that the path of a rupture during dynamic seismic

slip might not be completely controlled by differences in friction between stratigraphic units. Instead, earthquake rupture might propagate or branch in a more chaotic way [Poliakov et al., 2002]. Furthermore, low velocity friction experiments on samples from the JFAST core show that the younger mudstones, though frictionally stronger than the pelagic clay, are significantly more velocity weakening [Ikari et al., 2015b,a].

While we can determine that significant displacement took place on a fault by noting major stratigraphic inversions and age gaps, we cannot tell which earthquake, how many earthquakes, or even if an earthquake rather than aseismic creep was responsible for the displacement based on the chemostratigraphy presented here. Although the stratigraphy suggests large displacement, it does not require any particular inversion or age gap to have been produced specifically by the Tohoku earthquake. Nonetheless, the depth range over which significant faults are identified is not excluded by temperature data collected from a thermistor string installed during the JFAST project [Fulton et al., 2013]. Inversions of the temperature data are consistent with a fault that was frictionally heated during the earthquake, and several of the faults identified in the JFAST core could fit the slip location identified in the temperature data.

There are a number of additional factors that might affect the trace element method of identifying stratigraphic units, including overlapping elemental fingerprints, sediment mixing, fault heating and fluid flow. Western Pacific units in this study can be distinguished using multiple trace element signatures, however this could be an issue in other regions. Mixing of multiple units could occur if a sample is collected on a border between different units or as a result of faulting if there is soft-sediment deformation during an earthquake. Mixing would cause the sample to exhibit trace element signatures intermediate between the two homogenized units. While we do observe some JFAST samples that fall outside of the trace-element fields defined from DSDP Site 436, they are generally not along tie lines between fields, suggesting mixing is minimal. Bedding is also evident in non-faulted regions indicating mixing is unlikely to be an issue for many of the samples. Finally, we have not

explicitly considered the role of fault heating or faulting-related fluid flow to mobilize certain elements [Ishikawa et al., 2008] and, thus, change the trace element signature in the JFAST core relative to that of the corresponding stratigraphic unit in the reference cores. While Zn concentrations and Ce/Ce* could potentially be altered by this process, Ce and Th concentrations and Co/TiO_2 ratios that are also used to define the chemostratigraphy should be less susceptible to these processes.

2.6 Conclusions

Based on trace element geochemistry, we fingerprint stratigraphic units in the Western Pacific to develop a detailed stratigraphy of the JFAST core. The trace element stratigraphy agrees well with the coarse stratigraphy determined by radiolarian age dating, while also identifying several age inversions and sections of missing stratigraphy that were not apparent from the biostratigraphy. These features require multiple faults within a $\sim$15 m-thick zone of sediment above the Cretaceous chert layer at the bottom of the JFAST core. Our findings imply that deformation at the plate boundary was not limited to the frictionally weak pelagic clay layer as previously suggested. Rather, the large displacement faults identified here should be considered as candidate faults for the Tohoku earthquake.

2.7 Acknowledgements

Samples for this study were provided by the International Ocean Discovery Program (IODP). We thank the curatorial staff at the Kochi Core Center for help obtaining samples. Funding for this project was provided by U.S. National Science Foundation grant OCE 12-60555 and a Schlanger Ocean Drilling Fellowship to H.S.R., part of the NSF-sponsored U.S. Science Support Program for IODP that is administered by the Consortium for Ocean Leadership, Inc. Thanks to Siobhan Campbell for work in processing samples for trace element analysis. We thank editor An Yin and an anonymous reviewer for helpful suggestions on the manuscript.

3 | Reaction kinetics of alkenone and n-alkane thermal alteration at seismic timescales

Co-authors: P. J. Polissar and H. M. Savage

This chapter has been published: *Rabinowitz, H. S., Polissar, P. J., & Savage, H. M. (2017). Reaction kinetics of alkenone and n-alkane thermal alteration at seismic timescales. Geochemistry, Geophysics, Geosystems, 18(1), 204-219.*

Recent experiments and field observations have indicated that biomarker molecules can react over short timescales relevant to seismic slip, thereby making these compounds a useful tool in studying temperature rise in fault zones. However, short-timescale biomarker reaction kinetics studies have previously focused on compounds that have already experienced burial heating. Here, we present a set of hydrous pyrolysis experiments on Pleistocene-aged shallow marine sediment to develop the reaction kinetics of long-chain alkenone destruction, change in the alkenone unsaturation ratio ($U^{k'}_{37}$), and change in the n-alkane chain length distribution. Our results show that biomarker thermal maturity provides a useful method for detecting temperature rise in the shallow reaches of faults, such as subduction zone trench environments. Through the course of our work, we also noted the alteration of total alkenone concentrations and $U^{k'}_{37}$ values in crushed sediments stored dry at room temperature for durations of months to years but not in the solvent extracts of these materials. This result, though parenthetical for our work in fault zones, has important implications for proper storage of sedimentary samples to be used for alkenone paleotemperature and productivity

analysis.

3.1 Introduction

The distribution and structure of organic molecules (biomarkers) evolves in measurable ways when sediments are heated over a range of timescales and temperatures. Thermal maturity of organic molecules has long been studied in applications related to petroleum generation, which usually occurs on the scale of millions of years [Peters et al., 2004]. Only recently has biomarker thermal maturity over very short timescales been experimentally investigated [Sheppard et al., 2015]. The kinetics of biomarker maturation at short timescales are an important tool for constraining the temperature rise in sediments exposed to short duration heat sources such as earthquakes, forest fires, bolide impacts, dike intrusions, and hydrothermal fluids [Bishop and Abbott, 1993, Bowden et al., 2008, Kaiho et al., 2013, Parnell et al., 2010, 2005, Polissar et al., 2011, Savage et al., 2014, Schimmelmann et al., 2009, Simoneit et al., 1994, Simoneit, 1994]. In this paper, we focus on thermal alteration from earthquakes, but our results are applicable to other environments as well.

Temperature rise during earthquakes is a function of the absolute fault shear stress during sliding. However, determining earthquake temperature rise from the rock record has proven difficult. At shear stress values on the order of 10 to 100 MPa (typical values within the seismogenic zone), temperature rise could easily reach several hundred to over 1000 ^{o}C during large earthquakes, which is hot enough to melt rock. Some faults have unequivocally experienced such significant temperature rises, and can be identified by the presence of frictional melt known as pseudotachylyte [e.g. Sibson, 1975]. Pseudotachylyte in faults, however, is not ubiquitous and its absence in most faults raises the difficult question: why did the fault not get hot enough to melt? One possibility is that pseudotachylyte does not preserve well in the rock record, retrograding to minerals such as micas that make it difficult to pinpoint their earthquake-related origins [Kirkpatrick and Rowe, 2013, Rowe and Griffith, 2015]. Another possibility is that earthquakes generally do not produce sufficiently large

temperature excursions to melt fault rocks. A range of dynamic weakening mechanisms such as pore fluid pressurization, flash heating, and mineral dehydration, have been documented in laboratory experiments [e.g. Collettini et al., 2013, Di Toro et al., 2011, Han et al., 2007, Mase and Smith, 1985, Rice, 2006] and provide ways to reduce the effective shear stress on a fault during dynamic slip, thus limiting the temperature rise on the fault over the course of a seismic event. However, it is not well understood how effective these mechanisms may be in real faults.

Other methods have been developed more recently to investigate the sub-solidus coseismic temperature rise on a fault, such as thermally dependent alterations to the smectite structure, decarbonation of the fault host rocks, changes in the magnetic signatures of frictionally heated sediments, and fission-track thermochronology [D'Alessio et al., 2003, Hirono et al., 2007, Rowe and Griffith, 2015, Schleicher et al., 2015, Yang et al., 2016]. Additionally, organic thermal maturity is becoming an established paleoseismic indicator that can be applied to faults hosted in sedimentary rocks. Field studies of the thermal maturity of organic material have considered vitrinite reflectance [Barker and Pawlewicz, 1986, Burnham et al., 1989, Fulton and Harris, 2012, Sakaguchi et al., 2011], as well as molecular methods focusing on a range of biomarkers [Polissar et al., 2011, Savage et al., 2014].

Previous studies of biomarker thermal maturity have focused on faults hosted in moderate to deeply buried rocks where the suite of biomarkers useful for paleoseismic thermal maturity studies reflect a relatively high background thermal maturity (e.g. methylphenanthrenes and diamondoids) [Polissar et al., 2011, Savage et al., 2014, Sheppard et al., 2015]. In order to apply biomarkers as a fault thermometer in shallow sediments that have not experienced burial heating (such as would be expected in faults located within the shallowest portions of subduction zones that determine tsunamigenic potential) it is necessary to determine the kinetics of thermal alteration for immature biomarker molecules. In this study, we develop the kinetics of thermal maturity for long-chain alkenones and plant-wax n-alkanes. Plant-wax n-alkanes are ubiquitous in Cenozoic (and older) thermally immature sediments

[c.f. Brooks and Smith, 1967] while long-chain alkenones are present in most Neogene marine sediments [Brassell, 2014]. This widespread occurrence makes studies of their thermal alteration applicable to most subduction zone settings.

3.2 Background

3.2.1 Alkenones

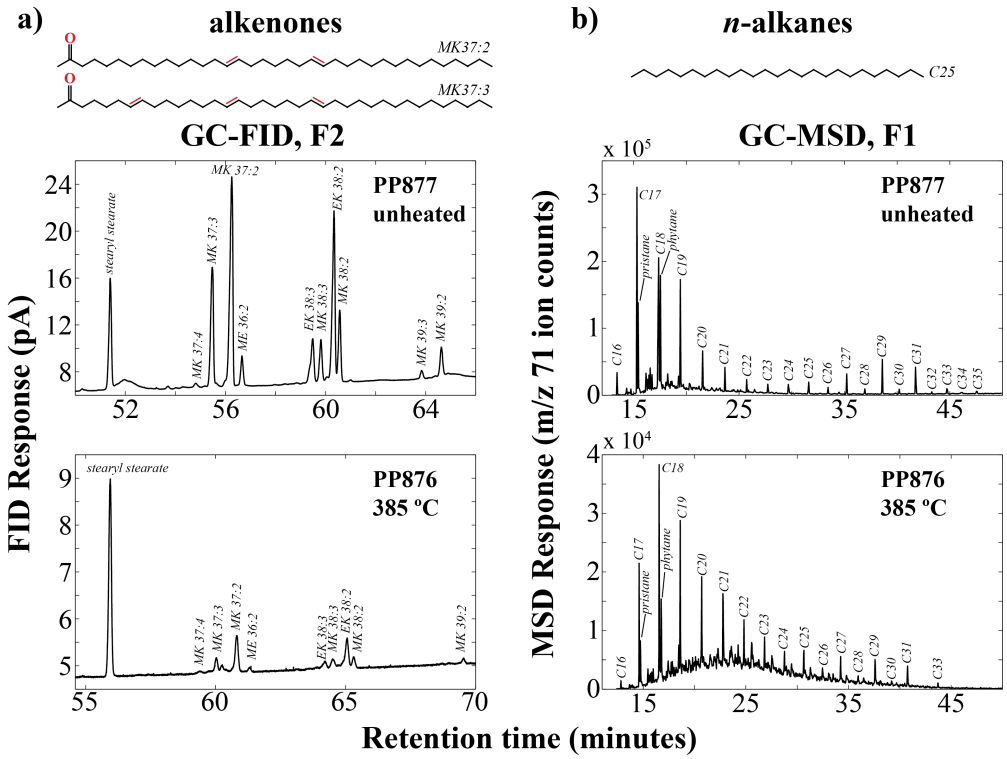

Figure 3.1: Molecular structure and gas chromatographic analysis of long-chain alkenones and *n*-alkanes. a) Alkenone concentrations are higher in an unheated sample (PP877) compared to a sample exposed to high temperature (PP876). Alkenone data (a) were collected on a GC-FID with stearyl stearate as an internal recovery standard. Alkenone peaks are labeled as methyl and ethyl ketones with the number of carbon atoms and number of double bonds. b) *n*-alkane data were collected on a GC-MSD. Shown are the m/z 71 extracted ion chromatograms that is characteristic for *n*-alkanes. Note that the *n*-alkane internal recovery standard, 5a-androstane, does not have a strong m/z 71 response and is not seen here. Retention times for the unheated and heated samples are slightly different due to slight changes in the column length resulting from column maintenance between run dates.

Long-chain unsaturated methyl and ethyl ketones (hereafter alkenones, Figure 3.1a) are produced by a number of haptophyte algae and are well preserved in ocean sediments [Herbert, 2014]. The relative proportion of alkenones with two, three or four double bonds is

thought to be controlled by sea surface temperature (SST) with the level of alkenone unsaturation ($U^{k'}_{37}$) varying linearly with temperature [Brassell et al., 1986, Prahl et al., 2000]. Hydrous pyrolysis experiments have shown that alkenones thermally mature to an unknown product at temperatures of ∼200 ^{o}C and entirely disappear from the sediment when held at 250 ^{o}C for 24 h [Simoneit et al., 1994]. However, these experiments do not confirm that alkenones react on the shorter time-scale associated with earthquakes and other short timescale heating processes. Here, we establish the kinetics of alkenone destruction and the change in $U^{k'}_{37}$ at short timescales.

3.2.2 *n*-Alkanes

n-Alkanes are linear hydrocarbons (Figure 3.1b) derived from a wide variety of natural sources. Long-chain *n*-alkanes are found in plant leaf waxes with a preference for odd-over-even chain lengths [Carbon Preference Index – CPI; Eglinton and Hamilton, 1967, Eglinton et al., 1962, Rieley et al., 1991]. The distribution of *n*-alkane chain lengths is known to change with increasing thermal maturity. Long-chain *n*-alkanes with no carbon preference are formed during kerogen cracking and petroleum formation. With further heating, cracking of the *n*-alkanes themselves reduces the long-chain *n*-alkane abundance [Eglinton et al., 1988]. The formation of *n*-alkanes during heating causes the *n*-alkane CPI to decrease, particularly in long chain *n*-alkanes [Simoneit, 1994]. These thermal alterations to the *n*-alkane chain length distribution have been studied in experiments on the scale of days [e.g. Eglinton et al., 1988]. However, the thermal maturity of *n*-alkanes has not previously been established on shorter timescales relevant to fast geologic heating processes such as earthquakes.

3.3 Methods

3.3.1 Hydrous Pyrolysis Experiments

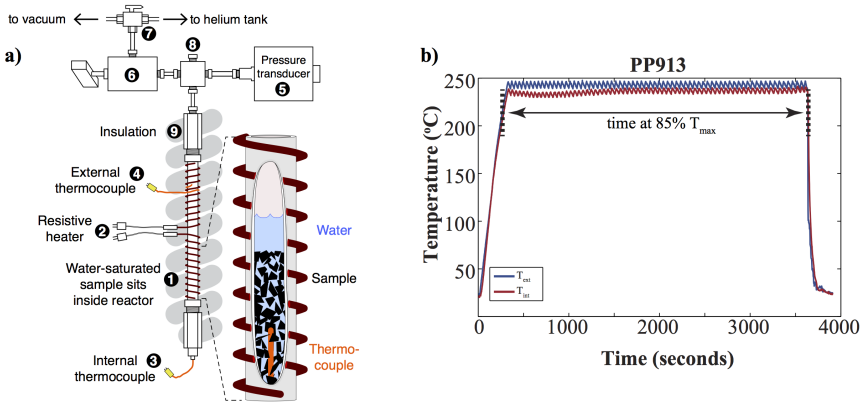

Figure 3.2: Heating apparatus used in hydrous pyrolysis experiments [a, after Sheppard et al., 2015]. Water and sediment are added to the reactor tube (1) with the internal thermocouple (3) inserted through the bottom fitting. This assembly is then mounted on the experimental frame and is leak-checked by pressurizing to 6895 kPa (1000 psi) of helium (5-8). The tube is then wrapped with a resistive heater (2) and the external thermocouple (4) is placed with its tip to the reactor tube. Finally, the assembly is wrapped with insulation (9). At the end of each experiment, the insulation is unwrapped and the sample is quenched by spraying DI water over the reactor tube. An example of the temperature data (b) collected during the experiments shows the internal and external thermocouple temperatures and typical heating and cooling times. Experiments that experienced peak temperature larger than 30 ^{o}C above the target temperature and a peak duration longer than 350 seconds were not used for later calculations in this paper.

We present a series of hydrous pyrolysis experiments performed on crushed and homogenized samples from deep-sea piston core RC14-99 [Morley and Heusser, 1997], taken near to the Japan trench (36^{o}57.9′N, 147^{o}55.7′E, 5652 m depth). This material was selected for its similarity to sediments being subducted in the Japan trench where tsunamigenic earthquakes have occurred [Maeda et al., 2011, Minoura et al., 2001]. Sediment was sampled from RC14-99, section 6b throughout its depth for 3 batches (Batch A: 1285–1405 cm, Batch B: 1280–1436 cm, Batch C: 1244–1454 cm; see Table B.1 for exact sampling depths). Three batches were required due to limitations on the amount of core that we were able to sample with our first two sample requests and because we depleted our initial batches before we had completed our experiments. The core pieces for each batch were crushed with mortar and

Table 3.1: Experimental Conditions

Purpose	Sample Number	Weight (g)[a]	Time (min)[b]	Temp (^{o}C)[c]	Sed. Batch
Unheated control and	PP877[d]	4.879	——-	20	A
	PP920[d]	5.006	——-	20	B
	PP1051[d]	5.027	——-	20	A+B
alkenone degradation analysis	PP1285[d]	2.003	——-	20	C
	PP1361[d]	1.94	——-	20	C
	PP1286[f]	1.936	——-	60	C
Low temperature	PP1287[f]	1.968	——-	60	C
	PP1288[f]	1.979	——-	60	C
	PP1362[f]	1.983	——-	100	C
thermal alteration	PP1363[f]	1.944	——-	100	C
	PP1364[f]	2.009	——-	100	C
	PP1045	4.701	178.55	124.08	A+B
	PP918	4.969	87.43	132.39	B
High temperature	PP873	3.37	28.88	134.25	A
	PP913	4.795	56.25	235.57	B
	PP854	5.077	25.63	237.38	A
	PP917	4.419	83.78	252.94	B
	PP914	4.455	53.93	263.7	B
thermal alteration	PP915	4.639	52.68	308.63	B
	PP875	1.905	22.27	349.97	A
	PP876	1.121	20.07	384.8	A

[a] Sediment weights measured after sample recovery
[b] Time at 85% T_{max} in minutes unless otherwise noted
[c] Mean temperature during time at 85% T_{max}
[d] Sample used as unheated control
[e] Sample used for alkenone degradation analysis
[f] Experiments conducted in glass vials in a GC oven.

pestle and mixed to homogenize the sample for the experiments. The prepared sediment was stored in an ashed Fisher 250 ml glass jar, covered with a screw cap lined with ashed foil and placed in a drawer at room temperature (∼20 ^{o}C) and experimental samples were removed at the time of the experiment using an ashed spatula.

Rapid high-temperature heating experiments were conducted using a small, carburized reactor designed for rapid heating [Figure 3.2; Sheppard et al., 2015]. To prepare these experiments, 5.0 g of sediment and 6 ml of Fisher Optima-grade ultra-pure deionized water (degassed with N_2 using a sparger) were poured into the reactor. First, about half of the sediment was added, followed by half of the water. The sample was tamped down with a metal push-rod to mix the sediment and water, and then this process was repeated with the remainder of the sediment and water. This procedure prevents un-wetted sediment from getting stuck to the bottom of the reactor or floating on top of the water layer. The metal pushrod, reactor and all other materials that contacted the sample were cleaned with

dichloromethane (DCM) and methanol (MeOH) before use.

Once loaded, the reactor was attached to the experimental frame (Figure 3.2a), evacuated using a vacuum pump, and then pressurized to 1000 psi (6.9 MPa) using He gas to check for leaks. Pressure was reduced to 10–100 psi of helium (69–690 kPa) prior to a run. Samples were heated using a resistive heater wrapped around the reactor tube. Temperature was measured using an inner thermocouple and an outer thermocouple (Omega J-type thermocouple, maximum temperature range 0–750 ^{o}C) and controlled using a proportional-integral-derivative (PID) controller. During the experiments, the reactor was wrapped with insulation to allow rapid heating and help maintain temperature. Experiments were conducted at temperatures ranging from 120–350 ^{o}C over durations of 20–180 min (Table 3.1). Samples achieved experimental temperatures in less than 10 min (Figure 3.2b). At the end of each experiment, insulation was quickly removed, the resistive heater was unplugged from the PID controller, and the reactor tube was quenched by spraying it with deionized water until the temperature read by the thermocouples was reduced to room temperature. Experiments were quenched in about 1 minute (Figure 3.2b). After the experiment, samples were removed from the reactor using the cleaned push-rod and an ashed (450 ^{o}C for 8 hours) glass fiber filter paper plug (Whatman GF/C) and pushed through into an ashed recovery beaker. The rolled filter paper was necessary to maximize sample recovery by preventing the sample (which had a fine-grained muddy consistency) from sticking to the reactor walls. The inside of the reactor tube was then rinsed with ultra-pure deionized water into the recovery beaker. Though we were able to recover almost all of the sediment for most experiments (within $\sim$0.5 g of the initial 5 g; Table 3.1), recovery of sediment from the reactors was sometimes incomplete, yielding variable sample weights for extraction of organic material. The variability in sample recovery was accounted for by re-weighing samples after extraction to obtain the weights used in the determination of biomarker concentrations.

Low temperature hydrous pyrolysis experiments were also conducted to constrain the low temperature kinetics of alkenone and n-alkane thermal maturity over longer times (Ta-

ble 3.1). Our experimental heating setup for the high temperature experiments was not designed for the longer experiments needed to measure reaction kinetics at low temperatures. Therefore, these experiments were conducted in the oven of a gas chromatograph at temperatures of 60 and 100 ^{o}C and times ranging from 2 h to 4 days. Two-gram samples were placed into 8 ml ashed borosilicate glass vials with 5 ml of degassed ultra-pure deionized water and thoroughly mixed using a spatula cleaned with DCM and MeOH. Vials were purged for 15 s with N_2 gas before being tightly capped. For each set of experiments (at 60 and 100 ^{o}C) a control vial was left at room temperature for the duration of the experiments. The experimental vials were placed in the oven into a beaker filled with sand that was pre-heated to the experimental temperature. The sand provided thermal mass to minimize temperature fluctuations when the oven door was opened. In each experiment the temperature was held constant throughout and at each of three pre-designated time points (2 h, 1 day, and 4 days), one vial was removed from the oven and quenched by running cold water over the vial until it reached room temperature.

3.3.2 Total Lipid Extraction

After recovery from the reactor, samples were freeze dried for 1–3 days under a vacuum of 60×10^{-3} mbar. The total lipid extract (TLE) was obtained by sonicating the freeze-dried sediments in a solution of 9:1 DCM: MeOH three times for 15 min. After each sonication, samples were left to settle for 10 min and then the solvent was poured into a 60 ml vial. The experimental samples were too fine grained to decant without pouring significant amounts of sediment into the 60 ml vial during the sonication extractions. Because of this, post-sonication solvent was filtered through an ashed glass fiber filter paper (Whatman GF/F) into the 60 ml recovery vials. We initially used sonication extractions to avoid further heating the sediment during Accelerated Solvent Extraction (ASE) where our standard 100 ^{o}C method could potentially contaminate the temperature signal from the experiments. However, upon further testing, we found that sonication extraction yielded incomplete recovery of all compounds and that ASE extraction at 100 ^{o}C effectively extracted all alkenone and

alkane molecules. We performed further testing to determine whether ASE extraction altered the distribution and thermal maturity of the extracted compounds in any way. These tests indicated no difference in biomarker signatures in 100 ^{o}C ASE extractions and multiple, lower temperature extractions of the same material (see Section B.2 for more detail).

To ensure complete recovery of organic molecules, samples were extracted a second time using ASE extractions with 9:1 (v/v) DCM:MeOH at an extraction temperature of 100 ^{o}C. Laboratory recovery standards were added to the collected TLE (5a-androstane and stearyl stearate) and the liquid was evaporated (by a combination of drying in a hood and under a stream of N_2) and then transferred to a 4 ml vial using DCM. Sonication extracted and ASE extracted samples were analyzed separately, with alkenone and *n*-alkane concentrations from the sonication and ASE extractions for each experimental sample summed after measurement. Sonication extractions yielded 40–100% of the total TLE (Figure B.1). Due to some sediment loss in the sonication procedure and the small amount of sediment used in the low temperature hydrous pyrolysis experiments, samples for the 60 and 100 ^{o}C experiments were only extracted using the ASE method.

3.3.3 Column Chromatography and Gas Chromatography

The TLE in the 4 ml vial was separated into three fractions (aliphatic, ketone, and polar) using silica gel column chromatography. First, the TLE was brought up in 1 ml hexane and pipetted onto a column containing 0.5 g DCM-rinsed silica gel. An additional 3 ml hexane was then added to the column to elute the F1 (aliphatic) fraction. This procedure was repeated for the F2 (ketone) and F3 (polar) fractions with DCM and MeOH, respectively. The aliphatic and ketone fractions were dried under N_2 and transferred to 2 ml vials with DCM. These were then dried under N_2 and brought up in hexane and toluene respectively for analysis using a gas chromatograph with a flame ionization detector (GC-FID) for the ketone fraction and a gas chromatograph with mass selective detection (GC-MSD) for the aliphatic fraction. Most alkenone samples were run on the GC-FID using the PTV injector with a 60 m DB1 column with a diameter of 0.25 mm and a stationary phase thickness

of 0.1 μm with a 10 m non-polar guard column. Samples were injected at a volume of 1 μl. Upon injection, the oven was held at 90 ^{o}C for 1.5 min, raised to 250 ^{o}C at a 25 ^{o}C/min ramp, then raised to 313 ^{o}C at a 1 ^{o}C/min ramp and finally raised to 320 ^{o}C at a 10 ^{o}C/min ramp and held at 320 ^{o}C for 20 min. Some of the ketone samples were run using a split-splitless (S/SL) injector with a 60 m VF-200 column (i.d. 0.25 mm, stationary phase thickness 0.1 μm) with a 10 m guard column into which 2 μl of sample was injected. Upon injection, the oven was held at 90 ^{o}C for 3 min, raised to 250 ^{o}C at a 25 ^{o}C/min ramp, then raised to 305 ^{o}C at a 1 ^{o}C/min ramp and finally raised to 320 ^{o}C at a 10 ^{o}C/min ramp and held at 320 ^{o}C for 20 min. The samples quantified with the S/SL injector and VF-200 column were analyzed during laboratory testing for the most effective method for alkenone quantification. As described below, we rigorously compared results from the two methods and found no significant differences in alkenone parameters and decided to combine results from the two methods rather than re-analyzing samples run with the S/SL-VF200 method.

We determined the repeatability of measured alkenone parameters with the PTV injector by comparing results from 26 runs of the same F2 ketone fraction acquired over the course of three years. Alkenone concentrations are repeatable within 4.4% and $U_{37}^{k'}$ values were repeatable within 0.006. We also evaluated whether the different injectors and columns produced the same alkenone concentrations and $U_{37}^{k'}$ values. No significant differences were found on measurements of the same samples using the PTV and S/SL injectors (mean difference as a fraction of the sample concentration was $+3.3 \pm 4.4\%$ for concentration and $+0.003 \pm 0.023$ for $U_{37}^{k'}$, N = 8, 1s uncertainties).

The precision of the full analytical procedure (extraction, purification, quantification) was determined by measuring biomarkers in seven aliquots of Batch C sediment extracted on the same day (in order to eliminate the effect of biomarker degradation; see Section 3.4.1 for more discussion) and analyzed together. Total alkenone concentrations (MK37:2 + MK37:3) are repeatable to 4.1% and $U_{37}^{k'}$ values are repeatable to 0.0033. These results are comparable to our long-term GC-FID precision and demonstrate the repeatability of our

analyses. Our results for precision on alkenone concentrations and $U^{k'}_{37}$ values are excellent compared to those from a laboratory ring test [Rosell-Melé et al., 2001].

n-Alkanes were measured using the GC-MSD run with a multi-mode inlet and a DB-5 column (30 m length, 0.25 mm i.d., 0.25 μm phase thickness). 1 μl of sample was injected and the oven held at 60 ^{o}C for 1.5 min. The temperature was ramped up to 150 ^{o}C at a rate of 15 ^{o}C/min and then to 320 ^{o}C at a rate of 4 ^{o}C/min where it was held for 10 min. *n*-alkane chain length distribution parameters are repeatable to <1.5% for the CPI and <1% for the ADI.

Alkenone chromatograms (Figure 3.1a) were integrated using ChromQuest software (GC-FID) and *n*-alkane chromatograms (Figure 3.1b) were integrated using Chemstation software (GC-MSD). Long-chain alkenone peak areas from the ketone fraction were converted to alkenone concentrations (Table B.2) by normalizing to the stearyl stearate internal standard peak area:

$$\left[\frac{ng\ molecule}{g\ sediment}\right] = \frac{M_{molecule}}{M_{standard}} * \frac{V_{standard} * [standard]}{sample\ weight} \tag{3.1}$$

where $M_{molecule}$ and $M_{standard}$ are the chromatographic peak areas corresponding to the molecule of interest and the standard molecule, respectively, $V_{standard}$ is the volume of recovery standard put into the TLE after extraction (μl), and [standard] is the concentration of the standard molecule in the recovery standard (ng/μl).

These concentrations of individual alkenone molecules were used to calculate the total alkenone concentration and $U^{k'}_{37}$ value for each sample (Table 3.2). Total alkenone concentration was calculated by adding the concentrations of the C_{37} alkenone molecules present in the RC14-99 sediment (MK37:3 and MK37:2). Note that MK37:4 was present in the samples (Figure 3.1a), but in concentrations too small to reliably quantify. $U^{k'}_{37}$ values were calculated by dividing the concentration of MK37:2 by the summed concentrations of MK37:2 and MK37:3.

Differences in the GC-MSD response for each *n*-alkane were corrected for by analyzing au-

Table 3.2: Biomarker parameters measured in hydrous pyrolysis experiments

Sample #	Time (sec)[a]	Temperature (^{o}C)[b]	Sediment Batch	Alkenone Conc. (ng/g)	$U^{k'}_{37}$	CPI	ADI
PP877[c]	——-	20	A	1714.22	0.668585777	4.288060066	1.343665114
PP920[c]	——-	20	B	1516.90	0.702396537	4.264641653	1.323593663
PP1051[c]	——-	20	A+B	1299.45	0.713562277	3.895173643	1.317586339
PP1285[c]	——-	20	C	1782.84	0.653841882	3.547071708	1.241436461
PP1361[c,d]	147 days	20	C	1617.22	0.664501099	3.074313675	1.186545578
PP1286	7290	60	C	1801.25	0.65234117	3.843986262	1.278804882
PP1287	86430	60	C	1821.65	0.653308122	4.070637274	1.312663375
PP1288	345600	60	C	1846.12	0.64716301	4.179085613	1.318003111
PP1362	7269	100	C	1513.18	0.661695436	3.295147066	1.230303204
PP1363	86428	100	C	1517.55	0.658769022	3.488213761	1.234888372
PP1364	345595	100	C	1384.86	0.676800736	3.28206312	1.234339767
PP1045	10713	124.08	A+B	1008.54	0.727526124	3.548612626	1.279816635
PP918	5246	132.39	B	1345.85	0.700675441	3.933209133	1.334383473
PP873	1733	134.25	A	1107.48	0.677751666	3.034503534	1.198156822
PP913	3375	235.57	B	659.05	0.721790501	1.961981691	1.011091689
PP854	1538	237.38	A	443.17	0.680802586	2.615239566	1.225968341
PP917	5027	252.94	B	298.41	0.741928181	3.093466722	1.227604833
PP914	3236	263.70	B	280.90	0.716337808	2.276250834	1.170371406
PP915	3161	308.63	B	126.38	0.77536705	2.321856006	1.205354484
PP875	1336	349.97	A	484.05	0.713566146	2.392124672	1.14585085
PP876	1204	384.80	A	288.96	0.72889014	1.77452984	1.061644896

[a] Time at 85% T_{max} in minutes unless otherwise noted
[b] Mean temperature during time at 85% T_{max}
[c] Sample used as unheated control
[d] Sample used for alkenone degradation analysis

thentic standards with the samples. A mixture of C_8-C_{40} *n*-alkanes plus the 5a-androstane recovery standard was analyzed with the aliphatic fraction of the samples and used to calculate a GC-MSD relative response factor for each *n*-alkane homologue relative to 5a-androstane. The area ratio of each *n*-alkane molecule to 5a-androstane was then multiplied by this response factor before calculating the concentration by multiplying by the concentration of 5a-androstane in the standard divided by the sample weight (Table B.3). *n*-Alkane concentrations were used to calculate the CPI (odd/even *n*-alkanes from C_{26}–C_{35}) and the ADI (alkane distribution index, C_{27}+C_{31}/C_{28}+C_{29}+C_{30}) (Table 3.2). Here we introduce the ADI index as a measure of the development of a secondary peak in the *n*-alkane chain-length distribution centered on C_{29}. Because this secondary peak develops at a slower rate than the reduction of the CPI or alkenone concentration, an analysis of this change in *n*-alkane distribution can help to place further constraints on coseismic temperature rise.

3.3.4 Determining the kinetics of biomarker thermal maturity

The rapid heating of the reactor during our experiments sometimes introduced temperature overshoots that could influence our results. Therefore, temperature data from the experiments were analyzed to ensure that only high-quality isothermal hydrous pyrolysis

experiments were used for the determination of the reaction kinetics of alkenone destruction and the change in n-alkane distribution. Experiments with an initial peak in temperature that was larger than $\sim$30 ^{o}C above the eventual steady-state temperature and longer in duration than $\sim$350 s were not used in the analysis. Such deviations from isothermal temperature profiles may have occurred due to factors such as variations in the degree of coupling between the resistive heaters and the reactor tube and differences in the wrapping of insulation around the heating apparatus.

After removing non-isothermal experiments, experimental temperatures were determined by taking the mean of the recorded temperature between the time at which the sample achieved 85% of its peak temperature at the beginning of the experiment and the time at which the sample had been cooled down to 85% of its peak temperature at the end of the experiment. Experimental times are considered to be the duration for which the sample was heated to the experimental temperature (Figure 3.2b). The reaction rate constant, k, for isothermal experimental samples was determined by rearranging the following equation [Lewis, 1993]:

$$p = 1 - e^{-kt} \tag{3.2}$$

where p is the fraction reacted in the given experiment relative to a control sample. Though all experiments were conducted using sediment from RC14-99, we determine the fraction reacted using control samples from the batch of RC14-99 that was used at the same time as each experiment. This allows us to examine the thermal effects on the biomarkers without superimposing signals from differences in the starting biomarker compositions of the batches or any degradation of the biomarkers resulting from long-term storage at room temperature (see Section 4.1). Thus, the controls for the high temperature heating experiments are PP877 (Batch A), PP920 (Batch B), and PP1051 (Batch A+B) for experiment groups PP854–876, PP913–918, and PP1045, respectively. The controls for the low temperature heating experiments are PP1285 and PP1361 for the 60 and 100 ^{o}C sets, respectively. The

fraction reacted value is determined by dividing the measured amount of the given biomarker parameter in each heated sample by the amount in the control sample to obtain the fraction of the parameter remaining (f). This can then be subtracted from 1 to obtain the fraction reacted ($p = 1 - f$). We use the experimentally determined p to obtain an expression for k:

$$k = \frac{-ln(1-p)}{t} \tag{3.3}$$

Experimental values of k were calculated using the p values determined for each experimental sample and the time, t, of each experiment as described above. Using Arrhenius plots, we determined the temperature dependence of kinetic parameters for alkenone destruction and changes in n-alkane distribution by rearranging the Arrhenius equation,

$$k = Ae^{\frac{E_a}{RT}} \tag{3.4}$$

to its linear form:

$$ln(k) = ln(A) - \frac{E_a}{R} * T^{-1} \tag{3.5}$$

,where A is the pre-exponential frequency factor (s^{-1}), E_a is the activation energy (kcal/mol), R is the gas constant (1.987x10^{-3} kcal/K*mol), and T is the temperature (K). Using this formulation, $-E_a/R$ is the slope and $ln(A)$ is the intercept of the best-fit line to the Arrhenius plot. Samples with $k < 0$ are excluded from the fit. These values result from uncertainty in the measurements themselves and only affect samples heated at the lowest temperatures. An alternative approach involves binning these low temperature experiments and determining the k value from the slope of a best fit line to the t vs. $ln(f)$ values for these experiments (Figure B.6). This approach yields similar kinetics for these samples. We also exclude samples PP854 and PP873, which are anomalous for all analyzed biomarkers. This indicates an inaccurate determination of the experimental temperature, possibly resulting from variations in packing the sediment into the reactor for early experiments. Error bounds on the

Arrhenius fits are calculated using a Monte Carlo approach as described in Sheppard et al. [2015].

3.4 Results

3.4.1 Alkenone and $U^{k'}_{37}$ degradation at room temperature

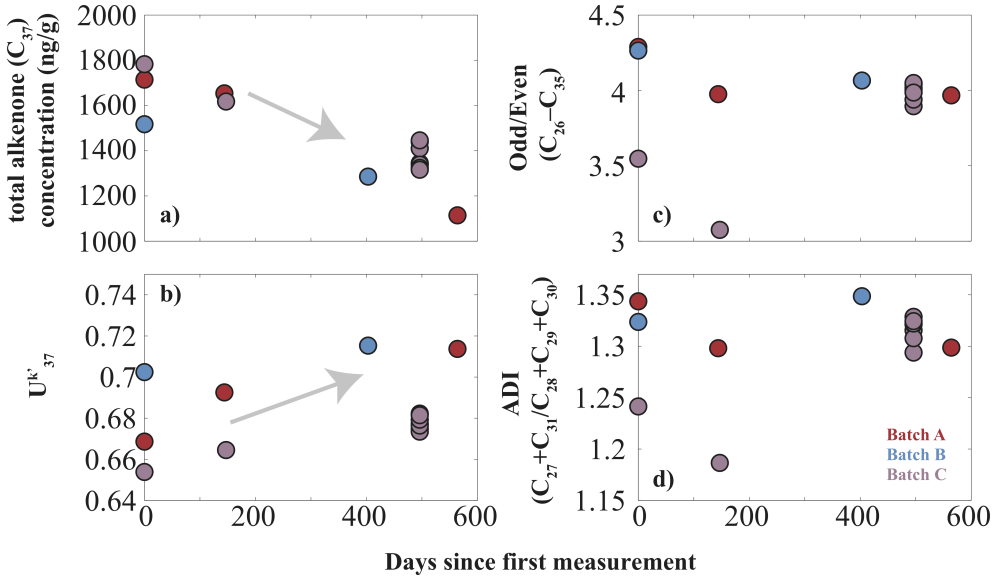

Figure 3.3: Alkenone concentration (a), $U^{k'}_{37}$ values (b), CPI (c), and ADI (d) measured for each sampled batch of core RC14-99 plotted against the time since the first measurement of the batch. Batch A is red, Batch B is blue, and Batch C is purple. General trends are shown with grey arrows and correspond with the trends observed in the thermal alteration of alkenones (decreasing alkenone concentration and increasing $U^{k'}_{37}$ values). *n*-Alkane indices do not show a consistent trend. The third extraction of Batch C in all parameters shows the samples used to calculate analytical uncertainty.

In order to ensure that our estimates of the fractional change in biomarker parameters were not contaminated by a possible signal from inter-batch variability, we measured biomarker parameters in control unheated samples during each set of experiments. While we did not observe a consistent inter-batch variability in the biomarker parameters (Figure 3.3), we found that alkenone parameters (total C_{37} concentration and $U^{k'}_{37}$) exhibited significant changes with storage time of the dry sediment on the scale of months to years.

After each sampling of RC14-99 (Batches A, B, and C; Table B.1), the sediment was crushed and combined in an ashed jar (Section 3.1). For each set of hydrous pyrolysis

experiments, the source batch was sampled until the sediment from that batch was exhausted, at which point, RC14-99 was re-sampled to make the next batch. This led to three instances of sampling Batch A, and two instances each of sampling Batches B and C for unheated control samples. We also conducted a third sampling of Batch C in which we sampled the batch seven times in one day. This had the additional benefit of demonstrating the precision of the biomarker measurements for different aliquots of the same sample.

We observe a systematic decrease in alkenone concentration and a systematic increase in $U_{37}^{k'}$ with storage time of the crushed dry sediment at room temperature between measurements made months to years apart in all three batches (Figure 3.3a,b). However, the batches did not show a systematic decrease in alkenone concentration or increase in $U_{37}^{k'}$ value as the core aged over the course of this study (i.e. between Batches A, B, and C on their first sampling). Based upon these findings, we control for the effect of storage time by using the control sample analyzed with each group of pyrolysis experiments to normalize our results.

We also measured *n*-alkane concentrations in the control samples over time (Figure 3.3c,d). While there is some scatter in both the CPI and ADI measured at different times in Batch C, Batches A and B show fairly stable values for these two parameters. We use the control sample of the batch that was extracted at the same time as each set of hydrous pyrolysis experiments to ensure that no potential *n*-alkane degradation overprints the thermal maturity signature.

An important additional observation is that repeat analyses of the same ketone fraction stored in toluene over several years did not show any change in alkenone parameters (Section 3.3). This fraction was stored in the dark at 3 ^{o}C (37 ^{o}F) when not being analyzed. This finding indicates that the change in alkenone parameters we observed with dry storage of crushed sediment is specifically related to either the sediment matrix or storage conditions and is not a process operating universally during storage of alkenone molecules. Furthermore, the observations that the initial alkenone parameters for each successive sediment batch did not systematically change and that the sediment core itself had any alkenones preserved

indicates that the degradation process is either accelerated or activated by the crushing and storage of the sediment samples after sampling the core.

3.4.2 Alkenone Destruction

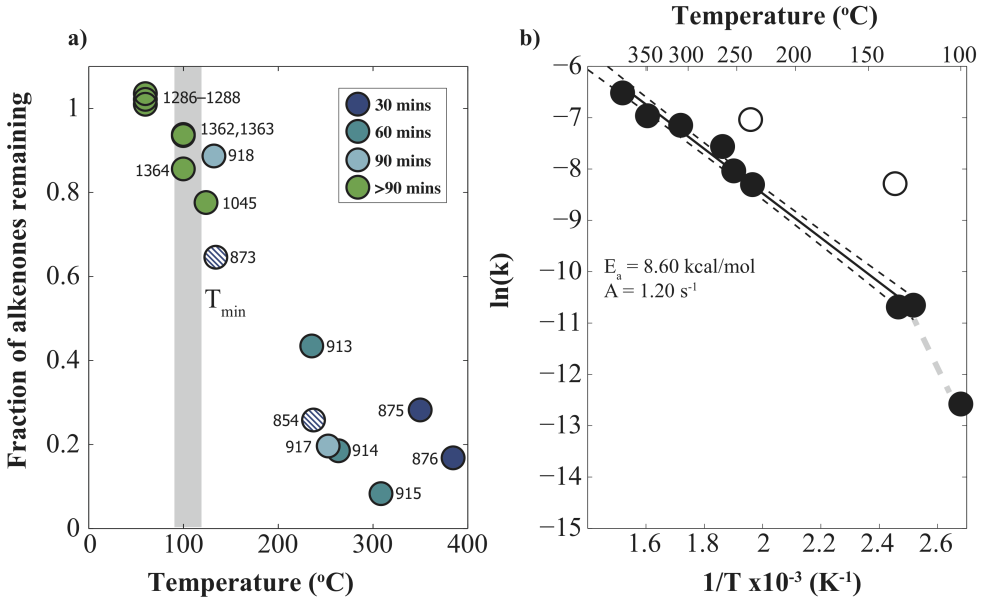

Figure 3.4: a) Alkenone concentration decreases with increasing temperature, over various durations. Long experiments (green) were conducted over 2 hours to 4 days. b) Arrhenius relationship of alkenone destruction showing the natural log of the reaction rate (k) plotted against inverse temperature in K. The linear fit demonstrates a first-order Arrhenius relationship. A clear difference in the reaction rate-temperature relationship occurs below 120 ^{o}C and, thus only experiments 100 ^{o}C are used to calculate the kinetic parameters of alkenone destruction. Hatched points (a) or open points (b) correspond to samples that exhibited anomalous results for all biomarker parameters are not used in the fit.

Hydrous pyrolysis experiments show that alkenone concentration decreases over short time periods at high temperatures (Figure 3.4a). Low temperature hydrous pyrolysis experiments conducted at 60 ^{o}C demonstrate that there is no measureable change in alkenone concentration at these temperatures, even over long periods of time (Figure 3.4a). Shorter experiments conducted above 120 ^{o}C show significant change in alkenone concentration (Figure 3.4a). Long-duration experiments conducted at 100 ^{o}C show a slight decrease in alkenone concentration; however, the reaction rate calculated for these experiments is lower than would be predicted from an Arrhenius fit to the higher temperature experiments, implying a change in mechanism (Figure 3.4b). As a result, the Arrhenius fit for alkenones (Figure

3.4b) only includes experiments above 120 ^{o}C. From this fit, we obtain values for E_a and A of 8.6 kcal/mol and 1.2 s^{-1}, respectively.

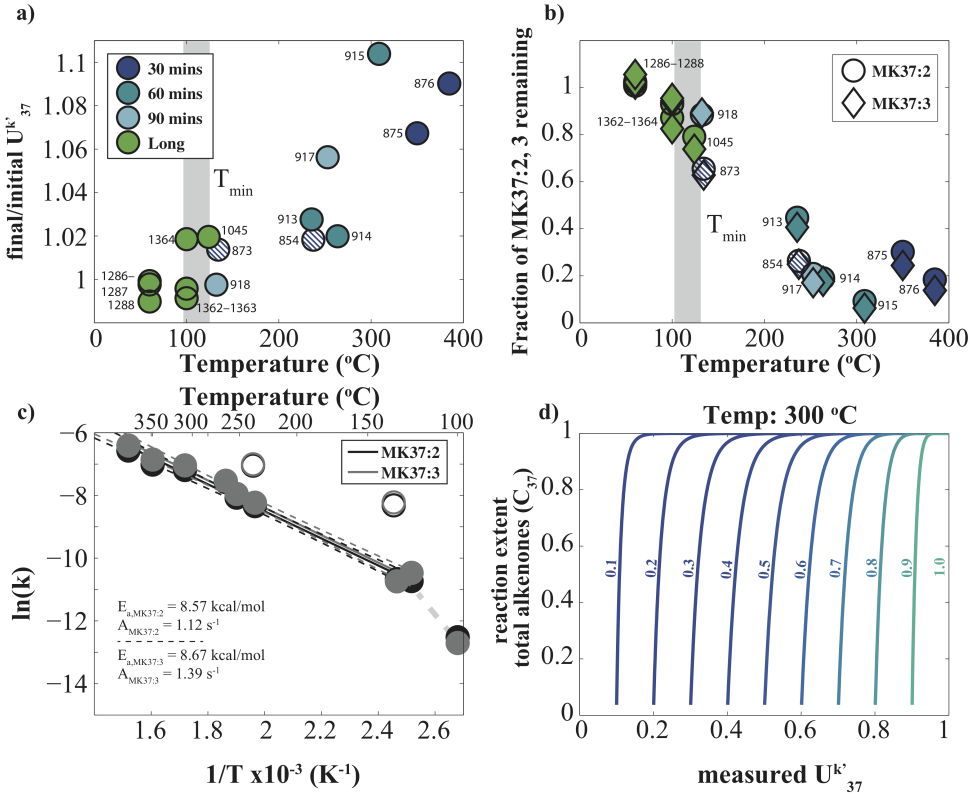

Figure 3.5: a) $U_{37}^{k'}$ change (final $U_{37}^{k'}$ value/initial $U_{37}^{k'}$ value) is positively correlated with temperature. b) MK37:2 and MK37:3 concentrations decrease with increasing temperature, though MK37:3 decreases more dramatically. c) Arrhenius relation for MK37:2 and MK37:3. In ac, hatched (a and b) and hollow points (c) correspond to samples not used in the fit. d) Examples of heating paths at 300 ^{o}C for samples with different initial $U_{37}^{k'}$ values. Each curve shows the $U_{37}^{k'}$ values as total alkenone destruction proceeds. At low to moderate alkenone reaction extents (0 to 0.8), the change in $U_{37}^{k'}$ is greatest for initial $U_{37}^{k'}$ values near 0.5. At very high alkenone reaction extents the $U_{37}^{k'}$ changes are greater for initial $U_{37}^{k'}$ near zero.

There is also an increasing trend in the proportion of di- to tri-unsaturated alkenones with higher temperatures and longer duration experiments. We report these changes using the $U_{37}^{k'}$ parameter typically used for paleoceanographic reconstruction of sea surface temperatures. The $U_{37}^{k'}$ parameter is defined as:

$$U_{37}^{k'} = \frac{MK37:2}{MK37:2 + MK37:3} \tag{3.6}$$

where MK37:2 and MK37:3 are methyl ketones with 37 C atoms and 2 or 3 unsaturated

bonds, respectively. In the case of $U^{k'}_{37}$, the values increase with increasing thermal maturity (Figure 3.5a). The increase in $U^{k'}_{37}$ is accompanied by a marked decrease in both the MK37:2 and MK37:3 concentrations (Figure 3.5b). The decrease in the concentration of these two molecules also becomes most notable at temperatures above ∼120 ^{o}C. Arrhenius analysis of MK37:2 and MK37:3 shows that the kinetics of destruction for these individual alkenone molecules are nearly identical to the kinetics of destruction calculated for the total alkenone concentrations with E_a values for MK37:2 and MK37:3 of 8.57 and 8.67 kcal/mol and A values of 1.12 and 1.39 s^{-1}, respectively. However, while the rates for MK37:2 and MK37:3 destruction are similar at lower temperatures, the MK37:3 destruction rate increases more at higher temperatures leading to greater destruction and an increase in the $U^{k'}_{37}$ value (Figure 3.5b). As the rate of $U^{k'}_{37}$ change will depend upon the relative concentrations of MK37:2 and MK37:3 initially present in the sediment (Figure 3.5d), it is more appropriate to use the individual kinetics of each alkenone molecule to interpret change in $U^{k'}_{37}$ values for samples that have a different starting $U^{k'}_{37}$ value from our sample material (see Section B.3 for more details).

3.4.3 *n*-Alkane Distribution

There are significant changes in the distribution of *n*-alkanes in our experiments (Figures 3.6a and 3.7a) as the biogenic signature in the long-chain *n*-alkane distributions of the unheated sediment are overprinted. We see a decrease in the odd/even preference in the long-chain *n*-alkanes and increasing amounts of mid-chain *n*-alkanes with no odd/even preference (Figure B.5). We examine two particular parameters that capture different trends in this distribution change. First, we focus on the Carbon Preference Index (CPI), which is defined as the ratio between the odd chain length and even chain length *n*-alkanes from C_{26}–C_{35}. We see a decrease in CPI with increasing temperature, beginning at temperatures of ∼120 ^{o}C (Figure 3.6a). We determine the kinetics of reduction in CPI using an Arrhenius analysis, fitting experiments above 120 ^{o}C, and obtain values for E_a and A of 8.08 kcal/mol and 0.302 s^{-1}, respectively (Figure 3.6b). While the decrease in odd/even preference is directly

measured in the CPI, we also observe the creation of low CPI long-chain n-alkanes with a maximum at C_{29} unlike the pre-existing n-alkanes in the sample, which have a maximum at C_{31}. To track the combined effects of this process, we also introduce the n-alkane distribution index (ADI), defined as:

$$ADI = \frac{C_{27} + C_{31}}{C_{28} + C_{29} + C_{30}} \tag{3.7}$$

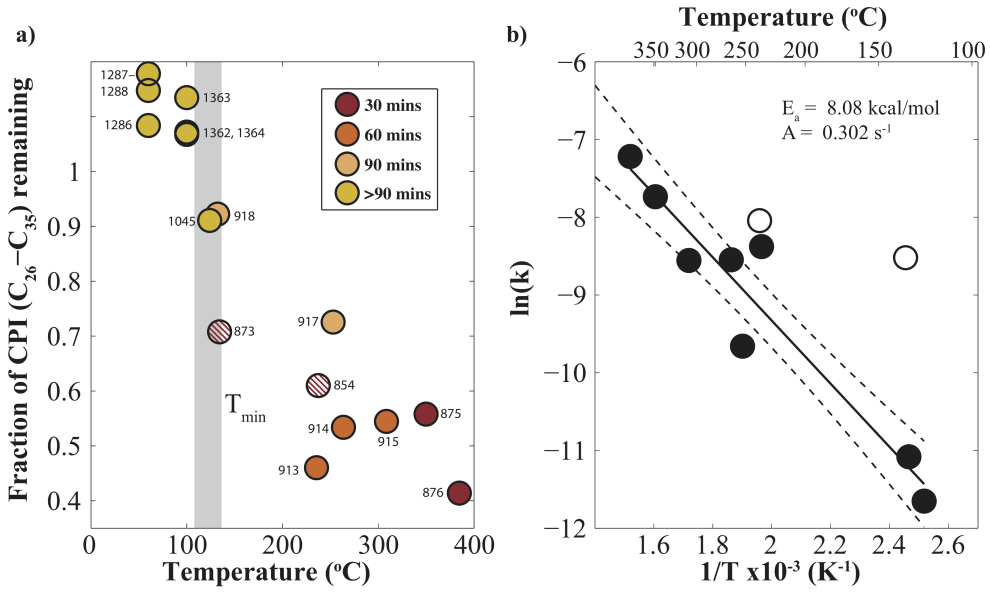

Figure 3.6: a) CPI (odd/even chain length n-Alkanes C_{26}–C_{35}) for hydrous pyrolysis experiments presented in this study. We see a decrease in CPI with increasing temperature, though the decrease is mostly apparent above 120 ^{o}C. b) Arrhenius relation for the CPI degradation rate constants. Hatched (a) and hollow (b) points correspond to samples not used in fit.

This parameter describes a relative change in long chain-length n-alkanes in the range of C_{28} to C_{30} with respect to the surrounding chain lengths with increasing temperature (Figure 3.7c). The ADI decreases as low CPI n-alkanes are created during heating and the average n-alkane chain length decreases, leading to the creation of n-alkanes with a maximum around C_{29}. The ADI shows a decrease with increasing time and temperature (Figure 3.7b), predominantly observed at temperatures above 120 ^{o}C. However, in this case, the scatter of the ADI values calculated for individual experiments at 120–135 ^{o}C includes one sample with a slight increase in ADI, indicating that this temperature range is very close to the

Table 3.3: Kinetic parameters of thermal maturity for biomarkers determined in this study

Biomarker Parameter	E (kcal/mol)	A (1/s)	minimum T (^{o}C)
MK37:2	8.57	1.12	120
MK37:3	8.67	1.39	120
Total alkenone (C_{37})	8.6	1.2	120
CPI	8.08	0.302	120
ADI	7.72	0.052	120

minimum temperature at which reaction might be expected. We determine the values of E_a and A for the thermal alteration of the ADI to be 7.72 kcal/mol and 0.052 s^{-1}, respectively.

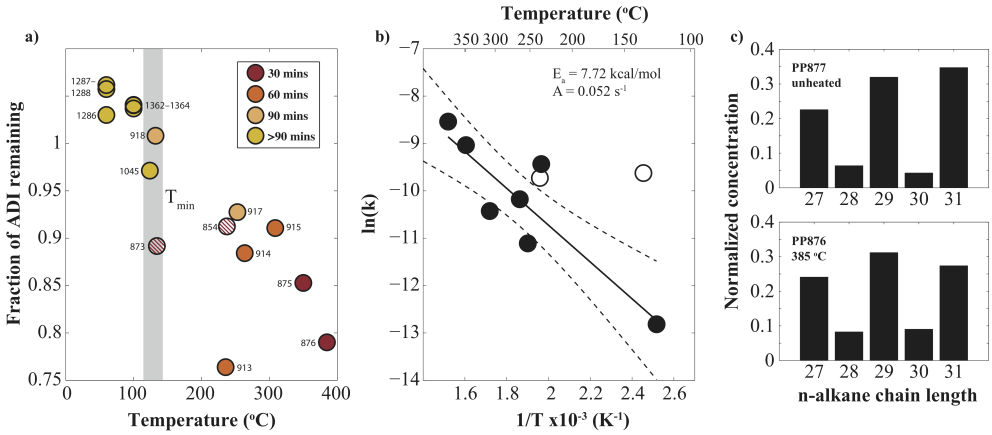

Figure 3.7: a) Change in the *n*-alkane distribution index (ADI) with increasing temperature for hydrous pyrolysis experiments in this study. b) Arrhenius plot for the ADI. c) Histograms of C_{27}–C_{31} *n*-alkane concentrations, normalized to the sum of C_{27}–C_{31}, for the sample heated to 340 ^{o}C (PP876) and the corresponding control (PP877). Hatched (a) and hollow (b) points correspond to samples not used in fit.

3.4.4 Sulfur Concentration

Although not the main focus of the work presented here, we note an increase in the concentration of solvent-extractable elemental sulfur detected in the highest temperature experiments (Figure B.4). Present as S_8 in the solvent extract, this product presumably reflects breakdown of other sulfur phases in the sediments at high temperature. Further studies with more high temperature experiments are required to understand the reactions

occurring and to determine kinetics based on this change (see Section B.4).

3.5 Discussion

3.5.1 Kinetics of biomarker thermal maturity

Our experiments exhibit first-order reaction kinetics whose temperature dependence can be described by an Arrhenius-type relationship (Figures 3.4–3.7b). We further find that within experimental uncertainty there is no destruction of alkenones below temperatures of ~60 ^{o}C (Figure 3.4a). Our low temperature experiments were run for up to four days to specifically investigate low temperature reactions. The lack of reaction in our long, 60 ^{o}C experiments and the small amount of reaction in the 100 ^{o}C experiments is not predicted from the higher temperature experiments and thus indicates a change in the temperature dependence of the reaction rate at low temperatures. Quantification of this change in temperature dependence will require an additional suite of experiments.

We also observe differences in the reaction rate of the di- and tri-unsaturated C_{37} methyl ketones. The reaction rate for the tri-unsaturated ketone is slightly greater, especially at higher temperatures, producing an increase in the $U^{k'}_{37}$ value with reaction extent. Changes in $U^{k'}_{37}$ could thus provide additional information on alkenone destruction independent of total alkenone concentration. This could be particularly beneficial as the precision and accuracy during measurement of the $U^{k'}_{37}$ index is better than for the total alkenone concentration [Section 3.3; Rosell-Melé et al., 2001]. The extent of $U^{k'}_{37}$ change with heating temperature (T) and time (t) also depends upon the initial $U^{k'}_{37}$ value:

$$U^{k'}_{37}(t,T) = \frac{1}{1 + \left[\frac{1}{U^{k'}_{37,0}}\right] * e^{(k_2(T) - k_3(T))t}} \tag{3.8}$$

where $U^{k'}_{37}$(t) and $U^{k'}_{37}$,0 are the final and initial $U^{k'}_{37}$ values, respectively, and k_2 and k_3 are the temperature-dependent reaction rate constants from MK37:2 and MK37:3, respectively (see Section B.3 for more detail). This relationship allows an estimate of the fractional change in MK37:2 or MK37:3 in a heated sample by comparing the measured $U^{k'}_{37}$ value with an initial

$U_{37}^{k'}$ value.

The only previous work on thermal alkenone destruction we can compare our results with is Simoneit et al. [1994]. They investigated the destruction of long-chain unsaturated alkenones in sediments from Middle Valley, in the north of the Juan de Fuca ridge system (ODP Leg 139). Their hydrous pyrolysis experiments, conducted at temperatures of 200–350 ^{o}C over 24 hours demonstrated complete destruction of alkenones at 250 ^{o}C and partial destruction at 200 ^{o}C. Interestingly, they found that the $U_{37}^{k'}$ value decreased from an initial value of 0.81 to 0.69 in the 200 ^{o}C experiment with partial alkenone destruction. We see the $U_{37}^{k'}$ value systematically increasing in all of our heated experiments in a manner consistent with slight differences in the rate constants for the MK37:2 and MK37:3 molecules. At this point we do not know the reason that the $U_{37}^{k'}$ value decreased in the Simoneit et al. [1994] experiments but increased in our experiments. Attack of the double bond positions is one pathway for alkenone destruction and would favor greater destruction of the tri-unsaturated molecule as found in our experiments.

While thermal maturity in alkenones is largely expressed as a change in absolute concentration, the thermal maturity of n-alkanes is observed as a change in chain length distribution (Figure 3.1b). We see a reduction in CPI at temperatures above 120 ^{o}C, consistent with previous observations of the changes in n-alkane chain length distribution [Eglinton et al., 1988, Simoneit, 1994]. This is indicative of overprinting of the biogenic signature for a strong preference for odd chain-lengths, derived from plant leaf waxes [Eglinton et al., 1962] by petrogenic hydrocarbons with a CPI of $\sim$1. The change in n-alkane distribution is also described by a decrease in the ADI. This parameter is representative of an increase in the C_{28}–C_{30} n-alkane concentration compared to the surrounding chain lengths (Figure 3.7c). This transition is likely caused by the superimposed effects of the formation of long chain n-alkanes due to high temperature cracking reactions, the breakdown of these long-chain n-alkanes to form shorter-chain molecules, and the reduction of odd chain lengths with respect to even chain lengths (Figure B.5). Because this parameter describes multiple processes, the

observed change in ADI yields a strong signal with increasing thermal maturity.

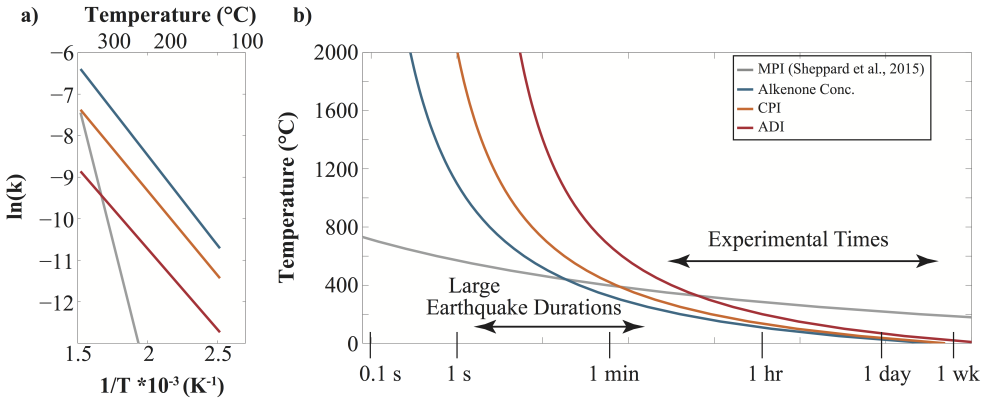

Figure 3.8: a) Arrhenius best-fit line for all compound parameters analyzed in this study. Methylphenanthrene kinetics (MPI-1) are from Sheppard et al. [2015]. b) Time-temperature diagram illustrating where 5% reaction occurs in each biomarker parameter. Time-temperature combinations above these curves should be detectable using these biomarker heating proxies.

Figure 3.8 shows the Arrhenius relationships for the biomarkers analyzed in this study (Figure 3.8a) and the predicted time-temperature values for samples that have experienced 5% biomarker reaction. Changes at this scale should be easily detectable given the precision of our measurements for all biomarker parameters discussed in this study, even with variable initial biomarker values. Notably, the kinetics of thermal maturity differ significantly between the alkenones and *n*-alkanes with the former reacting more quickly at lower temperatures (Figure 3.8a). Additionally, these kinetic parameters are quite different from those previously determined for methylphenanthrenes [Sheppard et al., 2015], indicating a higher reaction rate, but lower temperature sensitivity for biomarkers present in fresh sediments compared with biomarkers generated as a result of burial heating (Figure 3.8a). These results provide tantalizing evidence for a dramatic divergence in the kinetics of thermal maturation for different biomarker parameters. By measuring biomarker parameters with different kinetics in a heated sample, we gain better constraints on the possible time-temperature combinations that a sample has experienced.

3.5.2 Application as fault thermometers

We observe significant changes in concentration for marine and terrigenous organic mate-

rial in short-duration hydrous pyrolysis experiments. This suggests that the thermal maturity of biomarkers can be used to estimate temperature rise on faults hosted in unaltered marine sediments. This is particularly of interest for shallow faults active in subduction zones where large amounts of shallow slip can significantly enhance the tsunamigenic potential of a subduction zone margin [Fujii et al., 2011]. In these types of environments, thermal alteration of biomarkers in unaltered sediments can provide a constraint on coseismic temperature rise, which, in turn, can help to constrain the coseismic stress conditions that govern the propagation of shallow seismic slip. This is particularly important because subduction zones host the largest earthquakes due to the large amount of fault area available for slip relative to other tectonic environments.

The differences in kinetic parameters of thermal maturity in these biomarkers have the potential to provide added constraints on the maximum temperature rise experienced by marine sediments hosting seismic faults. This is because sediment that has experienced a given time-temperature history will record different degrees of alteration in the alkenone and n-alkane parameters. By constraining the degree of alteration of a suite of biomarkers, more precise estimates of temperature rise can be made than are possible using only one biomarker. By coupling thermal diffusion models with the kinetics for different biomarkers, a more thorough understanding of the coseismic temperature rise and subsequent temperature decay during earthquakes can be achieved. We note that the kinetics of thermal maturation analyzed in this paper are unlikely to be of use in sediments containing methylphenanthrenes. This is because, if the sediments are thermally mature enough to contain methylphenanthrenes, the n-alkanes are likely to have experienced enough thermal alteration to overprint the original biogenic fingerprint. Thus, in order to use the thermal maturity of n-alkanes to help constrain temperature rise on faults in sediments that have experienced burial heating, more experiments on sediment with a more thermally mature initial composition are required.

In order to accurately assess thermal alteration in sediments, it is of utmost importance to fully characterize the initial biomarker parameters of the unheated protolith. Concentrations

of different biomarkers can vary widely over short stratigraphic intervals and throughout the oceans. Therefore it is important to establish the natural variability within the protolith in order to confidently attribute anomalies to temperature rise. In settings such as subduction zones, initial concentrations can be measured in input sediments on the downgoing plate, as long as independent parameters are used to assess stratigraphic equivalence. For instance, Rabinowitz et al. [2015] showed that trace element geochemistry could be used to correlate stratigraphy between a core through the Japan trench décollement and a nearby reference core.

3.5.3 Implications of biomarker degradation for sediment sampling and storage

Our observations of significant alteration in alkenone concentration and n-alkane distribution with heating suggest that care should be taken when using samples that may have experienced heating (e.g. around faults or hydrothermal areas) for paleoclimatological studies. Notably, we observe a systematic difference in the kinetics of thermal maturity between alkenone molecules with different levels of unsaturation. This implies that samples that have been exposed to heating above 120 ^{o}C, even for a short amount of time, such as might be expected in a faulted or hydrothermal environment, should not be relied upon for representative $U^{k'}_{37}$ values. However, our long-duration experiments at 60 ^{o}C show no significant change in $U^{k'}_{37}$ value. We therefore suggest that samples exposed to such low levels of heating might retain their biogenic $U^{k'}_{37}$ values although extrapolation to thousands or millions of years of burial includes large uncertainties from our kinetic parameters. In addition, the observed changes in the distribution of n-alkane chain lengths due to heating support the conclusion that care should be taken when interpreting n-alkane data in hydrothermal and faulted areas [e.g. Simoneit, 1994].

We further observe the degradation of alkenone concentration and $U^{k'}_{37}$ values in our crushed control samples stored at room temperature over the span of months to years. Because the batches each sampled slightly different parts of core RC14-99 6b, variation in both initial alkenone concentration and $U^{k'}_{37}$ is to be expected between starting materials.

If alkenone degradation were taking place while the samples were still in the core, this trend might be expected to dominate any climatically-controlled inter-batch variability. In addition, if alkenone degradation in the cores was as dramatic as we observe in our control sediment, we might expect all alkenones to be destroyed in cores that have been stored at room temperatures for decades (as has core RC14-99, which was recovered in 1972). Since the presence of alkenones in our experimental sediment belies this possibility, we suggest that the degradation of alkenones in our control samples over the span of months to years occurred post-crushing and could be related to the resultant higher surface area of the sediment that is exposed to atmospheric conditions (e.g. higher oxidation).

3.6 Conclusions

Hydrous pyrolysis experiments conducted on Western Pacific sediment allow us to determine the kinetics of thermal maturation for a suite of biomarker parameters found in marine sediments, specifically alkenone destruction, increase in $U^{k'}_{37}$ and transformation of the plant-wax *n*-alkane signature to a petrogenic distribution observed as reductions in the CPI and ADI (*n*-alkane distribution index, $C_{27}+C_{31}/(C_{28}+C_{29}+C_{30})$). These thermal maturation kinetics can be used to constrain the temperature rise on seismic faults in marine environments and allow for a more thorough understanding of shallow seismic slip.

3.7 Acknowledgments

Samples for this study were provided by the Lamont-Doherty Core Repository. We thank two anonymous reviewers for helpful comments. Funding for this project was provided by U.S. National Science Foundation grant OCE 12-60555, a Schlanger Ocean Drilling Fellowship to H.S.R., part of the NSF-sponsored U.S. Science Support Program for IODP that is administered by the Consortium for Ocean Leadership, Inc, and an NSF GRFP (DGE-11-44155) to H.S.R. Data used in this paper can be found in the supplementary tables.

4 | Multiple shallow seismic faults in the region of the 2011 Tohoku-oki Earthquake

Co-authors: H. M. Savage and P. J. Polissar

Shallow slip during earthquakes is a major contributor to seismic hazard near large fault zones, but the fault structures and material properties that control shallow seismic slip remain poorly understood. IODP Expedition 343 JFAST drilled through a patch of the Japan Trench that hosted ∼50 m of slip during the M_w9.1 2011 Tohoku-oki earthquake. We use new biomarker thermal maturity indicators to identify faults in the JFAST core that have experienced considerable frictional heating, as can only occur during earthquake slip. We find that seismic slip has occurred on multiple faults and that any of these faults could have hosted the Tohoku-oki earthquake. Multiple structures could have hosted great earthquakes, implying that seismic slip to the trench is common. These faults occur in a range of lithologies suggesting that material properties do not predict the likelihood of shallow slip or seismic hazards in these settings.

4.1 Introduction and Background

During large earthquakes, coseismic slip can propagate to the seafloor and increase the severity of seismic hazards such as earthquake-related tsunamis. The 2011 March 11, M_w9.1 Tohoku-oki earthquake and tsunami was one such event, leading to significant damage in Japan, claiming the lives of over 15,000 people, and causing a meltdown in the Fukushima

Daiichi nuclear power plant. The tsunami was enhanced by an estimated ∼50 m of shallow earthquake slip that propagated to the subduction trench [Fujiwara et al., 2011, Ito et al., 2011, Sun et al., 2017]. On-shore tsunami deposits suggest that at least three similar tsunamis have occurred along this section of the Japan Trench with ∼1000 yr periodicity [Minoura et al., 2001]. The conditions that allow for shallow coseismic slip are not well understood, but could depend on such parameters as interactions with the seafloor [Kozdon and Dunham, 2013], frictional properties of the fault zone [Ikari et al., 2015b,a], and dynamic weakening of faults during rapid slip [Noda and Lapusta, 2013, Remitti et al., 2015, Ujiie et al., 2013]. Improving earthquake risk assessment requires understanding the conditions that favor earthquake propagation to the trench. We use indicators in the rock record to determine which faults within the Japan Trench experienced earthquake slip to understand how shallow slip relates to the composition and material properties of subducting sediments.

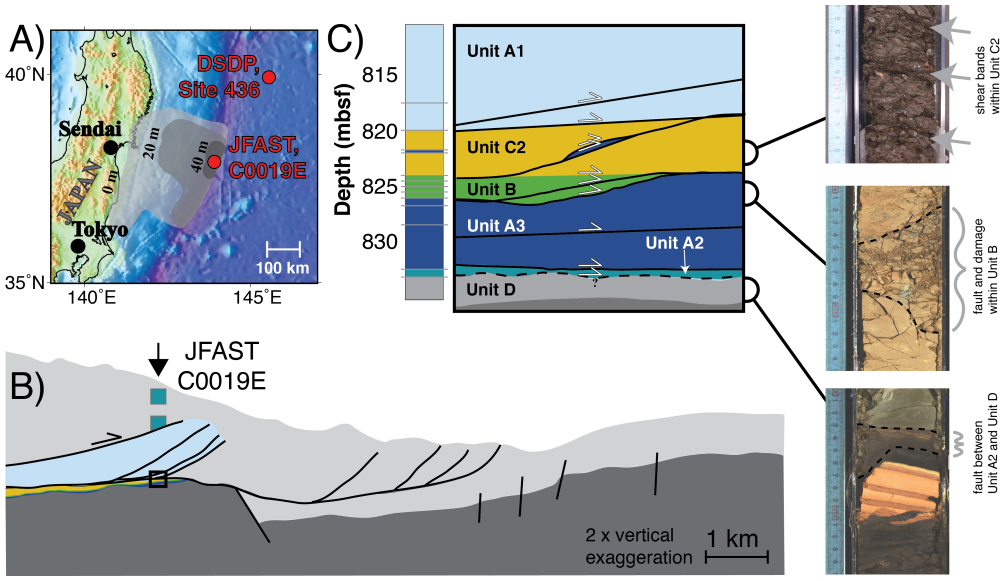

Figure 4.1: Location and structure of the JFAST core. A) Map of the Japan Trench with the rupture area of the Tohoku earthquake indicated in grey and the JFAST and Site 436 sites identified by red dots. Grey shades indicate regions of equal slip [Ammon et al., 2011, Chester et al., 2013, Fujii et al., 2011, Koper et al., 2011]. B) Schematic structure of the accretionary prism recovered at JFAST and C) close-up of JFAST stratigraphy [Rabinowitz et al., 2015] and pictures of typical structures from regions of the core where damage has been observed.

JFAST drilled through the subduction zone where the maximum slip occurred during the Tohoku-oki earthquake in order to study the physical controls on shallow seismic slip [Figure

4.1; Chester et al., 2013]. Structural and stratigraphic characterizations show that the core is comprised of mudstones and pelagic clays offset by several faults [Keren and Kirkpatrick, 2016a, Kirkpatrick et al., 2015, Rabinowitz et al., 2015]. Previous studies showed that one of these faults, a frictionally weak, thin pelagic clay with a penetrative scaly fabric (implying significant shear strain), was a major structural boundary. Furthermore, structural features also significantly change from one side of this fault to the other [Kirkpatrick et al., 2015, Yang et al., 2013]. Because of these observations, most of the 3.2 km displacement—including earthquakes—are thought to localize on this fault [Chester et al., 2013, Ikari et al., 2015b,a, Kirkpatrick et al., 2015, Remitti et al., 2015, Sawai et al., 2014, Ujiie et al., 2013, Yang et al., 2013]. However, other faults are present and form part of the subduction interface fault system, and it can be difficult to determine whether a fault has failed seismically or aseismically based on structural evidence alone.

The most robust, independent indication of seismic slip is temperature rise along the fault, because significant temperature rise only occurs during rapid slip (earthquakes) [Lachenbruch, 1986]. The JFAST expedition installed a temperature observatory to monitor the decay of the heat signal produced by frictional heating during the Tohoku-oki earthquake. The measured temperature decay suggests a low integrated coseismic shear stress of 0.54 MPa [Fulton et al., 2013]. However, the temperature anomaly cannot constrain which fault slipped during the earthquake, as there are several closely-spaced faults within the bottom 15 m of the core [Keren and Kirkpatrick, 2016a, Kirkpatrick et al., 2015, Rabinowitz et al., 2015].

A different way to determine whether the faults at JFAST have experienced elevated temperatures is to look for evidence in the fault rocks themselves. Thermal alteration inside or near the fault relative to the surrounding rock provides evidence of earthquake slip. Although this approach cannot pinpoint any particular earthquake, it places a bound on the highest temperature the fault has ever achieved during earthquake slip. Therefore, thermal alteration can determine which faults are candidates for hosting the Tohoku-oki or other

earthquakes. Co-seismic temperature rise in subduction zones has been investigated through a variety of methods including vitrinite reflectance, pseudotachylyte, and clay alteration [Rowe et al., 2005, Sakaguchi et al., 2011, Schleicher et al., 2015]. Here, we analyze the thermal maturity of organic matter (molecular biomarkers) in and around faults within the JFAST core. Biomarkers experience irreversible chemical alterations that permanently record the maximum temperature experienced by a fault hosted in sedimentary sequences, and have been used to detect heating signatures in ancient faults [Polissar et al., 2011, Savage et al., 2014]. Recent work establishing reaction kinetics of biomarkers at seismic timescales allows for estimates of peak temperature in the JFAST faults [Rabinowitz et al., 2017, Sheppard et al., 2015]. For slip zone thicknesses of centimeters or less, only earthquakes generate heat fast enough to create a significant temperature rise that is recorded by the biomarkers discussed here.

4.2 Biomarkers in sediments at the Japan Trench

Here we use coccolithophore algae-sourced long-chain unsaturated ketones [herein alkenones; Lawrence et al., 2007] and plant-derived long-chain n-alkane distributions to identify heating anomalies. C_{37} alkenones document heating through decreasing concentrations (C_{37} total) and preferential destruction of molecules with three double bonds compared to those with two double bonds (measured by increasing $U^{k'}_{37}$ values)[Rabinowitz et al., 2017, Simoneit et al., 1994]. n-Alkane distributions document heating through a decreasing carbon preference index (CPI) and by the addition of a secondary peak described by a decrease in the alkane distribution index [ADI, see Section C.1.2 for more detail; Rabinowitz et al., 2017]. We use kinetic parameters for these reactions [Rabinowitz et al., 2017] to infer peak temperatures from reaction extent. Dissimilar kinetic parameters between reactions mean that we will not observe identical alteration in all biomarker parameters. These differences help constrain temperature rise during earthquake slip.

4.3 Methods

4.3.1 Analysis of biomarker reaction in the JFAST core

Biomarker concentrations were measured following the methods of Rabinowitz et al. [2017] (see Section C.1.2 for more details). In order to use biomarker thermal maturity to reconstruct temperature rise, it is necessary to establish the initial values of the biomarker parameters before the rocks were faulted. We compare JFAST samples to a reference core on the incoming plate (DSDP Site 436; Figure 4.1A) in order to determine the level of biomarker alteration. Stratigraphic units were correlated between the two cores using trace element concentrations [Rabinowitz et al., 2015], which provide a way to accurately fingerprint units with similar lithologies and ages on a sample-by-sample basis. This stratigraphy demonstrates the presence of age gaps and inversions interpreted as faults at various depths [Figure 4.1C, see Section C.2.1 for more detail; Rabinowitz et al., 2015], and is consistent with faults identified through biostratigraphic age inversions and damage structures in the JFAST core [Keren and Kirkpatrick, 2016a, Kirkpatrick et al., 2015].

We analyzed the fractional change of C_{37} total, $U^{k'}_{37}$, CPI and ADI in JFAST samples compared to Site 436 as the ratio of the biomarker measured in a JFAST sample to the initial value measured from Site 436: $r = P_{JFAST}/P_{initial}$. For each JFAST sample, the distribution of r is calculated from the distribution of $P_{initial}$ values measured in the corresponding sedimentary unit at Site 436 (Figures C.1–C.5). The range in r for each sample (Figure 4.2) therefore reflects the range of $P_{initial}$ at Site 436. Seismically active faults that have experienced frictional heating are determined by values of r less than one for C_{37} total, CPI, and ADI and values of r greater than one for $U^{k'}_{37}$ (Figure 4.2). We take the most conservative approach to identifying heating signatures: for each biomarker parameter, only JFAST samples that express anomalies relative to all of the possible $P_{initial}$ values in the corresponding sedimentary unit of Site 436 are considered to reflect a temperature rise.

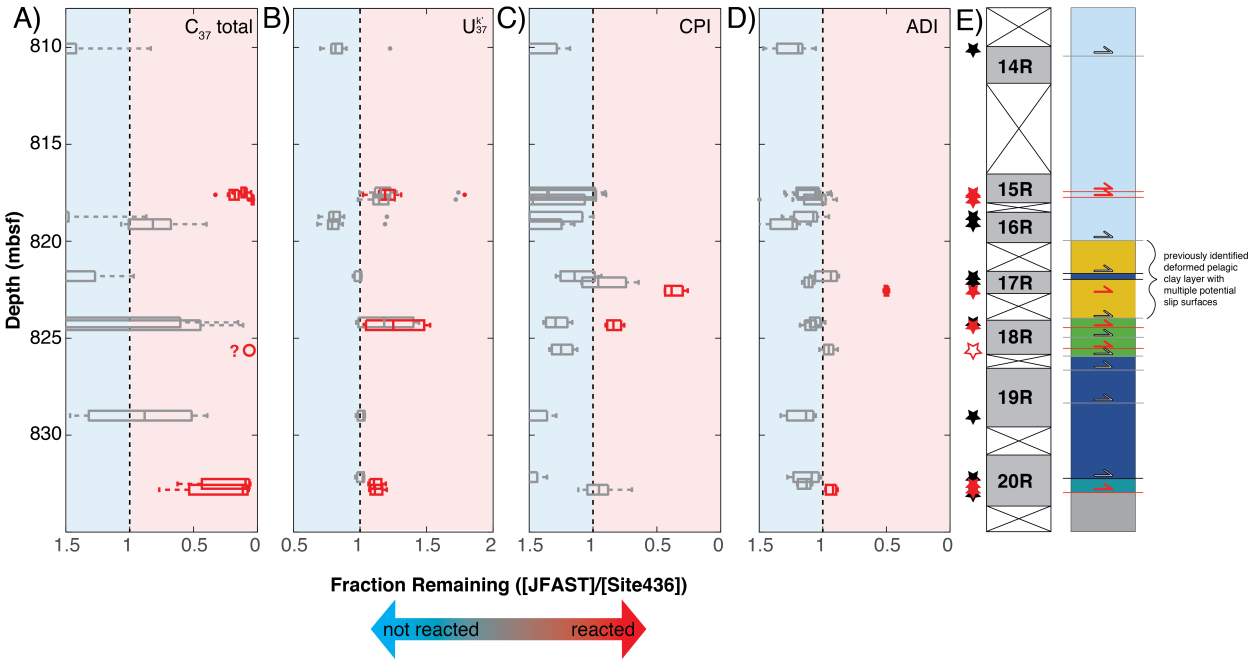

Figure 4.2: Biomarker indicators of heating in the JFAST core. Fraction remaining (i.e. not reacted) of (A)C_{37} total, (B)$U^{k'}_{37}$, (C)CPI, and (D)ADI are shown for samples in the plate boundary region. Box plots indicate the median and quartiles of the fraction remaining value (relative to the range of biomarker values measured in the corresponding sedimentary unit at Site 436) while, minimum and maximum values are indicated by the whiskers, and outliers by dots. (E) Sample locations shown as stars, colored red when biomarker anomalies indicate heating. Grey shading indicates JFAST core recovery. Stratigraphy is shown with previously observed faults indicated [Keren and Kirkpatrick, 2016a, Kirkpatrick et al., 2015, Rabinowitz et al., 2015], those with biomarker anomalies discussed in the main text in red, and those with samples close enough to observe an anomaly, but lacking one, in black. Sample PP948, represented by hollow symbols in (A) and (E), had alkenone concentrations below the quantification limit and thus, the magnitude of the heating anomaly is poorly constrained.

4.3.2 Modeling of temperature rise on faults

An integrated time-temperature history of a shear-heating event is used to analyze biomarker alteration in natural fault samples [Carslaw and Jaeger, 1959]. In order to account for the duration of elevated temperatures with distance from the observed faults, a fault-heating model with heat diffusing away from a fault using constant slip velocity, fault half-width, shear stress and sedimentary material properties was implemented [Lachenbruch, 1986]:

$$
\begin{aligned}
\theta(x < a, t) = \frac{\tau v}{\rho c a}[t &\left(1 - 2i^2 erfc\frac{a-x}{\sqrt{4\alpha t}} - 2i^2 erfc\frac{a+x}{\sqrt{4\alpha t}}\right) \\
&- (t - t^*)\left(1 - 2i^2 erfc\frac{a-x}{\sqrt{4\alpha (t-t^*)}} - 2i^2 erfc\frac{a+x}{\sqrt{4\alpha (t-t^*)}}\right)] \\
\theta(x > a, t) = \frac{\tau v}{\rho c a}[t &\left(i^2 erfc\frac{x-a}{\sqrt{4\alpha t}} - i^2 erfc\frac{x+a}{\sqrt{4\alpha t}}\right) \\
&- (t - t^*)\left(i^2 erfc\frac{x-a}{\sqrt{4\alpha (t-t^*)}} - i^2 erfc\frac{x+a}{\sqrt{4\alpha (t-t^*)}}\right)]
\end{aligned}
\tag{4.1}
$$

where θ is the temperature rise (K), a is the fault half-width (m), τ is shear stress on the fault (Pa), t is time (s), t^* is the slip duration (s), x is the distance from the center of the fault (m), ρ is the density of the material (kg/m^3), c is the heat capacity (J/kgK), v is the slip velocity (m/s), $i^2 erfc$ is the second integral of the complementary error function, and α is the thermal diffusivity (m^2/s). Absolute temperature is determined by adding θ to the background temperature, which is 20 ^{o}C (293.15 K) at $\sim$700 mbsf at the JFAST site [Fulton et al., 2013].

We note that this model does not take into account possible advection of fluids, which have been inferred to play an important role in heat and stress transfer during earthquakes in some fault zones, indicated by the presence of features such as mineral veining around faults [Robert et al., 1995, Sibson et al., 1988, 1975, Yamaguchi et al., 2011]. However, such features are not observed in the JFAST core [Keren and Kirkpatrick, 2016a, Kirkpatrick et al., 2015]. Here, we model the temperature rise generated only through seismic slip and heat diffusion on observed structures in the JFAST core. Advection of hydrothermal fluids immediately after seismic slip would serve to transport heat to further distances from the slipping surface. For samples within the slipping zone, this effect would lower the measurable peak temperature at the slip surface and Equation 4.1 would underestimate the temperature rise. Conversely, for samples outside of the slipping zone, hydrothermal fluid advection would yield a higher temperature further from the fault compared with values attained through

diffusion alone. In these cases, Equation 4.1 would overestimate the peak temperature at the center of the slipping zone.

Biomarker thermal alteration is modeled using an expanded form of the Arrhenius equation:

$$f = 1 - exp[-At * exp(-E_a/RT)] \tag{4.2}$$

where f is the fraction reacted $(1 - r)$, A is the pre-exponential frequency factor (s^{-1}), E_a is the activation energy (J/mol), R is the gas constant (8.314 J/K*mol), and T is temperature (K). Note that for $U^{k'}_{37}$, which increases with increasing thermal maturity, f is calculated as:

$$f_{U^{k'}_{37}} = 1 - \frac{1 - U^{k'}_{37,JFAST}}{1 - U^{k'}_{37,Site436}} \tag{4.3}$$

The time-temperature history for earthquakes with slip ranging from 5–150 m (hereafter referred to as event slip) is calculated using Equation 4.1, for a range of possible fault half-widths consistent with structural observations for each sample. These time-temperature histories are used, along with the experimentally determined kinetic parameters of biomarker thermal maturation [Rabinowitz et al., 2017], to calculate the predicted fraction of the biomarkers reacted for each half-width (Equation 4.2). Additionally, model f values are calculated for scenarios incorporating multiple earthquakes. For each half-width, we consider 100 random samples from the joint probability distribution of E_a/A pairs that define the uncertainty envelope on the biomarker kinetic parameters determined by Rabinowitz et al. [2017] and consider the degree of biomarker alteration resulting from repeated earthquakes. Calculated f values are compared to the measured f values for all biomarker parameters in each sample (e.g. Figure 4.3). For each biomarker parameter in a sample there is a range of measured f values due to the variation in the initial, unaltered values within each sedimentary unit at Site 436. A comparison between the model and the data is considered successful if the calculated f values at a given distance from the slipping zone (+/– half of the width of the sample) fall between the minimum and maximum measured f values for all biomarker

constraints in that sample. We note that, due to the large uncertainty in the $U_{37}^{k'}$ kinetics, $U_{37}^{k'}$ provides the least constraint of the four biomarker parameters investigated here.

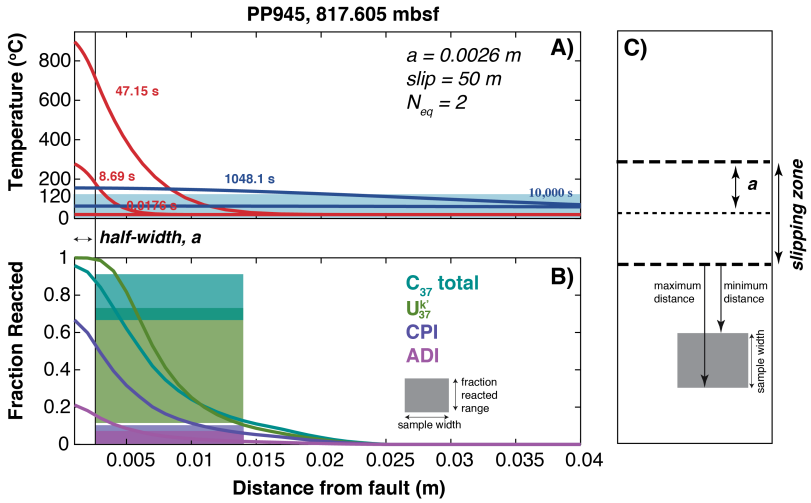

Figure 4.3: Example of a coupled fault heating and biomarker thermal maturity model for sample PP945 assuming a fault half-width of 0.0026 m and slip of 50 m for 2 earthquakes. Slip zone half-width is indicated by a black vertical line. (A) Temperature rise at a series of time-steps during (red) and after (blue) seismic slip at 1 m/s. The minimum temperature of biomarker reaction, 120 ^{o}C, is indicated by the light blue bar. (B) Fractions reacted with distance from the fault calculated for C_{37} total, $U_{37}^{k'}$, CPI, and ADI are represented by colored curves. Corresponding sample measurements are indicated by translucent boxes in the appropriate color. The height of the boxes indicates the range of measured fractions reacted for each biomarker and the width of the boxes indicates the sample width used in the model. Note that because this sample was not within the candidate slip zone, only distances further than the slip zone width are considered. (C) Schematic of model set-up. Candidate slipping zone is indicated by bold dashed lines. Half-width is half of the thickness of the candidate slipping zone (indicated by thin dotted line). Grey box represents the sampled region of core with the minimum and maximum distances from the slipping zone indicated with arrows. This model fit is considered a success because all modeled biomarker fraction reacted values are within the range of measured biomarker fraction reacted values at an allowable distance from the fault structure. The probability that this sample can be fit by two 50 m slip events is determined by dividing the total number of successful model fits (considering the uncertainty in biomarker parameters) by the total number of models.

We run a forward model for each sample that exhibits a biomarker anomaly (i.e. samples indicated in red in Figure 4.2) to determine potential temperature rise from large earthquakes. As stated above, temperature rise is a function of shear stress and slip during the earthquake, as well as fault parameters such as fault thickness and rock properties. Parameters used to model temperature rise are taken from observations of the JFAST borehole

and sediments (Figure 4.4), along with measurements of material properties from the core [Fulton et al., 2013]. Shear stress on the fault is 0.54 MPa, as determined by JFAST borehole temperature decay measurements reported by Fulton et al. [2013]. Estimates of shallow displacement during the Tohoku earthquake range from ∼40–80 m [Sun et al., 2017]. Our models span this range and, in addition, we explore displacements from 5–150 m to determine the minimum event slip required to replicate the observed biomarker anomalies, with models conducted every 10 m displacement. Sediment density ρ=1850 kg/m^3, thermal diffusivity α=3.92x10^{-7} m^2/s and heat capacity c=1515.7 J/kg*K are based on measurements of samples recovered at JFAST [Chester et al., 2012, Fulton et al., 2013].

We use core observations to find potential fault structures close to each anomalous biomarker sample. In some cases, samples were taken directly from a fault structure (samples PP829 and 948), while other samples were from intact sections of the core. In those cases, we measure the distance to the closest potential fault and compare our thermal maturity to an equivalent off-fault distance in our model (e.g. Figure 4.3).

Active slipping thickness can be difficult to ascertain from structure data alone because there are often multiple localized slip zones within a fault and determining whether these represent separate events or if the whole fault was active during a particular earthquake is impossible. For samples associated with a clear structure with easily definable boundaries, the maximum thickness of the slipping zone is considered to be the thickness of that structure. To further constrain fault width, we establish a minimum and maximum possible thickness based on known temperature limits of two reactions. The biomarkers used in this study do not react at short timescales (minutes–days) below 120 ^{o}C [Rabinowitz et al., 2017], which limits the maximum half-width of the fault due to the lower temperature rise with thicker half-widths (e.g. $a_{max} = 4.8$ cm assuming a displacement of 50 m; Figure 4.5A). Furthermore, forward models indicate that a Tohoku-sized earthquake would not generate temperature above 120 ^{o}C at distances more than ∼5 cm from the fault, which is an important constraint for off-fault anomalies (Figure 4.5B). On the hotter end of the spectrum, we expect smectite

clay to amorphize at 900 ^{o}C [Noyan et al., 2008, Spray, 1992]. Amorphous clay material is not observed in the JFAST core, suggesting temperatures remained below 900 ^{o}C for all samples and limiting the minimum fault half-widths because of the larger temperature rise with thinner half-widths (e.g. a_{min} = 0.26 cm for 50 m displacement; Figure 4.5A). By placing the modeled events along faults of different thicknesses, we get a range of possible temperature rises (e.g. Figure 4.6).

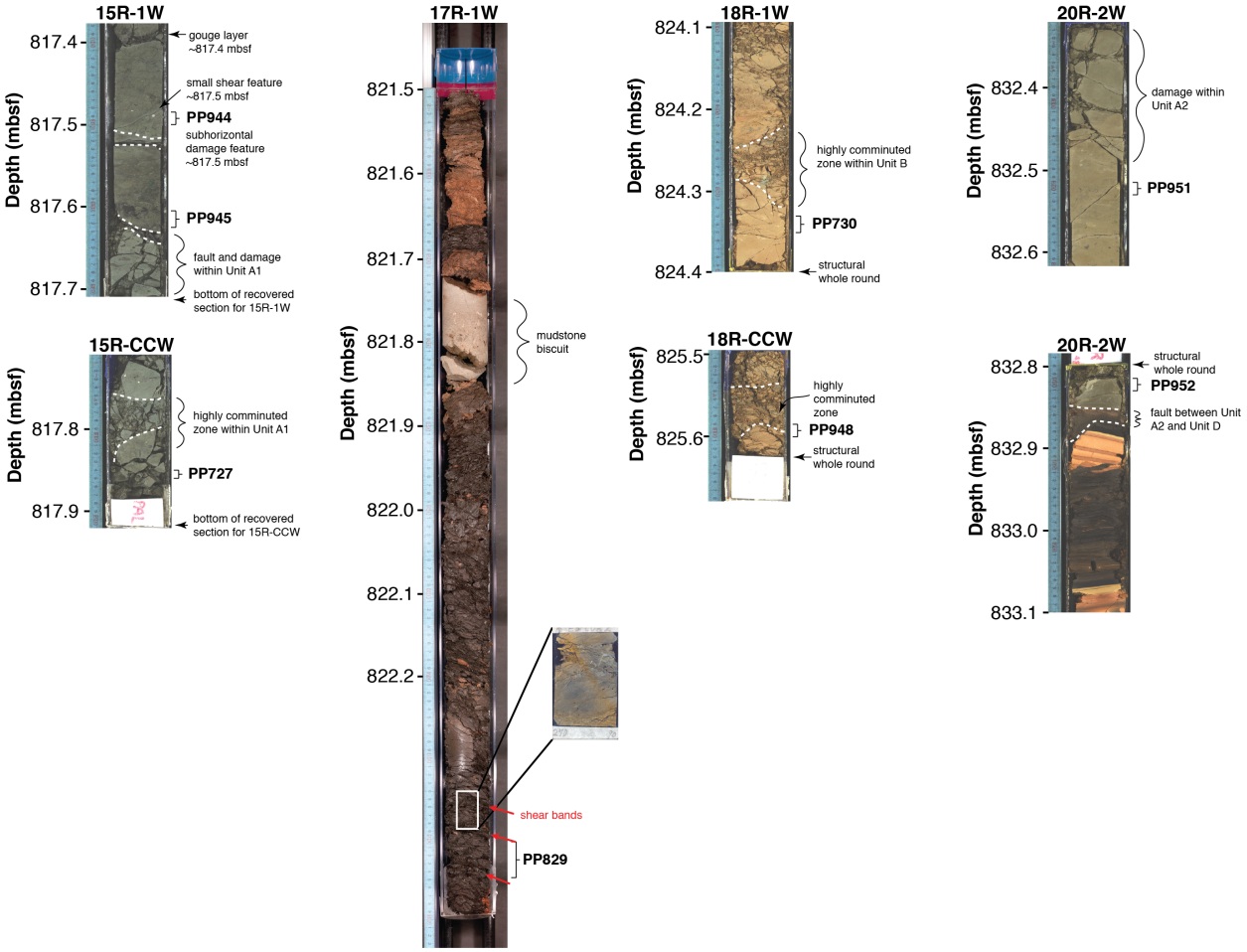

Figure 4.4: Temperature rise on faults modeled was constrained by core observations. Sample locations are indicated with brackets and sample numbers. Damage features described in the supplemental material, as well as the locations of structural whole rounds and core boundaries are indicated by dotted white lines as well as annotations to the right of the core pictures [Chester et al., 2012]. The images of Core 17, taken before structural whole rounds were removed from the core, are courtesy of J. Kirkpatrick.

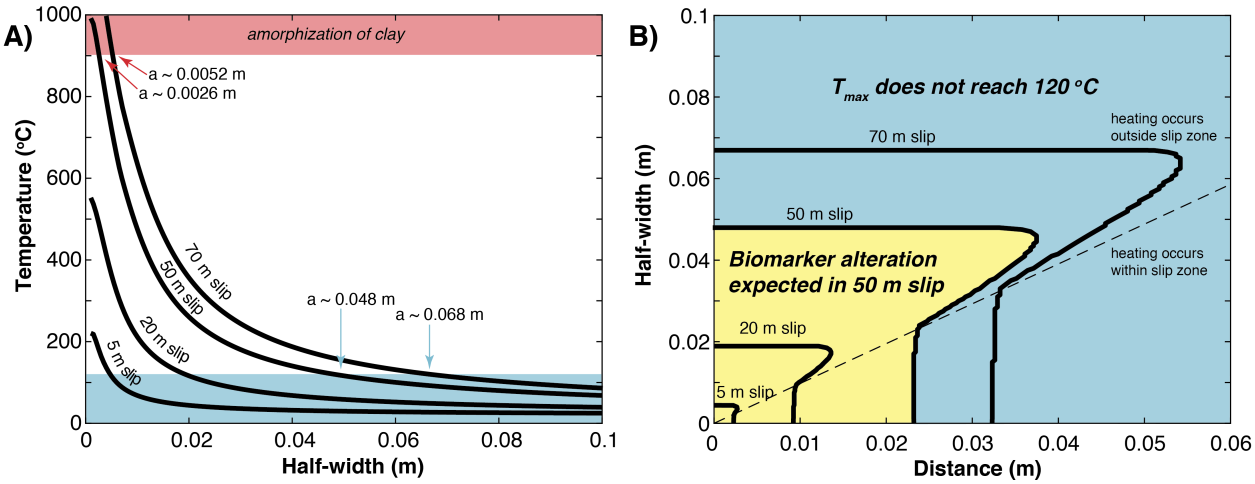

Figure 4.5: A) Temperature rise was additionally constrained by the fact that T_{max} could not exceed 900 ^{o}C, at which point smectite should become amorphous (red shaded region), or be less than 120 ^{o}C, the minimum temperature for the thermal maturation of the biomarkers considered here (blue shaded region). These temperature bounds put limits on the maximum and minimum fault half-widths (a) that could be considered for a given amount of seismic slip. B) Acceptable distances from the faults were constrained by the distances where temperatures reach $\geq$120 ^{o}C at a given fault a (indicated in yellow for 50 m slip).

In addition to the possible range in fault half-widths, we also consider the potential cumulative biomarker thermal maturity from multiple slip events to explore the possibility that the fault experienced multiple earthquakes. In the case of multiple slip events, we limit the total slip on a fault to 3.2 km, based on the palinspastic reconstruction of Chester et al. [2013]. This gives an end-member situation that all displacement accommodated in this plate boundary fault zone occurred on one of the faults observed at the JFAST site and gives a maximum number of events of any given slip for each structure [Keren and Kirkpatrick, 2016a, Kirkpatrick et al., 2015, Rabinowitz et al., 2015]. Clearly, this approximation overpredicts the maximum number of earthquakes on each structure as no structure analyzed here or present in unrecovered sections of the JFAST core could have accommodated all 3.2 km of displacement.

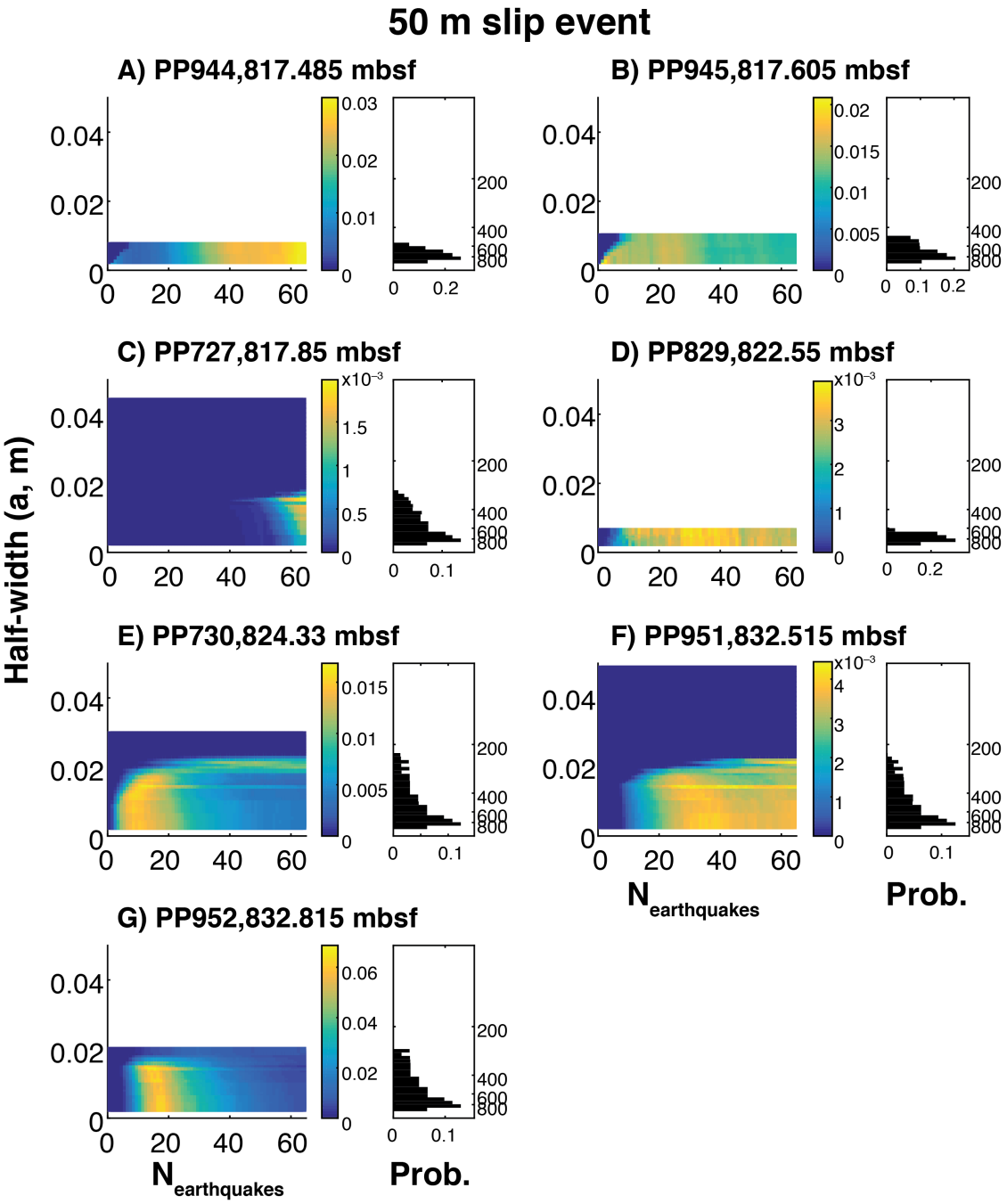

Figure 4.6: (A–G) Results from coupled fault heating and biomarker reaction models, assuming 50 m of slip as observed in the Tohoku earthquake and 0.54 MPa coseismic shear stress as determined by Fulton et al. [2013]. Colored plots show the probability of matching all biomarker constraints with a given fault half width, slipping in a given number of earthquakes. White areas correspond to half-widths that are either too thin (would yield a peak temperature above 900 ^{o}C) or thicker than the observed fault structure recovered in the JFAST core. Histograms to the right of each colored plot show the probability of a match for a range of half-widths (summed across number of earthquakes) with the right-hand y-axis label showing the corresponding peak temperature.

The probability of a given combination of half-width and number of earthquakes describing the core observations for each biomarker is taken to be the number of successes divided by the number of E_a/A pairs considered (100*the number of distances interrogated between the slipping zone and sample). The joint probability of a match for the given combination of a, $N_{earthquake}$, and distance from the fault is found by multiplying the probabilities of each individual biomarker. These constraints are used to generate a series of probability distributions of different a, $N_{earthquake}$ combinations for a given amount of slip for each sample (e.g. Figure 4.6 for 50 m of slip). The probability of each event slip is then evaluated to determine whether earthquakes of that size could be hosted on the structure (Figure C.10). For example, the 50 m symbols on Figure 4.7 are the maximum values from the probability distribution for each fault in Figure 4.6.

We are interested in the smallest earthquake that could cumulatively generate the biomarker signal, given the constraint of 3.2 km total slip. The probability of a given event slip is taken to be the maximum of the probabilities calculated for all (a, $N_{earthquake}$) pairs, and the smallest earthquake allowed by the data is taken to be the minimum event slip with a non-zero probability (Figure 4.7). This is a minimum constraint as it is the lowest slip magnitude where some of the models match the data within the uncertainty in the measured f and uncertainty in the biomarker kinetics. Larger events could also have generated the observed biomarker signature on these faults as evidenced by the non-zero probabilities (fraction of models matching the data) as event slip continues to increase (Figure 4.7). We emphasize that in the models presented here, the probability describes the half-width and number of earthquakes that have the most successful matches for the four biomarker parameters.

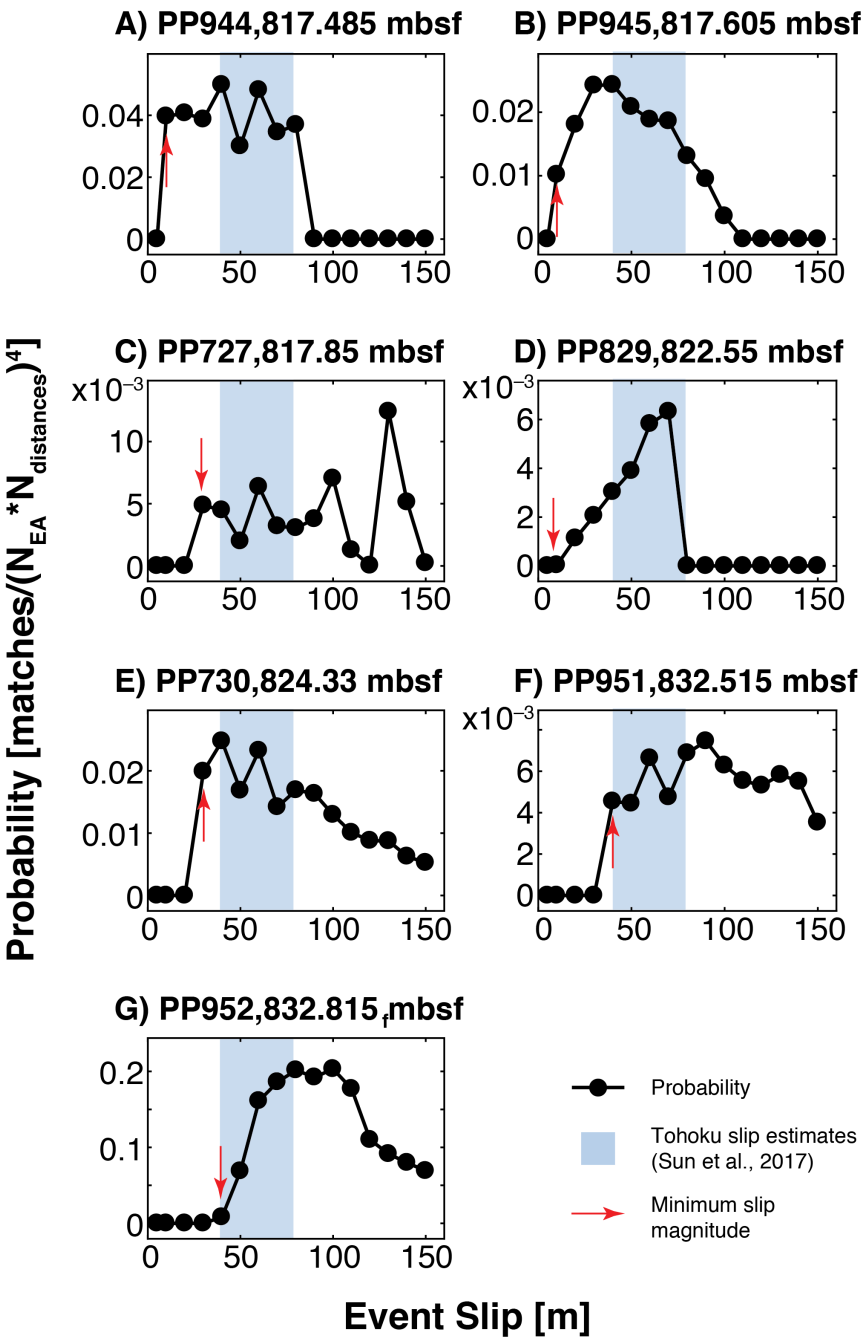

Figure 4.7: (A–G) Maximum probability (model matches to all four biomarker fraction reacted observations/ $N_{EA} * N_{distances}$, where N_{EA} is the number of kinetic E and A rate pairs sampled from their joint uncertainty distribution and $N_{distances}$ is the number of distances away from the center of the slipping zone that were sampled) for a range of slip magnitudes. Blue bars indicate the range of displacements that have been modeled for the Tohoku-oki earthquake [Sun et al., 2017] and red arrows indicate the minimum required slip magnitudes for each sample, corresponding to the minimum slip magnitude values plotted in Figure 4.8. The lowest slip magnitude where the probability is greater than zero determines the minimum required slip magnitude to explain the biomarker measurements given their uncertainty and the uncertainty of the biomarker kinetics. Higher slip magnitudes are allowed but not required.

4.4 Results and Discussion

Our biomarker analysis indicates that seven of the faults we sampled have experienced shear heating (Figure 4.2). Some faults only show a heating anomaly in the alkenone proxies, due to the faster reaction rates of alkenones compared to *n*-alkanes [Rabinowitz et al., 2017]. The pelagic clay layer has initial alkenone concentrations below the detection limit, so the temperature anomaly there is based solely on the *n*-alkanes. Of the two pelagic clay samples that we analyzed, only one exhibited biomarker anomalies, implying that seismic slip in this weak layer took place only on select localized features [Kirkpatrick et al., 2015].

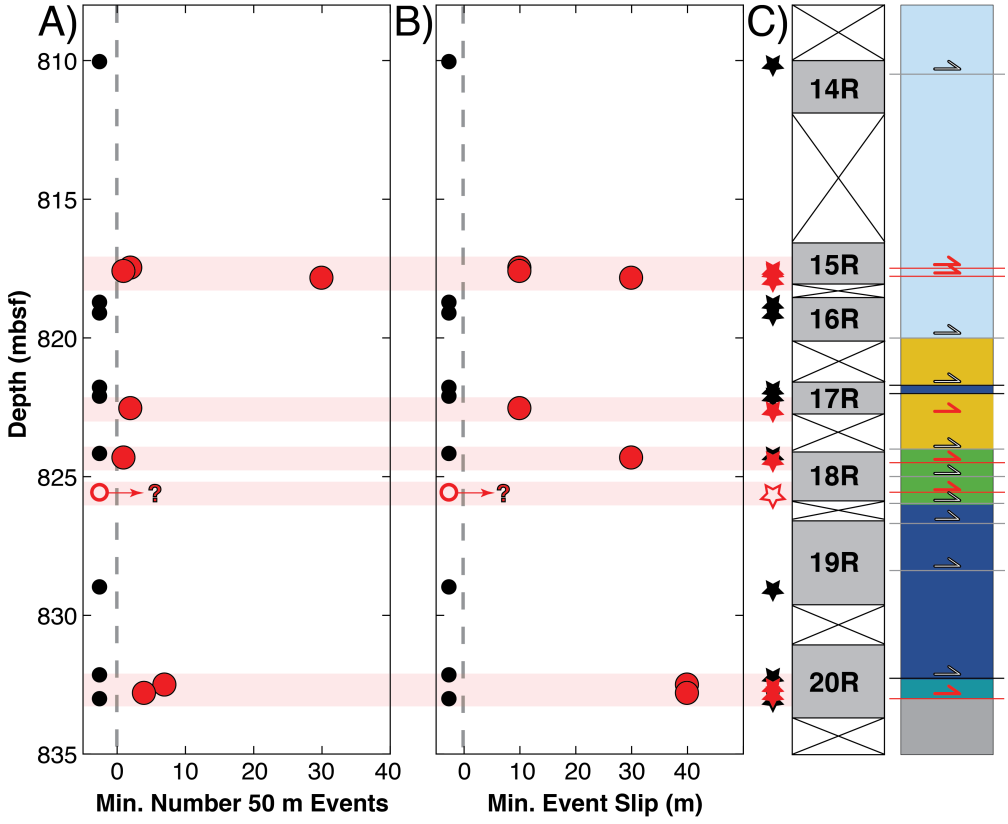

Figure 4.8: Model results. (A) Minimum number of 50 m slip events and (B) minimum event slip (assuming 3.2 km total displacement) required to generate the observed biomarker anomalies in JFAST samples. (C) Samples, core recovery, and stratigraphy as in Figure 4.2E. Red symbols in all plots indicate features with clear biomarker anomalies. Hollow symbols represent sample PP948, which has alkenone concentrations below the quantification limit and is not modeled.

4.5 Biomarker constraints on earthquakes hosted in the Japan Trench

Because biomarker thermal maturity is cumulative, it reflects the entire seismic history of the fault. This limits our ability to query specific earthquakes, but we can constrain two important questions: 1) Which faults recovered at JFAST could have hosted the 2011 Tohoku-oki earthquake? and 2) What is the minimum earthquake size needed to generate the biomarker signal on each fault? To answer these questions, we couple a forward model of heat generation and dissipation from earthquake slip [Carslaw and Jaeger, 1959, Lachenbruch, 1986] with the laboratory-derived reaction kinetics for the relevant biomarkers [Rabinowitz et al., 2017].

To determine which fault could have hosted the Tohoku-oki earthquake, we forward model an event with 50 m slip and the shear stress inferred from the JFAST temperature observatory [Fulton et al., 2013]. Given the possible range of fault thicknesses and distances from samples, we find that any of the faults with heating anomalies could have hosted at least one such event (Figure 4.8A). In several cases, additional 50 m earthquakes are required on a structure to generate the observed biomarker signal.

Although every fault could have hosted the Tohoku-oki earthquake, multiple smaller events could generate a similar biomarker anomaly on some faults (Figures 4.7, C.6). To constrain an absolute minimum earthquake size that could produce the observed biomarker anomalies, we model multiple earthquakes at a given slip magnitude up to the number of earthquakes that sum to 3.2 km of total displacement on the plate boundary [Chester et al., 2013]. If the observed anomalies cannot be reproduced by these earthquakes, the fault represented by that sample must have experienced at least one earthquake of larger magnitude (Table C.7, Figure 4.7). We model increasingly large earthquakes until we find a minimum event slip capable of reproducing the observed biomarker anomaly (Figure 4.8B). This does not mean that larger earthquakes did not occur on these faults, just that they are not required by our data. The minimum slip is useful because it means that earthquakes at or below this size do not significantly contribute to the cumulative biomarker thermal maturity

of the fault. We find that for all modeled samples, the biomarker signal is generated by earthquakes with more than 10 m of slip [$\sim M_w 8$ and larger; Wells and Coppersmith, 1994].

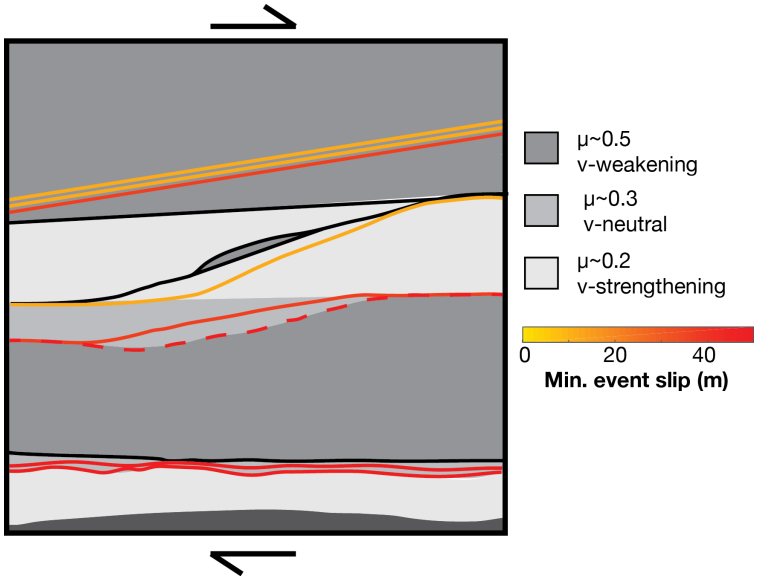

Figure 4.9: Schematic of the structure recovered at JFAST [Kirkpatrick et al., 2015, Rabinowitz et al., 2015]. Faults with biomarker thermal anomalies are colored by the minimum slip magnitude capable of reproducing the observations within the allowable amount of slip [Chester et al., 2013]. Dotted line represents PP948, which was not modeled. Shades of grey represent variations in steady-state frictional behavior [Ikari et al., 2015b].

Despite significant variations in steady-state friction and velocity dependence, seismic faults are present in almost all of the major lithologies [Figure 4.9; Ikari et al., 2015b]. Our findings suggest that while steady-state friction parameters are important for understanding earthquake nucleation, they are not a strong control for shallow rupture propagation. Instead, similarities in dynamic friction (<0.1) measured on two JFAST lithologies suggest that dynamic friction controls shallow rupture propagation [Sawai et al., 2014]. Additional high velocity experiments on all lithologies are needed to test this hypothesis. At present, paleoseismic history, rather than lithology, is the best predictor of shallow seismic hazard in subduction zones.

4.6 Conclusions

Our biomarker analysis highlights the frequency with which large earthquakes propagate into the shallow reaches of the subduction zone. However, there are little other available

data on seismic history of faults through shallow subduction zones [Sakaguchi et al., 2011] to determine whether the degree of shallow seismic activity at the Japan plate boundary is unusual. Future drilling projects at other subduction zones are necessary to determine whether shallow, tsunamigenic seismic slip is common over geologic time.

4.7 Acknowledgements

Funding was provided by NSF OCE 12-60555 to HMS and PJP and a Schlanger Ocean Drilling Fellowship and NSF GRFP (DGE-11-44155) to HSR. Instrumentation for biomarker analyses was supported by the Columbia Center for Climate and Life. The authors thank IODP and the Kochi core center for help obtaining samples and M. Pratt for help with modeling.

5 Frictional behavior of input sediments to the Hikurangi trench

Co-authors: H. M. Savage, R.M. Skarbek, M.J. Ikari, B.M. Carpenter, and C. Collettini

The Hikurangi subduction zone hosts shallow slow slip events, possibly extending to the seafloor. The mechanisms allowing for this slow seismic behavior are poorly understood, but are likely a function of the frictional properties of the down-going seafloor sediments. We conducted friction experiments at a range of effective stresses, temperatures, and velocities on the incoming sediments to the Hikurangi subduction zone to determine whether their frictional properties would promote SSEs. We find that the material frictionally weakens and becomes less velocity strengthening over our effective stress range, whereas temperature has only a small effect on both friction and frictional stability. At plate-rate velocities, the sediment exhibits velocity-weakening behavior. These results imply that the frictional properties of the sediment package subducting at Hikurangi could promote slow slip events at the pressures, temperatures, and strain rates expected along the slab interface up to 10 km depth. The transition to velocity strengthening behavior at faster slip rates could provide a mechanism for maintaining unstable slip at slow sliding velocities, rather than accommodating deformation through ordinary earthquakes.

5.1 Introduction

Strain at plate boundaries is accommodated over a wide range of deformation rates,

ranging from earthquake slip to aseismic creep. Within this spectrum are slow slip events (SSEs), which last for days to months [Dragert et al., 2001, 2004, Ide et al., 2007, Obara, 2002, Ozawa et al., 2007, Vallée et al., 2013, Wallace and Beavan, 2010]. SSEs at the Hikurangi Trench are observed at a range of depths [Wallace et al., 2012, Wallace and Beavan, 2010, 2006], and may play an important role in loading seismogenic fault segments [Hamling and Wallace, 2015, Ito et al., 2013, Kato et al., 2012]. Along the Hikurangi subduction zone of the North Island of New Zealand, shallow SSEs extend to depths <2 km [Wallace et al., 2016] and show a complex relationship with regional deformation, by triggering slip on upper plate faults [Hamling and Wallace, 2015] and being triggered by nearby earthquakes [Wallace et al., 2017]. In addition, the region in which shallow SSEs occur has hosted historical tsunami earthquakes, which are characterized by anomalously long source durations, slightly slower rupture velocities, and a relatively large amount of low-frequency energy relative to their moment [Bell et al., 2014]. These interactions between slow slip and damaging tectonic earthquakes highlight the importance of investigating the mechanisms that control SSEs.

Previous work has suggested that shallow slow slip at Hikurangi (<15 km depth) and other subduction zones might be promoted by elevated pore fluid pressures through a reduction in critical stiffness [Bell et al., 2010, Ellis et al., 2015, Kitajima and Saffer, 2012, Saffer and Tobin, 2011]. In addition, slow slip could be facilitated by a transition from frictionally stable to frictionally unstable or conditionally stable behavior through a reduction in the rate-and-state friction parameter $a - b$ [Ikari et al., 2013b, 2009]. Slow slip can be promoted over conventional earthquake slip by an increase in this $a - b$ parameter (indicating a transition towards frictional stability) with increasing sliding velocity. The transition between positive and negative values of $a - b$ is known as the cutoff velocity [Shibazaki and Iio, 2003, Shibazaki and Shimamoto, 2007]. However, the shallow parts of subduction zones tend to be dominated by clays, which often exhibit frictionally stable behavior and are frequently invoked as the cause of the up-dip limit of the seismogenic zone where earthquakes nucleate [Hyndman et al., 1997, Ikari and Saffer, 2011, Saffer and Marone, 2003, Scholz, 1998].

One important consideration is that subducting sediments often include multiple lithologies, which can impact frictional transitions along the slab interface. Sediments with a range of compositions (including clays and carbonates) become more frictionally unstable at higher pressure and temperature conditions relevant to shallow subduction zone environments [den Hartog et al., 2012b,a, Ikari et al., 2013b, Kurzawski et al., 2016], possibly allowing for the nucleation of unstable slip such as SSEs. It is important to characterize the frictional behavior of sediments subducting at individual subduction zones in order to assess the role that pressure, temperature and composition have in controlling the occurrence of SSEs.

In this work, we investigate the frictional behavior of sediment on the incoming plate of the Hikurangi trough [ODP Site 1124; Figure 5.1A; Plank, 2014]. The upper portion of the incoming stratigraphy consists of a mixture of carbonate and clay, and is likely similar to the material within the shallow subduction zone. Through velocity-stepping friction experiments at a range of effective stresses and temperatures, as well as new plate-rate experiments [Ikari et al., 2015a, Ikari and Kopf, 2017], we investigate the strength and stability of this mixed sedimentary material. We find that the frictional properties of the subducting sediments at Hikurangi could promote instability.

5.2 Background

5.2.1 Slow slip in subduction zones

Slow slip in subduction zones was first observed in Japan and Cascadia [Dragert et al., 2001, Rogers and Dragert, 2003, Sacks et al., 1978] and has now been observed in many subduction zones around the world [Ide et al., 2007, Ito et al., 2013, Ito and Obara, 2006, Kato et al., 2012, Obara, 2002, Ozawa et al., 2007, Peng and Gomberg, 2010, Vallée et al., 2013, Wallace et al., 2012, Wallace and Beavan, 2006]. Slow slip can be detected geodetically, or inferred through seismically detectable events such as non-volcanic tremor [Dragert et al., 2004, Obara and Hirose, 2006, Payero et al., 2008, Wallace and Beavan, 2010, Walter et al., 2011]. Here, we use the term slow slip to include all of these observations where a fault slips at subseismic velocities in a frictionally unstable manner. Slow slip is often observed

at the down-dip limit of the seismogenic zone [Peng and Gomberg, 2010]. It is generally interpreted as a frictionally transitional deformation behavior and is often associated with high pore fluid pressures [Saffer and Wallace, 2015]. Although harder to detect because of observational constraints, SSEs also occur above and within the seismogenic zone [Araki et al., 2017, Outerbridge et al., 2010, Wallace et al., 2016, Wallace and Beavan, 2010]. SSEs have been observed as precursors to large megathrust earthquakes, such as the 2001 M_w8.4 Peru earthquake [Melbourne and Webb, 2002], the 2011 M_w9.1 Tohoku-oki earthquake [Ito et al., 2013, Kato et al., 2012], and the 2014 M_w7.3 Papanoa earthquake [Radiguet et al., 2016], demonstrating that they may increase stress within seismogenic zones in some cases.

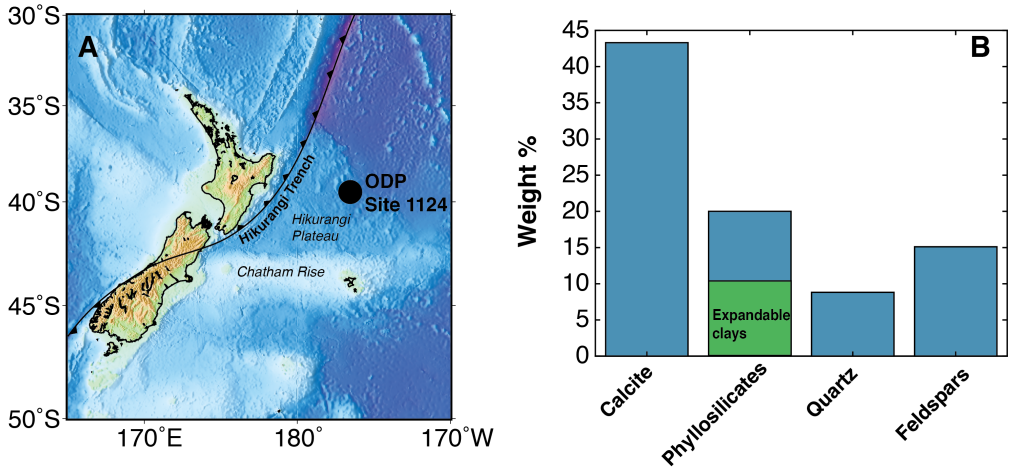

Figure 5.1: A) Map of New Zealand with location of the Hikurangi trench just east of the North Island. The samples used in this study come from ODP Site 1124. B) XRD analysis shows the sediment is composed of 43.3% calcite, 20% phyllosilicates (∼10% expandable clays shown in green), 8.8% quartz, and 15% feldspar.

5.2.2 Hikurangi shallow slow slip and Stratigraphy of Leg 181 ODP Site 1124

The Hikurangi margin can be divided into the northern and southern sections based both on geomorphic character and observed slip behavior. The convergence rate of the Australian and Pacific Plates also varies dramatically along the trench from a rate of ∼6 cm/y in the north, decreasing to ∼2 cm/y in the south [Wallace et al., 2004]. Geodetic coupling varies along the margin as well. The northern section is coupled only to ∼5–15 km depth while the southern section is coupled to ∼30 km depth [Wallace et al., 2004, Wallace and Beavan, 2010]. The Hikurangi margin exhibits a paucity of large magnitude megathrust

earthquakes. The largest recorded earthquakes at Hikurangi are two $\sim M_w 7$ events that occurred near Gisborne in 1947 [Bell et al., 2014, Doser and Webb, 2003], and there are no $M_w > 7.2$ earthquakes in the historic record [Wallace et al., 2009]. Instead, the deformation seems to be largely accommodated through SSEs with an equivalent seismic moment release of $\sim M_w$ 6.5–7 [Wallace et al., 2012]. These SSEs fall into two main categories. Deep SSEs occur in the southern section at depths of ∼20–70 km, have durations of ∼1.5 years, and repeat times of ∼5 years [Wallace et al., 2012, Wallace and Beavan, 2006]. Shallow SSEs have been observed in the northern section of the margin, where a relatively thin sedimentary package (∼1 km as compared to ∼3–6 km in the south) is subducting [Davy and Wood, 1994, Lewis et al., 1998]. Shallow SSEs with durations of 1–3 weeks occur approximately every 2 years and may propagate to the trench [Beavan et al., 2007, Douglas et al., 2005, Wallace et al., 2016, 2012, Wallace and Beavan, 2010]. These events appear to be correlated with zones of elevated pore fluid pressure [Bell et al., 2010, Ellis et al., 2015, Saffer and Wallace, 2015]. However, it remains unclear whether elevated pore pressure in the shallow portions of a subduction zone is the only mechanism required for slow slip.

One important factor to constrain in order to understand slow slip is the frictional behavior of the sediments subducting at the Hikurangi Trench. Extensive work on subduction zone sediments has highlighted the evolution of frictional behavior at a continuum of slip rates [Buijze et al., 2017, Faulkner et al., 2011, Ikari et al., 2013a, 2011a, Ikari and Kopf, 2017, Ikari et al., 2015a, Ujiie et al., 2013]. At a distance of ∼500 km, ODP Site 1124 is the closest existing ocean drill core through the input sediments to the Hikurangi Trench. Core recovered at this site extends to a depth of ∼470 mbsf and is composed primarily of nanofossil ooze interlayered with clays and mudstones [Carter et al., 2000]. The complete stratigraphy was determined using both this core and nearby DSDP Site 317, which penetrated to basement. The entire subducting sediment package is composed of ∼800 m of nanofossil ooze (∼40 wt% carbonate), underlain by ∼800 m of volcaniclastics [Plank, 2014]. In this study, we investigate the frictional behavior of carbonate-rich sediments sampled from

cores at Site 1124.

5.2.3 Friction of subducting sediments

Because clays are common in subducting sediments and fault gouges, there has been considerable effort towards characterizing clay friction [Vrolijk and Van Der Pluijm, 1999]. Studies consistently show that clays are weaker than most other materials, exhibiting friction (μ) values significantly below Byerlee friction ($\mu = 0.6$) in both dry and wet experiments [Bird, 1984, Byerlee, 1978, Faulkner et al., 2011, Ikari et al., 2009, Moore and Lockner, 2007, Morrow et al., 1992, Saffer et al., 2012, 2001, Saffer and Marone, 2003, Tembe et al., 2010]. Unlike many other materials, which maintain a pressure dependent shear strength (constant friction coefficient) through upper crustal conditions, some clays exhibit a rapid reduction in friction at relatively low effective stresses of ∼30 MPa, indicating a transition to pressure independent shear strength with increasing effective stress [Bird, 1984, Saffer et al., 2001, Saffer and Marone, 2003]. Fabric development in clays is also thought to lead to a decrease in steady-state frictional strength [Collettini et al., 2009, Ikari et al., 2011b, Ikari and Saffer, 2011].

Clays not only control the steady-state friction of a fault zone, but the fault stability as well. Frictional stability can be described using a rate-and-state friction framework, where friction is a function of both sliding velocity and time. With a step in velocity, there is an immediate change in friction described as the direct effect, a, followed by the evolution of μ to a new steady-state value, known as the evolution effect, b. Materials are considered velocity-strengthening, or frictionally stable, if $a - b > 0$ and velocity-weakening if $a - b < 0$ [Marone, 1998]. When a material is both velocity-weakening and its surroundings are sufficiently compliant, it is considered frictionally unstable. Clays are largely velocity-strengthening, though at low effective stresses and low sliding velocities they can be velocity-weakening [Ikari et al., 2013a, Saffer et al., 2001, Saffer and Marone, 2003]. At high effective stresses, steady-state friction coefficients of clays decrease, and they become consistently velocity-strengthening over the range of velocities used in conventional velocity-stepping experiments

[0.1–200 μm/s; Saffer and Marone, 2003]. These observations are attributed to a reduction in b with increasing effective stress.

While the behavior of clay-rich material at a range of effective stress conditions relevant to shallow subduction zones is well established, fewer studies have focused on the effects of temperature on clay friction. Talc strength decreases with increasing temperature and exhibits only velocity strengthening behavior over a range of $\sim$100–400 ^{o}C [Moore and Lockner, 2008]. Deformation experiments on illite at a range of temperatures have shown an increase in frictional strength with increasing temperature, and the occurrence of velocity-weakening behavior at temperatures ranging from 250–350 ^{o}C, as well as unstable stick-slip behavior at temperatures from 200–600 ^{o}C [den Hartog et al., 2012b,a, Moore et al., 1989, 1986, 1983]. Finally, recent plate-rate experiments show that gouge with high clay contents from a range of plate boundary faults exhibits velocity-weakening behavior and stick-slip instabilities when deformed at sliding velocities of 5–25 cm/yr, similar to tectonic plate rates [Ikari et al., 2015b, Ikari and Kopf, 2017].

Although clay has been shown to control frictional strength of materials, even when it does not constitute a large fraction of the bulk volume of the material [Giorgetti et al., 2015, Ikari et al., 2007, Moore and Lockner, 2011, Niemeijer et al., 2010, Saffer and Marone, 2003, Tembe et al., 2010], calcite is the largest mineral component of the sediment in the Hikurangi samples (Figure 5.1B) and has distinct frictional properties. Experiments on pure calcite and calcite-rich sediment from the Middle America trench offshore Costa Rica show that carbonate-rich sediment exhibits unstable, stick-slip, velocity-weakening behavior at a range of pressures and temperatures relevant to shallow subduction zone environments [Ikari et al., 2013b, Kurzawski et al., 2016, Verberne et al., 2014b,a, 2013]. Because of this velocity-weakening frictional behavior, the presence of calcite in a subducting sediment package could imply the potential for seismogenic conditions at shallow depths. While the carbonate-rich Costa Rica sediments had some phyllosilicates, the weight percent was much smaller than the Hikurangi sediments. More work on natural clay mixtures is necessary to fully characterize

range of possible frictional behaviors.

5.3 Methods

Friction experiments were conducted on input sediments from ODP Site 1124C (Figure 5.1A, Cores 20–5W, 21–5W, and 22–5W, 0–18 cm). Sediment from the cores was crushed and sieved to a grain size of <125 μm in order to homogenize the experimental gouge. The homogenized gouge was measured using XRD and was composed of 43.3 wt% calcite, 20 wt% phyllosilicates, 15.1 wt% feldspar, and 8.8 wt% quartz [Figure 5.1B; Vogt et al., 2002]. Experiments were conducted using a brine approximating the composition of seawater, made by combining 35 g of sea salt with 1 L of distilled water. Using a pore fluid composition that reflects natural compositions is essential because pore fluid composition can have dramatic effects on the deformation behavior of gouge. This is particularly true for calcite-rich gouge which has been shown to exhibit higher rates of pressure solution when deformed with NaCl brine compared with pure water [Zhang and Spiers, 2005].

Friction experiments were conducted on three deformation apparatus to test the range of stresses, temperatures, and velocities expected along the Hikurangi slab interface. By using multiple deformation apparatus, we are able to investigate a wider range of these conditions than is available on any one apparatus. In addition, interlab comparisons confirm that reported friction values are consistent, and that lab variability such as jacketing and piston friction in different apparatus is accurately accounted for. Low effective stress (σ_{eff}) experiments (σ_{eff} = 1–25 MPa) were conducted on the biaxial deformation apparatus at the Istituto Nazionale di Geofisica e Vulcanologia (INGV) in Rome while higher σ_{eff} (σ_{eff} = 25–150 MPa) and elevated temperature experiments were conducted on the triaxial deformation apparatus at the Lamont-Doherty Earth Observatory (LDEO) in New York. Further direct shear experiments (plate-rate experiments) were conducted at the University of Bremen to test the frictional behavior of the gouge at plate convergence rates of ∼5.3 cm/yr (1.68 nm/s).

Table 5.1: Friction experiments conducted on gouge from ODP Site 1124. Note that in biaxial deformation experiments, normal stress is independently controlled while in triaxial deformation experiments, normal stress is a function of the controlled confining pressure and the measured axial stress. Depths were calculated assuming a pressure gradient of 25 MPa/km less the hydrostatic pressure of 10 MPa/km.

Experiment Number	Apparatus Apparatus	Depth (km)	σ_N (BRAVA, slow) (MPa)	P_c (BRAVA, triax) (MPa)	P_p (MPa)	T, mean (^{o}C)	T, std (^{o}C)	Velocity steps (μm/s)
i205	BRAVA	0.067	0.8	0.7	0.5	20	——	1-300
i206	BRAVA	0.33	4	2	1	20	——	1-300
i207	BRAVA	1.67	16	10	1	20	——	1-300
B628	plate-rate	0.67	10	——	——	20	——	0.0017-0.0051
T035	LDEO Triax	10	——	165	12	106.69	3.93	1.41-42.43
T036	LDEO Triax	7	——	115	10	73.35	3.54	1.41-42.43
T037	LDEO Triax	5	——	65	5	47.43	3.15	1.41-141
T039	LDEO Triax	——	——	165	15	20	——	1.41-141
T040	LDEO Triax	——	——	165	15	73.26	3.78	1.41-141
T041	LDEO Triax	——	——	115	10	20	——	1.41-141
T042	LDEO Triax	——	——	65	5	20	——	1.41-141
T044	LDEO Triax	5	——	65	5	47.96	3.33	1.41-141
T045	LDEO Triax	2	——	25	1	20	——	1.41-141

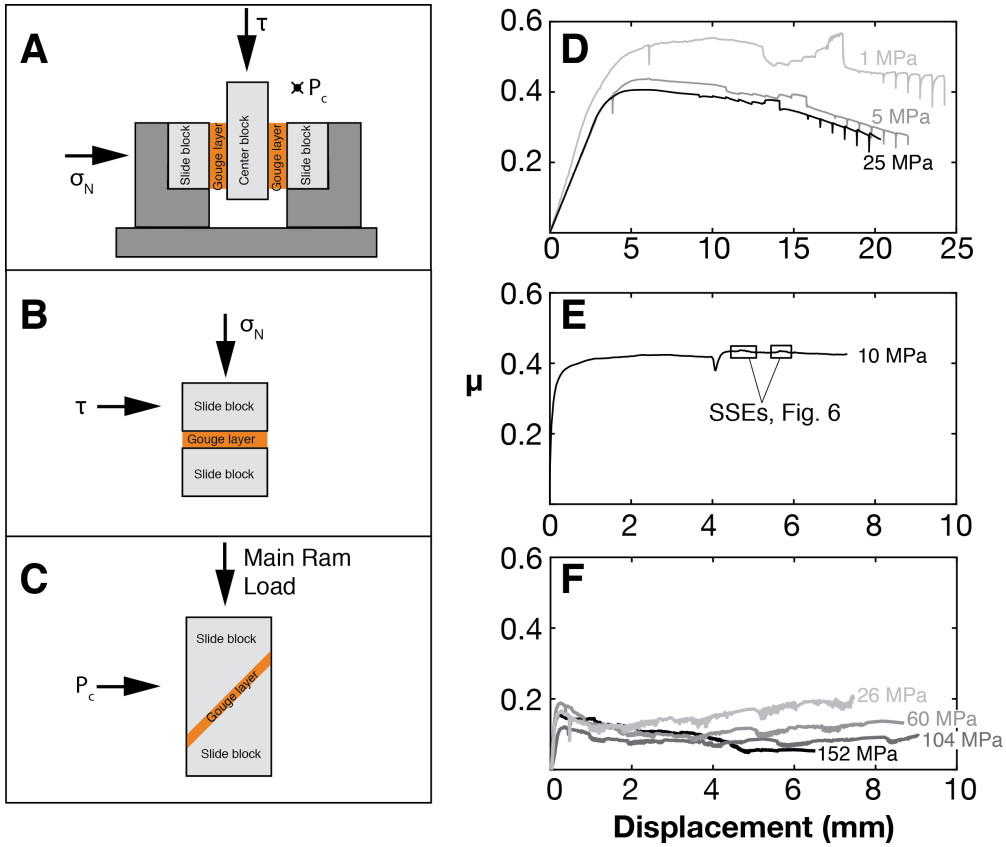

Figure 5.2: Sample configurations for the three apparatus used in this study (A, C, E) as well as friction vs. displacement plotted for each apparatus (B, D, F). Friction curves are labeled with the experimental effective stress. F) Only room temperature triaxial experiments are plotted here for clarity. Effective stress values indicated for the triaxial experiments are mean effective stress during the experiment (Table D.2). Note that the amount of displacement achieved in BRAVA is significantly greater than the other experiments.

5.3.1 Biaxial Deformation Experiments

Biaxial deformation experiments were conducted on the Brittle Rock deformAtion Versatile Apparatus (BRAVA) at INGV in a double-direct shear configuration [Figure 5.2A Collettini et al., 2014]. Horizontal and vertical forces were measured using stainless steel load cells with ±0.03 kN resolution. Displacements were measured using LVDTs with ±0.1 μm resolution. Data was recorded at 10 kHz and down sampled to 1–1000 Hz depending on the shearing velocity. Gouge was sandwiched in two layers between three grooved forcing blocks in ∼6 mm thick layers. This assembly was then jacketed in a rubber jacket to isolate the gouge from the confining fluid during the experiment. The jacketed assembly was placed in the pressure vessel and an initial normal stress of ∼1 MPa was applied to hold the assembly in place. The vessel was then sealed and a confining pressure of ∼0.5 MPa was applied by pumping silicone oil into the pressure vessel. Pore fluid pressure was then applied to ∼0.25 MPa. Confining pressure (P_c), normal stress (σ_N), and pore fluid pressure (P_p) were then raised in parallel to the experimental values. After the experimental values of P_c, σ_N, and P_p were attained, the sample was allowed to equilibrate for ∼1 h as the gouge layer compacted. After this, the central forcing block was driven downward at a rate of 10 μm/s for a run-in of ∼5 mm to achieve a steady-state friction. Due to the significant contribution of phyllosilicates in the gouge material, the samples exhibited significant strain weakening throughout the course of the experiments, so steady-state was taken to be the point at which friction began following a constant linear trend (Figure 5.2D). After steady-state was achieved, velocity-stepping tests were conducted at sliding velocities ranging from 1–300 μm/s to test the velocity-dependence of friction. Slide-hold-slide (SHS) tests were conducted with hold times ranging from 1–1000 s to test the healing rates of the material.

5.3.2 Triaxial Deformation Experiments

High pressure and temperature deformation experiments were conducted on the triaxial deformation apparatus at LDEO. These experiments were conducted using a 45^o sawcut configuration with 3.5 cm diameter cylindrical stainless steel forcing blocks (Figure 5.2C).

Gouge was mixed with some brine to create a paste that was then spread in an even ∼2.1 mm thick layer on one forcing block using a loading jig. The sample was pre-compressed between the two forcing blocks for 1 hour in a hydraulic press with an axial load of 4.5 MPa, yielding a gouge layer ∼1.85 mm thick. The sample assembly was then jacketed with an inner Cu foil jacket to hold the forcing blocks and gouge together throughout the rest of the loading process. This assembly was then placed within a silicone rubber jacket, which extended to cover an o-ring on the top end plug as well as an o-ring on the bottom end cap. The jacket was held in place using stainless steel tourniquets wrapped tightly over these o-rings in order to create a gas-tight seal around the sample.

Pore fluid pressure was applied through high-pressure tubing through the top stainless steel end plug and was distributed across the sample surface through five holes in the top forcing block. Stainless steel frits in the top forcing block prevented gouge from being extruded into the pore fluid system. A teflon shim was placed between the bottom forcing block and end cap to reduce the sliding friction between the forcing block and piston interface during deformation.

The assembly for high temperature experiments included insulating alumina end caps placed between the forcing blocks and upper end plug and lower end cap. For these experiments, a coiled resistive heater was tightly wrapped around the Si rubber jacket, followed by a layer of insulation and aluminum foil. The ends of the insulation were held in place with a layer of self-fusing silicone rubber tape.

This assembly was loaded into the pressure vessel and the piston was advanced until it hit the bottom forcing block. Confining pressure and pore pressure were applied in parallel, keeping P_c at least 5 MPa higher than P_p until the target P_p was reached, after which, P_c was raised to the target confining pressure. For high temperature experiments, the temperature was then increased to the target temperature (T_{set}) over the course of 2 h, controlled using a PID Omega controller which used a J-type thermocouple in contact with the top forcing block as an input. To account for temperature variations along the length of the sample

assembly, calibration tests were performed to determine the temperature at the sample interface relative to the control temperature. For these tests, we monitored the temperature at the interface between the top and bottom forcing blocks (sample location) while controlling temperature from the top forcing block (Figure D.1). Reported temperatures (T_{samp}) are corrected to account for this temperature difference to reflect the true temperature at the gouge layer and are plotted using the mean temperature during the experiment. For room temperature experiments, samples were allowed to equilibrate at the target P_c and P_p for 2 h for consistency. This equilibration time allowed for further compaction prior to the beginning of the run-in.

After equilibration, the piston was advanced at a rate of 10 μm/s for a run-in of $\sim$1–2 mm. Triaxial experiments consisted of velocity-stepping tests with axial velocities varying between 1–100 μm/s (velocities on the shear interface varying between 1.414–141.4 μm/s). Displacement during experiments was measured using an external LVDT. Axial load was measured using an external load cell with a resolution of 0.2 MPa and was corrected for pressure-dependent piston friction (Figure D.2). Confining pressure was decreased by servo control throughout the experiment to account for the decrease in contact area with increasing displacement [He et al., 2006]. In this way, normal stress was held nearly constant. Due to the 45^o sawcut configuration, normal stress (σ_N) and shear stress (τ) during experiments were calculated as

$$\sigma_N = \frac{\sigma_1 + P_c}{2} \tag{5.1}$$

and

$$\tau = \frac{\sigma_1 - P_c}{2} \tag{5.2}$$

where σ_1 is the measured axial stress. Friction ($\mu = \tau/\sigma$) was corrected for jacket strength by subtracting the displacement-dependent frictional strength of the assembly jacket. Multiple jacket strength tests indicated that the displacement-dependent jacket strength increases

with increasing confining pressure, but is insensitive to temperature. Displacement in all figures reflects the elastic-corrected displacement along the shear surface (45^o to the measured axial displacement). We note that, due to the 45^o sawcut configuration, normal stress is a function of axial load, which necessarily changes during velocity steps. The change in effective stress during all velocity steps in this study was <1 MPa. We more fully discuss the implications of this normal stress step in Section 5.3.4.

5.3.3 Plate-rate Deformation Experiments

Plate-rate experiments were conducted in order to test the frictional behavior of the gouge at near plate-rates using a Giesa RS5 direct shear apparatus (Figure 5.2B). Gouge was mixed with water to create a paste, which was placed into the sample cell and cold pressed in a 25 mm diameter, 30 mm height cylinder. These experiments were conducted at room temperature and saturated with seawater, but no controlled pore fluid pressure was applied. Normal stress was applied using a vertical ram with resolution of 0.15 kPa. After initial application of 10 MPa normal stress, the sample was allowed to compact overnight ($\sim$18 h). Pore fluid remained in communication with the sample through stainless steel frits in the bottom plate with the top plate in communication with the atmosphere. During this time, it is assumed that pore fluid pressure dissipates, and σ_{eff} is taken to be equivalent to the applied stress.

Run-in began after the compaction rate, determined as the change in distance between the top and bottom forcing block, became negligible. Initial run-in was achieved by displacing the top plate relative to the bottom plate at a sliding velocity of 10 μm/s. After steady-state friction was achieved, the slip velocity was decreased to 1.68 nm/s (equivalent to 5.3 cm/yr as observed at Hikurangi), followed by a subsequent velocity step to 5 nm/s. Shear stress was monitored using a horizontal load cell with resolution of 0.3 kPa.

5.3.4 Determining rate-and-state friction parameters

Friction (μ) was determined as the ratio of shear stress to effective stress:

$$\mu = \frac{\tau}{\sigma_{eff}} = \frac{\tau}{\sigma_N - P_p} \tag{5.3}$$

Velocity-dependence of friction is described as $a-b$, where a and b are dimensionless constants determined through analysis of velocity-step data. Velocity-steps in the biaxial experiments (BRAVA and the plate-rate experiments) were analyzed using the rate-and-state friction formulation, where friction is described as:

$$\mu = \mu_0 + aln\left(\frac{V}{V_0}\right) + b_1\left(\frac{V_0\theta_1}{D_{c1}}\right) + b_2\left(\frac{V_0\theta_2}{D_{c2}}\right) \tag{5.4}$$

and the state variable can be defined as

$$\frac{d\theta_{1,2}}{dt} = 1 - \frac{V\theta}{D_{c1,2}} \tag{5.5}$$

or

$$\frac{d\theta_{1,2}}{dt} = -\frac{V\theta}{D_{c1,2}} ln\left(\frac{V\theta}{D_{c1,2}}\right) \tag{5.6}$$

where μ_0 is the friction coefficient prior to a velocity-step, V_0 and V are the sliding velocities prior to and after the velocity-step, respectively (μm/s), θ_1 and θ_2 are the state parameters (s), and D_{c1} and D_{c2} are the critical slip distance (μm) [Dieterich, 1979, Marone, 1998, Ruina, 1983]. These parameters were determined using a least-squares iterative inversion [Table D.1; Reinen and Weeks, 1993]. We model velocity steps using the Dieterich (aging; Equation 5.5) for the BRAVA and plate-rate experiments and both the Dieterich (aging; Equation 5.5) and Ruina (slip; Equation 5.6) state evolution laws for the triaxial experiments. However, fits yield indistinguishable results (e.g. Figure D.3) and we report RSF parameters determined using the Dieterich law.

In the triaxial deformation experiments, due to the sample geometry, σ_{eff} changes with a velocity step. Because of this, velocity-dependence of friction in these experiments was modeled using an alternative evolution of the state variable that takes into account changing normal stress during the velocity steps [Hong and Marone, 2005, Linker and Dieterich, 1992, Perfettini et al., 2001]:

$$\frac{d\theta}{dt} = 1 - \frac{V\theta}{D_c} - \frac{\alpha\theta}{b\sigma}\frac{d\sigma}{dt},\ \alpha = \frac{\Delta\tau/\sigma}{ln(\sigma/\sigma_0)} \tag{5.7}$$

where α is the normalized frictional response to a step in normal stress. Typically, a normal stress step is considered to have a similar effect as a velocity step, with an increase in normal stress causing an increase in shear stress, which decays to a new steady-state value. Both modeling and experimental studies have shown that α is limited to a value between 0 and steady-state friction, μ_{ss}, after the velocity step or change in σ_N [Hong and Marone, 2005, Perfettini et al., 2001]. Thus, for each velocity step, we determined the parameters a, b, and D_c assuming the end member cases where α=0 and α=μ_{ss}. The changes in σ_{eff} during the velocity steps in our experiments are <1 MPa, and, thus, lower than is normally considered in normal stress stepping experiments and not expected to strongly influence the results reported here. Indeed, for all velocity steps in this study, while RSF parameters determined under these two bounding conditions vary slightly, $a-b$ values determined with the two approaches are indistinguishable (Figure D.3, Table D.1) and we plot only the values obtained using the α=0 case.

5.4 Results

Performing friction experiments on multiple apparatuses affords us the opportunity, not only to access a wider range of deformation conditions, but also to compare results across labs. We find that friction values measured at comparable σ_{eff} conditions in the different apparatus are consistent. The plate-rate experiment, conducted at σ_{eff}=10 MPa, has a friction coefficient of ∼0.4 and falls well within the range of friction coefficients measured

in the BRAVA experiments, which were conducted at σ_{eff}=1–25 MPa (Figure 5.3A). One overlapping experiment conducted in the triaxial apparatus at σ_{eff} ∼26 MPa shows a friction coefficient that is comparable to the σ_{eff}=25 MPa BRAVA experiment (Figure 5.3A). The BRAVA friction coefficient is found to be slightly higher than the value measured in the triaxial deformation apparatus. However, friction steadily decreased throughout the BRAVA experiments (Figure 5.2D), suggesting an evolution with increasing fabric development towards a lower steady-state friction coefficient. The gouge layers in the triaxial and plate-rate experiments samples, on the other hand, were much thinner (∼1.85 mm in triaxial and sliding along a surface between two forcing blocks in the plate rate experiments). This thinner shearing layer yields a higher shear strain at much shorter displacements, providing an opportunity for the alignment of clay layers prior to shearing as evidenced by the lack of strain weakening in these experiments.

5.4.1 Effect of effective stress on friction and velocity dependence

Our data show that friction and velocity-dependence vary as a function of effective stress (Figures 5.3A,B). This is apparent from initial observations of the friction data for experiments conducted on the three apparatus (Figure 5.2). Friction values in the lower stress experiments conducted on BRAVA are highest (up to ∼0.57 for the 1 MPa experiment), and show significant strain weakening, with friction decreasing by 0.0068 to 0.0106 /mm displacement. The plate-rate experiment conducted at σ_{eff}=10 MPa shows a friction coefficient of 0.4, which is constant with displacement. High effective stress experiments show overall lower friction coefficients (<0.3).

Velocity-dependence of friction shows a similar pattern, with values decreasing as a function of effective stress (Figure 5.3B). High effective stress experiments also show less scatter in $a-b$ values than lower effective stress experiments. We highlight that the plate-rate experiments, conducted at the relatively low effective stress of 10 MPa, show velocity-weakening behavior at sliding velocities <1 μm/s (Figure 5.3B). This observation, combined with the fact that $a-b$ decreases with increasing σ_{eff}, leads us to hypothesize that at plate-rate

velocities and higher σ_{eff}, the gouge would have mostly velocity-weakening behavior.

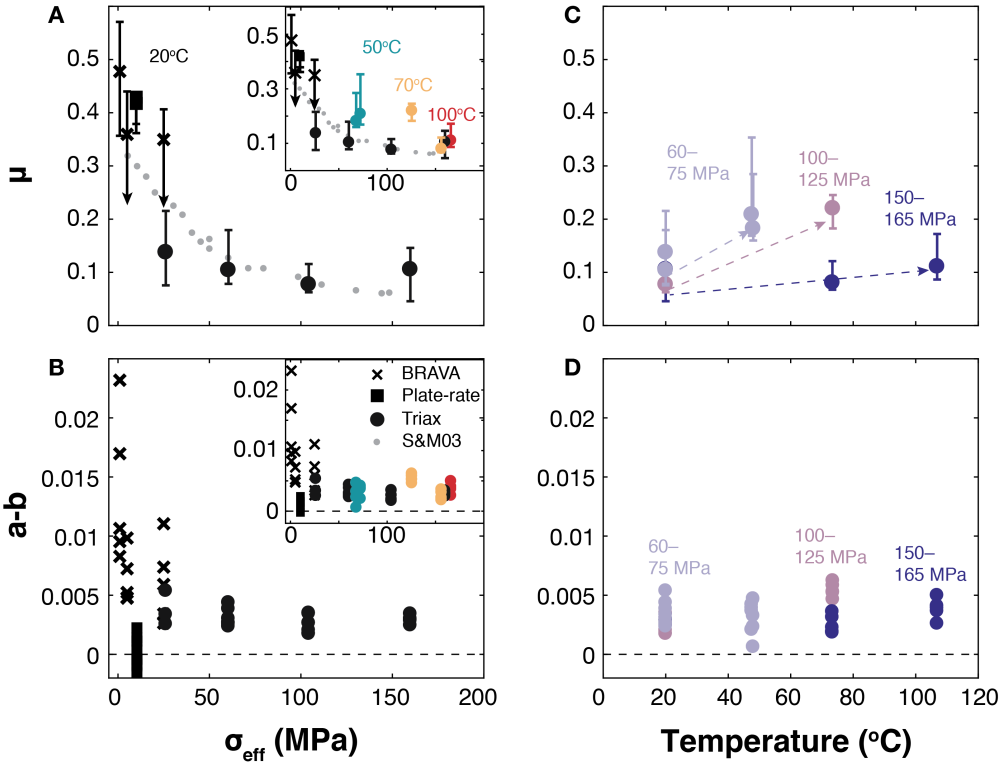

Figure 5.3: A) Friction (μ) and B) $a-b$ plotted against effective stress (σ_{eff}) for room temperature experiments with insets also showing high temperature experiments for completeness. Different symbols represent experiments conducted on different apparatus (xs for BRAVA, squares for slow experiments, and circles for triax experiments). Symbols represent the median friction value with error bars showing the range of friction values observed (A) and the range of $a-b$ values for all velocity steps in a given experiment (B). In (A), grey dots represent data from experiments on pure smectite from Saffer and Marone [2003]. At room temperature, both friction and $a-b$ decrease with increasing effective stress. C) Friction and D) $a-b$ plotted against temperature for triaxial experiments, with color representing effective stress as indicated. Note a slight positive correlation between both μ and $a-b$ and temperature.

5.4.2 Effect of temperature on friction and velocity dependence

The temperatures relevant in the shallow portion of the Hikurangi subduction zone have a much smaller impact than σ_{eff} on friction and frictional stability. Experiments conducted at elevated temperatures show higher friction coefficients than those conducted at the same σ_{eff} and lower temperature (Figure 5.3C). However, this trend becomes less pronounced for higher effective stress experiments. Similarly, we see a slight increase in $a-b$ with increasing temperature (Figure 5.3D), though for the highest stress experiments, this trend is much

less pronounced.

5.4.3 Effect of sliding velocity on velocity dependence

Sliding velocity has a strong effect on velocity dependence at low effective stresses (Figure 5.4). At σ_{eff}=1 MPa, $a-b$ ranges from 0.008 for the 1–3 μm/s velocity step to 0.023 for the 100–300 μm/s velocity step. At higher effective stresses of 5–25 MPa, $a-b$ remains more constant over the range of velocities tested, with values from 0.003–0.011, though the trend of increasing $a-b$ with increasing sliding velocity is still apparent. In the ∼26 MPa experiment conducted on the triaxial apparatus, $a-b$ values are close to those observed in the 25 MPa experiment on BRAVA, though two points are slightly lower, and there is no clear velocity dependence (Figure 5.4). In the plate-rate experiments, conducted at σ_{eff}=10 MPa, we see a transition to velocity-weakening behavior below an up-step velocity of ∼1 μm/s (Figure 5.4).

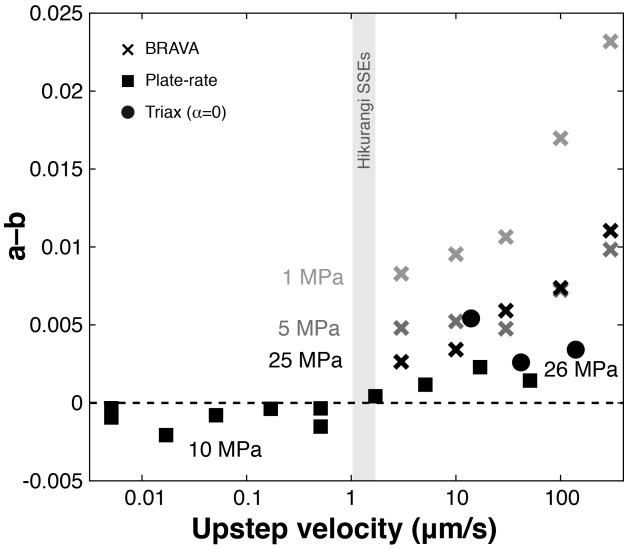

Figure 5.4: Velocity-dependence as a function of up-step velocity. Effective stress as indicated. A clear trend towards increasing $a-b$ values with higher sliding velocity is seen in the lowest effective stress experiments (BRAVA). The lowest $a-b$ values are seen in the plate-rate experiment, conducted at 10 MPa. The approximate range in sliding velocities [Saffer and Wallace, 2015] at the Hikurangi subduction zone is indicated by the grey bar.

5.4.4 Variation in RSF Parameters

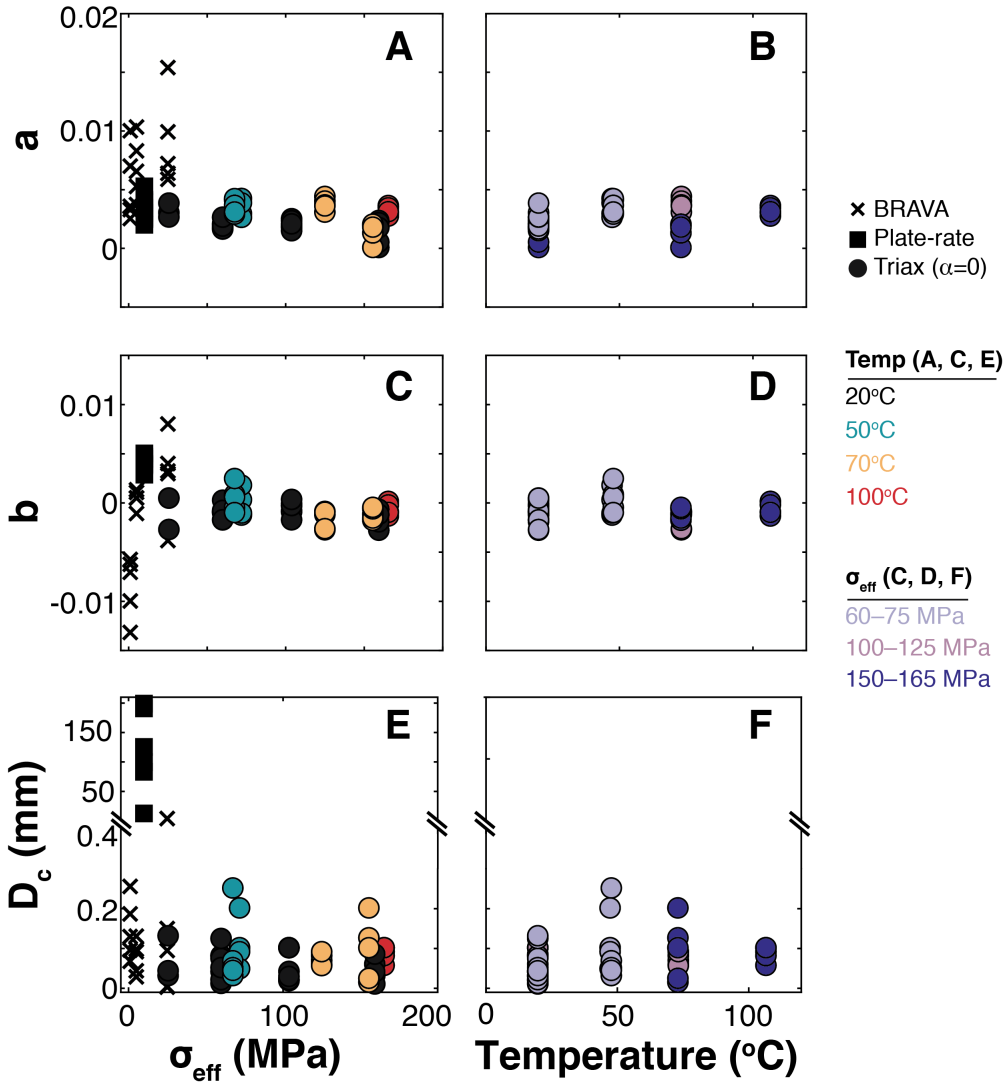

Figure 5.5: Rate-and-state friction parameters as a function of effective stress (A, C, and E) and temperature (B, D, and F). A) a values decrease with increasing effective stress and B) show a slight increase with increasing temperature. C) b values are more variable in the low stress experiments with values hovering around 0 for the high effective stress experiments and D) no clear trend as a function of temperature. E) D_c values show no significant trend with effective stress or F) temperature. C) Plotted b values in the BRAVA and plate-rate experiments represent $b_1 + b_2$. E) D_c in the BRAVA and plate-rate experiments, black symbols represents $D_{c1} + D_{c2}$. Note that the scale of the y-axis changes above the axis break in the D_c plots (E and F).

We see a systematic decrease with increasing effective stress in a values, as well as a slight increase with increasing temperature (Figure 5.5A,B). In all experiments conducted in this

study, we see mostly low values of b with no clear trend as a function of effective stress or temperature (Figure 5.5C,D). Scatter in b appears to decrease with increasing effective stress, implying a diminishing impact of changing sliding velocity on the b value with increasing effective stress. A similar pattern is seen in D_c, with no clear trend as a function of effective stress or temperature (Figure 5.5E,F).

5.4.5 Experimental SSEs

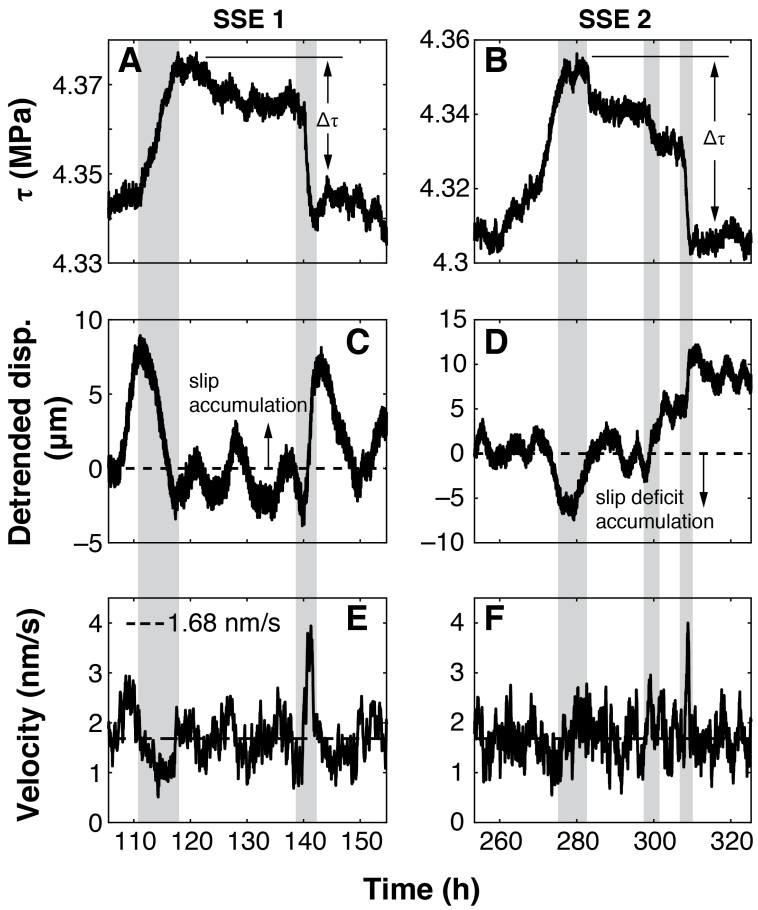

Figure 5.6: Slow slip events observed in the plate-rate experiment, zoomed in from Figure 5.2D. In both events, the final stress drop is ∼0.02 MPa. A) In SSE 1, shear stress drops by ∼0.01 for the ∼20 h at a higher steady state τ. B) In SSE 2, shear stress drops by a total of ∼0.02 MPa during the ∼20 h at elevated stress in two events with ∼0.01 MPa stress drop. C) Displacement in SSE 1 shows a decrease in slip accumulation at the beginning and an increase in slip accumulation at the end of the slip event. D) In SSE 2, a slip deficit is accumulated during the initial shear stress accumulation. Slip is accumulated during each stress drop during this slip event. E and F) During both SSEs, a peak in slip velocity is observed at the time of final stress drop.

Two slow slip events are observed in B628 (Figure 5.2D). The first SSE begins with an

accumulation of stress, accompanied by a reduction in slip velocity along the sample (Figure 5.6A, E). A slow stress release over ∼10 h relieves ∼0.01 MPa of stress and is followed by a relatively fast stress drop ($\Delta\tau$) over ∼1.5 h which relieves the remaining 0.02 MPa of shear stress accumulation, yielding a total $\Delta\tau$ of ∼0.03 MPa. This stress drop is accompanied by a doubling of the slip velocity from the imposed slip velocity of 1.68 nm/s to 4 nm/s (Figure 6E). The second SSE also begins with an accumulation of shear stress accompanied by a slip deficit accumulation. In this case, the gradual shear stress reduction is accommodated largely in two small stress drops of ∼0.01 MPa (Figure 5.6B), each accompanied by a small amount of slip accumulation (Figure 5.6D). The final stress drop occurs over ∼2 h and relieves ∼0.02 MPa shear stress. This stress drop is accompanied by another peak in slip velocity to 4 nm/s (Figure 5.6F).

5.5 Discussion

5.5.1 Mineralogical controls on friction and stability

While the gouge from ODP 1124 used in this study is largely composed of calcite (43 wt%) with smaller contributions of phyllosilicates (∼20 wt%), quartz (∼9 wt%), and feldspars (∼15 wt%), the low friction coefficients observed in our experiments are most consistent with previous observations of friction in smectite clay [Morrow et al., 1992, Saffer et al., 2001, Saffer and Marone, 2003]. This is consistent with previous studies in talc/calcite mixtures which have demonstrated that the phyllosilicate fraction dominates frictional behavior at talc contents of at least 20 wt% [Giorgetti et al., 2015]. Most striking is the strong dependence of friction and frictional stability on effective stress (Figure 5.3A,B). The dramatic reduction in friction coefficient with increasing effective stress is consistent with previous observations of the frictional behavior of smectite-rich gouge [Saffer et al., 2001, Saffer and Marone, 2003]. Saffer and Marone [2003] showed that the friction coefficient of pure smectite decreases to values $\leq$0.1 at effective stresses above 30–40 MPa (Figure 5.3A). They suggest two main mechanisms for this transition, which happens at significantly lower stresses than expected for most minerals. The first mechanism is that the low friction coefficient is controlled

by a weak, hydrated interlayer in the clay structure [Bird, 1984]. At higher stresses, this water could be expelled, leading to locally elevated pore fluid pressures. Alternatively, the transition to pressure-insensitive creep (indicated by the low friction coefficients measured in the high effective stress experiments) could be the result of a transition to achieving nearly full contact between clay grains (real area of contact $\sim$ nominal area of contact) at $\sim$30 MPa. This would be expected to happen at a lower stress for clays than other minerals as a result of the platy structure of the clays and is supported in our experiments by the low values of b observed in all high stress experiments (Figure 5.5C). We note that the evolution in $a-b$ to lower values with increasing effective stress and to higher values with increasing temperature is driven largely by changes in the direct effect, a. Decreases in a with increasing effective stress could be the result of more efficient alignment of the clay fabric, with disruption to that fabric during a velocity step being more dramatic at lower σ_{eff}. At higher temperatures, both friction and $a-b$ increase, with the change in $a-b$ driven by increases in a. The strengthened gouge material at the higher temperatures could exhibit a more substantial disruption to the fabric upon an up-step in sliding velocity. However, this effect is minor compared to the reduction in $a-b$ due to σ_{eff}, suggesting that clay layer alignment is the dominant control on frictional behavior of this sediment at shallow subduction zone conditions.

We note that our higher stress experiments are all on the triaxial deformation apparatus and show overall lower values of μ, even for an experiment conducted at an effective stress within $\sim$1 MPa of the highest stress experiment conducted on BRAVA. This could be the result of the longer pre-compaction time allowed in the triaxial experiments, which would lead to a higher state of fabric development in the gouge prior to deformation. Alternatively, the higher strain accommodated in the plate-rate and triaxial experiments due to the thinner shearing layers could lead to more dramatic fabric development. The interpretation of a fabric-dominated weakening is supported by the strain weakening observed in the BRAVA experiments throughout deformation (Figure 5.2D). Previous experiments

have demonstrated that fabric development can be a strong factor in friction reduction for clay-rich lithologies [Collettini et al., 2009, Ikari et al., 2011b, Tesei et al., 2012]. Low stress experiments on intact fault samples recovered from the upcoming drilling expedition to the Hikurangi Trench (IODP Exp. 375) could determine whether these lithologic effects would serve to lower the friction in the shallowest sediments.

5.5.2 Implications for the Hikurangi subduction zone

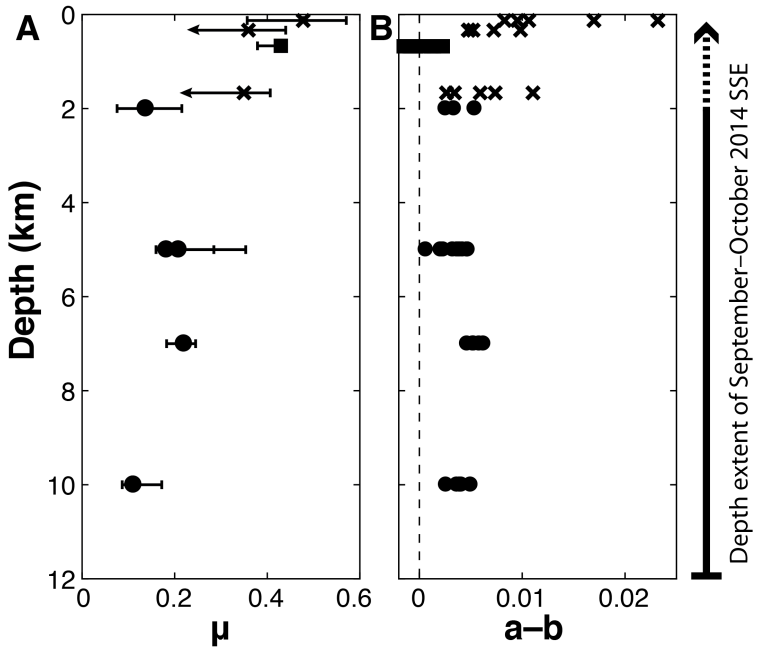

Figure 5.7: Frictional strength and stability with depth. A) Friction and B) velocity-dependence for samples conducted at effective stress and temperature conditions expected for a given depth in the Hikurangi subduction zone are plotted against depth. We see a reduction in friction coefficient and in $a - b$ with increasing depth for traditional velocity-stepping experiments. The depth extent of the September–October 2014 SSE in Hikurangi determined by Wallace et al. [2016] is shown to the right. The dotted line represents the possible extension of this SSE to the trench, though instrumental constraints prevented them from resolving this shallowest extent.

In Figure 5.7, we plot the friction and velocity-dependence of samples deformed at effective stress and temperature conditions consistent with the subducting slab at Hikurangi, assuming stress due to overburden less a hydrostatic pressure gradient and a geotherm of 10 ^{o}C/km [McCaffrey et al., 2008]. We see a reduction in friction coefficient and $a - b$ with increasing depth. We also note that our plate-rate experiments, which showed velocity-

weakening behavior below 1 μm/s, were conducted at 10 MPa, an effective stress below the frictional fall-off that we observe in the other experiments. Assuming that the trends in frictional strength and velocity-dependence with σ_{eff} hold true at lower sliding velocities, this implies velocity-weakening behavior in this gouge deformed at plate-rate velocities at depths of 2–10 km. However, rate-dependent processes such as pressure solution that could control frictional behavior [Bos and Spiers, 2001], are likely to be affected by changes in pressure and temperature. Slow experiments at higher pressure and temperature conditions are necessary to determine the evolution of μ and $a - b$ with increasing depth at plate-rate velocities.

Our results indicate that shallow slow slip in the Hikurangi Trench could be hosted in the sedimentary material tested here. At velocities in the range of 1–300 μm/s, material is velocity-strengthening at low stresses and room temperature, with some velocity-neutral behavior at higher stresses and temperatures, consistent with the occurrence of shallow SSEs at depths below 2 km [Figure 5.7; Wallace et al., 2017]. This is supported by the dramatic decrease in frictional strength at higher effective stress conditions, which would facilitate slip. Though the consistently velocity-strengthening nature of the gouge, particularly at the shallowest depths, supports the occurrence of aseismic slip in this material, our plate-rate experiments show that below the cutoff velocity of $\sim$1 μm/s, this lithology is velocity-weakening (Figure 5.4). This observation is further supported by the occurrence of two spontaneous SSEs in the plate rate experiment (Figure 5.6). These unstable behaviors at low effective stress imply that slow slip could extend even to shallower depths within faults of this composition. We note that elevated temperatures within the range expected for shallow SSEs at Hikurangi [McCaffrey et al., 2008] do not exert a strong control on either friction or frictional stability in this material, but the highest temperatures tested here are modest compared to the temperatures at which velocity-weakening behavior has previously been observed in clays [den Hartog et al., 2012b,a, Moore et al., 1989, 1986, 1983]. However, calcite is expected to exhibit velocity-weakening behavior at the highest temperatures tested

here [Ikari et al., 2013b, Kurzawski et al., 2016, Verberne et al., 2014b,a, 2013]. Therefore, we suggest it does not control the frictional behavior of sediment subducting at the shallow portions of the Hikurangi Trench at velocities higher than $\sim$1 μm/s. However, at lower velocities relevant to SSEs, where mechanisms such as pressure solution might be active, calcite could play a larger role in deformation style (Figure 5.4).

5.6 Conclusions

Our experiments show that even for a lithology with only 20 wt% phyllosilicate, the clay fraction of the gouge controls the frictional behavior. We see that frictional strength decreases dramatically with increasing effective stress, starting at a depth of $\sim$2–3 km, implying low friction at the depths of shallow SSEs in the Hikurangi subduction zone. At the temperatures expected in the shallow subduction zone at Hikurangi, temperature does not exert a strong control on friction or frictional stability. Plate-rate velocities promote velocity-weakening behavior, even at low stresses and temperatures, and suggest that the sediment subducting at Hikurangi is capable of hosting SSEs even without fluid overpressure. These experiments highlight that the normal stress, temperature, and sliding velocities expected in the region of Hikurangi margin slow slip events hover near velocity-neutral behavior. Small perturbations in these conditions could push a fault into instability.

5.7 Acknowledgements

Samples for this study were provided by the International Ocean Discovery Program (IODP). We thank the curatorial staff at the Gulf Coast Repository for help obtaining samples. Funding for this project was provided by an NSF GRFP (DGE-11-44155) to H.S.R. Many thanks to Ted Koczynski for help with the triaxial deformation apparatus.

Bibliography

C.J. Ammon, T. Lay, H. Kanamori, and M. Cleveland. A rupture model of the 2011 off the Pacific coast of Tohoku Earthquake. *Earth, Planets and Space*, 63(7):693–696, 2011. doi: 10.5047/eps.2011.05.015.

R.F. Anderson, M.P. Bacon, and P.G. Brewer. Removal of 230Th and 231Pa at ocean margins. *Earth and Planetary Science Letters*, 66:73–90, 1983.

E. Araki, D.M. Saffer, A.J. Kopf, L.M. Wallace, T. Kimura, Y. Machida, S. Ide, and E. Davis. Recurring and triggered slow-slip events near the trench at the Nankai Trough subduction megathrust. *Science*, 356(6343):1157–1160, 2017. doi: 10.1126/science.aan3120.

C.E. Barker and M.J. Pawlewicz. The correlation of vitrinite reflectance with maximum temperature in humic organic matter. In G. Buntebarth and L. Stegena, editors, *Lecture Notes in Earth Sciences, Paleogeothermics*, volume 5, pages 79–93. Springer, Berlin, 1986.

A. Bartolini. Cretaceous Radiolarian Biochronology and Carbon Isotope (Northwestern Pacific, Nadezhda Basin). Technical Report September 2002, Proceedings of the Ocean Drilling Program, 2003.

M. Bau and A. Koschinsky. Oxidative scavenging of cerium on hydrous Fe oxide : Evidence from the distribution of rare earth elements and yttrium between Fe oxides and Mn oxides in hydrogenetic ferromanganese crusts. *Geochemical Journal*, 43:37–47, 2009.

J. Beavan, L. Wallace, H. Fletcher, and A. Douglas. Slow slip events on the hikurangi subduction interface, New Zealand. *International Association of Geodesy Symposia*, 130(2001):438–444, 2007. ISSN 09399585.

R. Bell, R. Sutherland, D.H.N. Barker, S. Henrys, S. Bannister, L.M. Wallace, and J. Beavan. Seismic reflection character of the Hikurangi subduction interface, New Zealand, in the region of repeated Gisborne slow slip events. *Geophysical Journal International*, 180(1):34–48, January 2010. ISSN 0956540X. doi: 10.1111/j.1365-246X.2009.04401.x.

R. Bell, C. Holden, W. Power, X. Wang, and G. Downes. Hikurangi margin tsunami earthquake generated by slow seismic rupture over a subducted seamount. *Earth and Planetary Science Letters*, (397):1–9, 2014.

P. Bird. Hydration-phase diagrams and friction of montmorillonite under laboratory and geologic conditions, with implications for shale compaction, slope stability, and strength of fault gouge. *Tectonophysics*, (107):235–260, 1984.

A.N. Bishop and G.D. Abbott. The interrelationship of biological marker maturity parameters and molecular yields during contact metamorphism. *Geochimica et Cosmochimica Acta*, 57: 3661–3668, 1993.

M.L. Blanpied, D.A. Lockner, and J.D. Byerlee. Fault stability inferred from granite sliding experiments at hydrothermal conditions. *Geophysical Research Letters*, 18(4):609–612, April 1991.

B. Bos and C. J. Spiers. Experimental investigation into the microstructural and mechanical evolution of phyllosilicate-bearing fault rock under conditions favouring pressure solution. *Journal of Structural Geology*, 23(8):1187–1202, 2001. doi: 10.1016/S0191-8141(00)00184-X.

S.A. Bowden, R.W. Court, D. Milner, E.C. Baldwin, P. Lindgren, I.A. Crawford, J. Parnell, and M.J. Burchell. The thermal alteration by pyrolysis of the organic component of small projectiles of mudrock during capture at hypervelocity. *Journal of Analytical and Applied Pyrolysis*, 82(2): 312–314, July 2008. doi: 10.1016/j.jaap.2008.05.002.

S.C. Brassell. Climatic influences on the Paleogene evolution of alkenones. *Paleoceanography*, 29: 255–272, 2014. doi: 10.1002/2013PA002576.

S.C. Brassell, R.G. Brereton, G. Eglinton, J. Grimalt, G. Liebezeit, I.T. Marlowe, U. Pflaumann, and M. Sarnthein. Palaeoclimatic signals recognized by chemometric treatment of molecular

stratigraphic data. *Advances in Organic Geochemistry*, 10:649–660, 1986. doi: 10.1016/S0146-6380(86)80001-8.

J.D. Brooks and J.W. Smith. The diagenesis of plant lipids during the formation of coal, petroleum and natural gas–I . Changes in the n-paraffin hydrocarbons. *Geochimica et Cosmochimica Acta*, 31:2389–2397, 1967. doi: 10.1016/0016-7037(67)90010-5.

K.M. Brown, M.D. Tryon, H.R. Deshon, L.M. Dorman, and S.Y. Schwartz. Correlated transient fluid pulsing and seismic tremor in the Costa Rica subduction zone. *Earth and Planetary Science Letters*, 238:189–203, 2005. doi: 10.1016/j.epsl.2005.06.055.

L. Buijze, A.R. Niemeijer, R. Han, T. Shimamoto, and C.J. Spiers. Friction properties and deformation mechanisms of halite(-mica) gouges from low to high sliding velocities. *Earth and Planetary Science Letters*, 458:107–119, 2017. doi: 10.1016/j.epsl.2016.09.059.

A.K. Burnham, J. Sweeney, and L. Livermore. A chemical kinetic model of vitrinite maturation and reflectance. *Geochimica et Cosmochimica Acta*, 53:2649–2651, 1989.

J. Byerlee. Friction of Rocks. *Pure and Applied Geophysics*, 116(4):615–626, 1978.

H.S. Carslaw and J.C. Jaeger. *Conduction of Heat in Solids*. Oxford University Press, London, second edition, 1959.

R.M. Carter, I.N. McCave, C. Richter, L. Carter, Y. Aita, C. Buret, A. Di Stefano, J. Fenner, P. Fothergill, F. Gradstein, I. Hall, D. Handwerger, S. Harris, B. Hayward, S. Hu, L. Joseph, B. Keun Khim, Y. Lee, L. Millwood, J. Rinna, G. Smith, A. Suzuki, G. Weedon, K. Wei, G. Wilson, and A. Winkler. Volume 181 Initial Reports: Southwest Pacific Gateways. Technical report, Ocean Drilling Program, 2000.

F. M. Chester, C. Rowe, K. Ujiie, J. Kirkpatrick, C. Regalla, F. Remitti, J. C. Moore, V. Toy, M. Wolfson-Schwehr, S. Bose, and et al. Structure and composition of the plate-boundary slip zone for the 2011 tohoku-oki earthquake. *Science*, 342(6163):1208–1211, December 2013. doi: 10.1126/science.1243719.

F.M. Chester, J. Mori, N. Eguchi, S. Toczko, and Expedition 343/343T Scientists. Volume 343-343T Expedition Reports Japan Trench Fast Drilling Project (JFAST). Technical report, Integrated Ocean Drilling Program Management International, Inc., for the Integrated Ocean Drilling Program, 2012.

C. Collettini, A. Niemeijer, C. Viti, and C. Marone. Fault zone fabric and fault weakness. *Nature*, 462(7275):907–910, December 2009. doi: 10.1038/nature08585.

C. Collettini, G. Di Stefano, B. Carpenter, P. Scarlato, T. Tesei, S. Mollo, F. Trippetta, C. Marone, G. Romeo, and L. Chiaraluce. A novel and versatile apparatus for brittle rock deformation. *International Journal of Rock Mechanics and Mining Sciences*, 66:114–123, 2014. doi: 10.1016/j.ijrmms.2013.12.005.

C. Collettini, C.and Viti, T. Tesei, and S. Mollo. Thermal decomposition along natural carbonate faults during earthquakes. *Geology*, 41(8):927–930, August 2013. doi: 10.1130/g34421.1.

M.A. D'Alessio, A.E. Blythe, and R. Burgman. No frictional heat along the San Gabriel fault , California : Evidence from fission-track thermochronology. *Geology*, 31(6):541–544, 2003. doi: 10.1130/0091-7613(2003)031<0541:NFHATS>2.0.CO;2.

B. Davy and R. Wood. Gravity and Magnetic Modeling of the Hikurangi Plateau. *Marine Geology*, 118(1-2):139–151, 1994.

H.J.W. De Baar, M.P. Bacon, and P.G. Brewer. Rare-earth distributions with a positive Ce anomaly in the Western North Atlantic Ocean. *Nature*, 301:324–327, 1983.

S.M. den Hartog, A.R. Niemeijer, and C.J. Spiers. New constraints on megathrust slip stability under subduction zone P–T conditions. *Earth and Planetary Science Letters*, 353-354:240–252, November 2012a. doi: 10.1016/j.epsl.2012.08.022.

S.M. den Hartog, Colin J. Peach, D.a. Matthijs de Winter, Christopher J. Spiers, and Toshihiko Shimamoto. Frictional properties of megathrust fault gouges at low sliding velocities: New data on effects of normal stress and temperature. *Journal of Structural Geology*, 38:156–171, May 2012b. doi: 10.1016/j.jsg.2011.12.001.

G. Di Toro, R. Han, T. Hirose, N. De Paola, S. Nielsen, K. Mizoguchi, F. Ferri, M. Cocco, and T. Shimamoto. Fault lubrication during earthquakes. *Nature*, 471(7339):494–8, March 2011. doi: 10.1038/nature09838.

J.H. Dieterich. Modeling of rock friction 1. experimental results and constitutive equations. *Journal of Geophysical Research*, 84(B5):2161–2168, May 1979.

D.I. Doser and T.H. Webb. Source parameters of large historical (1917-1961) earthquakes , North Island, New Zealand. *Geophysical Journal International*, 152:795–832, November 2003.

A. Douglas, J. Beavan, L.M. Wallace, and J. Townend. Slow slip on the northern Hikurangi subduction interface, New Zealand. *Geophysical Research Letters*, 32(L16305):2–5, 2005. doi: 10.1029/2005GL023607.

P.S. Doyle and W.R. Riedel. Ichthyoliths from Site 436, Northwest Pacific, Leg 56, Deep Sea Drilling Project. Technical report, Proceedings of the Deep Sea Drilling Project, 1980.

G. Dragert, K. Wang, and T.S. James. A silent slip event on the deeper Cascadia subduction interface. *Science*, 292(5521):1525–1528, May 2001. doi: 10.1126/science.1060152.

H. Dragert, K. Wang, and G. Rogers. Geodetic and seismic signatures of episodic tremor and slip in the northern Cascadia subduction zone. *Earth, Planets and Space*, 56(12):1143–1150, 2004.

G. Eglinton and R.J. Hamilton. Leaf Epicuticular Waxes. *Science*, 156(3780):1322–1335, 1967.

G. Eglinton, A.G. Gonzalez, R.J. Hamilton, and R.A. Raphael. Hydrocarbon constituents of the wax coatings of plant leaves: a taxonomic survey. *Phytochemistry*, 1:89–102, 1962.

T.I. Eglinton, A.G. Douglas, and S.J. Rowland. Release of aliphatic, aromatic and sulphur compounds from Kimmeridge kerogen by hydrous pyrolysis: A quantitative study. *Organic Geochemistry*, 13(4-6):655–663, 1988. doi: 10.1016/0146-6380(88)90086-1.

S. Ellis, Å. Fagereng, D. Barker, S. Henrys, D. Saffer, L. Wallace, C. Williams, and R. Harris. Fluid budgets along the northern hikurangi subduction margin, new zealand: the effect of a subducting seamount on fluid pressure. *Geophysical Journal International*, 202(1):277–297, April 2015. doi: 10.1093/gji/ggv127.

D.R. Faulkner, T.M. Mitchell, J. Behnsen, T. Hirose, and T. Shimamoto. Stuck in the mud? Earthquake nucleation and propagation through accretionary forearcs. *Geophysical Research Letters*, 38(18):1–5, September 2011. doi: 10.1029/2011GL048552.

Y. Fujii, K. Satake, S. Sakai, M. Shinohara, and T. Kanazawa. Tsunami source of the 2011 off the Pacific coast of Tohoku Earthquake. *Earth, Planets and Space*, 63(7):815–820, September 2011. doi: 10.5047/eps.2011.06.010.

T. Fujiwara, S. Kodaira, T. No, Y. Kaiho, N. Takahashi, and Y. Kaneda. The 2011 Tohoku-Oki earthquake: displacement reaching the trench axis. *Science*, 334(6060):1240, December 2011. doi: 10.1126/science.1211554.

P. M. Fulton, E. E. Brodsky, Y. Kano, J. Mori, F. Chester, T. Ishikawa, R. N. Harris, W. Lin, N. Eguchi, S. Toczko, and et al. Low coseismic friction on the tohoku-oki fault determined from temperature measurements. *Science*, 342(6163):1214–1217, December 2013. doi: 10.1126/science.1243641.

P.M. Fulton and R.N. Harris. Thermal considerations in inferring frictional heating from vitrinite reflectance and implications for shallow coseismic slip within the Nankai Subduction Zone. *Earth and Planetary Science Letters*, 335-336:206–215, June 2012. doi: 10.1016/j.epsl.2012.04.012.

C. Giorgetti, B.M. Carpenter, and C. Collettini. Frictional behavior of talc-calcite mixtures. *Journal of Geophysical Research: Solid Earth*, (120):6614–6633, 2015.

I.J. Hamling and L.M. Wallace. Silent triggering: Aseismic crustal faulting by a subduction slow slip event. *Earth and Planetary Science Letters*, (421):13–19, 2015.

R. Han, T. Shimamoto, T. Hirose, J. Ree, and J. Ando. Ultralow friction of carbonate faults caused by thermal decomposition. *Science*, 316(5826):878–81, May 2007. doi: 10.1126/science.1139763.

C. He, W. Yao, Z. Wang, and Y. Zhou. Strength and stability of frictional sliding of gabbro gouge at elevated temperatures. *Tectonophysics*, 427(1-4):217–229, December 2006. doi: 10.1016/j.tecto.2006.05.023.

T.D. Herbert. Alkenone Paleotemperature Determinations. In H.D. Holland and K.K. Turekian, editors, *Tretise on Geochemistry (Second Edition)*, chapter 8.15, pages 399–433. Elsevier Ltd., Oxford, 2 edition, 2014. doi: 10.1016/B978-0-08-095975-7.00615-X.

T. Hirono, T.and Yokoyama, Y. Hamada, W. Tanikawa, T. Mishima, M. Ikehara, V. Famin, M. Tanimizu, W. Lin, W. Soh, and S. Song. A chemical kinetic approach to estimate dynamic shear stress during the 1999 Taiwan Chi-Chi earthquake. *Geophysical Research Letters*, 34(L19308), 2007. doi: 10.1029/2007GL030743.

T. Hong and C. Marone. Effects of normal stress perturbations on the frictional properties of simulated faults. *Geochemistry, Geophysics, Geosystems*, 6(3), March 2005. doi: 10.1029/2004gc000821.

R.D. Hyndman, M. Yamano, and D.A. Oleskevich. The seismogenic zone of subduction thrust faults. *The Island Arc*, 6:244–260, 1997.

S. Ide, G.C. Beroza, D.R. Shelly, and T. Uchide. A scaling law for slow earthquakes. *Nature*, 447 (7140):76–9, May 2007. doi: 10.1038/nature05780.

S. Ide, A. Baltay, and G.C. Beroza. Shallow dynamic overshoot and energetic deep rupture in the 2011 Mw 9.0 Tohoku-Oki earthquake. *Science*, 332(6036):1426–9, June 2011. doi: 10.1126/science.1207020.

M.J. Ikari and A.J. Kopf. Seismic potential of weak, near-surface faults revealed at plate tectonic slip rates. *Science Advances*, 3(e1701269):1–7, 2017. doi: 10.1126/sciadv.1701269.

M.J. Ikari and D.M. Saffer. Comparison of frictional strength and velocity dependence between fault zones in the Nankai accretionary complex. *Geochemistry Geophysics Geosystems*, 12(4): 1–16, April 2011. doi: 10.1029/2010GC003442.

M.J. Ikari, D.M. Saffer, and C. Marone. Effect of hydration state on the frictional properties of montmorillonite-based fault gouge. *Journal of Geophysical Research: Solid Earth*, 112(6):1–12, 2007. doi: 10.1029/2006JB004748.

M.J. Ikari, D.M. Saffer, and C. Marone. Frictional and hydrologic properties of a major splay fault system, Nankai subduction zone. *Geophysical Research Letters*, 36(20):1–5, October 2009. doi: 10.1029/2009GL040009.

M.J. Ikari, C. Marone, and D.M. Saffer. On the relation between fault strength and frictional stability. *Geology*, 39(1):83–86, January 2011a. doi: 10.1130/g31416.1.

M.J. Ikari, A.R. Niemeijer, and C. Marone. The role of fault zone fabric and lithification state on frictional strength, constitutive behavior, and deformation microstructure. *Journal of Geophysical Research*, 116(B08404), 2011b.

M.J. Ikari, C. Marone, D.M. Saffer, and A.J. Kopf. Slip weakening as a mechanism for slow earthquakes. *Nature Geoscience*, 6(6):468–472, 2013a. doi: 10.1038/ngeo1818.

M.J. Ikari, A.R. Niemeijer, C.J. Spiers, A.J. Kopf, and D.M. Saffer. Experimental evidence linking slip instability with seafloor lithology and topography at the Costa Rica convergent margin. *Geology*, 41(8):891–894, 2013b. doi: 10.1130/G33956.1.

M.J. Ikari, Y. Ito, K. Ujiie, and A.J. Kopf. Spectrum of slip behaviour in Tohoku fault zone samples at plate tectonic slip rates. *Nature Geoscience*, 8:870–874, November 2015a. doi: 10.1038/NGEO2547.

M.J. Ikari, J. Kameda, D.M. Saffer, and A.J. Kopf. Strength characteristics of Japan Trench borehole samples in the high-slip region of the 2011 Tohoku-Oki earthquake. *Earth and Planetary Science Letters*, 412:35–41, 2015b. doi: 10.1016/j.epsl.2014.12.014.

T. Ishikawa, M. Tanimizu, K. Nagaishi, J. Matsuoka, O. Tadai, M. Sakaguchi, T. Hirono, T. Mishima, W. Tanikawa, W. Lin, H. Kikuta, W. Soh, and S. Song. Coseismic fluid–rock interactions at high temperatures in the Chelungpu fault. *Nature Geoscience*, 1(10):679–683, September 2008. doi: 10.1038/ngeo308.

Y. Ito, T. Tsuji, Y. Osada, M. Kido, D. Inazu, Y. Hayashi, H. Tsushima, R. Hino, and H. Fujimoto. Frontal wedge deformation near the source region of the 2011 Tohoku Oki earthquake. *Geophysical Research Letters*, 5:1–5, 2011. doi: 10.1029/2011GL048355.1.

Y. Ito, R. Hino, M. Kido, H. Fujimoto, Y. Osada, D. Inazu, Y. Ohta, T. Iinuma, M. Ohzono, S. Miura, M. Mishina, K. Suzuki, T. Tsuji, and J. Ashi. Episodic slow slip events in the Japan subduction zone before the 2011 Tohoku-Oki earthquake. *Tectonophysics*, 600:14–26, 2013. doi: 10.1016/j.tecto.2012.08.022.

Yoshihiro Ito and Kazushige Obara. Very low frequency earthquakes within accretionary prisms are very low stress-drop earthquakes. *Geophysical Research Letters*, 33(9):1–4, 2006. ISSN 00948276. doi: 10.1029/2006GL025883.

C. Janssen, R. Naumann, L. Morales, R. Wirth, D. Rhede, and G. Dresen. Co-seismic and/or a-seismic microstructures of JFAST 343 core samples from the Japan Trench. *Marine Geology*, 362:33–42, 2015.

K. Kaiho, S. Yatsu, M. Oba, P. Gorjan, J. Casier, and M. Ikeda. A forest fire and soil erosion event during the Late Devonian mass extinction Brussels Late Devonian. *Palaeogeography, Palaeoclimatology, Palaeoecology*, 392:272–280, 2013. doi: 10.1016/j.palaeo.2013.09.008.

J. Kameda, M. Shimizu, K. Ujiie, T. Hirose, M. Ikari, J. Mori, K. Oohashi, and G. Kimura. Pelagic smectite as an important factor in tsunamigenic slip along the Japan Trench. *Geology*, 43(2): 155–158, 2015. doi: 10.1130/G35948.1.

A. Kato, K. Obara, T. Igarashi, H. Tsuruoka, S. Nakagawa, and N. Hirata. Propagation of Slow Slip Leading Up to the 2011 Mw 9.0 Tohoku-Oki Earthquake. *Science*, 335(705):705–708, 2012. doi: 10.1126/science.1215141.

T.T. Keren and J.D. Kirkpatrick. The damage is done: Low fault friction recorded in the damage zone of the shallow Japan Trench decollement. *Journal of Geophysical Research*, 121:3804–3824, 2016a. doi: 10.1002/2015JB012311.

T.T. Keren and J.D. Kirkpatrick. Data report : tectonic and induced structures in the JFAST core. Technical report, 2016b.

James D Kirkpatrick, Christie D Rowe, Kohtaro Ujiie, J Casey Moore, Christine Regalla, Francesca Remitti, Virginia Toy, Monica Wolfson-schwehr, Jun Kameda, Santanu Bose, and Frederick M

Chester. Structure and lithology of the Japan Trench subduction plate boundary fault. *Tectonics*, 34, 2015. doi: 10.1002/2014TC003695.Sciences.

J.D. Kirkpatrick and C.D. Rowe. Disappearing ink: How pseudotachylytes are lost from the rock record. *Journal of Structural Geology*, 52:183–198, 2013. doi: 10.1016/j.jsg.2013.03.003.

H. Kitajima and D.M. Saffer. Elevated pore pressure and anomalously low stress in regions of low frequency earthquakes along the Nankai Trough subduction megathrust. *Geophysical Research Letters*, 39(23):1–5, 2012. doi: 10.1029/2012GL053793.

S. Kodaira, T. No, Y. Nakamura, T. Fujiwara, Y. Kaiho, S. Miura, N. Takahashi, Y. Kaneda, and A. Taira. Coseismic fault rupture at the trench axis during the 2011 Tohoku-oki earthquake. *Nature Geoscience*, 5(1):646–650, 2012. doi: 10.1038/NGEO1547.

K.D. Koper, A.R. Hutko, T. Lay, C.J. Ammon, and H. Kanamori. Frequency-dependent rupture process of the 2011 M w 9 . 0 Tohoku Earthquake : Comparison of short-period P wave backprojection images and broadband seismic rupture models. *Earth, Planets and Space*, 63(7):599–602, 2011. doi: 10.5047/eps.2011.05.026.

J.E. Kozdon and E.M. Dunham. Rupture to the trench: Dynamic rupture simulations of the 11 March 2011 Tohoku earthquake. *Bulletin of the Seismological Society of America*, 103(2B): 1275–1289, 2013.

R.M. Kurzawski, M. Stipp, A.R. Niemeijer, C.J. Spiers, and J.H. Behrmann. Earthquake nucleation in weak subducted carbonates. *Nature Geoscience*, (9):717–722, 2016. doi: 10.1038/NGEO2774.

P. Labaume, A.J. Maltman, A. Bolton, D. Tessier, Y. Ogawa, and S. Takizawa. Scaly Fabrics in Sheared Clays from the Décollement Zone of the Barbados Accretionary Prism. *Proceedings of the Ocean Drilling Program, Scientific Results*, 156, 1997.

A.H. Lachenbruch. Simple models for the estimation and measurement of frictional heating by an earthquake. Technical report, United States Department of the Interior Geological Survey, 1986.

M. Langseth, H. Okada, C. Adelseck, T. Bruns, H.E. Harper, V. Kurnosov, G. Muller, I. Murdmaa, K.A. Pisciotto, P. Robinson, T. Sakai, P.R. Thompson, J. Whelan, and H. Wories. Site 436:

Japan Trench Outer Rise, Leg 56. Technical report, Joint Oceanographic Institutions for Deep Earth Sampling, October 1977.

K.T. Lawrence, T.D. Herbert, P.S. Dekens, and A.C. Ravelo. The application of the alkenone organic proxy to the study of Plio-Pleistocene climate. In M. Williams, A.M. Haywood, F.J. Gregory, and D.N. Schmidt, editors, *Deep-Time Perspectives on Climate Change: Marrying the Signal from Computer Models and Biological Proxies*, pages 539–562. The Geological Society, London, 2007.

C.A. Lewis. The Kinetics of Biomarker Reactions: Implications for the Assessment of the Thermal Maturity of Organic Matter in Sedimentary Basins. In Michael H. Engel and Stephen A. Macko, editors, *Organic Geochemistry*, chapter 22, pages 491–510. Plenum Press, New York, 1993.

K.B. Lewis, J.Y. Collot, and S.E. Lallemand. The dammed Hikurangi Trough: A channel-fed trench blocked by subducting seamounts and their wake avalanches (New Zealand-France GeodyNZ Project). *Basin Research*, 10(4):441–468, 1998. doi: 10.1046/j.1365-2117.1998.00080.x.

W. Lin, P.M. Fulton, R.N. Harris, O. Tadai, O. Matsubayashi, W. Tanikawa, and M. Kinoshita. Thermal conductivities, thermal diffusivities, and volumetric heat capacities of core samples obtained from the Japan Trench Fast Drilling Project (JFAST). *Earth, Planets and Space*, 66 (1):48, 2014. doi: 10.1186/1880-5981-66-48.

M.F. Linker and J.H. Dieterich. Effects of variable normal stress on rock friction: observations and constitutive equations. *Journal of Geophysical Research*, 97(B4):4923–4940, April 1992.

T. Maeda, T. Furumura, S. Sakai, and M. Shinohara. Significant tsunami observed at ocean-bottom pressure gauges during the 2011 off the Pacific coast of Tohoku Earthquake. *Earth, Planets and Space*, 63(7):803–808, September 2011. doi: 10.5047/eps.2011.06.005.

A. Maltman, P. Labaume, and B. Housen. Structural Geology of the Décollement at the Toe of the Barbados Accretionary Prism. *Proceedings of the Ocean Drilling Program, Scientific Results*, 156:279–292, 1997.

C. Marone. Laboratory-Derived Friction Laws and Their Application To Seismic Faulting. *Annual Review of Earth and Planetary Sciences*, 26(1):643–696, May 1998. doi: 10.1146/annurev.earth.26.1.643.

C. Marone and C.H. Scholz. The depth of seismic faulting and the upper transition from stable to unstable slip regimes. *Geophysical Research Letters*, 15(8):621–624, 1988.

C.W. Mase and L. Smith. Pore-Fluid Pressures and Frictional Heating on a Fault Surface. *Pure and Applied Geophysics*, 122(2-4):583 – 607, 1985. doi: 10.1007/BF00874618.

R. McCaffrey, L.M. Wallace, and J. Beavan. Slow slip and frictional transition at low temperature at the hikurangi subduction zone. *Nature Geoscience*, 1(5):316–320, April 2008. doi: 10.1038/ngeo178.

T.I. Melbourne and F.H. Webb. Precursory transient slip during the 2001 mw=8.4 peru earthquake sequence from continuous gps. *Geophysical Research Letters*, 29(21), 2002.

K. Minoura, F. Imamura, D. Sugawara, Y. Kono, and T. Iwashita. The 869 Jogan tsunami deposit and recurrence interval of large-scale tsunami on the Pacific coast of northeast Japan. *Journal of Natural Disaster Science*, 23(2):83–88, 2001.

D.E. Moore and D.A. Lockner. Friction of the Smectite Clay Montmorillonite. In T. Dixon and C. Moore, editors, *The Seismogenic Zone of Subduction Thrust Faults*, chapter 11, pages 317–345. New York, 2007.

D.E. Moore and D.A. Lockner. Talc friction in the temperature range 25 °-400 °C: Relevance for Fault-Zone Weakening. *Tectonophysics*, 449:120–132, March 2008. doi: 10.1016/j.tecto.2007.11.039.

D.E. Moore and D.A. Lockner. Frictional strengths of talc-serpentine and talc-quartz mixtures. *Journal of Geophysical Research: Solid Earth*, 116(1):1–17, 2011. doi: 10.1029/2010JB007881.

D.E. Moore, R. Summers, and J.D. Byerlee. Strengths of clay and non-clay fault gouges at elevated temperatures and pressures. In *The 24th U.S. Symposium on Rock Mechanics (USRMS), 20-23 June, College Station, Texas*, number June, pages 489–500, 1983.

D.E. Moore, R. Summers, and J.D. Byerlee. Sliding behavior and deformation textures of heated illite gouge. *Journal of Structural Geology*, 11(3):329–342, 1989.

G.F. Moore, T.H. Shipley, P.L. Stoffa, D.E. Karig, A. Taira, S. Kuramoto, H. Tokuyama, and K. Suyehiro. Structure of the Nankai Trough Accretionary Zone From Multichannel Seismic Reflection Data. *Journal of Geophysical Research*, 95(B6):8753–8765, 1990.

J.C. Moore and D. Saffer. Updip limit of the seismogenic zone beneath the accretionary prism of southwest Japan : An effect of diagenetic to low-grade metamorphic processes and increasing effective stress. *Geology*, 29(2):183–186, 2001. doi: 10.1130/0091-7613(2001)029¡0183.

J.C. Moore, S. Roeske, N. Lundberg, J. Schoonmaker, D.S. Cowan, E. Gonzales, and S.E. Lucas. *Scaly Fabrics in Deep Sea Drilling Project Cores From Forearcs*, volume 166, chapter Scaly Fabrics in Deep Sea Drilling Project Cores From Forearcs. Geological Society of America, 1986.

J.C. Moore, T.A. Plank, F.M. Chester, P.J. Polissar, and H.M. Savage. The Plate Boundary Thrust of the 2011 Great Tohoku Earthquake: Oceanographic Provenance and Controls on Slip Propagation. *Geosphere*, 11(3):533–541, 2015. doi: 10.1130/GES01099.1.

J.J. Morley and L.E. Heusser. Role of orbital forcing in east Asian monsoon climates during the last 350 kyr: Evidence from terrestrial and marine climate proxies from core RC14-99. *Paleoceanography*, 12(3):483–493, June 1997. doi: 10.1029/97PA00213.

C. Morrow, B. Radney, and J. Byerlee. Frictional strength and the effective pressure law of montmorillonite and illite clays. *International Geophysics*, 51:69–88, 1992.

Y. Nakamura, S. Kodaira, S. Miura, C. Regalla, and N. Takahashi. High-resolution seismic imaging in the Japan Trench axis area off Miyagi, northeastern Japan. *Geophysical Research Letters*, 40 (9):1713–1718, May 2013. doi: 10.1002/grl.50364.

A. Niemeijer, C. Marone, and D. Elsworth. Fabric induced weakness of tectonic faults. *Geophysical Research Letters*, 37(3):1–5, 2010. doi: 10.1029/2009GL041689.

H. Noda and N. Lapusta. Stable creeping fault segments can become destructive as a result of dynamic weakening. *Nature*, 493(7433):518–21, January 2013. doi: 10.1038/nature11703.

H. Noyan, M. Önal, and Y. Sarikaya. Thermal deformation thermodynamics of a smectite mineral. *Journal of Thermal Analysis and Calorimetry*, 91(1):299–303, 2008.

K. Obara. Nonvolcanic deep tremor associated with subduction in southwest Japan. *Science*, 296 (5573):1679–81, May 2002. doi: 10.1126/science.1070378.

K. Obara and H. Hirose. Non-volcanic deep low-frequency tremors accompanying slow slips in the southwest Japan subduction zone. *Tectonophysics*, 417(1-2):33–51, 2006. doi: 10.1016/j.tecto.2005.04.013.

D.A. Oleskevich, R.D. Hyndman, and K. Wang. The updip and downdip limits to great subduction earthquakes: Thermal and structural models of cascadia, south alaska, sw japan, and chile. *Journal of Geophysical Research*, 104(B7):14965–14991, July 1999.

K.C. Outerbridge, T.H. Dixon, S.Y. Schwartz, J.I. Walter, M. Protti, V. Gonzalez, J. Biggs, M. Thorwart, and W. Rabbel. A tremor and slip event on the CocosCaribbean subduction zone as measured by a global positioning system (GPS) and seismic network on the Nicoya Peninsula, Costa Rica. *Journal of Geophysical Research*, 115(B10408):1–17, 2010. doi: 10.1029/2009JB006845.

S. Ozawa, H. Suito, and M. Tobita. Occurrence of quasi-periodic slow-slip off the east coast of the Boso peninsula, central Japan. *Earth, Planets and Space*, 59(12):1241–1245, 2007. doi: 10.1186/BF03352072.

J. Parnell, G.R. Osinski, P.F. Green, and M.J. Baron. Thermal alteration of organic matter in an impact crater and the duration of postimpact heating. *Geology*, 33(5):373–376, 2005. doi: 10.1130/G21204.1.

J. Parnell, S. Bowden, P. Lindgren, M. Burchell, D. Milner, M. Price, E.C. Baldwin, and I.A. Crawford. The preservation of fossil biomarkers during meteorite impact events : Experimental evidence from biomarker-rich projectiles and target rocks. *Meteoritics & Planetary Science*, 45 (8):1340–1358, 2010. doi: 10.1111/j.1945-5100.2010.01100.x.

J.S. Payero, V. Kostoglodov, N. Shapiro, T. Mikumo, A. Iglesias, X. Perez-Campos, and R.W. Clayton. Nonvolcanic tremor observed in the Mexican subduction zone. *Geophysical Research Letters*, 35:L07305, 2008. doi: 10.1029/2007GL032877.

Z. Peng and J. Gomberg. An integrated perspective of the continuum between earthquakes and slow-slip phenomena. *Nature Geoscience*, 3(9):599–607, 2010. doi: 10.1038/ngeo940.

H. Perfettini, J. Schmittbuhl, J.R. Rice, and M. Cocco. Frictional response induced by time-dependent fluctuations of the normal loading. 106(B7):13455–13472, 2001. doi: 10.1029/2000JB900366.

K.E. Peters, C.C. Walters, and J.M. Moldowan. *The Biomarker Guide*. Cambridge University Press, Cambridge, UK, 2004.

T. Plank. The Chemical Composition of Subducting Sediments. In Holland H.D. and Turekian K.K., editors, *Tretise on Geochemistry*, volume 4, chapter 4, pages 607–629. Elsevier Ltd., 2 edition, 2014. doi: 10.1016/B978-0-08-095975-7.00319-3.

T. Plank, J.N. Ludden, C. Escutia, and Shipboard Scientific Party. 1 . LEG 185 SUMMARY: INPUTS TO THE IZU -MARIANA SUBDUCTION SYSTEM. *Proceedings of the Ocean Drilling Program, Initial Reports*, 185, 2000.

T. Plank, K.A. Kelley, R.W. Murray, and L.Q. Stern. Chemical composition of sediments subducting at the Izu-Bonin trench. *Geochemistry, Geophysics, Geosystems*, 8(4), April 2007. doi: 10.1029/2006GC001444.

Terry Plank and Charles H. Langmuir. The chemical composition of subducting sediment and its consequences for the crust and mantle. *Chemical Geology*, 145(3-4):325–394, April 1998. doi: 10.1016/S0009-2541(97)00150-2.

A.N.B. Poliakov, R. Dmowska, and J.R. Rice. Dynamic shear rupture interactions with fault bends and off-axis secondary faulting. *Journal of Geophysical Research*, 107(B11):2295, 2002. doi: 10.1029/2001JB000572.

P.J. Polissar, H.M. Savage, and E.E. Brodsky. Extractable organic material in fault zones as a tool to investigate frictional stress. *Earth and Planetary Science Letters*, 311(3-4):439–447, November 2011. doi: 10.1016/j.epsl.2011.09.004.

F. Prahl, T. Herbert, S.C. Brassell, N. Ohkouchi, M. Pagani, D. Repeta, A. Rosell-Melé, and E. Sikes. Status of alkenone paleothermometer calibration: Report from Working Group 3. *Geochemistry Geophysics Geosystems*, 1, 2000.

H.S. Rabinowitz, H.M. Savage, T. Plank, J. D. Kirkpatrick, and C.D. Rowe. Multiple major faults at the Japan Trench: Chemostratigraphy of the plate boundary at IODP Exp. 343: JFAST. *Earth and Planetary Science Letters*, (423), 2015.

H.S. Rabinowitz, P.J. Polissar, and H.M. Savage. Reaction kinetics of alkenone and n-alkane thermal alteration at seismic timescales. *Geochemistry, Geophysics, Geosystems*, 18, 2017. doi: 10.1002/2016GC006553.

M. Radiguet, H. Perfettini, N. Cotte, A. Gualandi, B. Valette, V. Kostoglodov, T. Lhomme, A. Walpersdorf, E. Cabral Cano, and M. Campillo. Triggering of the 2014 mw7.3 papanoa earthquake by a slow slip event in guerrero, mexico. *Nature Geoscience*, 9(11):829–833, October 2016. doi: 10.1038/ngeo2817.

L.A. Reinen and J.D. Weeks. Determination of rock friction constitutive parameters using an iterative least-squares inversion method. *Journal of Geophysical Research-Solid Earth*, 98(B9): 15937–15950, 1993. doi: 10.1029/93JB00780.

F. Remitti, S.A.F. Smith, S. Mittempergher, A.F. Gualtieri, and G. Di Toro. Frictional properties of fault zone gouges from the J-FAST drilling project (Mw 9.0 2011 Tohoku-Oki earthquake). *Geophysical Research Letters*, 42:2691–2699, 2015. doi: 10.1002/2015GL063507.

J.R. Rice. Heating and weakening of faults during earthquake slip. *Journal of Geophysical Research*, 111:1–29, August 2006. doi: 10.1029/2005JB004006.

G. Rieley, R.J. Collier, D.M. Jones, G. Eglinton, P.A. Eakin, and A.E. Fallick. Sources of sedi-

mentary lipids deduced from stable carbon-isotope analyses of individual compounds. 352(6334): 425–427, 1991. doi: 10.1038/352425a0.

F. Robert, A. Boullier, and K. Firdaous. Gold-quartz veins in metamorphic terranes and their bearing on the role of fluids in faulting. *Journal of Geophysical Research*, 100(B7):12861–12879, 1995.

G. Rogers and H. Dragert. Episodic tremor and slip on the Cascadia subduction zone: the chatter of silent slip. *Science*, 300(5627):1942–1943, June 2003. doi: 10.1126/science.1084783.

A. Rosell-Melé, E. Bard, K.-C. Emeis, J.O. Grimalt, and Etc. Precision of the current methods to measure the alkenone proxy Uk'37 and absolute abundance in sediments: Results of an interlaboratory comparison study. *Geochemistry Geophysics Geosystems*, 2, 2001.

C.D. Rowe and W.A. Griffith. Do faults preserve a record of seismic slip: A second opinion. *Journal of Structural Geology*, 78:1–26, 2015. doi: 10.1016/j.jsg.2015.06.006.

C.D. Rowe, F. Moore, J.C.and Meneghini, and A.W. McKeirnan. Large-scale pseudotachylytes and fluidized cataclasites from an ancient subduction thrust fault. *Geology*, 33(12):937–940, 2005. doi: 10.1130/G21856.1.

C.D. Rowe, J.C. Moore, F. Remitti, and Expedition 343/343T Scientists. The thickness of subduction plate boundary faults from the seafloor into the seismogenic zone. *Geology*, 41:991–994, 2013. doi: 10.1130/G34556.1.

A. Ruina. Slip instability and state variable friction laws. *Journal of Geophysical Research*, 88 (B12):10359–10370, December 1983.

I.S. Sacks, S. Suyehiro, A.T. Linde, and J.A. Snoke. Slow earthquakes and stress redistribution. *Nature*, 275(5681):599–602, October 1978. doi: 10.1038/275599a0.

D.M. Saffer and C. Marone. Comparison of smectite- and illite-rich gouge frictional properties: application to the updip limit of the seismogenic zone along subduction megathrusts. *Earth and Planetary Science Letters*, 215(1-2):219–235, October 2003. doi: 10.1016/S0012-821X(03)00424-2.

D.M. Saffer and H.J. Tobin. Hydrogeology and Mechanics of Subduction Zone Forearcs: Fluid Flow and Pore Pressure. *Annual Review of Earth and Planetary Sciences*, 39(1):157–186, May 2011. doi: 10.1146/annurev-earth-040610-133408.

D.M. Saffer and L.M. Wallace. The frictional, hydrologic, metamorphic and thermal habitat of shallow slow earthquakes. *Nature Geoscience*, 8(8):594–600, 2015. doi: 10.1038/ngeo2490.

D.M. Saffer, K.M. Frye, C. Marone, and K. Mair. Laboratory results indicating complex and potentially unstable frictional behavior of smectite clay. *Geophysical Research Letters*, 28(12): 2297–2300, June 2001.

D.M. Saffer, D.A. Lockner, and A. McKiernan. Effects of smectite to illite transformation on the frictional strength and sliding instability of intact marine mudstones. *Geophysical Research Letters*, 39(L11304), 2012.

A. Sakaguchi, F. Chester, D. Curewitz, O. Fabbri, D. Goldsby, G. Kimura, C. Li, Y. Masaki, E.J. Screaton, A. Tsutsumi, K. Ujiie, and A. Yamaguchi. Seismic slip propagation to the up-dip end of plate boundary subduction interface faults: Vitrinite reflectance geothermometry on Integrated Ocean Drilling Program NanTro SEIZE cores. *Geology*, 39(4):395–398, 2011. doi: 10.1130/G31642.1.

H.M. Savage, P.J. Polissar, R. Sheppard, C.D. Rowe, and E.E. Brodsky. Biomarkers heat up during earthquakes: New evidence of seismic slip in the rock record. *Geology*, 42(2):99–102, February 2014. doi: 10.1130/g34901.1.

M. Sawai, T. Hirose, and J. Kameda. Frictional properties of incoming pelagic sediments at the Japan Trench: implications for large slip at a shallow plate boundary during the 2011 Tohoku earthquake. *Earth, Planets and Space*, 66(1):65, 2014. doi: 10.1186/1880-5981-66-65.

Y. Sawai, Y. Namegaya, Y. Okamura, K. Satake, and M. Shishikura. Challenges of anticipating the 2011 Tohoku earthquake and tsunami using coastal geology. *Geophysical Research Letters*, 39(21), November 2012. doi: 10.1029/2012GL053692.

A. Schimmelmann, M. Mastalerz, L. Gao, and P.E. Sauer. Dike intrusions into bituminous coal, Illinois Basin : H, C, N, O isotopic responses to rapid and brief heating. *Geochimica et Cosmochimica Acta*, 73:6264–6281, 2009. doi: 10.1016/j.gca.2009.07.027.

A.M. Schleicher, A. Boles, and B.A. van der Pluijm. Response of natural smectite to seismogenic heating and potential implications for the 2011 Tohoku earthquake in the Japan Trench. *Geology*, 43(9):G36846.1, 2015. doi: 10.1130/G36846.1.

C.H. Scholz. The brittle-plastic transition and the depth of seismic faulting. *Geologische Rundschau*, 77(1):319–328, 1988.

C.H. Scholz. Earthquakes and friction laws. *Nature*, 391:37–42, 1998.

S.J. Shand. The pseudotachylyte of Parijs (Orange Free State) and its relation to 'trap-shotten gneiss' and 'flinty crush-rock'. *Quarterly Journal of the Geological Society*, 72(1-4):198–221, 1916.

R.E. Sheppard, P.J. Polissar, and H.M. Savage. Organic thermal maturity as a proxy for frictional fault heating: Experimental constraints on methylphenanthrene kinetics at earthquake timescales. *Geochimica et Cosmochimica Acta*, 151:103–116, February 2015. doi: 10.1016/j.gca.2014.11.020.

B. Shibazaki and Y. Iio. On the physical mechanism of silent slip events along the deeper part of the seismogenic zone. *Geophysical Research Letters*, 30(9):1489, 2003. doi: 10.1029/2003GL017047.

B. Shibazaki and T. Shimamoto. Modelling of short-interval silent slip events in deeper subduction interfaces considering the frictional properties at the unstable-stable transition regime. *Geophysical Journal International*, 171(1):191–205, 2007. doi: 10.1111/j.1365-246X.2007.03434.x.

R.H. Sibson. Generation of Pseudotachylyte by Ancient Seismic Faulting. *Geophysical Journal International*, 43(3):775–794, 1975.

R.H. Sibson. Fault zone models, heat flow, and the depth distribution of earthquakes in the continental crust of the United States. *Bulletin of the Seismological Society of America*, 72(1): 151–163, 1982.

R.H. Sibson and V.G. Toy. The Habitat of Fault-Generated Pseudotachylyte: Presence vs. Absence of Friction-Melt. In R. Abercrombie, A. McGarr, G. Di Toro, and H. Kanamori, editors, *Earthquakes: Radiated Energy and the Physics of Faulting*, number Geophysical Monograph Series 170, pages 153–166. American Geophysical Union, 2006. doi: 10.1029/170GM16.

R.H. Sibson, J.M.M. Moore, and A.H. Rankin. Seismic pumping - a hydrothermal fluid transport mechanism. *Journal of the Geological Society*, 131(6):653–659, 1975. doi: 10.1144/gsjgs.131.6.0653.

R.H. Sibson, F. Robert, and K.H. Poulsen. High-angle reverse faults, fluid-pressure cycling, and mesothermal gold-quartz deposits. *Geology*, 16(June):551–555, 1988. doi: 10.1130/0091-7613(1988)016<0551:HARFFP>2.3.CO;2.

B.R.T Simoneit. Lipid/bitumen maturation by hydrothermal activity in sediments of Middle Valley, Leg 139. In *Proceedings of the Ocean Drilling Program, Scientific Results*, volume 139, pages 447–465. Ocean Drilling Program, 1994.

B.R.T. Simoneit, F.G. Prahl, R.N. Leif, and S. Mao. Alkenones in sediments of Middle Valley, Leg 139: Application as thermal sensors. In M.J. Mottl, E.E. Davis, A.T. Fisher, and J.F. Slack, editors, *Proceedings of the Ocean Drilling Program, Scientific Results*, volume 139, pages 479–484. Ocean Drilling Program, College Station, TX, 1994.

M. Simons, S.E. Minson, A. Sladen, F. Ortega, J. Jiang, S.E. Owen, L. Meng, J.-P. Ampuero, S. Wei, R. Chu, D.V. Helmberger, H. Kanamori, E. Hetland, A.W. Moore, and F.H. Webb. The 2011 magnitude 9.0 Tohoku-Oki earthquake: mosaicking the megathrust from seconds to centuries. *Science*, 332(6036):1421–1425, June 2011. doi: 10.1126/science.1206731.

J.G. Spray. A physical basis for the frictional melting of some rock-forming minerals. *Tectonophysics*, 204(3-4):205–221, 1992. doi: 10.1016/0040-1951(92)90308-S.

T. Sun, T. Fujiwara, S. Kodaira, J. He, and K. Wang. Large fault slip peaking at trench in the 2011 Tohoku-oki earthquake. *Nature Communications*, 8:1–8, May 2017. doi: 10.1038/ncomms14044.

W. Tanikawa, T. Hirose, H. Mukoyoshi, O. Tadai, and W. Lin. Fluid transport properties in sediments and their role in large slip near the surface of the plate boundary fault in the Japan Trench. *Earth and Planetary Science Letters*, 382:150–160, November 2013. doi: 10.1016/j.epsl.2013.08.052.

S. Tembe, D.A. Lockner, and T. Wong. Effect of clay content and mineralogy on frictional sliding behavior of simulated gouges: Binary and ternary mixtures of quartz, illite, and montmorillonite. *Journal of Geophysical Research*, 115(B03416), 2010.

T. Tesei, C. Collettini, B.M. Carpenter, C. Viti, and C. Marone. Frictional strength and healing behavior of phyllosilicate-rich faults. *Journal of Geophysical Research*, 117, September 2012. doi: 10.1029/2012JB009204.

K. Ujiie and G. Kimura. Earthquake faulting in subduction zones: insights from fault rocks in accretionary prisms. *Progress in Earth and Planetary Science*, 1:7, 2014. doi: 10.1186/2197-4284-1-7.

K. Ujiie and A. Tsutsumi. High-velocity frictional properties of clay-rich fault gouge in a megasplay fault zone, Nankai subduction zone. *Geophysical Research Letters*, 37(24), December 2010. doi: 10.1029/2010GL046002.

K. Ujiie, H. Tanaka, T. Saito, A. Tsutsumi, J.J. Mori, J. Kameda, E.E. Brodsky, F.M. Chester, N. Eguchi, S. Toczko, and Expedition 343/343T Scientists. Low coseismic shear stress on the tohoku-oki megathrust determined from laboratory experiments. *Science*, 342(6163):1211–1214, December 2013. doi: 10.1126/science.1243485.

M. Vallée, J.M. Nocquet, J. Battaglia, Y. Font, M. Segovia, M. Régnier, P. Mothes, P. Jarrin, D. Cisneros, S. Vaca, H. Yepes, X. Martin, N. Béthoux, and M. Chlieh. Intense interface seismicity triggered by a shallow slow slip event in the Central Ecuador subduction zone. *Journal of Geophysical Research: Solid Earth*, 118(6):2965–2981, 2013. doi: 10.1002/jgrb.50216.

P. Vannucchi, A. Maltman, G. Bettelli, and B. Clennell. On the nature of scaly fabric and scaly clay. *Journal of Structural Geology*, 25(5):673–688, May 2003. doi: 10.1016/S0191-8141(02)00066-4.

B.A. Verberne, J.H.P. De Bresser, A.R. Niemeijer, C.J. Spiers, D.A.M. De Winter, and O. Plümper. Nanocrystalline slip zones in calcite fault gouge show intense crystallographic preferred orientation : Crystal plasticity at sub- seismic slip rates at 18 – 150 ° C. *Geology*, 41(8):863–866, 2013. doi: 10.1130/G34279.1.

B.A. Verberne, O. Plümper, D.A.M. de Winter, and C.J. Spiers. Superplastic nanofibrous slip zones control seismogenic fault friction. *Science*, 346(6215):1342–1344, December 2014a.

B.A. Verberne, C.J. Spiers, A.R. Niemeijer, J.H.P. De Bresser, D.A.M. De Winter, and O. Plümper. Frictional properties and microstructure of calcite-rich fault gouges sheared at sub-seismic sliding velocities. *Pure and Applied Geophysics*, 171(10):2617–2640, December 2014b. doi: 10.1007/s00024-013-0760-0.

C. Vogt, J. Lauterjung, and R.X. Fischer. Investigation of the clay fraction (<2 μm) of the clay minerals society reference clays. *Clays and Clay Minerals*, 50(3):388–400, 2002. doi: 10.1346/000986002760833765.

P. Vrolijk and B.A. Van Der Pluijm. Clay gouge. *Journal of Structural Geology*, 21(8-9):1039–1048, 1999. doi: 10.1016/S0191-8141(99)00103-0.

J.A. Wade, T. Plank, R.J. Stern, D.L. Tollstrup, J.B. Gill, J.C. O'Leary, J.M. Eiler, R.B. Moore, J.D. Woodhead, F. Trusdell, T.P. Fischer, and D.R. Hilton. The May 2003 eruption of Anatahan volcano, Mariana Islands: Geochemical evolution of a silicic island-arc volcano. *Journal of Volcanology and Geothermal Research*, 146(1-3):139–170, August 2005. doi: 10.1016/j.jvolgeores.2004.11.035.

L.M. Wallace and J. Beavan. A large slow slip event on the central Hikurangi subduction interface beneath the Manawatu region, North Island, New Zealand. *Geophysical Research Letters*, 33 (11):2–5, 2006. doi: 10.1029/2006GL026009.

L.M. Wallace and J. Beavan. Diverse slow slip behavior at the Hikurangi subduction margin, New Zealand. *Journal of Geophysical Research*, 115:B12402, December 2010. doi: 10.1029/2010JB007717.

L.M. Wallace, J. Beavan, R. McCaffrey, and D. Darby. Subduction zone coupling and tectonic block rotations in the North Island, New Zealand. *Journal of Geophysical Research B: Solid Earth*, 109(12):1–21, 2004. doi: 10.1029/2004JB003241.

L.M. Wallace, M. Reyners, U. Cochran, S. Bannister, P.M. Barnes, K. Berryman, G. Downes, D. Eberhart-Phillips, A. Fagereng, S. Ellis, A. Nicol, R. McCaffrey, R.J. Beavan, S. Henrys, R. Sutherland, D.H.N. Barker, N. Litchfield, J. Townend, R. Robinson, R. Bell, K. Wilson, and W. Power. Characterizing the seismogenic zone of a major plate boundary subduction thrust: Hikurangi Margin, New Zealand. *Geochemistry, Geophysics, Geosystems*, 10(10), 2009. doi: 10.1029/2009GC002610.

L.M. Wallace, J. Beavan, S. Bannister, and C. Williams. Simultaneous long-term and short-term slow slip events at the Hikurangi subduction margin, New Zealand: Implications for processes that control slow slip event occurrence, duration, and migration. *Journal of Geophysical Research B: Solid Earth*, 117(11):1–18, 2012. doi: 10.1029/2012JB009489.

L.M. Wallace, S.C. Webb, Y. Ito, K. Mochizuki, R. Hino, S. Henrys, S.Y. Schwartz, and A.F. Sheehan. Slow slip near the trench at the Hikurangi subduction zone, New Zealand. *Science*, 352(6286):701–704, 2016.

L.M. Wallace, Y. Kaneko, S. Hreinsdóttir, I. Hamling, Z. Peng, N. Bartlow, E. D'Anastasio, and B. Fry. Large-scale dynamic triggering of shallow slow slip enhanced by overlying sedimentary wedge. *Nature Geoscience*, 10(10):765–770, September 2017. doi: 10.1038/ngeo3021.

J.I. Walter, S.Y. Schwartz, J.M. Protti, and V. Gonzalez. Persistent tremor within the northern Costa Rica seismogenic zone. *Geophysical Research Letters*, 38(1):1–5, 2011. doi: 10.1029/2010GL045586.

D.L. Wells and K.J. Coppersmith. New Empirical Relationships among Magnitude, Rupture Length, Rupture Width, Rupture Area, and Surface Displacement. *Bulletin of the Seismological Society of America*, 84(4):974–1002, 1994.

A. Yamaguchi, S.F. Cox, G. Kimura, and S. Okamoto. Dynamic changes in fluid redox state

associated with episodic fault rupture along a megasplay fault in a subduction zone. *Earth and Planetary Science Letters*, 302(3-4):369–377, 2011. doi: 10.1016/j.epsl.2010.12.029.

T. Yang, T. Mishima, K. Ujiie, F.M. Chester, J.J. Mori, N. Eguchi, and S. Toczko. Strain decoupling across the décollement in the region of large slip during the 2011 Tohoku-Oki earthquake from anisotropy of magnetic susceptibility. *Earth and Planetary Science Letters*, 381:31–38, November 2013. doi: 10.1016/j.epsl.2013.08.045.

T. Yang, M.J. Dekkers, and B. Zhang. Seismic heating signatures in the Japan Trench subduction plate-boundary fault zone: evidence from a preliminary rock. *Geophysical Journal International*, 205:332–344, 2016. doi: 10.1093/gji/ggw013.

X. Zhang and C.J. Spiers. Compaction of granular calcite by pressure solution at room temperature and effects of pore fluid chemistry. *International Journal of Rock Mechanics and Mining Sciences*, 42(7-8):950–960, October 2005. doi: 10.1016/j.ijrmms.2005.05.017.

Appendices

A | Appendix A

This appendix includes supplementary materials submitted with *Rabinowitz, H. S., Savage, H. M., Plank, T., Polissar, P. J., Kirkpatrick, J. D., & Rowe, C. D. (2015). Multiple major faults at the Japan Trench: Chemostratigraphy of the plate boundary at IODP Exp. 343: JFAST. Earth and Planetary Science Letters, 423, 57-66.*

Table A.1: IODP Expedition 343 JFAST trace element data

Sample JFAST	DSDP -ODP core numbers	Depth in core (cm)	Depth	Orig. Units Site 436	Age	Units - this work	Short litho description	Li ppm	Be ppm	Sc ppm	TiO_2 ppm
PP720	1R-5W	123.0–125.0	683.035		Early Plio	A2	Gray and dark gray clay, fine-grained mudstone with some siliciclastic material	15.448	1.301	11.811	0.264
PP721	4R-CCW	6.0–8.0	690.495		Mid Pleist	A1	Dark gray mudstone with lighter gray layer and green coloration, clay sized grains	46.61	1.62	16.38	0.59
PP722	5R-1W	92.5–94.5	696.925		Mid Pleist	A1	Discrete pieces, more indurated. More finely laminated, fine-grained dark gray mudstone.	46.98	1.61	16.05	0.64
PP723	6R-1W	28.0–33.0	704.280		Mid Pleist	A1	Tannish gray fine-grained mudstone	42.55	1.39	17.99	0.66
PP724	6R-1W	101.0–104.0	705.010		Mid Pleist	A1	Dark gray fine-grained mudstone, layer of discontinuous black mottling/lenses	41.30	1.48	16.37	0.57
PP828	8R-2W	124–130	720.240		Late Plio	A1	Dark gray mudstone	43.038	1.819	16.450	0.582
PP725	10R-2W	65.0–68.0	771.660		Mid Pleist	A1	Dark gray fine-grained mudstone from small shear surface. Less indurated than other samples.	41.890	1.932	21.611	0.738
PP726	14R-1W	6.0–8.0	810.060		Plio–Pleist	A1	Carbonaceous mudstone	40.955	1.985	16.897	0.653
PP944	15R-1W	98.5–100	817.485		Mid-Early Plio	A1	Greenish grey mudstone a little mottled	44.072	1.886	21.751	0.653
PP945	15R-1W	110.5–112.5	817.605		Mid-Early Plio	A1	Grey mudstone	34.058	1.466	29.592	0.837
PP727	15R-CCW	14.0–15.0	817.850		Mid–Plio	A1	Brecciated muddy ash, dark gray to green	36.855	1.995	20.462	0.653
PP946	16R-1W	23.5–25	818.735		Late Plio	A1	Dark grey to olive green mudstone	39.391	1.552	16.083	0.466
PP728	16R-1W	62.0–64.0	819.120		Late Plio	A1	Cuttings from black mudstone	48.379	1.906	20.773	0.692
PP923	17R-1W	30–34.5	821.800		Late Mio	A2/A3/B	Light grey mudstone, little fractures, top of sample has some brown clay material (scraped off and was much softer than the rest of the sample); this is the mudstone biscuit in the pelagic clay	41.426	2.387	16.498	0.561
PP729	17R-1W	62.0–64.0	822.120		Late Mio	C2	Scaley black shiny clay, phacoids	54.470	3.226	24.773	0.732
PP829-CB127	17R-1W	105.0–110.0	822.550		unknown	C2	Scaley black clay cuttings, phacoids	54.649	3.599	27.124	0.606
PP829-SC73	17R-1W	105.0–110.0	822.550		unknown	C2	Scaley black clay cuttings, phacoids	59.229	3.411	26.359	0.636
PP947	18R-1W	18.5–20	824.185		Late Mio	B	Coffee-brown clayey mudstone	48.621	3.094	19.431	0.637
PP730	18R-1W	33.0–35.0	824.330		Late Mio	B	Tan mudstone (uniform light brown)	41.214	2.954	15.935	0.518
PP948	18R-CCW	9.0–10.5	825.585		Late Mio	B	Coffee-brown clayey mudstone	40.925	2.803	19.189	0.605
PP732	19R-3W	25.5–27.5	828.995		Late Mio	A2/A3	Tan mudstone, similar to Core18R, but slightly more coarse-grained.	40.007	2.649	17.786	0.618
PP949	20R-1W	116.5–118	832.165		Late Mio	A2/A3	Dark grey-brown clay	46.347	2.355	18.587	0.602
PP951	20R-2W	19.5–21	832.515		Late Mio	A2/A3	Dark tan clay with lighter streaks	34.734	2.215	16.287	0.513
PP952	20R-2W	49.5–51	832.815		Late Mio	A2/A3	Grey-brown clay with some lighter streaks	30.864	1.885	15.853	0.456
PP733	20R-2W	70.5–72.0	833.025		Cret	D	Dark brown pieces with fine tan lamination, tan pieces w dark brown spots and lines. One tan piece has pink side w/ dark brown laminations <1mm. Small pieces of red clay, as seen in PP729.	32.274	1.471	14.827	0.312

Table A.2: Continuation of Table A.1

Sample	V ppm	Cr ppm	Co ppm	Ni ppm	Cu ppm	Zn ppm	Rb ppm	Sr ppm	Y ppm	Zr ppm	Nb ppm	Cs ppm	Ba ppm	Ba ppm	La ppm	Ce ppm	Pr ppm	Nd ppm
PP720	26.459	9.738	11.474	-5.903	60.223	63.411	69.174	99.070	38.221	156.469	6.131	3.178	511.929	510.233	18.178	41.608	5.185	21.120
PP721	118.45	56.49	14.31	37.46	92.18	91.74	77.33	149.13	19.21	91.68	7.62	5.67	571.21	571.09	17.12	39.72	4.44	17.11
PP722	125.20	58.59	14.14	37.40	94.95	97.34	78.82	150.58	19.33	97.14	8.07	5.86	505.17	502.84	17.61	40.72	4.61	17.68
PP723	137.36	51.15	15.46	33.31	104.36	93.38	68.29	178.84	18.02	84.42	6.85	5.35	489.80	489.78	15.33	35.73	4.10	15.80
PP724	108.87	51.27	9.07	24.25	84.24	82.00	71.16	138.93	21.89	96.97	6.89	5.18	495.26	494.38	15.92	36.98	4.30	16.85
PP828	114.773	56.444	13.345	22.567	85.851	104.885	85.512	135.029	20.781	94.584	8.574	6.161	554.350	552.626	17.983	41.798	5.112	18.867
PP725	147.995	67.316	18.074	29.485	77.826	106.437	84.942	241.150	23.832	106.455	8.832	5.663	750.611	746.198	19.824	44.192	5.338	20.996
PP726	123.876	51.263	16.743	25.490	83.277	99.725	89.697	193.157	22.518	120.129	9.413	6.048	577.087	573.291	22.282	49.691	5.986	23.329
PP944	122.469	52.710	14.705	31.450	81.151	86.713	91.359	144.092	23.457	116.049	7.618	6.589	410.273	409.097	18.224	45.087	4.940	19.459
PP945	219.953	43.543	19.212	27.351	133.112	92.841	65.762	146.826	20.264	79.074	5.422	4.972	351.606	349.900	12.859	30.092	3.488	14.014
PP727	133.997	45.199	17.026	20.310	97.279	89.044	91.680	132.525	21.818	97.998	7.709	6.301	400.775	399.171	18.921	44.088	5.124	19.986
PP946	97.736	44.314	14.247	31.354	67.620	76.311	64.554	198.072	16.717	76.220	6.376	4.744	458.705	457.422	14.694	33.978	3.756	14.381
PP728	144.681	55.275	16.212	29.020	86.555	105.384	87.957	187.735	21.247	96.639	9.151	6.484	457.865	457.541	19.924	46.592	5.701	21.021
PP923	191.694	54.542	34.617	59.051	63.585	101.072	116.528	111.125	24.033	120.682	10.158	8.660	805.060	801.599	25.167	60.008	6.194	23.440
PP729	146.230	62.989	150.387	266.905	217.064	149.606	150.536	151.386	79.242	156.793	14.342	12.227	784.993	781.544	57.757	183.333	18.338	73.390
PP829-CB127	134.730	57.363	176.127	289.770	229.086	145.372	143.330	147.519	110.141	164.158	13.358	11.494	885.244	880.334	71.484	188.979	22.489	90.695
PP829-SC73	135.621	56.705	173.926	294.249	234.767	147.753	142.277	153.420	107.708	164.072	14.116	11.853	906.232	901.512	68.953	184.292	21.960	88.768
PP947	130.273	63.663	27.081	60.545	143.947	98.132	135.281	115.283	23.965	115.062	10.930	10.737	881.051	862.492	27.675	72.795	6.787	25.326
PP730	87.896	48.885	26.647	42.138	141.227	94.113	148.538	111.624	27.847	136.924	12.676	9.604	1022.836	1017.484	32.651	80.701	8.689	30.863
PP948	115.989	57.170	22.320	48.880	152.239	91.011	131.473	113.732	24.765	110.720	10.362	9.846	743.006	741.808	26.974	68.382	6.620	24.765
PP732	102.074	58.718	22.687	34.602	228.058	97.550	126.396	120.117	22.421	116.131	10.786	8.795	713.035	709.024	24.964	62.147	6.443	23.870
PP949	275.246	62.982	23.307	43.906	66.238	98.852	111.924	117.395	25.265	114.955	9.573	8.382	774.775	780.028	22.762	56.027	5.818	22.166
PP951	77.376	44.872	15.109	34.692	85.603	80.132	105.120	117.276	26.775	110.089	8.598	7.464	812.795	807.306	22.014	52.854	5.597	21.526
PP952	65.679	34.297	14.884	42.065	98.157	78.466	89.005	114.955	29.497	132.962	7.773	6.426	543.762	542.044	21.063	53.800	5.622	21.705
PP733	57.338	28.076	30.005	93.411	220.126	140.198	63.373	131.548	94.147	68.156	6.523	4.577	360.656	359.129	53.675	57.949	14.413	58.123

Table A.3: Continuation of Table A.1

Sample	Sm ppm	Eu ppm	Gd ppm	Tb ppm	Dy ppm	Ho ppm	Er ppm	Yb ppm	Lu ppm	Hf ppm	Ta ppm	Pb ppm	Th ppm	U ppm	Ce/Ce*	Co/TiO2	Zn/Ce
PP720	4.867	0.923	5.941	1.017	6.598	1.439	4.163	4.272	0.670	4.494	0.498	17.706	6.243	1.520	1.04	43.51	1.52
PP721	3.76	0.89	3.55	0.60	3.46	0.70	1.99	2.04	0.32	2.57	0.54	18.49	6.85	2.77	1.10	24.13	2.31
PP722	3.85	0.92	3.67	0.61	3.52	0.71	2.04	2.01	0.32	2.69	0.59	18.03	7.01	2.30	1.09	21.97	2.39
PP723	3.53	0.89	3.38	0.57	3.28	0.67	1.88	1.85	0.29	2.37	0.49	16.63	5.86	1.89	1.09	23.51	2.61
PP724	3.84	0.91	3.84	0.66	3.89	0.80	2.27	2.31	0.36	2.75	0.50	16.07	6.30	2.06	1.08	16.03	2.22
PP828	3.907	0.905	3.887	0.644	3.862	0.815	2.364	2.385	0.373	2.589	0.613	18.501	7.630	3.479	1.05	22.94	2.51
PP725	4.782	1.247	4.893	0.814	4.695	0.970	2.701	2.707	0.426	2.918	0.664	18.047	7.170	2.782	1.04	24.50	2.41
PP726	4.759	1.174	4.762	0.762	4.503	0.920	2.580	2.590	0.395	3.250	0.716	20.643	8.315	2.106	1.04	25.65	2.01
PP944	4.319	1.044	4.460	0.752	4.395	0.901	2.595	2.619	0.412	3.253	0.591	16.020	7.546	1.519	1.15	22.52	1.92
PP945	3.252	0.900	3.587	0.611	3.689	0.772	2.222	2.153	0.340	2.313	0.407	16.552	5.132	0.996	1.09	22.94	3.09
PP727	4.074	0.990	4.263	0.688	4.185	0.878	2.496	2.506	0.383	2.681	0.589	14.877	6.511	1.109	1.08	26.08	2.02
PP946	3.013	0.742	2.957	0.498	2.822	0.583	1.693	1.652	0.262	1.930	0.448	14.016	5.628	2.272	1.11	30.59	2.25
PP728	4.359	1.021	4.245	0.697	4.070	0.841	2.414	2.443	0.384	2.675	0.655	19.362	8.148	2.173	1.06	23.42	2.26
PP923	5.169	1.189	5.049	0.850	4.741	0.961	2.685	2.728	0.432	3.252	0.775	20.908	9.081	1.635	1.16	61.67	1.68
PP729	16.749	3.891	16.521	2.659	14.836	2.917	7.845	6.870	1.051	4.269	1.052	64.654	18.718	3.171	1.36	205.46	0.82
PP829-CB127	21.266	4.786	20.201	3.272	18.189	3.685	10.388	9.645	1.536	4.099	0.970	51.939	20.795	3.432	1.14	290.58	0.77
PP829-SC73	20.774	4.783	20.972	3.365	18.976	3.777	10.312	9.198	1.443	4.331	0.987	51.431	20.446	3.533	1.15	273.55	0.80
PP947	5.158	1.220	4.806	0.811	4.541	0.921	2.583	2.549	0.402	2.887	0.785	25.586	11.290	1.956	1.28	42.49	1.35
PP730	5.968	1.276	5.634	0.916	5.280	1.091	3.147	3.127	0.495	3.678	0.953	22.971	13.384	2.627	1.16	51.41	1.17
PP948	5.121	1.185	4.818	0.823	4.689	0.961	2.721	2.695	0.424	3.009	0.807	26.085	11.616	2.223	1.24	36.90	1.33
PP732	5.000	1.146	4.540	0.750	4.221	0.862	2.456	2.543	0.402	3.181	0.848	26.871	9.748	1.807	1.19	36.69	1.57
PP949	4.712	1.089	4.725	0.816	4.609	0.981	2.821	2.832	0.448	3.202	0.730	21.962	9.727	1.910	1.18	38.69	1.76
PP951	4.548	1.017	4.609	0.803	4.773	0.997	2.903	2.958	0.477	3.312	0.678	22.438	9.352	1.923	1.15	29.45	1.52
PP952	4.878	1.050	5.018	0.868	5.156	1.113	3.222	3.307	0.537	3.855	0.610	16.748	8.241	1.776	1.20	32.62	1.46
PP733	12.813	3.097	14.524	2.269	13.321	2.804	7.764	6.790	1.073	1.809	0.463	16.751	5.879	2.669	0.50	96.20	2.42

Table A.4: Continuation of Table A.1

Sample	SiO_2** wt%	TiO_2 wt%	Al_2O_3 wt%	Fe_2O_3 wt%	MnO wt%	MgO wt%	CaO wt%	Na_2O wt%	K_2O wt%	P_2O_5 wt%	LOI wt%	Sr ppm	Ba ppm
PP720	70.037	0.254	11.433	2.856	0.057	0.683	1.634	3.315	2.437	0.034	7.26	96.6	477.4
PP721	62.288	0.589	14.250	5.615	0.115	2.215	2.409	2.872	2.280	0.107	7.26	156.9	567.7
PP722	61.030	0.635	14.946	6.775	0.069	2.129	2.268	2.796	2.288	0.099	6.97	159.1	504.3
PP723	62.168	0.644	15.069	5.648	0.060	2.084	3.000	3.045	2.032	0.096	6.15	185.9	484.6
PP724	65.448	0.544	13.752	4.505	0.056	1.801	1.977	2.965	2.171	0.089	6.69	146.2	491.5
PP828	62.479	0.609	14.167	5.665	0.086	2.162	1.686	3.184	2.384	0.086	7.49	138.9	544.5
PP725	49.856	0.738	17.821	9.449	0.202	3.086	5.348	3.276	2.577	0.155	7.49	241.8	735.2
PP726	62.561	0.634	14.728	5.477	0.355	2.250	3.178	2.541	2.481	0.141	5.65	194.0	549.9
PP944	63.171	0.619	15.072	5.994	0.062	1.798	2.210	2.839	2.474	0.106	5.65	142.8	371.7
PP945	58.859	0.820	15.426	8.200	0.105	2.340	4.516	2.805	1.872	0.081	4.97	146.0	322.4
PP727	63.547	0.641	14.375	6.700	0.085	2.066	2.603	2.396	2.257	0.063	5.27	130.8	381.5
PP946	47.990	0.473	11.702	5.194	0.819	2.137	12.218	2.185	1.851	0.231	15.20	195.9	439.2
PP728	57.569	0.722	17.080	6.239	0.346	2.397	3.278	3.271	2.437	0.095	6.57	189.4	446.3
PP923	63.078	0.559	15.227	5.701	0.264	1.964	1.291	2.207	2.621	0.056	7.03	112.7	777.3
PP729	52.074	0.765	19.806	7.732	2.133	3.029	1.110	1.992	3.899	0.425	7.03	154.5	772.0
PP829-CB127	55.048	0.602	18.262	6.831	2.013	2.987	1.336	1.572	3.798	0.565	6.99	151.3	866.2
PP829-SC73	54.173	0.661	19.009	6.965	2.021	2.811	1.207	1.837	3.777	0.553	6.99	154.2	868.8
PP947	59.777	0.641	16.982	6.621	0.159	2.095	1.421	2.337	2.881	0.089	7.00	118.1	864.1
PP730	62.178	0.538	16.528	5.448	0.267	1.687	0.983	2.736	3.440	0.068	6.13	113.4	1001.5
PP948	61.323	0.591	16.217	6.330	0.274	1.870	1.647	2.389	2.959	0.082	6.32	114.7	708.5
PP732	61.446	0.612	15.864	6.482	0.251	2.093	1.602	2.392	2.771	0.074	6.41	120.0	683.7
PP949	61.815	0.586	16.053	5.743	0.316	1.806	1.588	2.581	2.761	0.073	6.68	119.6	735.8
PP951	64.440	0.494	14.825	4.867	0.139	1.414	1.572	2.846	2.938	0.073	6.39	117.6	762.1
PP952	66.009	0.438	14.704	4.081	0.163	1.199	1.769	2.999	2.743	0.058	5.84	115.9	497.1
PP733	72.699	0.327	8.087	4.320	0.844	1.974	1.868	1.513	1.635	0.941	5.79	134.6	351.3

Table A.5: DSDP Site 436 trace element data

Sample Site 436	DSDP -ODP core numbers	Depth in core (cm)	Depth	Orig. Units Site 436	Age	Units - this work	Short litho description	Li ppm	Be ppm	Sc ppm	TiO_2 ppm
PP925	5R-03-WW	80–81.5	40.300	1A	Quat	A1	dark, olive green clay, lighter green/grey phacoids	49.89	1.79	18.32	0.57
PP926	13R-02-WW	60–61.5	114.600	1A	Upp Plio	A1	dark, olive green color, one little red blob and a tiny fleck of something shiny and silver-grey (vitric ash?). Otherwise very uniform in color and texture	45.33	1.65	16.40	0.50
PP928	16R-02-WW	59–60.5	142.990	1A	Upp Plio	A1	dark olive green mudstone, little bleb of light grey material (ash?)	42.19	1.51	16.72	0.46
PP929	18R-01-WW	71.5–73	160.715	1A	Low Plio	A1	light greenish grey mudstone with a couple of darker shiny grey flecks	36.69	1.50	15.47	0.40
PP932	22R-01-WW	47.5–49	198.475	1A	Low Plio	A1	olive green clay, thin bands of slightly darker olive green material, some red-brown blebs	61.01	2.12	16.34	0.53
PP933	25R-02-WW	50–51.5	227.000	1A	Low Plio	A1	light grey mudstone/clay	57.05	2.05	16.09	0.53
PP934	27R-02-WW	70–71.5	247.700	1B	upp Mio	A2	grey-olivish clay, very faint foliation	42.49	1.87	14.20	0.48
PP935	28R-01-WW	68–69.5	255.680	1B	upp Mio	A2	light grey clay with a couple of slightly darker grey blebs	54.67	2.10	14.80	0.53
PP936	29R-01-WW	61–62.5	265.110	1B	upp Mio	A2	light grey clay with very faint mottling	27.34	1.61	15.94	0.31
PP938	31R-02-WW	60–61.5	285.050	1B	upp Mio	A2	light tan clay, some veins of lighter greyish material	31.45	1.75	14.88	0.42
PP939	32R-02-WW	68.5–70	295.185	1B	upp Mio	A3	tan clay with some white flecks	49.33	2.21	16.91	0.54
PP941	33R-03-WW	83–84.5	306.330	1B	upp Mio	A3	brown-tan clay	50.18	2.38	18.91	0.59
PP943	35R-01-WW	78.5–80	322.285	2	mid-upp Mio	B	light brown/tan clay, no significant texture	52.12	2.94	18.67	0.60
PP886	36R-06-WW	38.5–42.5	338.340	2	mid-upp Mio	B	tan-buff shale with faint layers (∼2mm thick banding) that are slightly darker	45.72	3.14	16.79	0.55
PP887	37R-05-WW	80–84	347.300	2	mid-upp Mio	B	light tan mudstone	44.10	2.95	19.06	0.58
PP888	38R-04-WW	40–44	354.850	2	mid Mio	B	tan, not as light; layer of ∼6mm clasts that are lighter tan than the rest; grayish ∼1mm vein (2 parallel veins ∼5mm apart)	46.08	3.26	18.26	0.58
PP889	39R-01-WW	65–69	360.150	3	early Mio	C1	dark tan to olive brown clay with redder parts (oxidation effect); conchoidal surfaces; black layers (some really pure black like graphite/almost coal-like)	68.57	3.52	21.97	0.62
PP890	39R-02-WW	55–59	361.550	3	early Mio	C1	much darker brown clay with red layers; some small black pieces some red pieces ∼7mm (also clay)	84.76	3.22	19.92	0.61
PP891	39R-04-WW	30–34	364.300	3	early Mio	C1	really dark, olivey brown clay; thin (∼1mm) red clay slightly undulating layer	85.00	3.49	21.47	0.66
PP892	39R-06-WW	56–60	367.460	3	early Mio	C2	dark brown almost black clay weathered (?) to lighter greenish brown on edges; thin oxidizing layer (∼1mm); burrows(?)	80.91	3.81	25.38	0.69
PP893	40R-01-WW	30–34	369.300	3	Olig	C2	dark brown almost black; no red bits; some lighter brown (∼1mm) pieces	78.99	3.25	29.40	0.66
PP894	40R-03-WW	82–86	372.820	3	Olig	C2	dark brown almost black clay; red oxidizing layers (very faint and more diffuse than in the other samples)	73.85	3.53	24.89	0.66
PP895	40R-06-WW	54–58	376.440	3	Olig	C2	dark brown almost black clay; small (∼0.5mm) slightly lighter spots	63.99	3.18	28.13	0.63
PP896	40R-CC-WW	8.0–12	377.680	3	Eoc	C3	dark olive brown clay; light brownish red oxidizing clasts (∼1mm)	54.08	2.50	33.05	1.12
PP897	41R-01-WW	3.0–7	378.570	3	late Cret	C3	dark brown clay with little red oxidizing spots (∼2mm)	49.87	2.31	31.91	1.05

Table A.6: Continuation of Table A.5

Sample	V ppm	Cr ppm	Co ppm	Ni ppm	Cu ppm	Zn ppm	Rb ppm	Sr ppm	Y ppm	Zr ppm	Nb ppm	Cs ppm	Ba ppm	Ba ppm	La ppm	Ce ppm	Pr ppm	Nd ppm
PP925	128.40	57.90	15.02	43.50	84.56	108.06	85.59	154.98	17.70	99.35	8.23	6.64	874.53	868.61	19.05	43.98	4.82	18.40
PP926	104.58	72.49	13.12	47.16	110.39	94.06	72.12	148.40	20.00	91.19	6.84	5.35	813.00	810.88	16.64	38.93	4.41	17.08
PP928	112.84	46.79	10.48	36.49	132.70	97.35	61.13	125.96	18.11	76.39	5.65	4.74	822.43	817.84	14.30	34.76	3.83	14.84
PP929	86.30	59.46	9.43	26.80	84.57	98.01	67.22	123.02	19.75	96.19	6.11	4.66	673.87	678.14	15.78	36.16	4.12	15.81
PP932	114.45	56.53	11.61	35.12	120.21	92.13	96.88	118.21	21.12	94.17	8.30	7.68	787.04	787.37	20.82	47.71	5.34	20.32
PP933	105.39	63.03	21.46	51.89	114.83	86.10	106.39	112.87	21.17	92.56	9.14	8.37	711.48	712.25	22.48	51.03	5.54	20.68
PP934	84.37	45.67	10.72	27.62	58.48	76.84	95.77	106.87	23.46	122.27	9.14	7.23	746.83	744.38	21.96	52.22	5.48	21.07
PP935	118.90	59.74	20.61	46.33	89.17	86.12	100.74	108.53	20.91	94.10	8.67	7.46	745.68	744.80	20.81	49.91	5.25	19.74
PP936	42.29	23.39	4.93	15.28	32.54	76.13	71.29	102.05	38.52	127.94	6.44	4.36	605.79	604.94	18.73	43.73	5.24	21.25
PP938	59.98	39.41	10.90	27.76	82.11	69.16	86.36	117.36	23.96	121.30	6.80	5.88	673.79	679.70	18.47	44.74	4.85	18.70
PP939	100.16	56.66	21.73	47.53	153.75	85.05	105.96	113.38	23.20	103.85	8.70	7.90	1068.74	1067.37	22.65	56.62	5.74	21.92
PP941	100.96	55.11	22.44	52.41	140.38	88.16	109.72	118.61	26.15	107.01	9.16	8.16	762.75	762.71	24.67	67.57	6.31	24.11
PP943	134.38	62.97	31.43	57.44	69.78	91.08	131.20	110.51	21.97	116.99	10.71	9.59	740.14	738.05	27.59	72.10	6.79	25.06
PP886	82.26	46.08	23.58	55.81	128.88	92.51	133.86	110.47	24.44	127.62	12.13	9.83	1029.04	1027.75	28.78	81.88	7.65	29.45
PP887	94.40	47.41	21.91	52.13	232.10	87.97	127.11	113.47	25.58	107.72	10.37	10.27	930.36	931.01	25.64	72.56	6.94	27.08
PP888	84.60	44.04	34.32	68.37	218.47	101.74	133.41	133.93	28.90	130.75	11.08	10.49	1420.30	1414.94	28.95	84.60	7.79	30.71
PP889	87.40	46.80	58.60	146.69	324.83	136.18	126.11	130.65	44.64	149.59	11.92	10.54	1302.74	1302.61	35.69	112.86	9.88	39.45
PP890	96.25	41.95	52.05	120.52	277.42	134.18	117.85	136.15	38.04	153.16	11.52	9.80	1061.51	1062.67	33.33	105.83	9.17	36.60
PP891	135.78	52.44	65.06	102.79	309.21	143.34	154.70	138.83	37.08	163.40	13.47	12.45	971.29	973.14	37.70	121.02	10.22	40.10
PP892	157.57	53.58	194.43	322.06	359.58	153.35	140.05	187.78	64.89	191.69	15.68	11.95	907.58	910.93	48.94	202.05	13.98	56.51
PP893	138.59	48.58	294.43	432.95	357.67	156.87	127.56	293.16	96.49	193.57	14.53	10.60	724.91	725.56	61.70	194.34	18.82	76.16
PP894	138.77	58.27	157.99	363.64	238.18	155.42	158.34	200.54	64.17	157.29	13.83	14.41	493.84	496.61	49.10	181.34	14.55	58.53
PP895	133.25	50.50	182.90	419.15	256.50	163.07	144.77	239.39	80.94	169.49	13.64	12.29	484.16	487.19	56.07	203.50	17.97	73.18
PP896	121.01	82.03	149.62	369.70	312.53	186.13	109.31	222.24	151.45	182.71	15.30	8.79	405.69	409.71	90.62	207.91	31.26	126.99
PP897	111.86	55.51	143.61	349.15	287.72	174.98	100.83	209.19	177.27	168.27	13.87	8.15	350.35	353.27	101.86	174.32	33.91	138.08

Table A.7: Continuation of Table A.5

Sample	Sm ppm	Eu ppm	Gd ppm	Tb ppm	Dy ppm	Ho ppm	Er ppm	Yb ppm	Lu ppm	Hf ppm	Ta ppm	Pb ppm	Th ppm	U ppm	Ce/Ce*	Co/TiO_2	Zn/Ce
PP925	3.82	0.93	3.63	0.60	3.34	0.69	1.96	1.99	0.32	2.63	0.62	77.35	7.89	5.33	1.11	26.22	2.46
PP926	3.86	0.95	3.70	0.63	3.65	0.76	2.18	2.19	0.35	2.55	0.49	34.33	7.21	3.88	1.10	26.44	2.42
PP928	3.36	0.86	3.31	0.57	3.29	0.68	1.95	1.94	0.31	2.04	0.40	115.96	5.36	4.09	1.14	22.88	2.80
PP929	3.45	0.81	3.51	0.60	3.53	0.74	2.12	2.20	0.35	2.65	0.47	842.61	6.30	2.77	1.08	23.80	2.71
PP932	4.33	0.98	4.05	0.68	3.85	0.79	2.24	2.23	0.36	2.56	0.61	49.93	8.44	3.32	1.09	21.95	1.93
PP933	4.23	0.96	3.90	0.64	3.64	0.75	2.16	2.15	0.34	2.50	0.68	36.02	9.26	2.23	1.11	40.26	1.69
PP934	4.33	0.94	4.33	0.72	4.16	0.87	2.48	2.54	0.40	3.34	0.66	26.62	8.39	2.59	1.15	22.39	1.47
PP935	4.13	0.94	3.86	0.65	3.73	0.77	2.19	2.24	0.35	2.57	0.63	80.68	8.66	2.34	1.15	39.19	1.73
PP936	5.24	1.11	5.83	1.03	6.42	1.37	3.98	4.12	0.65	3.77	0.47	18.36	7.19	1.58	1.07	15.88	1.74
PP938	4.07	0.97	4.24	0.72	4.27	0.90	2.58	2.66	0.42	3.39	0.51	20.65	7.69	1.80	1.14	26.15	1.55
PP939	4.69	1.10	4.42	0.74	4.21	0.84	2.36	2.36	0.37	2.82	0.63	24.88	9.01	1.69	1.20	40.06	1.50
PP941	5.19	1.22	4.98	0.84	4.79	0.97	2.74	2.65	0.42	2.75	0.66	31.81	9.34	1.75	1.31	37.98	1.30
PP943	5.02	1.17	4.69	0.78	4.24	0.88	2.43	2.44	0.38	2.85	0.80	28.76	11.16	2.01	1.27	52.12	1.26
PP886	5.86	1.25	5.39	0.88	4.99	1.00	2.83	2.83	0.44	3.53	0.92	33.70	12.30	2.21	1.33	42.95	1.13
PP887	5.52	1.25	5.30	0.87	5.01	1.02	2.90	2.86	0.45	2.98	0.78	33.59	11.41	2.09	1.32	37.73	1.21
PP888	6.27	1.40	5.94	0.97	5.64	1.15	3.25	3.23	0.51	3.61	0.84	29.84	12.86	2.34	1.36	59.63	1.20
PP889	8.38	1.88	8.65	1.42	8.30	1.72	4.88	4.85	0.77	4.09	0.86	32.44	14.56	2.00	1.45	94.44	1.21
PP890	7.78	1.69	7.66	1.27	7.31	1.50	4.23	4.21	0.67	4.28	0.86	42.06	13.84	1.89	1.46	85.29	1.27
PP891	8.32	1.83	7.86	1.28	7.21	1.46	4.14	4.10	0.65	4.27	0.97	51.11	16.39	2.32	1.49	97.84	1.18
PP892	12.58	2.81	12.57	2.05	11.77	2.42	6.82	6.57	1.05	4.99	1.05	60.53	20.56	2.96	1.87	282.47	0.76
PP893	17.50	4.02	18.07	2.92	16.81	3.42	9.52	8.97	1.45	4.92	0.97	61.59	21.12	3.01	1.38	446.35	0.81
PP894	12.98	2.90	12.79	2.08	11.68	2.36	6.54	6.06	0.95	4.33	1.00	56.37	19.17	2.47	1.64	240.06	0.86
PP895	17.00	3.85	16.80	2.74	15.29	3.03	8.24	7.36	1.14	4.57	0.96	57.66	19.37	2.35	1.55	288.28	0.80
PP896	30.95	7.21	31.15	5.01	27.55	5.38	14.24	12.06	1.84	4.91	1.13	69.71	21.53	2.25	0.94	133.08	0.90
PP897	33.50	7.89	34.79	5.56	30.87	6.16	16.42	13.88	2.09	4.70	1.03	69.85	20.61	2.17	0.72	137.42	1.00

Table A.8: Continuation of Table A.5

Sample	SiO_2** wt%	TiO_2 wt%	Al_2O_3 wt%	Fe_2O_3 wt%	MnO wt%	MgO wt%	CaO wt%	Na_2O wt%	K_2O wt%	P_2O_5 wt%	LOI wt%	Sr ppm	Ba ppm
PP925	61.252	0.558	13.584	5.232	0.059	2.285	2.016	3.690	2.420	0.076	8.83	157.6	832.6
PP926	59.913	0.485	12.559	5.371	0.074	2.098	1.743	5.152	2.246	0.067	10.29	153.9	795.4
PP928	65.819	0.438	11.153	4.497	0.057	1.697	1.751	3.900	1.826	0.064	8.80	130.9	807.5
PP929	62.375	0.377	11.519	5.778	0.083	1.537	1.453	4.456	2.298	0.054	10.07	123.7	637.3
PP932	61.520	0.518	13.339	5.178	0.048	2.207	1.367	4.084	2.660	0.068	9.01	124.6	784.9
PP933	63.148	0.521	13.517	4.288	0.052	2.114	1.024	3.664	2.689	0.068	8.92	120.1	713.4
PP934	64.715	0.458	13.428	3.649	0.044	1.552	1.099	3.777	2.959	0.047	8.27	109.5	713.3
PP935	62.338	0.515	13.716	4.337	0.042	1.952	1.055	4.084	2.624	0.065	9.27	115.2	747.2
PP936	68.393	0.290	12.887	2.880	0.079	0.862	1.253	3.764	2.933	0.040	6.62	107.1	599.4
PP938	64.788	0.402	13.654	4.247	0.144	1.251	1.705	3.547	2.679	0.137	7.45	119.1	644.0
PP939	62.201	0.522	14.135	5.218	0.253	1.955	1.125	3.477	2.670	0.068	8.37	120.4	1068.5
PP941	59.405	0.578	14.789	6.109	0.286	2.026	1.648	3.430	2.612	0.107	9.01	124.7	750.1
PP943	59.480	0.580	15.348	5.834	0.411	2.122	0.970	3.376	2.927	0.096	8.86	111.9	705.7
PP886	59.469	0.580	15.643	5.741	0.309	1.911	0.911	3.299	3.181	0.099	8.86	113.6	1046.3
PP887	59.188	0.605	15.569	6.319	0.253	2.013	1.325	3.024	2.717	0.131	8.86	114.8	938.9
PP888	58.417	0.603	16.125	6.042	0.439	2.279	1.071	3.115	2.922	0.130	8.86	137.1	1437.6
PP889	54.779	0.642	17.766	7.108	0.750	3.393	0.989	2.908	2.654	0.155	8.86	132.6	1313.8
PP890	54.472	0.635	17.837	6.849	0.972	3.539	1.082	3.016	2.611	0.128	8.86	138.6	1075.8
PP891	53.988	0.684	18.508	6.997	1.119	3.203	0.784	2.660	3.057	0.143	8.86	139.8	971.6
PP892	50.977	0.707	19.701	7.668	2.313	2.886	0.878	2.294	3.391	0.328	8.86	190.9	910.3
PP893	51.059	0.684	18.933	7.282	2.865	2.963	1.090	2.387	3.397	0.481	8.86	295.1	728.7
PP894	50.454	0.696	19.832	7.635	2.187	3.161	0.807	2.059	3.995	0.318	8.86	209.8	505.6
PP895	51.005	0.663	19.193	7.253	2.478	3.170	1.043	2.158	3.808	0.374	8.86	247.7	490.3
PP896	49.370	1.167	18.402	8.756	1.888	3.154	2.120	2.274	3.198	0.815	8.86	224.3	410.9
PP897	50.700	1.108	17.412	8.376	1.667	3.086	2.395	2.514	2.952	0.934	8.86	215.7	360.9

B | Appendix B

This appendix includes supplementary materials submitted with *Rabinowitz, H. S., Savage, H. M., & Polissar, P. J. Reaction kinetics of alkenone and n-alkane thermal alteration at seismic timescales. Geochemistry, Geophysics, Geosystems, 18(1), 204-219.*

B.1 Introduction

The supporting information contains descriptions of tests conducted to assess the efficacy of ASE vs. sonication extractions, a more in-depth description of the $U_{37}^{k'}$ modeling, and additional information about the increase in extractable sulfur observed during the heating experiments as well as supporting figures. In addition, we include data tables with specific sampling locations in RC14-99, measured concentrations of all molecules discussed in this paper, biomarker parameters for all molecules measured, and an extended table with kinetic parameters for all biomarker parameters presented in Figure B.7.

B.2 ASE vs. Sonication Extractions

Due to this studys focus on the effect of heating on the biomarker composition of sediments, care was taken to avoid heating the sediments in all steps of the procedure aside from the hydrous pyrolysis experiments. Sonication extractions were initially assumed to provide the lowest chance of thermally altering sediment during the extraction procedure due to the fact that organic solvents are maintained at room temperature during the sonication procedure. However, upon re-extracting sediment using the ASE, it became clear that a significant and variable amount of the long-chain alkenones were not extracted by sonication (Figure B.1). Initial concerns about the potential thermal alteration of sediment during ASE extraction (which is regularly performed at an extraction temperature of 100 ^{o}C) led us to perform tests of the extraction methods. Two potential competing

effects could lead to differences in extraction yield at different extraction temperatures. First, a higher extraction temperature could lead to a higher yield by dissociating organic molecules from their sediment matrix more efficiently and increasing solubility. Conversely, a higher extraction temperature could lead to a lower yield due to the thermal alteration of the molecules during the extraction process.

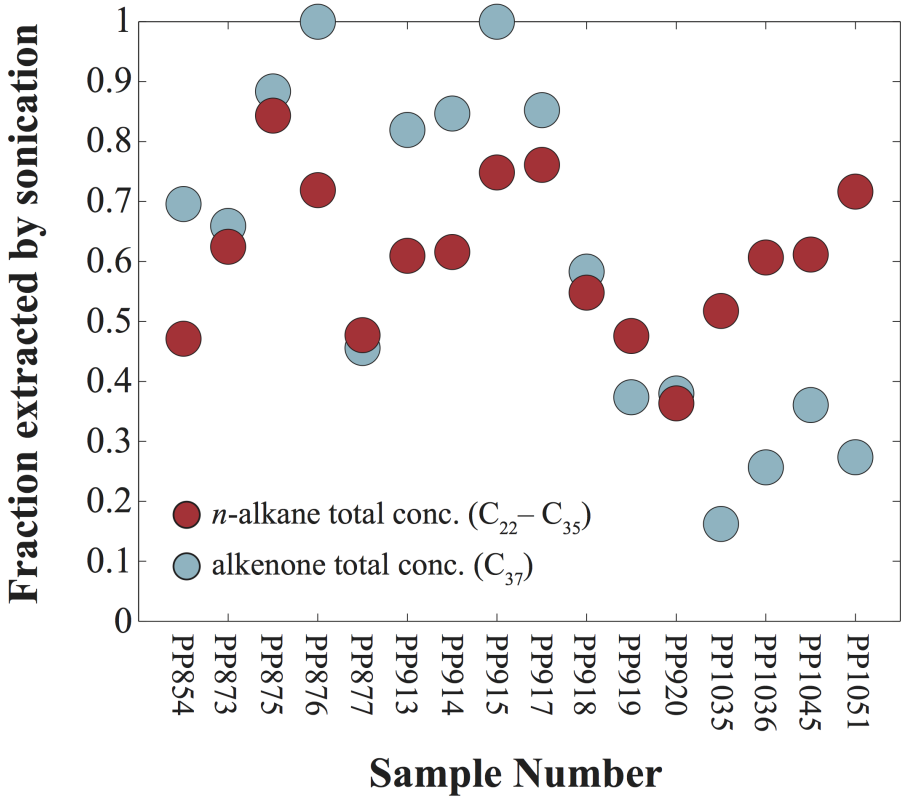

Figure B.1: Alkenone (blue) and *n*-alkane (red) concentrations obtained through ASE and sonication extraction techniques. While there is a general trend of larger ASE yields from samples that had higher sonication yields, some samples exhibited near total extraction through sonication while some retained over half of their TLE after sonication, prior to ASE extraction.

The result of these two potential effects was tested by extracting two samples of Batch C sediment three times using the ASE. The first sequence (PP1294) involved sequentially extracting one aliquot of the sample first at 100 ^{o}C, then at 50 ^{o}C, and finally at 100 ^{o}C again. This extraction schedule was designed to test whether the higher extraction temperature (100 ^{o}C) would yield the complete TLE in one extraction or if, in fact, the heated solvent would destroy alkenones, reducing the total yield. If there was incomplete extraction, there would be organic matter remaining that

could be extracted at the lower temperature (50 ^{o}C) or, if this lower temperature was insufficient to extract the resistant organic matter, the final 100 ^{o}C extraction could yield the remainder of the organic material. The second sequence (PP1295) involved extracting an aliquot of the sample at 50 ^{o}C, followed by another extraction at 50 ^{o}C, and finally, an extraction at 100 ^{o}C. This extraction schedule was aimed at testing whether the lower extraction temperature would lead to a higher yield by causing less thermal alteration of the sediment.

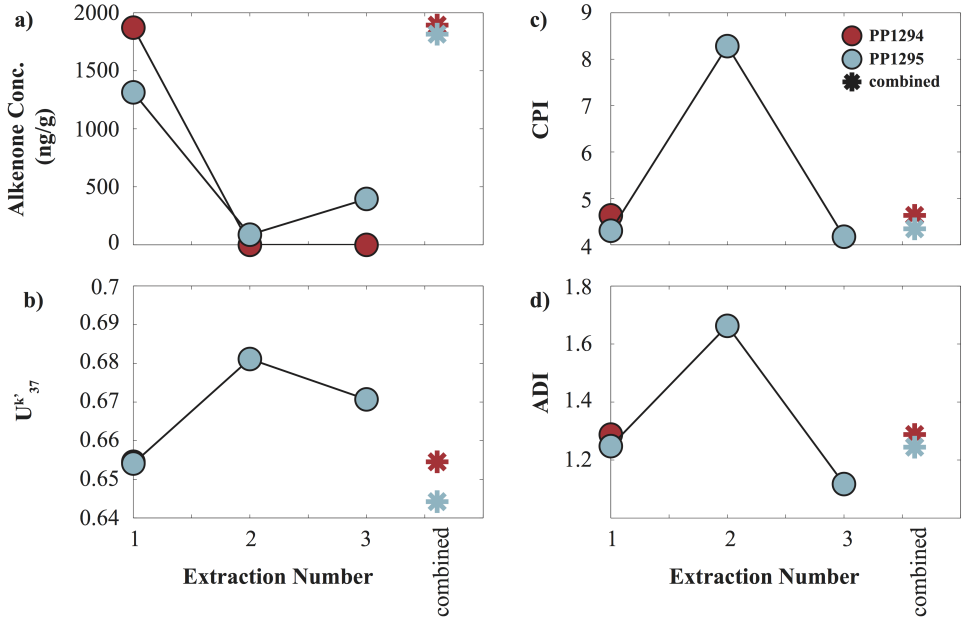

Figure B.2: The effect of ASE extraction at different temperatures on a) alkenone concentration, b) $U^{k'}_{37}$, c) CPI and d) ADI was tested by extracting two samples three times with two different extraction schedules. We find that in all cases, a 50 ^{o}C extraction temperature is insufficient to extract all organic material.

We found that the 100 ^{o}C extraction temperature was the more effective extraction temperature, extracting 100% of the TLE in one extraction for PP1294 (Figure B.2). The second experiment (PP1295) showed that the 50 ^{o}C extractions only provided partial yields. However, upon the final 100 ^{o}C extraction, the remainder of the TLE was extracted. The complete extraction for PP1295 was confirmed by summing the extracted concentrations for each sequence. These summed alkenone concentrations showed only a 4.2% difference between the two samples. $U^{k'}_{37}$ values were found to vary by ~0.01. These observations imply that, while the 100 ^{o}C extraction temperature does not lead to excess alkenone destruction relative to the 50 ^{o}C extraction temperature, the 50 ^{o}C extractions provides less effective extraction. Based on these results, we suggest that the

complete yield of long-chain alkenones from sediments can be obtained by ASE extraction at 100 ^{o}C without thermally altering the extracted organic material. We also find an incomplete extraction of n-alkanes with sonication (Figure B.1) and find that ASE extraction at 50 and 100 ^{o}C yield the values for CPI and ADI which vary only by 0.29 and 0.044, respectively (Figure B.2).

B.3 $U^{k'}_{37}$ Modeling

Due to the strong dependence of $U^{k'}_{37}$ thermal alteration on the initial $U^{k'}_{37}$ value, we do not use an Arrhenius analysis to determine the kinetics of thermal alteration of this parameter. The reasons for this are two-fold. First, we observe a change in $U^{k'}_{37}$ in our starting material throughout the course of this study. This change makes a direct calculation of $U^{k'}_{37}$ kinetics from the experiments uncertain. Second, such a direct determination of kinetics might suggest that the kinetic parameters calculated from our experiments could be applied to any heated marine sediment, though our kinetics would be inapplicable to sediments with a different starting $U^{k'}_{37}$ value. Rather, we suggest that a time-temperature history for sediment be inferred by using the known initial $U^{k'}_{37}$ value and measured final $U^{k'}_{37}$ value to determine the relative reaction extent of MK37:2 or MK37:3. Then, the kinetics of these two molecules can be used to model time-temperature history.

We relate the fractional change of $U^{k'}_{37}$ to that of its component molecules as follows. We can re-arrange the equation defining the $U^{k'}_{37}$ value (Equation 3.6):

$$U^{k'}_{37} = \frac{MK37:2}{MK37:2 + MK37:3} \tag{B.1}$$

to define $U^{k'}_{37}$ in terms of a ratio of MK37:3 to MK37:2

$$\frac{1 - U^{k'}_{37}}{U^{k'}_{37}} = \frac{1}{U^{k'}_{37}} = \frac{MK37:3}{MK37:2} \tag{B.2}$$

We can then solve for the $U^{k'}_{37}$ value as a function of heating time and temperature using the kinetics of MK37:2 and MK37:3 destruction:

$$\frac{1}{U^{k'}_{37}} = \frac{MK37:3_0 * e^{-k_3 t}}{MK37:2_0 * e^{-k_2 t}} \frac{1}{U^{k'}_{37}} = \frac{MK37:3_0}{MK37:2_0} * e^{(k_2 - k_3)t} \tag{B.3}$$

where k_2 and k_3 are the reaction rate constants for MK37:2 and MK37:3, respectively, at a given

temperature as defined in Equation 3.4 ($k = Ae^{(-E_a/RT)}$). The values for E_a and A are those determined experimentally for each molecule. This equation can be rearranged to derive a function for the measured $U^{k'}_{37}$ value as a function of heating time in terms of the initial $U^{k'}_{37}$ value:

$$U^{k'}_{37}(t,T) = \frac{1}{1 + \left[\frac{1}{U^{k'}_{37}} - 1\right] * e^{(k_2(T) - k_3(T))t}} \tag{B.4}$$

This can be compared to the fraction reacted (p) in terms of time (t) in seconds and temperature (T) in Kelvin of MK37:2, MK37:3, or C_{37} concentration using the equation for p:

$$p = 1 - exp(-Ate^{\frac{-E_a}{RT}}) \tag{B.5}$$

where A is the pre-exponential frequency factor (s^{-1}), E_a is the activation energy (kcal/mol), R is the gas constant ($1.987*10^{-3}$ kcal/K*mol).

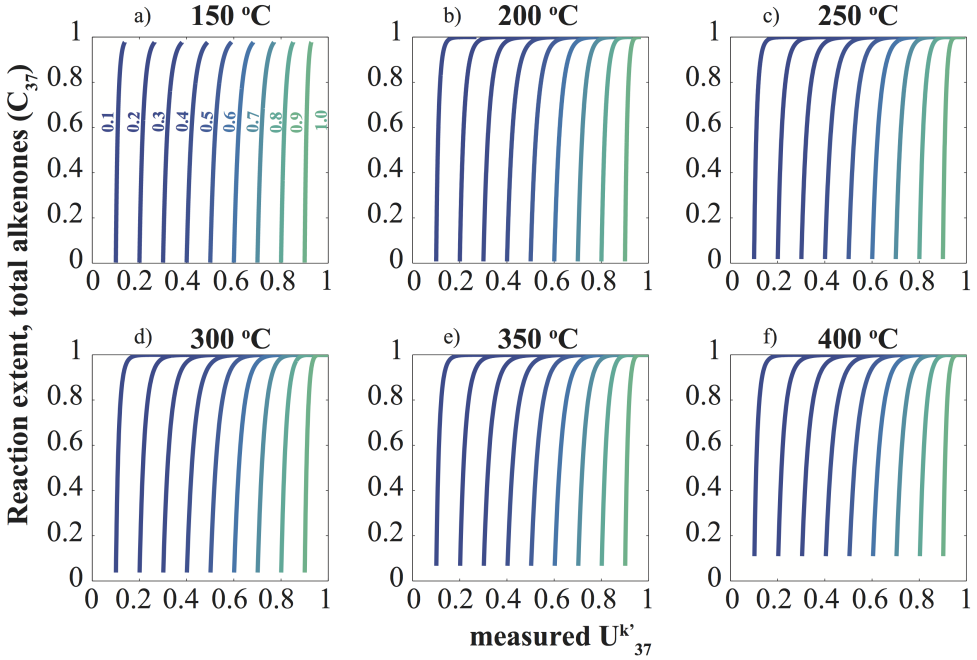

Figure B.3: The measured $U^{k'}_{37}$ value of heated sediment depends strongly on the initial $U^{k'}_{37}$ value of the unheated sediment. Here, we show the variation of measured $U^{k'}_{37}$ values as a function of the initial $U^{k'}_{37}$ value (contoured in increments of 0.1 in color on each plot) of the sediment. This is plotted against the reaction extent of total alkenones (though a similar plot could be made using the reaction extent of MK37:2 or MK37:3) with each subplot representing a different heating temperature. This plot can be used to estimate the reaction extent of a sediment of known (measured) $U^{k'}_{37}$ if the initial $U^{k'}_{37}$ value is also known (e.g. from paleoclimate records providing an estimate of SST at the time of deposition).

We show the dependence of reaction extent of different measured $U_{37}^{k'}$ values on initial $U_{37}^{k'}$ value in Figure B.3. Using a plot such as this, the reaction extent of a sediment can be determined simply by estimating the initial $U_{37}^{k'}$ value from a known SST history and measuring the $U_{37}^{k'}$ value exhibited by the sediment after it has experienced heating. The reaction extent of MK37:2 or MK37:3 determined in this way can be used to model a potential time/temperature path for the sample even if the absolute initial concentrations of the molecules remains unknown.

B.4 Extractable Sulfur

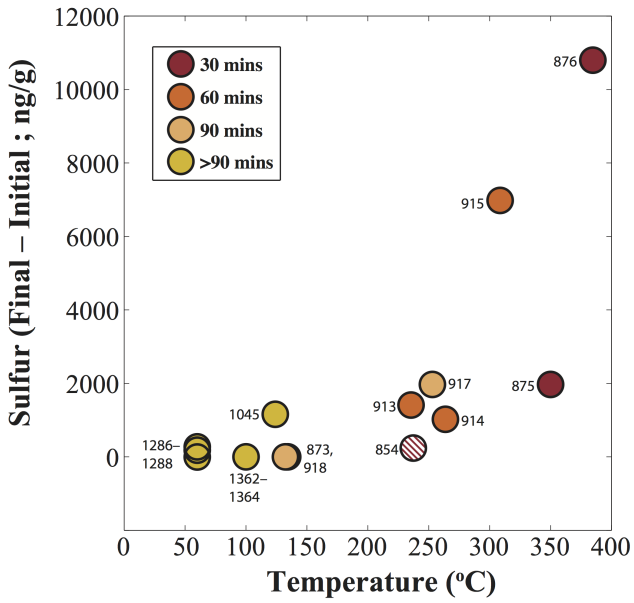

Figure B.4: We observe a marked increase in extractable S_8 in our experiments T $\geq$ 250 ^{o}C and most notably above 300 ^{o}C. Hatched symbols represent points not used in Arrhenius fits.

We also observe the formation of extractable elemental sulfur, measured as S_8, during our experiments at high temperature (Figure B.4). Below temperatures of $\sim$250 ^{o}C, the sulfur concentration remains at the initial value (measured in the appropriate control sample). Above this temperature, the sulfur concentration increases by $\sim$1,000–11,000 ng/g. We note that absolute concentrations reported are very uncertain as they are uncorrected for the MSD response. However, relative changes between samples are robust. Because the dramatic increase in sulfur concentration is most significantly observed only in our very highest temperature experiments, we do not determine the kinetic

parameters for sulfur production here. However, when biologic sources can be ruled out, a dramatic increase in elemental sulfur concentration in a fault zone relative to that observed in the host rock could be suggestive of a significant coseismic temperature rise. If such a signal is rapidly removed through chemical redox reactions (abiotic or biotically mediated) its presence could perhaps be an indicator of recent heating along the fault surface.

B.5 Additional Figures

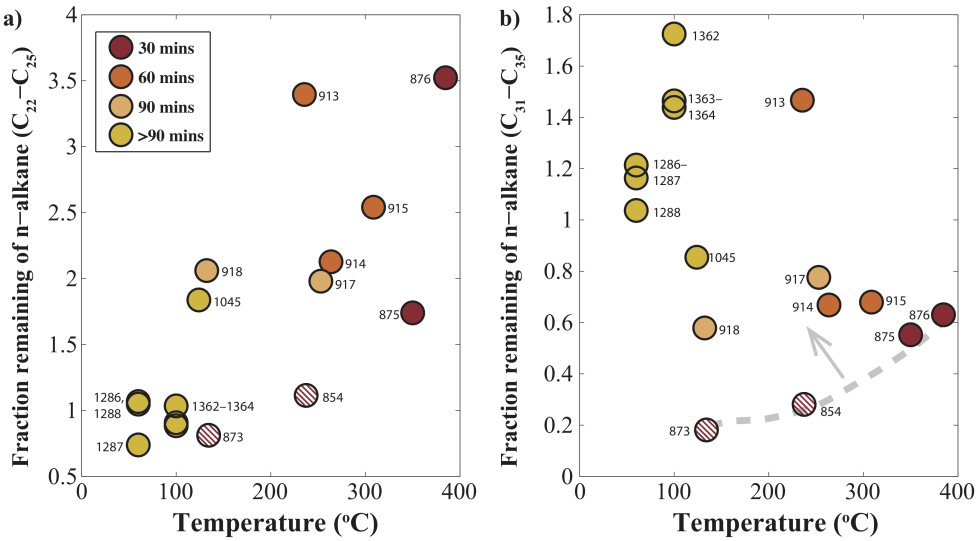

Figure B.5: The distribution of n-alkane chain lengths changes throughout heating. Shorter-chain lengths ($<C_{25}$) are produced at all temperatures (a) while longer-chain length n-alkanes (C_{31}–C_{35}) are consistently produced upon heating, but also show indications of immediate breakdown to shorter-chain lengths at higher temperatures (b). At higher temperatures, production of shorter-chain *n*-alkanes occurs more rapidly, leading to an initial decrease in longer-chain *n*-alkane concentration until cracking reactions that produce longer-chain *n*-alkanes compensate for this decrease in concentration at longer times. Hatched symbols represent samples not used in Arrhenius fits.

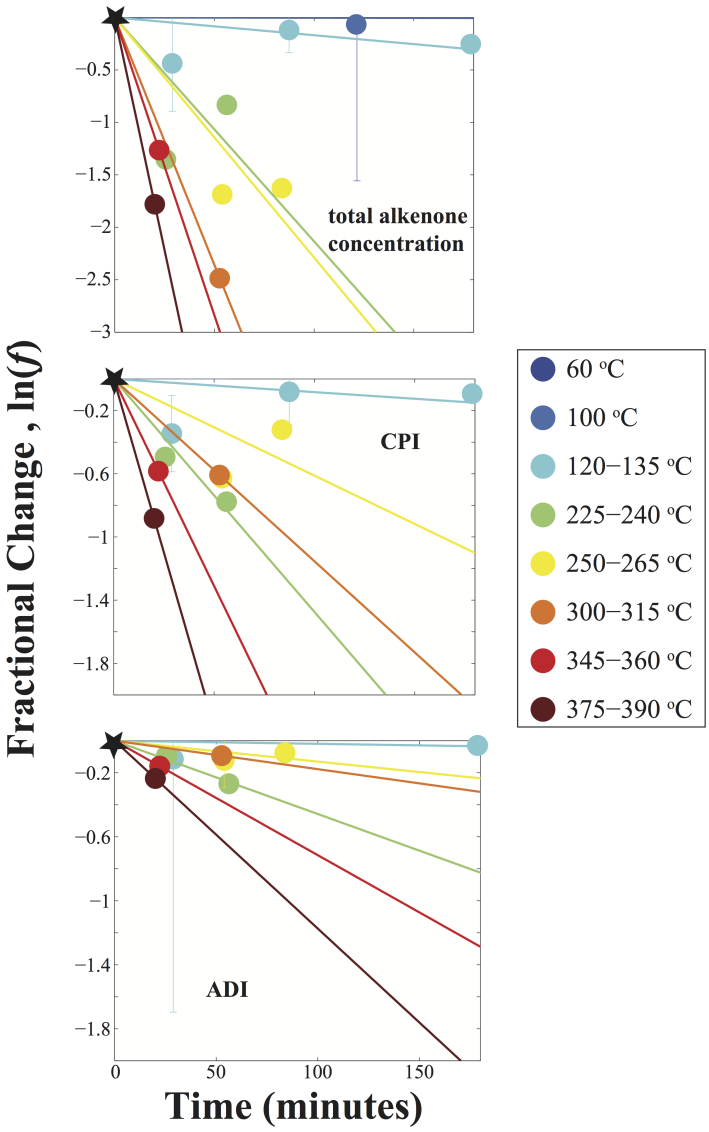

Figure B.6: Plots showing the fractional change of biomarkers used in this study with time. Colors represent temperature bins of 15 ^{o}C. Error bars are the propagated uncertainty in the fractional change that includes the analytical uncertainty of the initial, unheated sample and the heated sample. Slopes are the rate constants for each temperature bin.

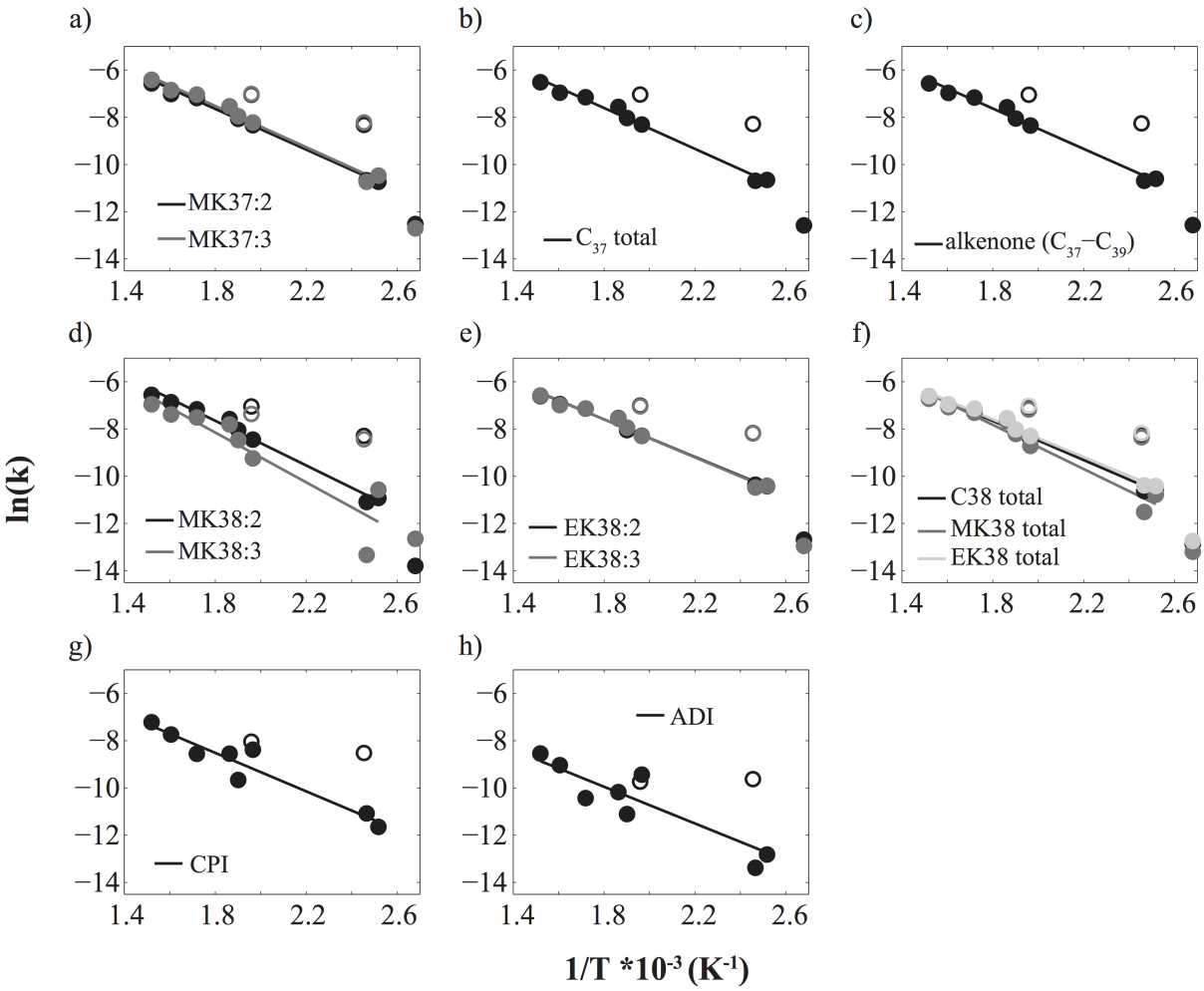

Figure B.7: Arrhenius plots for a) MK37:2, MK37:3, MK37:4, b) C_{37} total (total alkenone in main text), c) C_{36}–C_{39} total, d) MK38:2, MK38:3, e) EK38:2, EK38:3, f) C_{38} total, MK38 total, EK38 total, g) CPI, and h) ADI.

B.6 Supplemental Tables

Table B.1: Sampling depths from core RC14-99 6b for hydrous pyrolysis experiments

Batch A, sampled 11/13/12		Batch B, sampled 01/11/13		Batch C, sampled 01/13/15	
Sample depth (cm in core)	Size (cc)	Sample depth (cm in core)	Size (cc)	Sample depth (cm in core)	Size (cc)
1285	5	1280	5	1244	10
1285	5	1283	5	1248	5
1290	5	1287	5	1258	5
1300	5	1292	5	1275	5
1305	5	1294	5	1345	10
1305	5	1305	5	1355	5
1310	5	1312	5	1365	10
1315	5	1313	5	1365	5
1317	5	1314	5	1377	5
1325	5	1322	5	1390	5
1335	5	1323	5	1395	5
1345	5	1331	5	1411	10
1350	5	1332	5	1422	5
1355	5	1333	5	1435	5
1365	5	1371	5	1447	5
1375	5	1372	5	1454	5
1390	5	1405	5		
1405	5	1415	5		
1405	5	1416	5		
		1436	5		

Table B.2: Concentrations of molecules measured in the ketone fraction (F2) of hydrous pyrolysis samples

Sample #	Weight (g)	Time (min)[a] *unless otherwise noted	Temp. (^oC)[b]	Sediment Batch	MK 37:3	MK 37:2	ME 36:2	EK 38:3	MK 38:3	EK 38:2	MK 38:2	MK 39:3	MK 39:2
Hydrous Pyrolysis Experiments													
PP877[c]	4.879	——-	20	A	568.12	1146.11	149.55	292.61	212.28	904.99	326.59	43.08	162.26
PP920[c]	5.006	——-	20	B	451.43	1065.46	128.66	237.92	179.42	821.90	296.86	36.07	137.51
PP1051[c]	5.027	——-	20	A+B	372.21	927.24	114.47	207.23	156.87	755.62	263.30	30.20	129.65
PP1285[c]	2.003	——-	20	C	617.15	1165.70	133.95	283.28	233.65	882.75	343.54	43.20	148.97
PP1361[c,d]	1.94	147 days	20	C	542.58	1074.65	115.74	237.46	190.56	757.98	296.63	50.81	173.65
PP1286	1.936	7290	60	C	626.22	1175.03	135.91	289.33	235.93	878.58	344.12	51.07	159.11
PP1287	1.968	86430	60	C	631.55	1190.10	135.34	291.15	235.14	879.32	344.07	39.70	148.76
PP1288	1.979	345600	60	C	651.38	1194.74	137.09	294.45	243.35	898.62	350.66	41.89	148.10
PP1362	1.983	7269	100	C	511.91	1001.26	109.88	226.47	177.59	711.33	291.18	39.94	141.91
PP1363	1.944	86428	100	C	517.84	999.72	105.99	231.28	194.59	733.72	290.52	43.56	120.07
PP1364	2.009	345595	100	C	447.59	937.28	95.95	212.66	179.27	708.70	270.92	49.45	151.49
PP1045	4.701	10713	124.08	A+B	274.80	733.74	79.85	149.84	119.36	549.57	217.16	33.37	107.67
PP918	4.969	5246	132.39	B	402.85	943.00	99.46	205.20	177.90	695.96	274.01	43.48	134.76
PP873	3.37	1733	134.25	A	356.88	750.60	90.27	181.15	145.82	555.61	211.69	38.57	100.86
PP913	4.795	3375	235.57	B	183.35	475.70	48.35	102.85	129.55	352.50	144.26	16.49	60.55
PP854	5.077	1538	237.38	A	141.46	301.71	31.55	76.15	80.11	226.07	85.63	15.67	42.65
PP917	4.419	5027	252.94	B	77.01	221.40	17.33	39.71	62.33	163.61	59.26	7.38	29.24
PP914	4.455	3236	263.70	B	79.68	201.22	23.08	44.23	48.25	145.80	56.80	7.18	26.41
PP915	4.639	3161	308.63	B	28.39	97.99	9.51	19.27	32.19	67.37	26.09	1.87	8.84
PP875	1.905	1336	349.97	A	138.65	345.40	36.41	85.50	93.04	249.57	81.16	13.10	46.84
PP876	1.121	1204	384.80	A	78.34	210.62	20.81	55.32	67.18	177.70	59.28	5.18	25.35
Biomarker Degradation Tests													
PP877[c]	4.879	——-	20	A	568.12	1146.11	149.55	292.61	212.28	904.99	326.59	43.08	162.26
PP919	5.002	144 days	20	A	508.44	1145.19	138.15	268.42	211.39	873.58	315.24	38.14	145.14
PP1035	4.955	564 days	20	A	318.99	795.18	117.41	226.87	166.50	771.89	227.70	32.38	128.01
PP920[c]	5.006	——-	20	B	451.43	1065.46	128.66	237.92	179.42	821.90	296.86	36.07	137.51
PP1036	4.964	403 days	20	B	365.90	919.39	115.83	214.67	155.76	761.27	260.53	31.29	129.08
PP1285[c]	2.003	——-	20	C	617.15	1165.70	133.95	283.28	233.65	882.75	343.54	43.20	148.97
PP1361[c,d]	1.94	147 days	20	C	542.58	1074.65	115.74	237.46	190.56	757.98	296.63	50.81	173.65
PP1959	2.922	496 days	20	C	467.91	971.21	96.09	244.60	187.11	773.53	284.00	33.75	131.23
PP1960	2.949	496 days	20	C	434.13	910.74	93.22	230.38	175.93	735.28	265.84	30.79	126.89
PP1961	2.999	496 days	20	C	460.37	949.44	99.72	248.03	184.02	776.31	276.25	34.18	133.56
PP1962	3.139	496 days	20	C	432.99	905.09	97.02	232.90	178.21	742.41	260.92	31.41	123.66
PP1963	3.011	496 days	20	C	463.71	982.02	100.66	241.91	198.68	762.57	287.83	32.74	130.35
PP1964	3.254	496 days	20	C	420.88	903.57	95.46	234.00	203.01	732.21	264.10	30.03	124.41
PP1965	2.951	496 days	20	C	419.11	896.54	92.00	221.55	180.72	697.65	253.88	28.24	112.78
ASE Tests													
PP1294A	2.305	——-	100		646.65	1225.24	140.42	310.88	246.85	942.64	364.13	44.77	159.10
PP1294B			50	C	0	0	0	0	0	0	0	0	0
PP1294C			100		0	0	0	0	0	0	0	0	0
PP1295A	2.137	——-	50		454.39	859.25	96.52	216.42	174.25	665.80	261.68	34.38	116.28
PP1295B			50	C	27.95	59.71	9.20	14.05	9.03	42.91	20.57	1.74	6.51
PP1295C			100		130.08	264.91	36.36	69.01	48.83	207.43	84.78	9.24	28.94

[a] Time at 85% T_{max} in minutes unless otherwise noted
[b] Mean temperature during time at 85% T_{max}
[c] Sample used as unheated control
[d] Sample used for alkenone degradation analysis

Table B.3: Concentrations of molecules measured in the aliphatic fraction (F1) of hydrous pyrolysis samples

Sample #	Weight (g)	Time (min)[a] *unless otherwise noted	Temp. (°C)[b]	Sediment Batch	nC_{15} alkane	nC_{16} alkane	nC_{17} alkane	nC_{18} alkane	nC_{19} alkane	nC_{20} alkane	nC_{21} alkane	nC_{22} alkane	nC_{23} alkane	nC_{24} alkane	nC_{25} alkane	nC_{26} alkane
Hydrous Pyrolysis Experiments																
PP877[c]	4.879	——-	20.00	A	29.95	265.12	1068.80	1278.17	537.73	213.35	117.53	73.09	61.94	49.58	62.29	30.02
PP920[c]	5.006	——-	20.00	B	90.04	614.20	1671.85	1514.12	576.20	204.96	111.76	68.07	62.64	45.25	66.97	32.13
PP1051[c]	5.027	——-	20.00	A+B	113.07	576.42	1594.51	1587.76	663.29	256.04	147.54	90.23	84.87	55.03	97.00	47.00
PP1285[c]	2.003	——-	20.00	C	913.75	2064.84	2744.98	2099.44	842.77	485.52	337.74	204.53	138.74	78.30	94.03	49.34
PP1361[c,d]	1.94	147 days	20.00	C	103.27	591.66	1489.20	1466.88	632.33	278.38	222.90	130.72	129.15	87.29	111.36	56.91
PP1286	1.936	7290	60.00	C	1009.34	2287.36	3025.48	2329.92	955.89	540.58	353.90	210.72	146.63	80.85	102.67	55.35
PP1287	1.968	86430	60.00	C	1085.61	2286.07	3002.84	2251.10	845.92	401.73	242.68	129.27	98.04	60.59	93.23	50.57
PP1288	1.979	345600	60.00	C	1091.17	2355.15	2970.85	2326.40	918.27	567.86	388.98	223.72	150.18	81.21	95.44	46.52
PP1362	1.983	7269	100.00	C	34.90	374.54	1203.53	1343.49	609.77	280.59	213.46	125.72	111.70	73.32	105.20	54.22
PP1363	1.944	86428	100.00	C	9.84	270.76	1147.90	1330.99	600.82	309.73	276.10	156.64	124.61	82.09	111.41	53.89
PP1364	2.009	345595	100.00	C	2.62	74.70	741.92	1176.10	581.97	255.88	193.19	122.80	107.05	71.54	104.26	50.55
PP1045	4.701	10713	124.08	A+B	80.55	520.86	1518.14	1557.87	900.72	596.78	448.05	235.54	152.29	101.99	111.48	50.45
PP918	4.969	5246	132.39	B	100.85	646.21	1498.55	1392.72	648.15	401.15	391.75	198.34	128.16	81.14	92.85	33.29
PP873	3.37	1733	134.25	A	12.53	235.18	1018.25	1130.98	463.98	208.07	138.85	80.43	51.56	31.60	36.97	14.36
PP913	4.795	3375	235.57	B	92.69	577.40	1341.11	1318.00	757.44	547.89	506.74	268.54	171.18	161.79	223.33	98.65
PP854	5.077	1538	237.38	A	25.33	247.46	734.89	767.62	363.62	207.25	160.53	110.68	69.55	42.10	52.64	20.53
PP917	4.419	5027	252.94	B	21.30	283.06	931.13	1049.75	588.77	378.94	383.29	191.31	116.48	80.82	92.59	39.43
PP914	4.455	3236	263.70	B	13.01	298.74	966.18	948.67	501.22	353.27	382.62	191.29	123.07	87.98	114.43	55.56
PP915	4.639	3161	308.63	B	41.57	345.97	968.81	1039.41	594.83	427.06	438.02	226.71	156.60	97.88	135.91	61.66
PP875	1.905	1336	349.97	A	152.69	850.10	1804.71	1622.39	750.11	407.11	371.05	166.57	116.34	65.07	81.69	37.87
PP876	1.121	1204	384.80	A	47.87	391.11	1050.61	1395.94	853.36	673.05	659.32	355.32	227.94	149.82	136.61	95.24
Biomarker Degradation Tests																
PP877[c]	4.879	——-	20	A	29.95	265.12	1068.80	1278.17	537.73	213.35	117.53	73.09	61.94	49.58	62.29	30.02
PP919	5.002	144 days	20	A	116.45	510.89	1498.89	1506.57	587.11	218.95	121.42	76.19	72.93	58.59	83.73	40.34
PP1035	4.955	564 days	20	A	116.46	452.60	1380.13	1466.41	585.34	218.07	128.45	82.95	80.63	56.90	97.72	47.81
PP920[c]	5.006	——-	20	B	90.04	614.20	1671.85	1514.12	576.20	204.96	111.76	68.07	62.64	45.25	66.97	32.13
PP1036	4.964	403 days	20	B	67.03	322.13	1190.29	1371.26	585.69	225.79	132.67	85.81	79.94	50.72	84.95	39.60
PP1285[c]	2.003	——-	20	C	913.75	2064.84	2744.98	2099.44	842.77	485.52	337.74	204.53	138.74	78.30	94.03	49.34
PP1361[c,d]	1.94	147 days	20	C	103.27	591.66	1489.20	1466.88	632.33	278.38	222.90	130.72	129.15	87.29	111.36	56.91
PP1959	2.922	496 days	20	C	149.14	666.98	1655.91	1452.85	550.04	205.85	116.71	72.93	72.80	49.74	88.26	45.70
PP1960	2.949	496 days	20	C	114.55	606.70	1592.62	1442.02	555.22	202.47	110.77	69.30	66.62	46.03	81.69	41.50
PP1961	2.999	496 days	20	C	120.92	665.74	1707.00	1517.43	569.60	206.22	120.35	73.22	72.10	49.76	89.35	47.00
PP1962	3.139	496 days	20	C	212.71	871.99	1835.41	1490.21	546.14	201.22	112.90	69.29	69.39	48.10	89.57	48.83
PP1963	3.011	496 days	20	C	124.44	652.74	1669.05	1512.31	565.35	209.99	118.67	73.87	73.33	48.11	92.04	48.40
PP1964	3.254	496 days	20	C	93.08	630.36	1666.17	1461.68	551.25	199.94	111.44	71.48	67.95	45.73	82.16	44.11
PP1965	2.951	496 days	20	C	110.30	638.25	1669.20	1479.47	551.80	203.81	113.74	71.16	71.18	47.01	87.82	47.24
ASE Tests																
PP1294A	2.305	——-	100	C	966.53	2225.30	2928.74	1927.27	618.72	207.28	105.69	67.06	62.62	40.34	75.48	38.22
PP1294B			50		0.00	0.00	0.00	0.00	0.00	0.00	0.00	0.00	0.00	0.00	0.00	0.00
PP1294C			100		0.00	0.00	0.00	0.00	0.00	0.00	0.00	0.00	0.00	0.00	0.00	0.00
PP1294 total					966.53	2225.30	2928.74	1927.27	618.72	207.28	105.69	67.06	62.62	40.34	75.48	38.22
PP1295A	2.137	——-	50	C	586.62	1302.42	2188.50	1525.45	489.11	159.39	80.86	47.18	43.78	27.70	50.52	25.21
PP1295B			50		0.00	6.69	31.78	38.33	13.42	3.76	2.36	1.60	1.43	1.19	1.36	0.82
PP1295C			100		4.58	29.81	93.22	104.57	38.77	11.46	5.87	3.55	3.20	2.91	3.51	1.92
PP1295 total					591.20	1338.92	2313.50	1668.35	541.30	174.61	89.09	52.33	48.41	31.81	55.38	27.94

[a] Time at 85% T_{max} in minutes unless otherwise noted
[b] Mean temperature during time at 85% T_{max}
[c] Sample used as unheated control
[d] Sample used for alkenone degradation analysis

Table B.4: Continuation of Table B.3

nC27 alkane	nC28 alkane	nC29 alkane	nC30 alkane	nC31 alkane	nC32 alkane	nC33 alkane	nC34 alkane	nC35 alkane	pristane	phytane	sulfur, S8e
Hydrous Pyrolysis Experiments											
82.71	23.41	117.11	15.76	127.27	7.92	33.30	10.23	14.11	334.20	408.16	0.00
88.12	23.96	110.64	14.55	109.29	6.90	27.14	4.27	13.66	570.10	486.12	0.00
132.26	35.36	162.45	22.05	157.43	10.07	41.01	17.61	21.35	529.35	527.06	0.00
120.41	40.33	173.58	29.55	181.84	15.24	49.41	19.65	21.40	1205.17	1100.82	702.57
120.73	34.75	135.18	18.15	102.43	4.57	16.17	9.85	7.43	537.55	543.76	0.00
132.33	46.50	196.92	30.80	218.34	14.82	56.78	16.95	27.65	1422.97	1346.42	883.81
134.47	43.48	198.76	32.77	226.53	14.90	60.83	17.88	29.09	1365.51	1145.63	698.20
122.87	38.03	179.74	28.33	201.49	12.46	53.74	12.47	18.13	1393.46	1294.02	976.00
125.88	40.31	165.34	24.38	157.14	11.31	31.01	21.67	21.14	423.13	502.58	0.00
120.62	37.21	153.39	22.08	142.02	7.10	28.61	11.81	16.13	398.88	486.42	0.00
115.28	35.77	146.93	20.20	135.17	7.59	27.07	19.19	13.06	230.05	379.44	0.00
119.01	33.97	148.70	21.51	142.31	8.97	32.04	13.75	14.47	552.34	610.11	1158.69
74.45	18.71	81.15	7.73	69.12	2.84	15.59	0.00	5.74	486.41	479.03	0.00
32.13	9.69	33.80	5.90	27.04	2.46	5.38	0.00	0.00	328.27	364.55	0.00
123.60	61.52	156.15	48.13	145.14	17.50	33.90	18.84	21.18	446.31	481.50	1409.65
34.52	10.54	37.72	9.01	35.69	3.54	8.54	2.42	3.93	194.67	207.18	236.90
79.42	26.44	94.21	15.16	87.31	5.00	19.14	6.76	6.98	307.30	385.81	1971.72
69.29	24.77	80.51	15.04	71.53	7.89	14.96	4.47	8.92	352.27	371.77	1023.67
92.14	33.16	90.68	14.43	74.52	5.71	16.37	5.96	7.06	320.80	374.50	6978.80
58.40	22.13	71.04	16.89	67.72	7.27	14.91	8.04	8.49	640.51	595.03	1970.80
78.15	26.82	101.08	29.30	88.73	11.61	21.23	0.00	0.00	396.70	565.64	10800.51
Biomarker Degradation Tests											
82.71	23.41	117.11	15.76	127.27	7.92	33.30	10.23	14.11	334.20	408.16	0.00
113.60	31.74	148.75	20.33	147.10	8.96	38.74	16.61	20.86	521.77	541.08	3985.07
129.26	35.99	166.40	23.13	163.61	10.29	41.54	14.73	22.61	430.80	503.99	4119.52
88.12	23.96	110.64	14.55	109.29	6.90	27.14	4.27	13.66	570.10	486.12	0.00
110.49	29.11	135.82	18.28	136.58	7.53	33.45	12.37	18.16	367.90	436.42	0.00
120.41	40.33	173.58	29.55	181.84	15.24	49.41	19.65	21.40	1205.17	1100.82	702.57
120.73	34.75	135.18	18.15	102.43	4.57	16.17	9.85	7.43	537.55	543.76	0.00
116.44	34.40	153.13	20.59	157.35	9.17	36.44	9.34	13.54	562.99	507.59	0.00
108.06	32.55	140.70	20.85	143.05	8.50	33.63	9.90	15.90	538.48	497.59	0.00
120.96	36.83	160.34	23.92	171.18	10.45	42.24	12.01	18.11	578.63	532.13	0.00
127.01	40.21	174.56	25.56	187.29	11.42	47.74	11.25	17.82	626.10	511.84	0.00
123.81	37.25	165.76	23.75	177.47	10.26	43.79	12.00	17.92	570.40	530.12	0.00
114.00	33.50	154.27	22.07	163.44	10.00	42.37	12.15	19.20	567.34	516.48	0.00
118.97	36.08	156.96	22.55	166.54	9.44	43.03	11.00	17.92	568.16	522.58	0.00
ASE Tests											
109.54	28.38	141.22	15.43	128.78	6.13	21.62	0.00	7.29	1063.60	685.14	0.00
0.00	0.00	0.00	0.00	0.00	0.00	0.00	0.00	0.00	0.00	0.00	0.00
0.00	0.00	0.00	0.00	0.00	0.00	0.00	0.00	0.00	0.00	0.00	0.00
109.54	28.38	141.22	15.43	128.78	6.13	21.62	0.00	7.29	1063.60	685.14	0.00
67.60	17.71	85.47	10.03	73.65	4.00	12.65	0.00	5.71	799.19	596.11	0.00
2.07	0.00	2.56	0.00	2.18	0.00	0.00	0.00	0.00	8.73	7.02	0.00
5.97	2.20	8.15	1.32	7.07	0.00	1.51	0.00	0.00	20.93	12.67	0.00
75.64	19.90	96.17	11.35	82.90	4.00	14.16	0.00	5.71	828.85	615.80	0.00

Table B.5: Biomarker parameters measured in hydrous pyrolysis experiments, degradation tests, and ASE tests

Sample #	Weight (g)	Time (min)b *unless otherwise noted	Temp. (C)c	Sediment Batch	Alkenone Conc. (C_{37})	$U^{k'}_{37}$	CPI	ADI
Hydrous Pyrolysis Experiments								
PP877[c]	4.879	——-	20.00	A	1714.22	0.67	4.29	1.34
PP920[c]	5.006	——-	20.00	B	1516.90	0.70	4.26	1.32
PP1051[c]	5.027	——-	20.00	A+B	1299.45	0.71	3.90	1.32
PP1285[c]	2.003	——-	20.00	C	1782.84	0.65	3.55	1.24
PP1361[c,d]	1.94	147 days	20.00	C	1617.22	0.66	3.07	1.19
PP1286	1.936	7290	60.00	C	1801.25	0.65	3.84	1.28
PP1287	1.968	86430	60.00	C	1821.65	0.65	4.07	1.31
PP1288	1.979	345600	60.00	C	1846.12	0.65	4.18	1.32
PP1362	1.983	7269	100.00	C	1513.18	0.66	3.30	1.23
PP1363	1.944	86428	100.00	C	1517.55	0.66	3.49	1.23
PP1364	2.009	345595	100.00	C	1384.86	0.68	3.28	1.23
PP1045	4.701	10713	124.08	A+B	1008.54	0.73	3.55	1.28
PP918	4.969	5246	132.39	B	1345.85	0.70	3.93	1.33
PP873	3.37	1733	134.25	A	1107.48	0.68	3.03	1.20
PP913	4.795	3375	235.57	B	659.05	0.72	1.96	1.01
PP854	5.077	1538	237.38	A	443.17	0.68	2.62	1.23
PP917	4.419	5027	252.94	B	298.41	0.74	3.09	1.23
PP914	4.455	3236	263.70	B	280.90	0.72	2.28	1.17
PP915	4.639	3161	308.63	B	126.38	0.78	2.32	1.21
PP875	1.905	1336	349.97	A	484.05	0.71	2.39	1.15
PP876	1.121	1204	384.80	A	288.96	0.73	1.77	1.06
Biomarker Degradation Tests								
PP877[c]	4.879	——-	20.00	A	1714.22	0.67	4.29	1.34
PP919	5.002	144 days	20.00	A	1653.63	0.69	3.98	1.30
PP1035	4.955	564 days	20.00	A	1114.17	0.71	3.97	1.30
PP920[c]	5.006	——-	20.00	B	1516.90	0.70	4.26	1.32
PP1036	4.964	403 days	20.00	B	1285.29	0.72	4.07	1.35
PP1285[c]	2.003	——-	20.00	C	1782.84	0.65	3.55	1.24
PP1361[c,d]	1.94	147 days	20.00	C	1617.22	0.66	3.07	1.19
PP1959	2.922	496 days	20.00	C	1439.12	0.67	4.00	1.32
PP1960	2.949	496 days	20.00	C	1344.88	0.68	3.90	1.29
PP1961	2.999	496 days	20.00	C	1409.81	0.67	3.94	1.32
PP1962	3.139	496 days	20.00	C	1338.07	0.68	4.04	1.31
PP1963	3.011	496 days	20.00	C	1445.73	0.68	4.02	1.33
PP1964	3.254	496 days	20.00	C	1324.45	0.68	4.05	1.32
PP1965	2.951	496 days	20.00	C	1315.65	0.68	3.99	1.32
ASE Tests								
PP1294A		——-	100.00	C	1871.89	0.65	4.63	1.29
PP1294B	2.305		50.00		0.00	——-	——-	——-
PP1294C			100.00		0.00	——-	——-	——-
PP1295A		——-	50.00	C	1313.63	0.65	4.30	1.25
PP1295B	2.137		50.00		87.66	0.68	8.28	1.66
PP1295C			100.00		394.99	0.67	4.17	1.12

[a] Time at 85% T_{max} in minutes unless otherwise noted
[b] Mean temperature during time at 85% T_{max}
[c] Sample used as unheated control
[d] Sample used for alkenone degradation analysis

Table B.6: Kinetic parameters of thermal maturity for all biomarkers determined in this study

Biomarker Parameter	E (kcal/mol)	A (1/s)	T_{min} (^oC)
alkenone conc. (C_{36}–C_{39})	8.48	1.05	120
MK37:2	8.57	1.12	120
MK37:3	8.67	1.39	120
C_{37} total	8.6	1.2	120
MK38:2	9.38	2.33	120
MK38:3	10.48	3.83	120
MK38 total	9.29	1.81	120
EK38:2	7.91	0.653	120
EK38:3	8.01	0.716	120
EK38 total	7.93	0.666	120
C_{38} total	8.22	0.81	120
CPI	8.08	0.302	120
ADI	7.72	0.052	120

C | Appendix C

C.1 Materials and Methods

C.1.1 Samples

We sampled the JFAST core throughout its recovered depth (183–833 mbsf, sample spacing ranging from 0.7–507 m) with finer sample spacing near the bottom of the core (817–833 mbsf, sample spacing ranging from 0.12–1.6 m), where multiple faults are present [Chester et al., 2013, Keren and Kirkpatrick, 2016a, Kirkpatrick et al., 2015, Rabinowitz et al., 2015]. DSDP Site 436 was selected as a reference for incoming sediments at JFAST due to its proximity to the JFAST site [Chester et al., 2012]. One of the most important components of the biomarker analysis is determining the initial biomarker content of the faulted sediments. Analysis of trace elements shows that western Pacific sedimentary units are broadly consistent over large distances [Rabinowitz et al., 2015]. Therefore, by correlating the chemostratigraphy between the JFAST and 436 sites, we calibrate the range of initial organic content for each sedimentary unit.

C.1.2 Quantification of biomarker concentrations

Biomarker concentrations were determined following methods described in Rabinowitz et al. [2017]. Sediment was freeze dried at a vacuum of 6 Pa and then crushed in a mortar and pestle that was solvent-rinsed with dichloromethane (DCM) and methanol (MeOH). The total lipid extract (TLE) was obtained through sonication extraction using a solution of 9:1 DCM:MeOH with three 15-minute sonications. In order to ensure that all extractable organic material was analyzed,

a second extraction of the sediment was performed using an Accelerated Solvent Extraction system (ASE) following the methods of Rabinowitz et al. [2017], again with an extraction solvent of 9:1 DCM:MeOH. The ASE extractions were conducted at 100 ^{o}C, which has been demonstrated to effectively extract organic material without degrading the biomarkers analyzed in this study [Rabinowitz et al., 2017].

Once the sediment was extracted, 50 μl of a recovery standard containing 5α-androstane and stearyl stearate was added to each TLE. The TLEs were then evaporated under N_2, transferred into a 4 ml vial using DCM, and dried down again. TLEs were separated into three fractions (aliphatic, ketone, and polar) using silica gel column chromatography. The F1 (aliphatic) fraction was obtained by pipetting the sample in 1 ml of hexane into a Pasteur pipette column half-filled with DCM-rinsed silica gel that had been activated at 100 ^{o}C for >24 hours. An additional $\sim$3 ml of hexane was pipetted onto the column to elute the aliphatic fraction. This procedure was repeated using DCM and MeOH to separate the F2 (ketone) and F3 (polar) fractions, respectively. The F1 and F2 fractions were evaporated and transferred to 2 ml vials using DCM. These were then evaporated and brought up in hexane (F1) and toluene (F2) for analysis by gas chromatograph. At the Lamont-Doherty Earth Observatory, n-alkanes (F1) were analyzed using an Agilent gas chromatograph with a mass selective detector (GC-MSD) and alkenones (F2) were analyzed with a Thermo gas chromatograph with a flame ionization detector (GC-FID). TLEs from sonication and ASE extractions were analyzed separately (see below). Total n-alkane concentrations in a sample were obtained by summing the concentrations of each molecule determined in the sonication and ASE extracts. Alkenone concentrations in the ASE extracted fraction of the samples were found to be below the detection limit and only sonication extractions were used for analysis.

The GC-MSD was run with a multi-mode inlet using a DB5 column. One μl of sample was injected and the oven was held at 60 ^{o}C for 1.5 min. The temperature was ramped to 150 ^{o}C at 15 ^{o}C/min and then to 320 ^{o}C at 4 ^{o}C/min followed by a 10-minute hold. Chromatograms were quantified using Chemstation software. The Thermo Trace GC Ultra GC-FID was run using a PTV injector with a 2 mm i.d. silicosteel liner and a 60 m x 0.250 mm i.d. DB1 column with a stationary phase thickness of 0.1 μm and a 10 m x 0.250 mm non-polar retention gap. One μl of sample was injected, after which, the oven was held at 90 ^{o}C for 1.5 min, raised to 250 ^{o}C at 25

^{o}C/min, then raised to 313 ^{o}C at 1 ^{o}C/min and finally raised to 320 ^{o}C at 10 ^{o}C/min and held for 20 min. To quantify alkenone concentrations, we integrated the chromatograms from the F2 fraction using ChromQuest software.

We analyzed an *n*-alkane drift, a mixture of C_8–C_{40} *n*-alkanes containing the 5α-androstane standard, along with the F1 fractions of the samples. This *n*-alkane drift is used to calculate a response factor for each *n*-alkane homologue relative to 5α-androstane. We multiply the area ratio of each *n*-alkane molecule to 5α-androstane by that molecules response factor to obtain the amount ratio of each *n*-alkane molecule relative to the 5α-androstane standard added to that sample. F2 fractions of samples were analyzed with a stearyl stearate standard contained within the recovery standard added to each sample. The amount ratio of alkenone molecules is determined by dividing the area of each alkenone molecule peak by the area of the stearyl stearate standard. Concentrations are calculated by multiplying the amount ratio of each molecule by the amount of the respective standard added to the sample and dividing by the sample weight (Table C.1).

We report C_{12}–C_{35} *n*-alkane concentrations as these were the molecules with concentrations high enough to reliably quantify (Table C.1). We use these concentrations to calculate the *n*-alkane parameters used in the analysis (Table C.3). The carbon preference index (CPI) is calculated by dividing the summed concentrations of odd chain-length *n*-alkanes by the summed concentrations of even chain-length *n*-alkanes between chain lengths of 26–35 ($\sum C_{\text{odd,27–35}}$ / $\sum C_{\text{even,26–34}}$). The alkane distribution index (ADI), defined by Rabinowitz et al. [2017], is calculated as (C_{27}+C_{31})/(C_{28}+C_{29}+C_{30}). CPI is repeatable to <1.5% and ADI is repeatable to <1% (1s) [Rabinowitz et al., 2017]. We calculate the alkenone concentration by adding the concentrations of the measured C_{37} alkenone molecules (MK37:3 and MK37:2). $U^{k'}_{37}$ values are determined as (MK37:2)/(MK37:2+MK37:3) (Table C.1). Alkenone concentrations are repeatable to 4.1% and $U^{k'}_{37}$ values are repeatable to 0.0033 (1s) [Rabinowitz et al., 2017].

C.1.3 Total organic carbon

After the TLE was extracted from each sample, about one gram of sediment was set aside to measure total organic carbon (TOC). The dried sediment was transferred to a weighed 50 ml centrifuge tube and the tube was weighed again to determine the sample size. About 20 ml of 1 N HCl (1:11 12 N HCl:ultra-pure distilled water) was added to each tube to dissolve any carbonate.

The tubes were shaken by hand and then using a vortex mixer and allowed to sit for 2 h. Another 20 ml of HCl was then added and the tubes were shaken again and allowed to sit overnight.

Tubes were then filled the rest of the way with ultra-pure distilled water and centrifuged for 15 min. The supernatant was carefully decanted and the rinsing procedure was repeated until the pH of the liquid after centrifugation was about equal to the rinse water, typically six rinses (after the third rinse, distilled water from the tap was used). The pellets at the bottom of the vials were then freeze-dried for 1 day. Tubes were again weighed to determine the amount of sample lost during the decarbonation procedure. Small amounts of sample (10–50 mg) were weighed into aluminum boats and TOC was measured on a Costech Elemental Analyzer. Because the samples have low organic carbon concentrations, TOC was measured at the H8 sensitivity setting on the EAs thermal conductivity detector (Table C.1). Uncertainty in TOC values is ∼4.04% based upon replicate analysis of 15 samples.

C.1.4 Calculation of fraction reacted

To determine whether thermal alteration has occurred, we compare JFAST biomarker concentrations to the biomarker concentrations of undeformed sediments in samples from corresponding sedimentary units in the reference core. Samples were correlated to sedimentary units at Site 436 using the trace element stratigraphy developed by Rabinowitz et al. [2015]. To calculate the biomarker reaction, the fraction remaining (r) was determined by dividing the alkenone concentration, $U^{k'}_{37}$ value, CPI or ADI of the JFAST sample by corresponding biomarker parameter values in the protolith unit measured at Site 436. For each JFAST sample, r values were calculated with respect to each sample in the correlated Site 436 unit. The range of these fraction remaining values are plotted in Figure 4.2 as box plots with the median value of the fraction remaining indicated by the vertical line, the boxes corresponding to the quartiles (Q_1=25th and Q_3=75th percentiles) and the whiskers to values lying ∼2.7σ from the median. Outliers, plotted as individual data points in Figure 4.2 are values that are less than Q_1–1.5*(Q_3–Q_1) or greater than Q_3+1.5*(Q_3–Q_1).

C.2 Supplementary Text

C.2.1 JFAST Stratigraphy

The lithostratigraphy of the JFAST core was described in the JFAST Science Party Report

[Chester et al., 2012] and refined through a chemostratigraphic analysis [Rabinowitz et al., 2015]. Here, we summarize the stratigraphy presented by Rabinowitz et al. [2015], which provides the most detailed correlations between JFAST samples and their protolith in the reference core used in this study (Site 436). The shallowest sediments recovered at JFAST are Unit A2 Late Miocene mudstones. Below these, at a depth of ∼690 mbsf, lie Holocene to Late Pliocene Unit A1 diatomaceous silty mudstones. This age inversion suggests a fault between the two units, though core recovery in this interval is insufficient to analyze variations in the thermal maturity of the faulted material. The Unit A1 material persists to a depth of ∼820 mbsf where a <5 m thick layer of Early Miocene Unit C2 pelagic clay, interpreted as the main slip zone of the Tohoku earthquake [Chester et al., 2013, Ujiie et al., 2013, Yang et al., 2013], was recovered. Thrust into this pelagic clay layer is a sliver of Unit A3 mudstone. Below the pelagic clay layer is an inverted sequence of Unit B underlain by Unit A3 and then A2. This series of age inversions implies the presence of faults at ∼824, 825, and 832 mbsf. The deepest sediments in the JFAST core are Unit D partially silicified clay. Here, the 60 Myr age gap is interpreted as another fault at a depth of ∼833 mbsf [Rabinowitz et al., 2015].

C.2.2 Biomarkers at JFAST

Alkenone concentrations (C_{37} total) measured in the JFAST core (Figure C.1A) demonstrate relatively constant values in the top part of the core while concentrations drop and are more variable closer to the plate boundary (at depths $\geq$ 810 mbsf). The alkenone concentration at Site 436 changes over 3 orders of magnitude, with the oldest samples having the lowest alkenone concentration. The oldest sedimentary units (Units C and D) have alkenone concentrations that are below the detection limit. This trend in alkenone concentration is likely dominated by changes in productivity, rather than changes in preservation of alkenone molecules. The low concentrations of middle-late Miocene samples reflect low productivity as the site passed under oligotrophic subtropical gyre waters. Increasing concentrations occurred in the late Miocene as the site entered the more productive western boundary current. Although the changes in concentrations in alkenones throughout Site 436 are large, the concentrations in JFAST samples are only compared to the alkenone concentrations for the corresponding sedimentary unit at Site 436 (Figure C.1B).

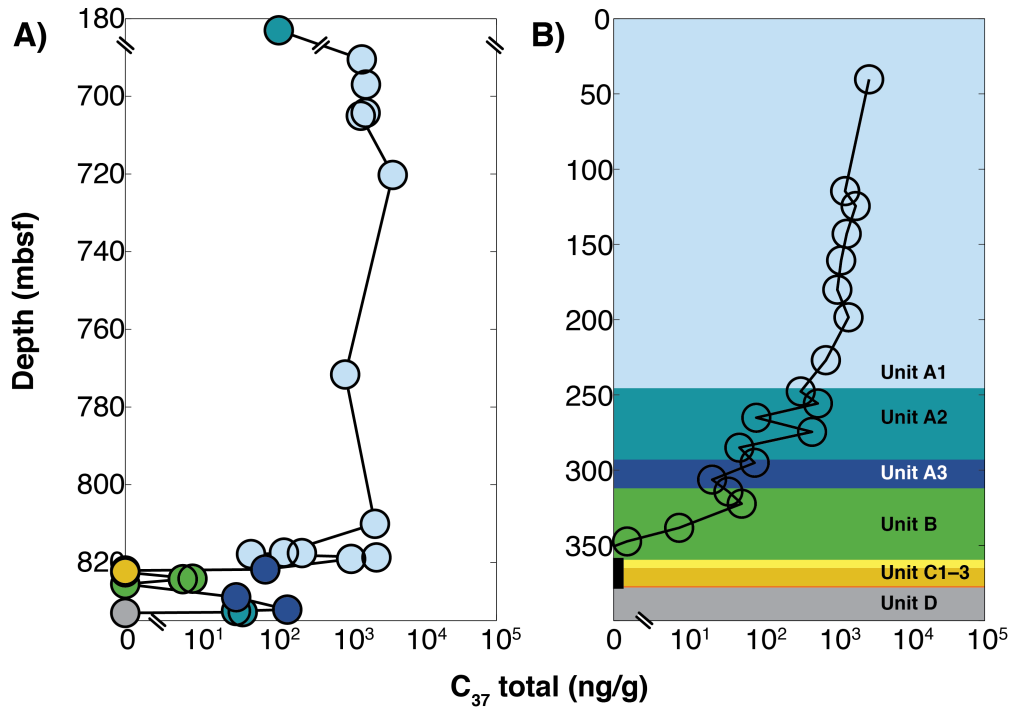

Figure C.1: Alkenone concentrations measured in the JFAST core (A) and in the reference core, Site 436 (B). Colors indicate unit designations, labeled in (B), of the samples [Rabinowitz et al., 2015]. JFAST alkenone concentrations are constant in the shallower sections of the core while concentrations are decreased and more variable near the bottom of the core. In Site 436, concentrations decrease with depth and are below the detection limit in Unit C, represented by the black bar at these depths.

The alkenone unsaturation index ($U^{k'}_{37}$) generally decreases at Site 436 from higher values during the middle Miocene to lower values in the late Miocene (with a few exceptions). Interpreted as sea surface temperature, this trend indicates cooling from middle Miocene to present times. Unlike other biomarker proxies used in this study, $U^{k'}_{37}$ values increase with increasing thermal maturity [Rabinowitz et al., 2017]. We find that $U^{k'}_{37}$ values in Site 436 and the shallower sediments in the JFAST core are similar (if somewhat variable, Figure C.2B), whereas samples from the bottom of the JFAST core near the plate boundary (Figure C.2A) are consistently higher, with four unambiguous thermal anomalies (Figure C.2B).

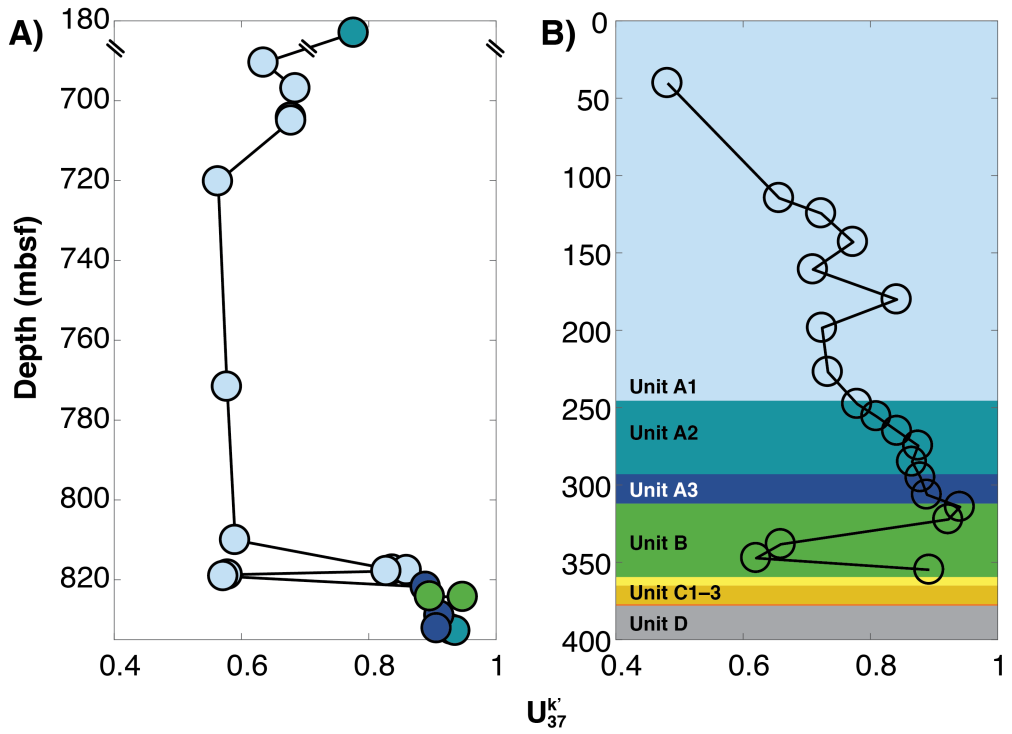

Figure C.2: $U^{k'}_{37}$ measured in the JFAST core (A) and in the reference core, Site 436 (B). Colors correspond to sedimentary units defined by Rabinowitz et al. [2015]. $U^{k'}_{37}$ values are constant near the top of the JFAST core, and near to the lower values observed in corresponding sedimentary units at Site 436. $U^{k'}_{37}$ values increase approaching the plate boundary. Note that $U^{k'}_{37}$ cannot be calculated in Unit C samples due to the lack of alkenones measured in these subunits.

In order to address concerns that local heterogeneities in deposition of organic material and dilution by inorganic sediments (dust, volcanics, terrigenous sediment, carbonate etc.) might yield variable alkenone concentrations, we analyzed the TOC of samples from JFAST and Site 436 (Figure C.3). TOC values at JFAST are constant for most of the Unit A1 sediments and within ∼0.0008 g/g from the range of Site 436 Unit A1 values. The exception to this is at ∼818 mbsf, where the TOC values in Unit A1 JFAST samples drop and are within ∼0.0015 g/g from the minimum values observed in Site 436. The other sedimentary units show similar consistency in TOC with Unit A2 samples at JFAST within 0.0007 g/g from Site 436 values, Unit A3 and B samples at JFAST within 0.0003 g/g from Site 436 values, and Unit C samples at JFAST within 0.0002 g/g from Site 436 values. When the ratio of alkenones to TOC in the JFAST core is considered (Figure C.3C), the major alkenone anomalies remain, indicating that the alkenone anomalies that we observe are larger than any variations caused by differential dilution between JFAST and Site 436.

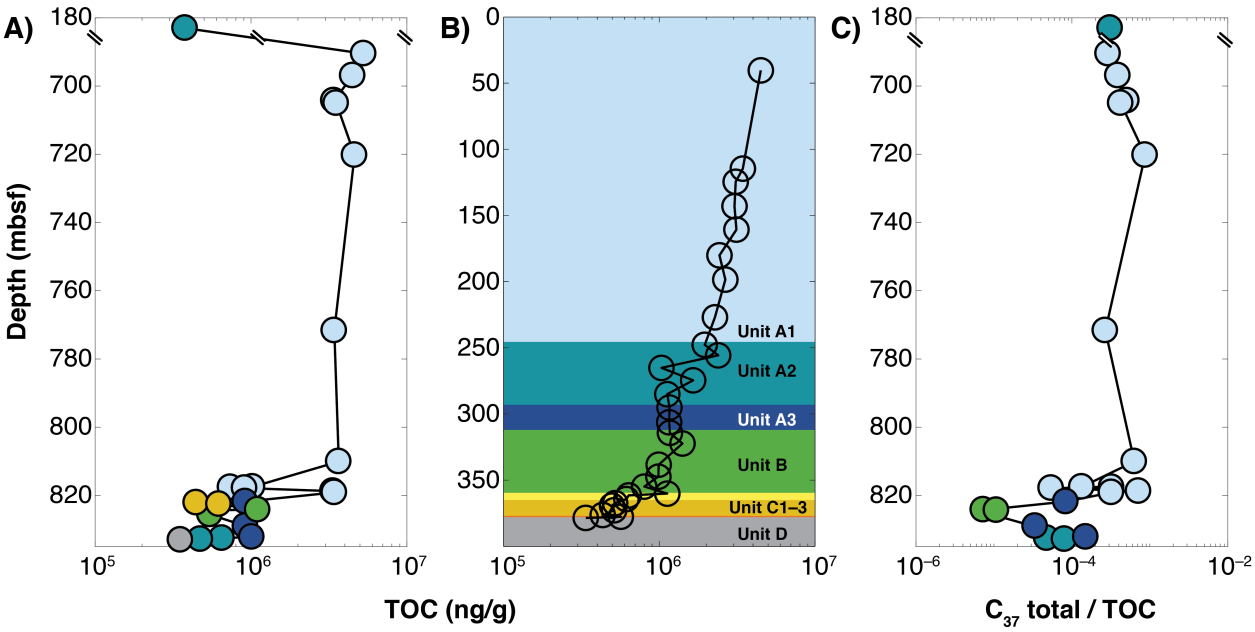

Figure C.3: Total organic carbon (TOC) measured in the JFAST core (A) and in the reference core, Site 436 (B). The alkenone/TOC ratio is also shown for the JFAST core (C). While some variability in TOC is observed in samples near the plate boundary in the JFAST core, anomalies can still be seen in the alkenone/TOC ratios, implying that alkenone anomalies are beyond that which can be explained by depositional effects.

CPI at Site 436 shows no clear trend with age and values fluctuate around a CPI of ∼3. Units A1 and A3 have a larger range of CPI values than the other sedimentary units, with Unit B showing the least variability (Figure C.4B). CPI values in the hanging wall sediments in the JFAST core are relatively constant, with values near the upper end of the range of values for Unit A1 measured in Site 436 (Figure C.4A). While significantly lower CPI values are observed near the plate boundary, the variance in the initial CPI values as measured at Site 436 limits the number of samples that exhibit anomalous values with respect to the whole range of initial CPI (Figure 4.2C). Anomalies with respect to the range of CPI values in the corresponding sedimentary unit at Site 436 are observed at 822 and 824 mbsf.

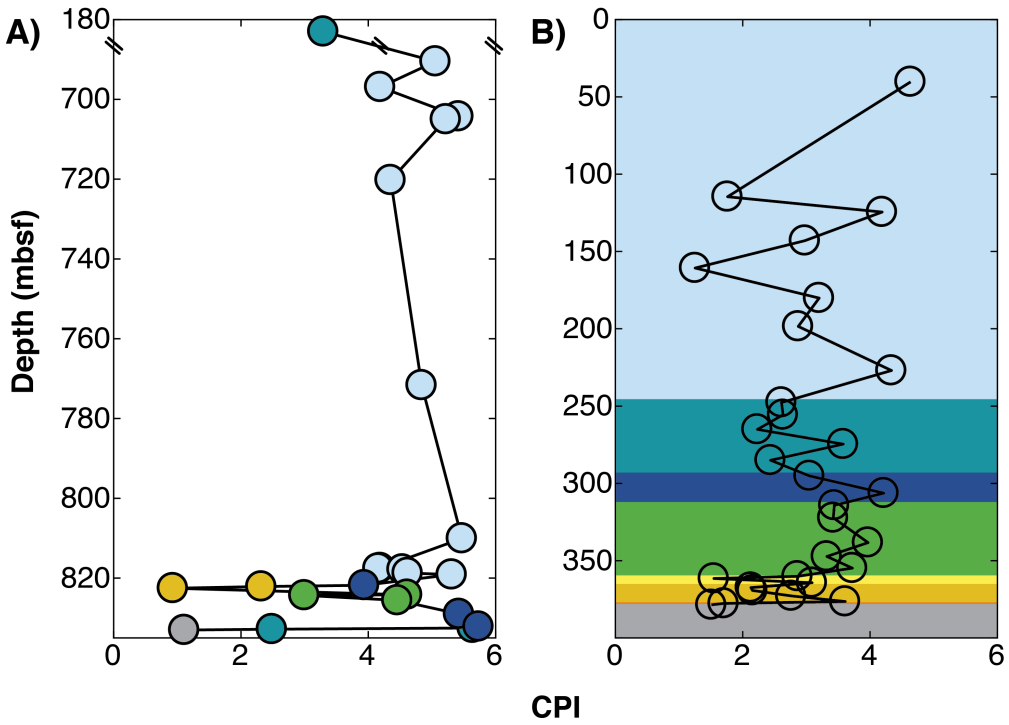

Figure C.4: CPI values measured in the JFAST core (A) and in the reference core, Site 436 (B). CPI at the top of the JFAST core is within the range of observations for corresponding units at Site 436, while values in decrease below those observed in corresponding units at Site 436 in two samples approaching the plate boundary region.

ADI is fairly constant throughout Site 436, with most values lying between an ADI of ∼1 and 1.5 and only Unit A3 showing a significantly larger variation (Figure C.5B). This stability in ADI is also seen in the hanging wall sediments in the JFAST core with lower ADI values approaching the plate boundary (Figure C.5A). Again, an anomaly with respect to the range of possible initial values is seen at 822 mbsf in the pelagic clay. The agreement of both *n*-alkane parameters that a biomarker anomaly exists here supports the conclusion that this is a localized seismic structure within the pelagic clay. However, two other samples analyzed within the previously interpreted décollement layer (including a sample from the mudstone biscuit thrust into this layer) do not show clear evidence for fault heating (Figure 4.2). This observation supports previous suggestions that some of the deformation in this layer has been accommodated through aseismic or distributed slip [Janssen et al., 2015, Kirkpatrick et al., 2015]. Another ADI anomaly is observed at 832 mbsf (Figure C.5a), supporting the interpretation of a thermal anomaly implied by the alkenone anomalies.

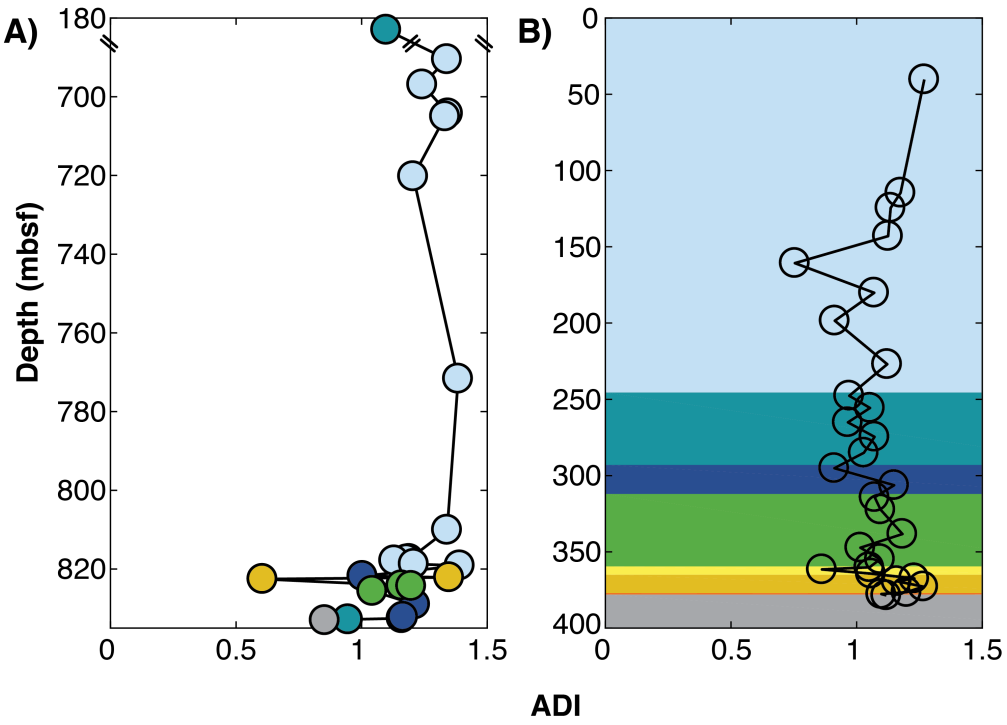

Figure C.5: ADI values measured in the JFAST core (A) and in the reference core, Site 436 (B). ADI values in the JFAST core are constant in the top portion of the core and show more variability and decreased values (beyond those observed at Site 436) in the deeper samples near the plate boundary region.

C.2.3 Analysis of minimum size earthquakes at damage structures in the JFAST core

818 mbsf anomalies

The shallowest biomarker anomalies in the plate-boundary region were observed at ~818 mbsf in three samples between 817.4–817.9 mbsf (PP944, PP945, and PP727). While these samples are relatively closely spaced, they are far enough apart that it is unlikely that they all were heated by slip on the same fault (Figure 4.5b). Candidate structural features in Core 15 are observed at 817.5 mbsf, 817.6 mbsf, and 817.8 mbsf (Figure 4.4).

While the structure at 817.6 mbsf appears more significant, it is too distant (>10 cm) to cause any biomarker anomaly at sample PP944 (817.485 mbsf). Even with multiple slip events, there would be no biomarker anomaly from this feature recorded at this sample. One candidate structure near to PP944 is a high angle crack in the core, which is, indeed, close enough to have caused significant biomarker alteration; however, this feature appears very minor (Figure 4.4) and

is unlikely to have accommodated 50–70 m of coseismic slip, much less to have hosted multiple megathrust earthquakes. Another nearby structure is a near horizontal gouge layer at 817.5 mbsf with a maximum thickness of ∼1.5 cm (Figure 4.4), lying 0–4 cm away from PP944. Such horizontal features have been previously interpreted as resulting from drilling damage to the core rather than being tectonic structures [Keren and Kirkpatrick, 2016b] , however due to its proximity to the reacted sample and the shallow dip of many of the larger features in the core, we consider this the most likely candidate for slip. The thermal anomaly at this sample is best fit by a model with multiple earthquakes with a slip magnitude of ∼40 m. The smallest event that could have contributed to the signal is a 10 m slip earthquake (Figure 4.7a, Table C.6).

The next sample down, PP945, is adjacent to the $\leq$ 2 cm thick structural feature at 817.6 mbsf (0–3 cm away). This structure is at the border of a zone of fragmented core near the bottom of core 15R–1W that could be related to fault damage. The biomarker anomalies here are well fit by 30 m slip events and can be fit with a minimum size event of 10 m slip (Figure 4.7B).

Similarly, PP727 lies within damaged material recovered in 15R–CCW and near (0.5–10 cm) to a more highly comminuted region at 817.8 mbsf with a maximum thickness of ∼9 cm (Figure 4.4). In this case, the maximum thickness of the modeled slipping zone is limited by the minimum temperature of biomarker reaction (Figure 4.5A). While this sample shows biomarker anomalies in alkenone concentration, $U^{k'}_{37}$, and ADI, the lack of an observed anomaly in CPI provides a strong additional constraint in our models. The anomalies observed in this sample are best fit by several 100 m slip events, implying that this sample could represent the cumulative effect of several large megathrust events. The minimum slip magnitude that could contribute to the biomarker anomalies measured in this sample is 30 m (Figure 4.7c, Table C.6). A relatively large amount of displacement here is consistent with the broad damage zone observed at this depth in the core (Figure 4.4).

Pelagic clay anomaly

We sampled three locations within the pelagic clay layer: at 821.8 (mudstone biscuit), 822.12, and 822.55 mbsf. Though the entire layer has been interpreted as having hosted displacement, with multiple features near the top of the recovered pelagic clay interpreted as localization features for seismic slip [Kirkpatrick et al., 2015], only one of the three samples that we analyzed within this layer exhibited unambiguous biomarker anomalies. This indicates that, while the whole pelagic

clay layer is significantly sheared, only certain locations have experienced localized seismic slip. We note that the pelagic clay is not expected to have any alkenones in it, based on the lack of alkenones in the Site 436 pelagic clay units (Figure C.1B), and thus, the lack of alkenones in the pelagic clay samples cannot be interpreted in terms of biomarker thermal maturity. However, both the CPI and ADI show anomalies for sample PP829 (822.55 mbsf). This sample is within a region of structures interpreted as shear localization bands which are ∼0.5–1 cm thick [J. Kirkpatrick, personal communication] and thus, distance from the fault is taken to be 0–10 cm (Figure 4.4). The *n*-alkane anomalies are well fit by a slip magnitude of 70 m (Figure 4.7D). Larger slip magnitudes are precluded because they would require a minimum half-width that is larger than that allowed by the observed thickness range of the shear localization bands in order for temperature rise to remain below 900 ^{o}C. The biomarker anomalies in this sample require earthquakes with slip magnitudes of at least 10 m (Figure 4.7d, Table C.6).

824.3 mbsf anomaly

Core 18 exhibits a significant amount of apparent damage [Figure 4.4 Keren and Kirkpatrick, 2016b,a] with few obvious localization features. This damage has been interpreted as a combination of damage induced by core recovery and tectonic damage related to the damage zone focused around the pelagic clay layer [Keren and Kirkpatrick, 2016a]. There is a stratigraphic inversion above this core between the pelagic clay unit and the underlying mudstone unit [Rabinowitz et al., 2015] and both observations together imply a major fault below the pelagic clay layer. Sample PP730 lies within a significantly brecciated section of the core. While the brecciation in this core is extensive, a zone of elevated damage is about 4 cm thick (Figure 4.4). The sample was taken from ∼4 cm away from this highly comminuted band, but could be closer (∼1 cm) to a slip zone if the entire damage zone is considered. This sample is well fit by 40 m slip events and requires earthquakes with a minimum slip magnitude of 30 m (Figure 4.7E, Table C.6).

825.6 mbsf anomaly

The biomarker anomaly observed at 825.6 mbsf in sample PP948 is found in the core catcher section of Core 18. This sample is found in a heavily brecciated section of the core, right above a stratigraphic inversion interpreted to be a fault by Rabinowitz et al. [2015], and is likely to be

immediately adjacent to (or even within) the fault (Figure 4.4). The implication that this sample represents a seismic fault from structural observation is supported by the large amount of alkenone reaction (near complete alkenone destruction), though the lower reaction rates from the n-alkane parameters seem to have generated negligible reaction. Because alkenone concentration is below the quantification limit, constraints on the fraction of alkenones reacted are poor, though the chromatograms qualitatively appear to have lower alkenone concentrations than even the lowest alkenone concentrations observed in the Unit B samples at Site 436. The inability to accurately quantify alkenone concentrations in this sample also prevents us from determining the $U_{37}^{k'}$ value. Due to the relatively poor constraints on the level of biomarker reaction in this sample, we do not model the number of earthquakes that could be hosted on this fault and instead represent the sample with open red symbols in Figsures 4.2 and 4.8.

833 mbsf anomalies

We find that two samples near the mudstone/silicifying clay boundary at ∼833 mbsf [Rabinowitz et al., 2015] exhibit biomarker anomalies. The shallower sample (PP951, 832.515 mbsf) shows anomalies in both alkenone parameters but in neither of the n-alkane parameters. This sample is close to a peak in tectonic damage features [Keren and Kirkpatrick, 2016a], implying the presence of a fault at this depth (Figure 4.4). The biomarker anomalies measured in this sample are best fit by earthquakes of slip magnitude equal to ∼90 m and can be fit by earthquakes with a minimum slip magnitude of 40 m (Figure 4.7F, Table C.6). The deeper sample, PP952, is better constrained through structural observations of the JFAST core (Figure 4.4). This sample was taken ∼1.5 cm away from a very visible contact between late Miocene mudstone and Cretaceous silicifying clay at 832.85 mbsf. This sample is well fit by 100 m slip events and also requires events with a minimum slip magnitude of 40 m (Figure 4.7G, Table C.6).

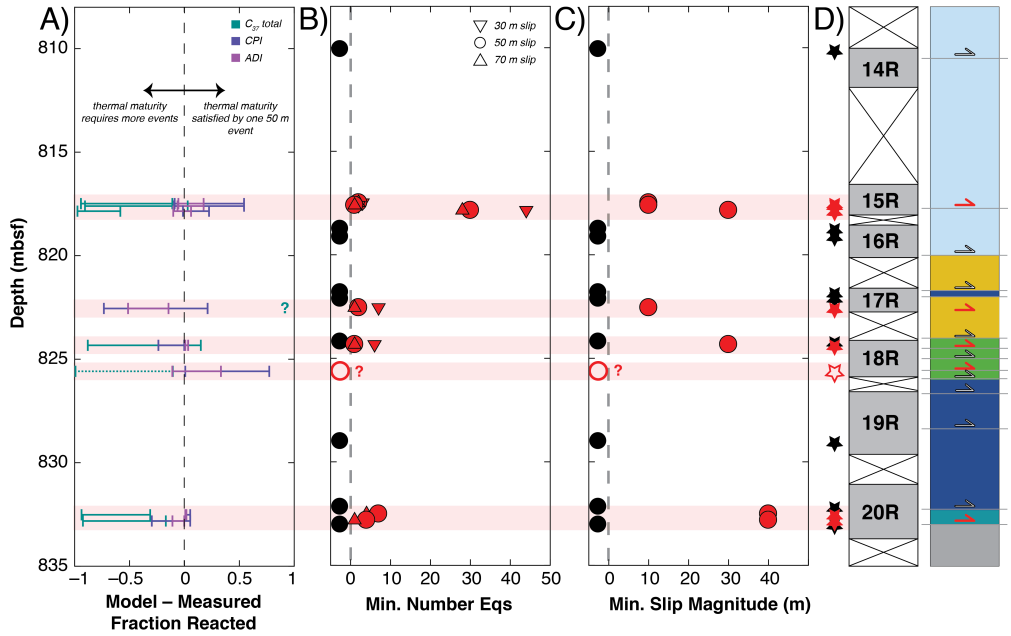

Figure C.6: (A) Difference between modeled fraction reacted values for one Tohoku-sized earthquake with 50 m slip and measured biomarker values (C_{37} total, CPI, and ADI) indicates that all faults with heating anomalies could have hosted at least one event of this size. (B) Minimum number of 30, 50, and 70 m slip events and (C) minimum slip magnitude required to generate the observed biomarker anomalies in JFAST samples given the constraints discussed in the text. Red symbols in all plots indicate features with clear biomarker anomalies. Question mark in (A) indicates the pelagic clay sample, where alkenone concentrations are below the detection limit and cannot be used as a model constraint. Dashed line (A) and hollow symbol (B–D) represent sample PP948, which has alkenone concentrations below the quantification limit and is not modeled.

C.2.4 Temperature rise estimates and implications for dynamic weakening mechanisms

One of the central goals of earthquake mechanics research is to understand the dynamic weakening mechanisms that control seismic slip. This better understanding is essential for improving seismic hazard estimates because the conditions required for dynamic instability likely exert a strong control on where and when an earthquake will nucleate and how far it will propagate. A key parameter to constrain in the search for plausible dynamic weakening mechanisms is the coseismic temperature because many of these mechanisms are thought to be thermally activated [Rice, 2006].

We present a temperature constraint based on the minimum slip magnitude required to reproduce the biomarker anomalies in each sample. Specifically, we report the minimum temperature required for this minimum slip magnitude earthquake (Table C.6). Because this is a lower-bound

limit for the temperature rise on these faults, plausible dynamic weakening mechanisms must be activated by temperatures greater than or equal to these temperature estimates. The average minimum temperature determined in this way is $\sim$279$\pm$43 (1σ) ^{o}C with a range of 233–335 ^{o}C (Table C.6). We emphasize that this minimum temperature estimate is based on the minimum size earthquake that could replicate the observed biomarker anomalies in the allowable displacement. Because it is unlikely that one of the observed faults accommodated all, or even most, of the displacement in this décollement, the faults likely hosted earthquakes with slip magnitudes higher than the minimum values reported here. Accordingly, the temperature experienced during these earthquakes could be significantly higher than the minimum temperatures reported here. An upper bound on the temperature achieved in these faults comes from the fact that there were no observations of clay amorphization or pseudotachylyte. As discussed above, this limits the peak temperature to 900 ^{o}C. We note that temperature estimates on natural faults are best constrained by the application of a wide range of paleoseismic indicators with different temperature sensitivities.

Table C.1: Alkenone data for JFAST and Site 436 samples

Lab Number	Leg	Site	Hole	Core	Section	Section top depth (cm)	Section bottom depth (cm)	Depth (mbsf)	Sample weight (g)	Unit	TOC (g/g sed)	MK37:4	MK37:3	MK37:2	ME36:2	EK38:3	MK38:3
JFAST																	
PP720	343	C0019	E	1R	5W	123	125	183.015	19.273	A2	0.0004	2.1001	26.2058	91.0239	4.6879	9.1395	9.9589
PP721	343	C0019	E	4R	CCW	6	8	690.495	28.574	A1	0.0053	39.9759	563.0189	978.8236	36.3934	219.9228	222.9820
PP722	343	C0019	E	5R	1W	92.5	94.5	696.925	17.512	A1	0.0045	69.1174	551.0687	1198.0076	38.8050	196.7406	252.0910
PP723	343	C0019	E	6R	1W	28	33	704.28	25.657	A1	0.0034	33.7517	555.6819	1169.9877	39.1525	185.2963	218.8703
PP724	343	C0019	E	6R	1W	101	104	705.01	25.795	A1	0.0035	28.9149	479.9542	1011.8231	30.5561	174.5274	179.4830
PP828	343	C0019	E	8R	2W	124	130	720.24	9.207	A1	0.0046	108.8555	1757.3588	2266.7766	93.8340	701.9976	634.0254
PP725	343	C0019	E	10R	2W	65	68	771.66	20.372	A1	0.0034	40.2337	388.9982	531.3059	25.0886	158.9694	167.0463
PP726	343	C0019	E	14R	1W	6	8	810.06	16.029	A1	0.0037	71.2853	947.8397	1364.6959	67.9544	354.5557	350.3793
PP944	343	C0019	E	15R	1W	98.5	100	817.485	14.31	A1	0.0010	1.0759	22.3558	115.0492	2.6211	7.7767	7.7563
PP945	343	C0019	E	15R	1W	110.5	112.5	817.605	9.489	A1	0.0007	1.4470	33.5496	205.7729	4.7661	13.1225	15.1614
PP727	343	C0019	E	15R	CCW	14	15	817.85	25.998	A1	0.0009	0.5856	8.4990	40.8727	0.7944	3.1259	3.3750
PP946	343	C0019	E	16R	1W	23.5	25	818.735	11.705	A1	0.0034	71.1463	1015.2814	1393.1529	78.1365	390.3662	384.5758
PP728	343	C0019	E	16R	1W	62	64	819.12	23.67	A1	0.0034	38.1161	472.7558	630.8098	36.9788	186.1918	189.2892
PP923	343	C0019	E	17R	1W	30	34.5	821.8	9.058	A3	0.0009	1.1805	8.5045	68.5414	1.0053	4.4942	3.2347
PP729	343	C0019	E	17R	1W	62	64	822.12	16.639	C2	0.0004	0	0	0	0	0	0
PP829	343	C0019	E	17R	1W	105	110	822.55	8.386	C2	0.0006	0	0	0	0	0	0
PP947	343	C0019	E	18R	1W	18.5	20	824.185	9.113	B	0.0011	0.0000	0.8387	7.2380	0.1417	0.1178	0.4718
PP730	343	C0019	E	18R	1W	33	35	824.33	17.203	B	0.0006	0.3130	0.3111	5.6562	0.1803	0.2229	0.2744
PP948	343	C0019	E	18R	CCW	9	10.5	825.585	14.266	B	0.0005	0	0	0	0	0	0
PP732	343	C0019	E	19R	3W	25.5	27.5	828.995	21.585	A3	0.0009	0.1564	2.7752	28.4293	0.3719	1.1120	1.2293
PP949	343	C0019	E	20R	1W	116.5	118	832.165	7.39	A3	0.0010	0.7285	14.2323	138.5195	3.2227	6.9959	8.2595
PP951	343	C0019	E	20R	2W	19.5	21	832.515	9.287	A2	0.0007	0.0000	2.1645	28.9172	0.3325	1.2503	1.8875
PP952	343	C0019	E	20R	2W	49.5	51	832.815	11.995	A2	0.0005	0.8524	2.4349	35.7177	0.8211	1.2437	1.7392
PP733	343	C0019	E	20R	2W	70.5	72	833.025	13.297	D	0.0004	0	0	0	0	0	0
Site 436																	
PP925	56	436		5R	3W	80	81.5	40.3	9.872	A1	0.0045	162.6719	1436.1980	1333.0073	228.3233	663.1058	564.0015
PP926	56	436		13R	2W	60	61.5	114.6	8.388	A1	0.0034	29.9437	451.1331	862.8748	77.6841	196.8527	160.3499
PP927	56	436		14R	2W	100	101.5	124.5	8.219	A1	0.0031	20.9317	507.5117	1323.4357	117.2263	215.2820	171.3411
PP928	56	436		16R	2W	59	60.5	142.99	8.265	A1	0.0030	16.6701	314.5049	1069.9089	45.0943	104.2271	113.4497
PP929	56	436		18R	1W	71.5	73	160.715	10.369	A1	0.0031	35.8087	337.4470	825.9387	35.6943	81.5195	159.5621
PP931	56	436		20R	1W	115	116.5	180.15	9.137	A1	0.0024	19.2056	163.9346	870.5108	36.4279	81.9338	116.2451
PP932	56	436		22R	1W	47.5	49	198.475	9.075	A1	0.0027	16.0285	404.5671	1062.4483	40.2050	141.4354	176.6481
PP933	56	436		25R	2W	50	51.5	227	8.591	A1	0.0023	8.4171	193.9121	533.1510	18.8735	82.7572	76.6170
PP934	56	436		27R	2W	70	71.5	247.7	9.139	A2	0.0020	2.8202	73.3607	259.1299	8.9997	1.8683	24.9603
PP935	56	436		28R	1W	68	69.5	255.68	6.003	A2	0.0024	8.6560	107.7087	457.6576	16.4525	42.4903	52.8820
PP936	56	436		29R	1W	61	62.5	265.11	11.292	A2	0.0010	0.8857	13.2093	70.4537	2.0067	4.2005	5.0282
PP937	56	436		30R	1W	62	63.5	274.62	14.515	A2	0.0017	1.4323	58.9941	413.4896	4.4683	23.8818	23.4917
PP938	56	436		31R	2W	60	61.5	285.05	8.382	A2	0.0011	1.7472	6.6740	42.9637	1.1364	2.0883	1.8050
PP939	56	436		32R	2W	68.5	70	295.185	6.294	A3	0.0012	0.8355	9.6424	69.9348	1.7037	3.3948	3.6213
PP941	56	436		33R	3W	83	84.5	306.33	7.508	A3	0.0012	0.6214	2.3638	18.9170	0.9517	0.5713	0.9636
PP942	56	436		34R	2W	72.5	74	314.225	8.111	A3	0.0012	2.5629	2.0910	33.2420	0.7344	2.4201	0.6567
PP943	56	436		35R	1W	78.5	80	322.285	9.04	B	0.0014	0.4175	4.1315	49.2048	1.7335	1.1863	1.9819
PP886	56	436		36R	6W	38.5	42.5	338.335	16.546	B	0.0010	0.4570	2.6042	5.0419	0.0767	0.4842	0.3641
PP887	56	436		37R	5W	80	84	347.3	17.231	B	0.0010	0.0693	0.5770	0.9442	0.1610	0.0673	0.0534
PP888	56	436		38R	4W	40	44	354.85	29.714	B	0.0008	0.0617	0.0647	0.5380	0.0810	0.3950	0.1473
PP889	56	436		39R	1W	65	69	360.15	24.617	C1	0.0011	0	0	0	0	0	0
PP890	56	436		39R	2W	55	59	361.55	24.945	C1	0.0006	0	0	0	0	0	0
PP891	56	436		39R	4W	30	34	364.3	31.294	C1	0.0006	0	0	0	0	0	0
PP892	56	436		39R	6W	56	60	367.46	45.917	C2	0.0005	0	0	0	0	0	0
PP893	56	436		40R	1W	30	34	369.3	38.375	C2	0.0005	0	0	0	0	0	0
PP894	56	436		40R	3W	82	86	372.82	44.831	C2	0.0005	0	0	0	0	0	0
PP895	56	436		40R	6W	54	58	376.44	34.999	C2	0.0004	0	0	0	0	0	0
PP896	56	436		40R	CCW	8	12	377.68	28.318	C3	0.0006	0	0	0	0	0	0
PP897	56	436		41R	1W	3	7	378.57	29.541	C3	0.0003	0	0	0	0	0	0

Table C.2: Continuation of Table C.1

Lab Number	EK38:2	MK38:2	MK39:3	MK39:2
JFAST				
PP720	55.7835	22.1006	1.0067	7.4286
PP721	702.1187	278.4936	41.0380	112.8381
PP722	872.1268	343.7693	86.7543	161.7983
PP723	819.0167	324.0424	51.5121	144.0025
PP724	712.9036	290.5757	32.6634	114.8086
PP828	1781.1263	681.0920	122.0057	298.7663
PP725	429.1594	160.3440	33.7200	72.9651
PP726	927.3435	373.6232	66.3317	142.7280
PP944	63.7020	30.5458	0.8643	8.7820
PP945	115.1891	56.3427	1.7263	14.7955
PP727	23.8045	10.8240	0.4698	3.5532
PP946	918.0432	407.5236	76.4404	140.7377
PP728	461.6152	176.1561	36.4264	72.5595
PP923	41.8537	17.8113	0	0
PP729	0	0	0	0
PP829	0	0	0	0
PP947	4.7548	2.4420	0	0.8755
PP730	3.3385	1.5085	0.2832	0.8146
PP948	0	0	0	0
PP732	17.5808	6.9480	0	2.4247
PP949	80.0473	34.3686	2.7765	13.7285
PP951	15.8648	8.7985	0	2.3318
PP952	18.7040	10.2126	0	2.5334
PP733	0	0	0	0
Site 436				
PP925	1014.8341	322.9882	119.0940	158.8803
PP926	565.9888	216.0962	30.1651	85.8668
PP927	835.4166	303.3996	40.7721	117.7064
PP928	680.9364	255.9745	14.2228	100.1301
PP929	594.3459	175.0562	16.2540	81.9529
PP931	529.4396	168.9354	15.0095	63.5085
PP932	713.5029	263.9113	20.4710	106.8870
PP933	362.4736	142.1631	12.1101	56.1210
PP934	181.1664	61.3111	3.8357	24.6250
PP935	296.3859	110.2014	5.8491	41.9349
PP936	43.8786	17.1053	0.5385	6.2084
PP937	273.5047	100.1350	5.5587	39.9635
PP938	23.3930	10.7519	0.0000	3.3407
PP939	38.5031	18.3865	0.0000	5.4865
PP941	10.8061	5.6303	0.0000	2.2553
PP942	19.9847	8.9982	1.9649	3.3318
PP943	30.7776	14.1760	0.0000	4.8861
PP886	1.5177	3.1912	0.4750	0.2088
PP887	0.4858	0.5548	0.0554	0.1166
PP888	0.0480	0.1148	0.4816	0.2437
PP889	0	0	0	0
PP890	0	0	0	0
PP891	0	0	0	0
PP892	0	0	0	0
PP893	0	0	0	0
PP894	0	0	0	0
PP895	0	0	0	0
PP896	0	0	0	0
PP897	0	0	0	0

Table C.3: *n*-Alkane data for JFAST and Site 436 samples

Lab Number	Leg	Site	Hole	Core	Section	Section top depth (cm)	Section bottom depth (cm)	Depth (mbsf)	Sample weight (g)	Unit	C12-alkane	C13-alkane	C14-alkane	C15-alkane	C16-alkane	C17-alkane
JFAST																
PP720	343	C0019	E	1R	5W	123	125	183.015	19.273	A2	1.9575	2.1531	0.4543	0.5567	6.6757	13.1056
PP721	343	C0019	E	4R	CCW	6	8	690.495	28.574	A1	1.0963	3.8695	30.1363	44.0580	59.8764	47.0727
PP722	343	C0019	E	5R	1W	92.5	94.5	696.925	17.512	A1	1.0217	1.9035	8.7934	52.9521	136.3391	126.6403
PP723	343	C0019	E	6R	1W	28	33	704.28	25.657	A1	0.0000	1.0270	4.1746	24.7633	75.8822	69.3441
PP724	343	C0019	E	6R	1W	101	104	705.01	25.795	A1	0.1338	0.9217	1.5303	11.9159	57.3335	74.6805
PP828	343	C0019	E	8R	2W	124	130	720.24	9.207	A1	0.0000	2.7973	23.9492	116.2073	293.4807	303.3633
PP725	343	C0019	E	10R	2W	65	68	771.66	20.372	A1	0.1446	1.1251	1.4332	14.8129	76.7212	89.9871
PP726	343	C0019	E	14R	1W	6	8	810.06	16.029	A1	0.2603	1.1674	1.6932	13.5958	82.7337	93.8209
PP944	343	C0019	E	15R	1W	98.5	100	817.485	14.31	A1	5.0920	5.7419	3.1447	0.1656	3.7387	13.7346
PP945	343	C0019	E	15R	1W	110.5	112.5	817.605	9.489	A1	5.1747	7.7433	3.7388	0.4926	2.3887	15.9110
PP727	343	C0019	E	15R	CCW	14	15	817.85	25.998	A1	0.1867	1.2066	0.2860	1.3309	15.1163	25.0584
PP946	343	C0019	E	16R	1W	23.5	25	818.735	11.705	A1	0.0000	0.9498	0.6700	0.6546	5.4914	20.3131
PP728	343	C0019	E	16R	1W	62	64	819.12	23.67	A1	0.1612	2.2248	8.2283	55.8009	173.1404	147.6714
PP923	343	C0019	E	17R	1W	30	34.5	821.8	9.058	A3	0.0000	3.4641	0.0000	2.7594	33.0373	43.7357
PP729	343	C0019	E	17R	1W	62	64	822.12	16.639	C2	0.0000	1.1322	0.9491	7.7378	62.8536	85.6743
PP829	343	C0019	E	17R	1W	105	110	822.55	8.386	C2	0.3129	1.8538	2.8181	16.0411	70.8450	128.9006
PP947	343	C0019	E	18R	1W	18.5	20	824.185	9.113	B	1.4096	2.2570	1.0510	0.5014	8.2053	23.6868
PP730	343	C0019	E	18R	1W	33	35	824.33	17.203	B	0.1137	4.3832	0.3747	1.4167	16.9795	29.9249
PP948	343	C0019	E	18R	CCW	9	10.5	825.585	14.266	B	6.4202	8.8184	8.5549	13.7041	22.0400	12.5428
PP732	343	C0019	E	19R	3W	25.5	27.5	828.995	21.585	A3	0.9080	0.9971	2.7077	25.3390	197.1914	202.3016
PP949	343	C0019	E	20R	1W	116.5	118	832.165	7.39	A3	4.9352	6.5114	4.2056	0.4059	4.0303	17.3644
PP951	343	C0019	E	20R	2W	19.5	21	832.515	9.287	A2	0.0000	4.1380	2.1327	0.2638	4.1605	9.9537
PP952	343	C0019	E	20R	2W	49.5	51	832.815	11.995	A2	3.0012	3.2020	0.2528	1.9656	2.8072	10.4536
PP733	343	C0019	E	20R	2W	70.5	72	833.025	13.297	D	0.0000	2.0173	0.5182	4.1002	43.6115	84.3214
Site 436																
PP925	56	436		5R	3W	80	81.5	40.3	9.872	A1	0	1.8955	1.9671	3.6912	9.8661	28.5893
PP926	56	436		13R	2W	60	61.5	114.6	8.388	A1	0	2.1167	12.7789	86.1882	297.7495	601.6554
PP927	56	436		14R	2W	100	101.5	124.5	8.219	A1	0	3.1630	3.9023	7.0319	20.0788	45.5700
PP928	56	436		16R	2W	59	60.5	142.99	8.265	A1	1.8218	2.1402	3.0719	5.5807	28.8422	174.1972
PP929	56	436		18R	1W	71.5	73	160.715	10.369	A1	0.0000	2.6626	9.5301	243.4171	1958.2513	6476.1671
PP931	56	436		20R	1W	115	116.5	180.15	9.137	A1	1.3139	3.1893	2.1454	8.8073	323.4493	1713.9709
PP932	56	436		22R	1W	47.5	49	198.475	9.075	A1	2.6666	1.6594	2.7706	9.2516	364.0334	1876.1992
PP933	56	436		25R	2W	50	51.5	227	8.591	A1	0.0000	2.8958	5.7028	690.8886	7143.2180	22192.7051
PP934	56	436		27R	2W	70	71.5	247.7	9.139	A2	1.9115	3.0475	1.6230	4.2542	244.3531	1909.0520
PP935	56	436		28R	1W	68	69.5	255.68	6.003	A2	1.5057	2.0227	2.8478	129.8094	1962.4377	7250.7715
PP936	56	436		29R	1W	61	62.5	265.11	11.292	A2	0.0000	3.6440	2.3203	9.5807	421.0583	2237.6927
PP937	56	436		30R	1W	62	63.5	274.62	14.515	A2	0.2697	1.4854	1.3653	35.6896	563.5413	2025.5148
PP938	56	436		31R	2W	60	61.5	285.05	8.382	A2	0.6850	4.0089	2.0036	15.2962	427.9691	2896.0057
PP939	56	436		32R	2W	68.5	70	295.185	6.294	A3	3.7438	3.6684	2.0568	8.3581	300.5950	1904.5580
PP941	56	436		33R	3W	83	84.5	306.33	7.508	A3	0.5090	0.7502	1.4838	12.9971	139.2100	424.2761
PP942	56	436		34R	2W	72.5	74	314.225	8.111	A3	0.4126	3.1187	0.6464	2.9340	114.7289	1233.1606
PP943	56	436		35R	1W	78.5	80	322.285	9.04	B	3.9370	3.5542	1.7207	22.0027	634.9785	3789.5225
PP886	56	436		36R	6W	38.5	42.5	338.335	16.546	B	0.2168	0.4043	0.5750	17.8477	154.3355	464.0607
PP887	56	436		37R	5W	80	84	347.3	17.231	B	0.9979	3.8854	24.7842	61.3784	155.8338	230.9325
PP888	56	436		38R	4W	40	44	354.85	29.714	B	0.0885	0.1926	0.4852	4.3309	35.3000	101.1221
PP889	56	436		39R	1W	65	69	360.15	24.617	C1	0.4125	0.7050	0.4010	3.6668	54.5148	190.0579
PP890	56	436		39R	2W	55	59	361.55	24.945	C1	0.3478	1.0439	5.8769	17.6996	51.9926	77.4371
PP891	56	436		39R	4W	30	34	364.3	31.294	C1	0.1341	0.2846	1.2115	8.3348	27.9695	48.2808
PP892	56	436		39R	6W	56	60	367.46	45.917	C2	0.0548	0.1383	0.3541	2.0436	10.5887	25.7513
PP893	56	436		40R	1W	30	34	369.3	38.375	C2	0.0800	0.1537	0.4600	2.8761	16.9171	44.2693
PP894	56	436		40R	3W	82	86	372.82	44.831	C2	0.3135	1.2633	3.9525	9.1050	25.7798	26.4275
PP895	56	436		40R	6W	54	58	376.44	34.999	C2	0.1002	0.1582	0.2301	5.5497	55.7738	175.5396
PP896	56	436		40R	CCW	8	12	377.68	28.318	C3	0.0685	0.0963	0.7529	7.2296	40.9333	70.1356
PP897	56	436		41R	1W	3	7	378.57	29.541	C3	0.0474	0.1882	0.9945	30.6325	204.3477	661.7252

Table C.4: Continuation of Table C.3

Lab Number	C18-alkane	C19-alkane	C20-alkane	C21-alkane	C22-alkane	C23-alkane	C24-alkane	C25-alkane	C26-alkane	C27-alkane	C28-alkane	C29-alkane	C30-alkane	C31-alkane
JFAST														
PP720	42.8544	47.7401	53.3646	76.3052	37.4425	25.8332	19.3986	15.7719	8.1582	14.7822	3.9934	19.7089	2.0654	13.5176
PP721	59.4627	56.0243	50.5366	79.6910	52.4613	85.6781	47.5593	100.2991	43.0279	153.8259	39.2936	207.2644	27.3294	213.1926
PP722	145.9002	126.9430	111.5850	160.5629	103.4272	126.7923	78.1944	130.8834	62.9475	183.7953	61.8035	249.6262	36.2804	247.9107
PP723	83.2890	70.2011	60.1650	90.8649	56.1505	76.5951	42.2633	85.8884	36.4826	133.2888	31.2040	181.2090	20.1496	179.2772
PP724	84.9120	75.3791	65.7896	90.6611	53.6399	73.9807	40.7582	78.7859	33.1669	124.0637	29.3082	159.6690	19.3067	153.4737
PP828	285.2142	212.3605	172.5810	226.3717	109.3086	113.8926	63.7850	113.0267	47.5040	170.5933	74.5119	237.1619	28.5571	239.5015
PP725	94.4925	78.3847	68.3957	103.2003	65.8890	106.3687	54.9687	125.3014	51.5327	205.9494	47.9512	258.2967	36.7836	268.8639
PP726	101.0591	76.4896	62.9156	98.0859	53.9674	66.2379	37.5375	75.8548	32.3046	118.2863	30.9680	175.1394	24.0359	190.1693
PP944	39.1686	46.6960	43.5897	62.2181	39.3909	37.6037	21.9104	23.7584	11.6835	26.4908	9.5308	42.8127	4.9342	41.6401
PP945	45.0139	47.4588	44.1162	59.6195	36.0777	38.1353	22.1693	26.6612	13.3287	32.6600	12.4043	57.8809	8.1031	59.8157
PP727	50.4770	52.1116	45.9807	64.3484	31.6908	24.9114	16.0943	18.3192	8.1786	18.7833	5.7960	32.3967	3.5343	28.3712
PP946	35.3574	34.7150	29.6092	46.2278	33.3818	51.1790	29.6315	65.1976	27.6920	113.4483	52.5591	171.9745	21.9159	184.2357
PP728	209.8395	186.0525	155.7254	219.7269	133.8483	160.2439	88.3863	166.0136	66.1340	219.2203	50.7864	283.7814	31.7878	290.2566
PP923	63.1212	53.9891	45.1982	56.1378	31.1306	32.6288	17.6435	24.4168	8.4511	21.6996	4.4909	25.7166	1.9779	10.6065
PP729	115.3233	110.3552	93.5470	105.7323	55.0546	37.4842	19.9206	13.5396	5.2016	6.0604	2.3336	6.4190	1.6946	8.0279
PP829	173.2492	141.8566	144.1026	175.0913	71.9401	52.8279	54.8671	78.2272	89.7959	107.2010	103.5424	97.7036	73.9106	59.4622
PP947	55.2072	60.5654	49.1040	52.6730	33.8081	30.5351	17.6908	16.5093	6.9506	17.1622	5.0188	31.0467	3.6571	28.8635
PP730	90.6326	89.5320	89.8929	160.1150	76.0058	65.1089	39.3733	34.6775	16.1149	25.4555	7.7887	31.8048	4.6118	27.4804
PP948	20.0024	24.7769	25.6333	39.4183	26.6429	31.1537	18.1747	20.2917	9.4656	22.2621	4.6906	31.5220	2.5339	18.1466
PP732	169.0690	112.5004	89.2729	115.9469	50.4091	39.7395	23.8487	30.8702	13.0079	32.9892	8.9761	59.9709	5.6396	57.4956
PP949	39.8861	41.0213	44.6203	59.0416	43.8887	42.7251	22.2272	25.4505	10.6500	29.6197	8.0104	56.0673	4.5841	50.3933
PP951	26.4438	30.5137	35.9732	56.9601	39.1380	43.7038	22.8754	24.0532	8.7260	25.1929	6.3956	43.9565	3.8636	37.6900
PP952	28.4804	28.8385	26.0876	39.4200	24.0686	23.5093	13.7057	14.3964	9.1369	19.6744	11.5115	37.8296	11.1761	37.5795
PP733	178.5326	166.7092	161.9282	166.1088	97.9497	59.1013	36.6344	26.9076	10.5516	8.5406	5.0679	7.3332	3.6802	5.1867
Site 436														
PP925	45.3868	51.6654	42.3781	70.1011	58.7278	111.1963	64.3799	147.6479	59.7132	224.4618	63.5376	272.3245	31.5475	241.8993
PP926	940.6476	1079.3001	1017.1238	975.2645	697.0319	506.8261	355.2411	255.2235	135.1899	144.7034	52.5810	135.9454	27.2427	108.7943
PP927	68.7163	62.3275	46.0604	52.4354	35.4440	42.3261	29.8017	46.2275	18.6567	61.3259	13.9424	71.2586	6.8481	43.1778
PP928	265.7227	194.8702	105.7496	91.1886	61.2157	63.1157	42.1405	70.5182	30.3849	81.0542	22.4675	81.7663	12.5822	50.3870
PP929	8948.0007	8233.2088	4222.6708	1915.1326	769.0396	400.7414	308.5673	478.2054	216.6371	209.2354	181.5180	257.8526	145.8961	232.2020
PP931	2772.0553	2302.6031	953.6279	394.3667	139.0753	73.3306	37.2242	49.2934	21.2149	46.8017	13.0265	55.6814	6.4938	33.6520
PP932	2753.8538	2169.5090	864.0504	373.6555	146.2388	94.8830	55.1632	79.1383	30.6210	72.5654	35.3960	94.0327	9.5023	54.2963
PP933	24413.4472	16932.1664	5946.5297	1738.3309	413.3107	136.3176	69.4936	71.2026	29.3241	76.1609	22.4710	109.0207	11.4670	84.1888
PP934	3340.8467	2693.2534	1077.6703	430.6602	158.1114	96.1377	60.4865	69.0417	32.3304	57.9676	24.8912	82.2234	16.4656	61.9735
PP935	9754.5720	7069.7581	2581.4904	875.3825	259.7513	95.8371	52.3225	57.6285	24.8644	37.2959	15.5052	55.4229	10.7429	48.7211
PP936	3213.5406	2545.8465	1089.7160	449.9123	160.9993	69.3074	38.2151	32.6988	12.2409	18.3518	7.8777	20.5739	2.2588	11.2878
PP937	2638.8213	2002.3654	790.5149	319.9797	116.2097	58.6405	30.2913	40.5212	16.2521	33.9623	10.3166	49.1021	5.9673	36.0890
PP938	5924.4058	5833.7493	2597.7777	994.8339	308.8750	124.9873	62.8282	50.7792	19.6563	25.3337	8.7886	34.3498	5.0127	24.2039
PP939	3206.8992	2626.2317	1056.6021	443.9151	163.6479	88.1647	53.0459	42.9645	18.2095	33.6119	15.2749	52.3008	5.7708	33.2222
PP941	591.6667	478.1965	209.7058	111.6002	48.5766	32.2948	19.1184	18.2653	7.8352	16.9367	5.7173	29.8062	3.7522	28.2129
PP942	3010.2496	3484.7256	1757.9741	720.2361	215.2511	99.2713	52.0445	51.9964	20.4552	38.9926	11.1375	52.9198	4.2554	34.2282
PP943	6245.5606	5140.5166	2065.1370	738.5915	219.6456	92.5853	46.2113	46.4098	17.7677	33.9603	8.8067	41.6563	2.2669	23.7744
PP886	584.2854	530.6279	291.4837	159.2259	65.4752	31.7341	19.4850	20.7328	9.0782	15.2642	5.7982	32.8223	4.7667	36.0319
PP887	215.2738	146.0843	79.7107	53.5741	27.5737	18.6257	11.0870	12.5605	5.3118	9.3239	2.8997	13.7024	1.3875	8.9325
PP888	126.3936	93.7545	50.0847	35.8705	22.9845	22.4919	13.4582	18.4856	8.8000	17.9928	6.5216	33.7394	4.6625	31.1193
PP889	245.9947	192.0218	93.5355	58.8789	31.7156	26.2454	15.8993	17.5768	9.2874	12.7860	5.0549	21.4251	3.1764	18.3818
PP890	93.6385	73.2776	44.2205	38.1100	21.1485	20.2797	14.3612	16.8547	11.2505	14.7203	10.4233	21.8720	11.2539	22.8208
PP891	57.0845	42.9995	30.5563	34.8786	17.2545	18.4635	12.0739	13.7090	7.0322	10.6516	3.9087	18.7673	2.6743	16.1482
PP892	36.2155	30.7211	21.3026	21.1829	11.6503	10.6200	6.8330	6.6702	3.1007	3.3914	1.2965	4.2720	0.8288	4.4749
PP893	58.6860	45.2011	25.2899	20.8950	11.2388	8.4661	5.4826	5.1601	2.0594	2.0199	0.8789	2.7284	0.5954	2.8539
PP894	25.9421	16.8818	10.6228	12.8098	6.3808	5.8844	3.5280	3.2601	1.3590	1.6561	0.5858	2.4204	0.3273	2.5625
PP895	227.1604	204.9469	106.6282	55.1462	21.0339	10.5775	5.5716	6.7262	2.8718	5.1395	1.8379	8.8770	1.3285	9.3022
PP896	87.4019	69.1299	35.5323	24.3451	11.0894	7.1733	5.3174	5.2151	2.1737	2.1689	1.2399	2.6229	1.1100	3.2933
PP897	735.8184	460.0283	150.3375	58.9652	21.2057	11.5703	7.8921	7.8111	3.7023	3.0199	1.8502	3.7702	1.8063	5.2858

Table C.5: Continuation of Table C.3

Lab Number	C32-alkane	C33-alkane	C34-alkane	C35-alkane	pristane	phytane	Sulfur S8
JFAST							
PP720	0.6657	1.9649	0.4336	0.4908	9.1423	25.7168	6176.9237
PP721	13.0190	63.5727	6.9684	17.6794	35.0458	33.0240	6527.9165
PP722	15.6328	76.3048	10.9434	28.1265	105.7446	76.4584	17030.8359
PP723	8.7299	41.7584	3.8957	8.7047	42.7877	49.6657	10333.9948
PP724	9.6840	48.0292	4.6217	16.3032	42.8734	43.2030	15812.7892
PP828	13.2616	65.6147	5.0667	22.0819	205.3150	247.1469	3469.7767
PP725	23.5577	90.8635	18.1435	37.1128	59.6421	51.8765	15954.4822
PP726	13.1925	72.9562	7.2681	33.0918	48.5631	49.8571	10678.6723
PP944	2.5531	11.3909	1.0657	2.3079	7.3622	20.4084	0
PP945	4.9924	15.8608	1.7957	2.7746	6.8416	27.6969	0
PP727	1.3811	7.7323	0.6389	1.3399	15.6927	28.7130	356.4029
PP946	10.9443	61.1486	4.9208	14.4696	17.7555	24.0375	927.9708
PP728	15.0106	83.9783	6.0471	24.5544	83.6269	103.3408	25492.7448
PP923	0	0.7034	0	0	32.3935	53.1958	0
PP729	0.6539	2.6406	0.3538	0.6194	40.9131	45.8878	0
PP829	34.4470	21.2951	9.2341	4.2560	131.4031	179.1065	0
PP947	1.9224	5.8094	0.5669	0.6736	21.0192	47.1480	0
PP730	1.5356	5.9437	0.5291	0.9496	23.2998	57.0352	0
PP948	0.0000	2.4653	0.0000	0.0000	5.5427	15.7231	0
PP732	2.4573	13.7824	0.4572	1.4555	84.9677	85.9072	0
PP949	1.7514	8.5766	0.3673	0.7435	10.3613	24.3418	0
PP951	0.9146	6.0171	0.1674	0.3304	6.4124	19.0032	0
PP952	8.6757	12.5802	4.1372	3.3696	7.7151	20.8435	0
PP733	1.4862	1.7622	1.2758	1.6780	32.7622	63.5166	0
Site 436							
PP925	12.7653	57.9091	7.2408	13.8867	18.6733	22.7192	4005.8878
PP926	13.4255	25.0889	17.4180	18.7247	282.4055	429.7426	149.9443
PP927	1.9718	4.7007	2.0407	1.6026	32.3541	38.2735	3249.7260
PP928	6.3138	10.5908	4.3350	2.7683	66.0148	107.7961	5381.9119
PP929	97.2564	112.7702	180.1114	216.8078	2003.5084	1761.4918	1886.4849
PP931	1.3664	3.7505	1.6108	0	407.9927	399.8643	289.2187
PP932	2.0330	6.8976	1.7667	0	295.8358	372.2303	832.7916
PP933	2.5147	15.8357	0	0	11225.8200	1394.1124	457.0846
PP934	8.6968	17.1650	3.3794	4.4441	198.7461	287.8701	0
PP935	4.8013	13.6739	5.0604	5.4369	767.5546	686.4518	23.9347
PP936	0.6636	1.1770	0	0	259.4943	262.0123	0
PP937	1.5020	5.8322	1.1663	1.0015	221.9388	219.9272	106.6675
PP938	1.4326	3.5084	1.2895	0.7695	291.2159	364.4187	0
PP939	1.3119	4.5354	0	0	379.6594	393.5268	0
PP941	1.2927	4.8847	0.5180	0.7363	147.9037	154.0994	0
PP942	1.4251	3.5460	0.5649	0.4150	226.9465	321.9002	0
PP943	0.6680	1.5956	0	0	509.9154	584.0467	0
PP886	2.5928	9.0430	1.6784	1.7411	196.4813	159.7550	0
PP887	0.4589	1.2907	0.0000	0.1553	124.6429	102.3913	0
PP888	2.2985	7.2185	2.7593	3.1318	58.0356	58.0997	0
PP889	1.6802	4.0275	1.1107	1.4943	79.3738	79.3792	0
PP890	11.4871	14.5149	13.1655	15.1761	42.2084	44.2185	0
PP891	1.2583	3.2680	1.5204	1.8069	26.9980	28.4877	0
PP892	0.5325	1.3507	1.0433	0.9882	15.5085	18.5714	0
PP893	0.3144	0.7630	0.2699	0.5035	24.7610	26.3404	0
PP894	0.1606	0.6218	0.2587	0.1744	15.4205	15.1421	0
PP895	0.6416	2.1759	0.4979	0.4152	58.8031	51.2549	0
PP896	0.7107	1.4339	1.0705	1.2065	38.5937	36.3692	0
PP897	1.3248	2.3887	2.5966	2.5447	143.5956	131.6378	0

Table C.6: Biomarker parameters measured in JFAST and Site 436 samples

Lab Number	Depth (mbsf)	Leg	Site	Hole	Core	Section	Section top depth (cm)	Section bottom depth (cm)	Depth (mbsf)	Unit	C_{37} total (ng/g)	$U^{k'}_{37}$	CPI	ADI
JFAST														
PP720	183.015	343	C0019	E	1R	5W	123	125	183.015	A2	117.23	0.78	3.29	1.10
PP721	690.495	343	C0019	E	4R	CCW	6	8	690.495	A1	1541.84	0.63	5.06	1.34
PP722	696.925	343	C0019	E	5R	1W	92.5	94.5	696.925	A1	1749.08	0.68	4.19	1.24
PP723	704.28	343	C0019	E	6R	1W	28	33	704.28	A1	1725.67	0.68	5.42	1.34
PP724	705.01	343	C0019	E	6R	1W	101	104	705.01	A1	1491.78	0.68	5.22	1.33
PP828	720.24	343	C0019	E	8R	2W	124	130	720.24	A1	4024.14	0.56	4.35	1.21
PP725	771.66	343	C0019	E	10R	2W	65	68	771.66	A1	920.30	0.58	4.84	1.38
PP726	810.06	343	C0019	E	14R	1W	6	8	810.06	A1	2312.54	0.59	5.47	1.34
PP944	817.485	343	C0019	E	15R	1W	98.5	100	817.485	A1	137.40	0.84	4.19	1.19
PP945	817.605	343	C0019	E	15R	1W	110.5	112.5	817.605	A1	239.32	0.86	4.16	1.18
PP727	817.85	343	C0019	E	15R	CCW	14	15	817.85	A1	49.37	0.83	4.54	1.13
PP946	818.735	343	C0019	E	16R	1W	23.5	25	818.735	A1	2408.43	0.58	4.62	1.21
PP728	819.12	343	C0019	E	16R	1W	62	64	819.12	A1	1103.57	0.57	5.31	1.39
PP923	821.8	343	C0019	E	17R	1W	30	34.5	821.8	A3	77.05	0.89	3.94	1.00
PP729	822.12	343	C0019	E	17R	1W	62	64	822.12	C2	0.00	———	2.32	1.35
PP829	822.55	343	C0019	E	17R	1W	105	110	822.55	C2	0.00	———	0.93	0.61
PP947	824.185	343	C0019	E	18R	1W	18.5	20	824.185	B	8.08	0.90	4.61	1.16
PP730	824.33	343	C0019	E	18R	1W	33	35	824.33	B	5.97	0.95	3.00	1.20
PP948	825.585	343	C0019	E	18R	CCW	9	10.5	825.585	B	0.00	———	4.46	1.04
PP732	828.995	343	C0019	E	19R	3W	25.5	27.5	828.995	A3	31.20	0.91	5.43	1.21
PP949	832.165	343	C0019	E	20R	1W	116.5	118	832.165	A3	152.75	0.91	5.73	1.17
PP951	832.515	343	C0019	E	20R	2W	19.5	21	832.515	A2	31.08	0.93	5.64	1.16
PP952	832.815	343	C0019	E	20R	2W	49.5	51	832.815	A2	38.15	0.94	2.49	0.95
PP733	833.025	343	C0019	E	20R	2W	70.5	72	833.025	D	0.00	———	1.11	0.85
Site 436														
PP925	40.3	56	436		5R	3W	80	81.5	40.3	A1	2769.21	0.48	4.64	1.27
PP926	114.6	56	436		13R	2W	60	61.5	114.6	A1	1314.01	0.66	1.76	1.17
PP927	124.5	56	436		14R	2W	100	101.5	124.5	A1	1830.95	0.72	4.19	1.14
PP928	142.99	56	436		16R	2W	59	60.5	142.99	A1	1384.41	0.77	2.98	1.13
PP929	160.715	56	436		18R	1W	71.5	73	160.715	A1	1163.39	0.71	1.25	0.75
PP931	180.15	56	436		20R	1W	115	116.5	180.15	A1	1034.45	0.84	3.20	1.07
PP932	198.475	56	436		22R	1W	47.5	49	198.475	A1	1467.02	0.72	2.87	0.91
PP933	227	56	436		25R	2W	50	51.5	227	A1	727.06	0.73	4.34	1.12
PP934	247.7	56	436		27R	2W	70	71.5	247.7	A2	332.49	0.78	2.61	0.97
PP935	255.68	56	436		28R	1W	68	69.5	255.68	A2	565.37	0.81	2.63	1.05
PP936	265.11	56	436		29R	1W	61	62.5	265.11	A2	83.66	0.84	2.23	0.97
PP937	274.62	56	436		30R	1W	62	63.5	274.62	A2	472.48	0.88	3.58	1.07
PP938	285.05	56	436		31R	2W	60	61.5	285.05	A2	49.64	0.87	2.44	1.03
PP939	295.185	56	436		32R	2W	68.5	70	295.185	A3	79.58	0.88	0.52	0.25
PP941	306.33	56	436		33R	3W	83	84.5	306.33	A3	21.28	0.89	4.22	1.15
PP942	314.225	56	436		34R	2W	72.5	74	314.225	A3	35.33	0.94	3.44	1.07
PP943	322.285	56	436		35R	1W	78.5	80	322.285	B	53.34	0.92	3.42	1.09
PP886	338.335	56	436		36R	6W	38.5	42.5	338.335	B	7.65	0.66	3.97	1.18
PP887	347.3	56	436		37R	5W	80	84	347.3	B	1.52	0.62	3.32	1.01
PP888	354.85	56	436		38R	4W	40	44	354.85	B	0.60	0.89	3.72	1.09
PP889	360.15	56	436		39R	1W	65	69	360.15	C1	0.00	———	2.86	1.05
PP890	361.55	56	436		39R	2W	55	59	361.55	C1	0.00	———	1.55	0.86
PP891	364.3	56	436		39R	4W	30	34	364.3	C1	0.00	———	3.09	1.06
PP892	367.46	56	436		39R	6W	56	60	367.46	C2	0.00	———	2.13	1.23
PP893	369.3	56	436		40R	1W	30	34	369.3	C2	0.00	———	2.15	1.16
PP894	372.82	56	436		40R	3W	82	86	372.82	C2	0.00	———	2.76	1.27
PP895	376.44	56	436		40R	6W	54	58	376.44	C2	0.00	———	3.61	1.20
PP896	377.68	56	436		40R	CCW	8	12	377.68	C3	0.00	———	1.70	1.10
PP897	378.57	56	436		41R	1W	3	7	378.57	C3	0.00	———	1.51	1.12

Table C.7: Model results. Estimates of temperature rise, minimum number of earthquakes, and minimum slip magnitude for faults in the JFAST core that exhibit biomarker anomalies

Lab Number	Leg	Site	Hole	Core	Section	Section top top depth (cm)	Section bottom bottom depth (cm)	Depth (mbsf)	Min Distance from fault center (m) [a]	Max Distance from fault center (m) [a]	Maximum fault thickness (m) [d]	Minimum slip magnitude (m)	Min T at minimum slip (^{o}C)	Min # of eqs at minimum slip
PP944	343	C0019	E	15R	1W	98.5	100	817.485	0	0.14	0.015	10	311.72	115
PP945	343	C0019	E	15R	1W	110.5	112.5	817.605	0	0.04	0.02	10	311.72	77
PP727	343	C0019	E	15R	CCW	14	15	817.85	0.005	0.1	0.09	30	334.58	44
PP829	343	C0019	E	17R	1W	105	110	822.55	0[c]	0.1[b]	0.0125	10	287.94	256
PP730	343	C0019	E	18R	1W	33	35	824.33	0.01	0.1	0.06	30	233.25	6
PP951	343	C0019	E	20R	2W	19.5	21	832.515	0.015	0.14	0.11	40	236.84	21
PP952	343	C0019	E	20R	2W	49.5	51	832.815	0.015	0.06	0.04	40	236.84	12

[a] negative values are above the sample, positive values below
[b] candidate structures on either side of sample
[c] sample is located within candidate structure
[d] minimum thickness is constrained by 900 C upper temperature limit and differs for each slip scenario (Fig. S7a)

D Appendix D

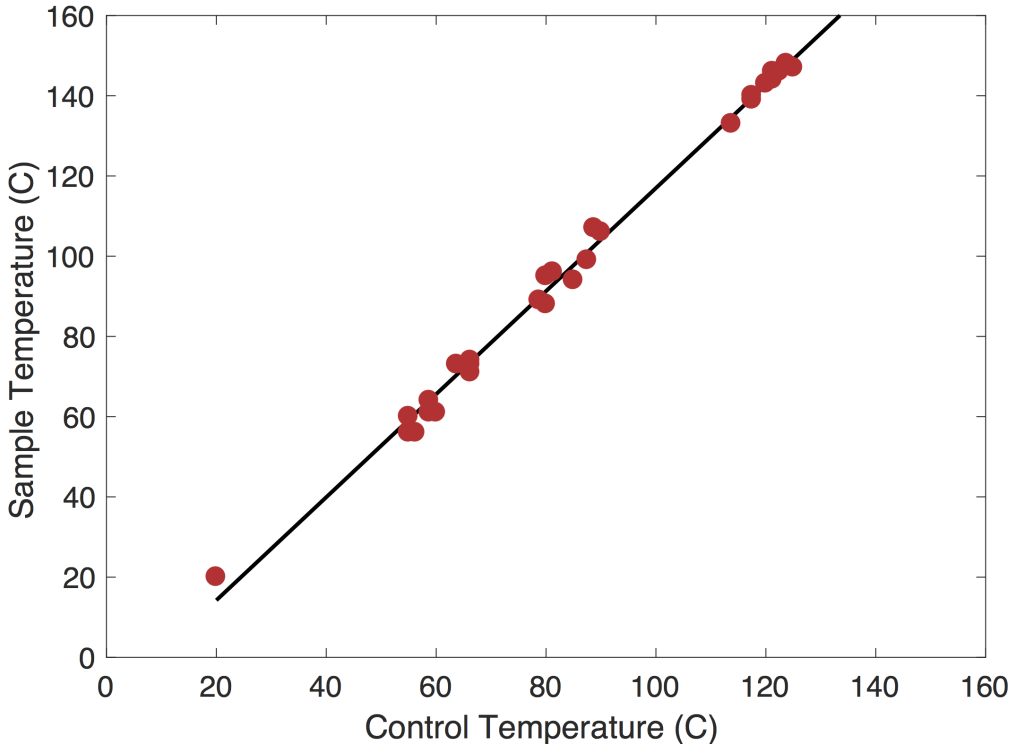

Figure D.1: Temperature calibration. Temperatures at the sample interface are consistently higher than the control temperature.

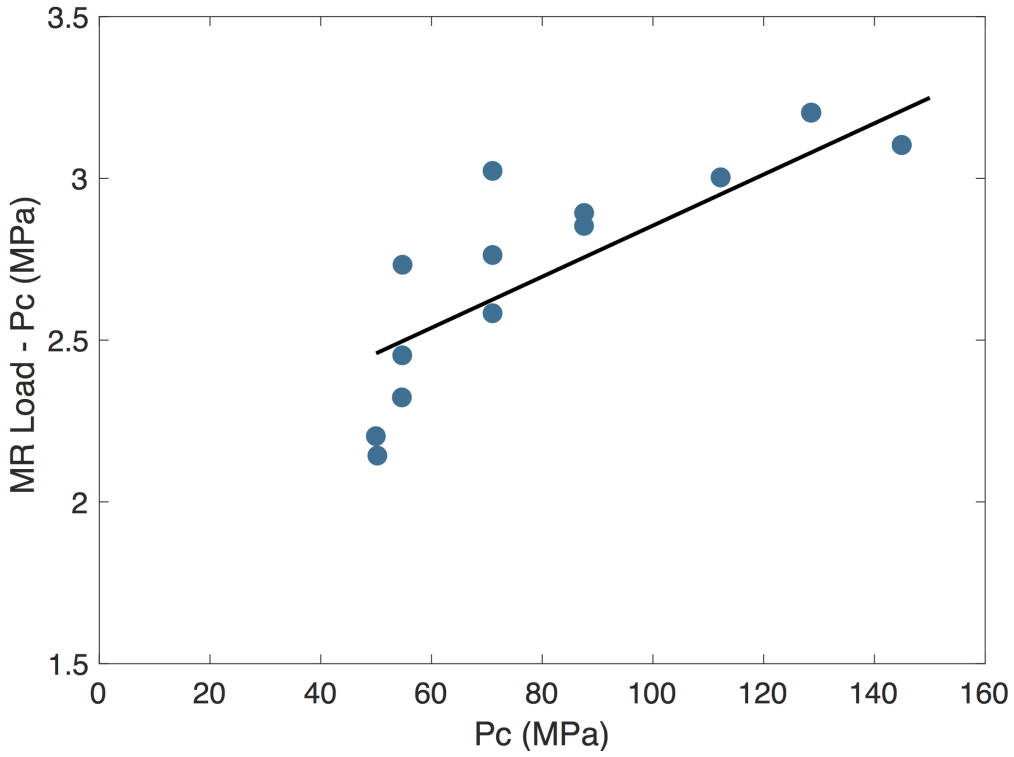

Figure D.2: Piston friction correction. Piston friction due to o-ring seals increases with increasing confining pressure.

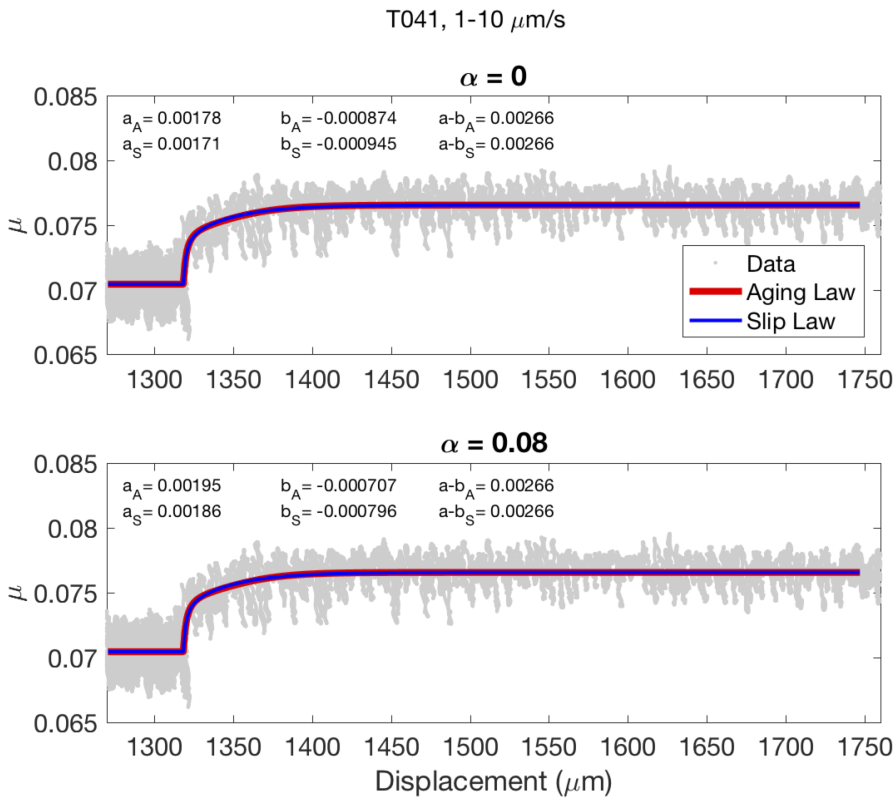

Figure D.3: Example of a velocity step from 1 to 10 μm/s from experiment T041 modeled for this study. Red curves show Aging (Dieterich) fit and blue curves show Slip (Ruina) fit. A) Model fits assuming α=0 and B) α=μ_{ss}. While a and b values show small variation between fits, all $a-b$ values are identical.

Table D.1: Rate-and-state friction parameters for BRAVA and plate-rate experiments

Sample Number	σ_{eff} [+/- std] (MPa)	Temp [+/- std] (^oC)	μ [min, max]	V_0 (μm/s)	V_1 (μm/s)	a	a std	b	b std	b2	b2 std	Dc (μm)	Dc std (μm)	Dc2 (μm)	Dc2 std (μm)	a-b
BRAVA																
i205	1	20	0.48	1	3	0.0025	9.30E-05	-0.0050	4.60E-05	-0.0007	4.60E-05	48	1	48	4	0.0083
	[NA]	[NA]	[0.36, 0.57]	3	10	0.0033	2.87E-04	-0.0059	7.28E-04	-0.0004	6.65E-04	53	4	15	131	0.0095
				10	30	0.0036	9.80E-05	-0.0064	4.90E-05	-0.0007	4.80E-05	65	1	65	8	0.0106
				30	100	0.0070	3.54E-04	-0.0036	4.61E-04	-0.0064	3.77E-04	28	7	159	16	0.0170
				100	300	0.0100	4.72E-04	-0.0125	4.64E-03	-0.0006	4.61E-03	71	18	185	14100	0.0232
i206	5	20	0.36	1	3	0.0037	8.30E-05	0.0016	8.30E-05	-0.0027	3.50E-05	7	1	91	2	0.0048
	[NA]	[NA]	[0.24, 0.44]	3	10	0.0066	1.20E-05	0.0033	1.20E-05	-0.0020	2.20E-05	2	0	129	3	0.0052
				10	30	0.0053	1.29E-04	0.0024	1.23E-04	-0.0019	7.30E-05	3	0	26	1	0.0048
				30	100	0.0083	3.60E-05	0.0037	3.90E-05	-0.0027	7.40E-05	2	0	42	1	0.0072
				100	300	0.0103	4.40E-05	0.0047	4.50E-05	-0.0042	8.70E-05	1	0	91	3	0.0098
i207	25	20	0.35	1	3	0.0059	9.10E-05	0.0032	9.10E-05	0.0000	0.00E+00	5	0	0	0	0.0026
	[NA]	[NA]	[0.23, 0.41]	3	10	0.0064	6.00E-04	0.0030	6.00E-04	0.0000	0.00E+00	3	1	0	0	0.0034
				10	30	0.0099	5.00E-06	0.0049	5.00E-06	-0.0009	7.30E-05	1	0	3923	349	0.0059
				30	100	0.0154	7.90E-05	0.0100	7.90E-05	-0.0020	1.50E-04	1	0	94	14	0.0074
				100	300	0.0072	4.10E-05	-0.0038	3.90E-05	0.0000	0.00E+00	150	3	0	0	0.0110
plate-rate																
B628	10	20	0.43	0.0017	0.0051	0.0025	2.54E-04	0.0014	2.50E-04	0.0015	4.80E-05	3.559	1.011	96.095	4.328	-0.0003
	[NA]	[NA]	[0.38, 0.44]													

Table D.2: Rate-and-state friction parameters using Aging Law for triaxial experiments, α=0

Sample Number	σ_{eff} [+/- std] (MPa)	Temp [+/- std] (^{o}C)	μ [min, max]	V_0 (μm/s)	V_1 (μm/s)	a	a std	b	b std	Dc (μm)	Dc std (μm)	a-b
T035	165.87	106.86	0.11	1.414	14.14	0.0029	5.99E-05	-0.0010	5.55E-05	55.76	4.77	0.0039
	[6.64]	[3.88]	[0.09, 0.17]	1.414	4.243	0.0036	1.24E-04	-0.0014	1.43E-04	90.00	26.47	0.0050
				4.243	42.43	0.0027	8.52E-05	7.65E-05	7.48E-05	80.00	139.65	0.0026
				1.414	14.14	0.0034	5.13E-05	-0.0003	4.45E-05	100.00	33.97	0.0037
				14.14	42.43	0.0031	2.19E-04	-0.0010	2.20E-04	100.00	62.20	0.0041
T036	125.48	73.50	0.22	1.414	14.14	0.0044	5.21E-05	-0.0009	4.75E-05	58.06	4.69	0.0053
	[7.11]	[3.52]	[0.18, 0.25]	1.414	4.243	0.0040	8.04E-05	-0.0013	6.47E-05	68.11	6.71	0.0052
				4.243	42.43	0.0030	8.65E-05	-0.0028	7.65E-05	80.36	4.12	0.0058
				1.414	14.14	0.0036	6.43E-05	-0.0010	5.87E-05	55.03	5.43	0.0047
				14.14	42.43	0.0035	2.27E-04	-0.0027	1.87E-04	90.00	13.30	0.0062
T037	72.36	47.54	0.21	1.414	14.14	0.0042	7.89E-05	0.0002	7.09E-05	100.00	57.79	0.0039
	[2.67]	[3.13]	[0.17, 0.35]	1.414	4.243	0.0029	1.61E-04	-0.0013	1.24E-04	90.01	20.08	0.0042
				4.243	42.43	0.0026	2.05E-04	-0.0011	1.94E-04	47.30	12.09	0.0037
				14.14	141.4	0.0038	1.79E-04	0.0017	4.55E-04	200.00	100.21	0.0021
T039	152.08	20	0.11	1.414	14.14	0.0023	2.54E-05	-0.0007	2.44E-05	30.08	2.14	0.0030
	[14.86]	[NA]	[0.05, 0.15]	1.414	4.243	0.0021	2.81E-05	-0.0013	2.39E-05	58.76	2.25	0.0034
				4.243	42.43	9.49E-07	8.55E-05	-0.0029	8.48E-05	8.89	0.33	0.0029
				1.414	14.14	0.0005	2.37E-05	-0.0020	2.28E-05	39.42	0.66	0.0025
				14.14	141.4	0.0017	3.45E-05	-0.0012	3.13E-05	83.87	3.37	0.0029
T040	156.01	73.34	0.08	1.414	14.14	4.49E-06	6.70E-05	-0.0018	6.57E-05	13.45	0.57	0.0019
	[5.35]	[3.80]	[0.07, 0.12]	1.414	4.243	0.0019	3.48E-05	-0.0012	2.67E-04	200.00	67.93	0.0031
				4.243	42.43	0.0020	2.97E-05	-0.0016	2.71E-05	124.90	3.97	0.0036
				1.414	14.14	0.0012	5.08E-05	-0.0007	4.86E-05	23.12	2.09	0.0019
				14.14	141.4	0.0017	5.25E-05	-0.0005	4.82E-05	100.00	18.14	0.0023
T041	104.30	20	0.08	1.414	14.14	0.0018	5.04E-05	-0.0009	4.95E-05	17.08	1.19	0.0027
	[6.80]	[NA]	[0.06, 0.12]	1.414	4.243	0.0025	3.45E-05	-0.0010	3.04E-05	100.01	7.78	0.0035
				4.243	42.43	0.0023	3.32E-05	-0.0004	3.21E-05	100.00	18.06	0.0027
				1.414	14.14	0.0017	2.87E-05	-0.0018	2.74E-05	40.37	0.86	0.0035
				14.14	141.4	0.0019	3.92E-05	-0.0002	4.35E-05	100.00	63.83	0.0020
				4.243	42.43	0.0014	7.76E-05	-0.0003	7.58E-05	20.00	5.73	0.0018
				14.14	141.4	0.0020	8.10E-05	0.0003	7.90E-05	27.78	10.38	0.0017
T042	60.40	20	0.10	1.414	4.243	0.0026	4.76E-05	0.0002	3.91E-05	80.00	35.46	0.0024
	[4.25]	[NA]	[0.08, 0.18]	4.243	42.43	0.0017	1.68E-04	-0.0010	1.66E-04	10.42	2.32	0.0027
				1.414	14.14	0.0020	3.07E-05	-0.0018	2.89E-05	79.43	2.34	0.0039
				14.14	141.4	0.0020	7.15E-05	-0.0011	6.57E-05	73.21	7.90	0.0030
				1.414	4.243	0.0016	7.96E-05	-0.0010	7.17E-05	39.79	4.69	0.0025
				4.243	42.43	0.0016	1.12E-04	-0.0011	1.10E-04	19.66	2.75	0.0027
				1.414	14.14	0.0018	4.86E-05	-0.0008	4.68E-05	50.01	4.79	0.0027
				14.14	141.4	0.0026	6.50E-05	-0.0018	6.26E-05	123.13	9.10	0.0044
T044	68.00	48.00	0.18	1.414	14.14	0.0040	5.09E-05	0.0008	4.83E-05	29.95	2.48	0.0033
	[3.58]	[3.36]	[0.16, 0.28]	1.414	4.243	0.0042	5.43E-05	-0.0005	4.39E-05	67.26	9.85	0.0047
				4.243	42.43	0.0028	5.41E-05	0.0005	4.99E-05	50.00	8.29	0.0023
				1.414	14.14	0.0036	4.60E-05	-0.0011	4.32E-05	42.98	2.35	0.0047
T045	26.15	20	0.14	4.243	42.43	0.0030	1.27E-04	0.0004	1.18E-04	30.01	13.24	0.0026
	[0.84]	[NA]	[0.08, 0.22]	1.414	14.14	0.0026	7.65E-05	-0.0028	7.15E-05	42.14	1.80	0.0054
				14.14	141.4	0.0038	1.22E-04	0.0004	1.28E-04	130.01	92.26	0.0034

Table D.3: Continuation of Table D.2, α=μ_{ss}

Sample Number	α	a	a std	b	b std	Dc (μm)	Dc std (μm)	a-b
T035	0.118	0.0034	6.60E-05	-0.0006	6.33E-05	36.40	2.24	0.0039
	0.101	0.0041	1.27E-04	-0.0011	2.57E-04	90.00	35.36	0.0051
	0.106	0.0030	1.34E-04	0.0004	1.19E-04	70.00	197.73	0.0026
	0.11	0.0038	1.74E-04	0.0002	1.66E-04	100.00	73.89	0.0036
	0.106	0.0035	2.20E-04	-0.0007	4.00E-04	100.00	85.86	0.0042
T036	0.235	0.0059	1.77E-04	0.0007	1.73E-04	80.00	17.58	0.0052
	0.232	0.0057	1.88E-04	0.0005	1.74E-04	70.00	15.57	0.0052
	0.234	0.0040	1.11E-04	-0.0018	1.03E-04	48.87	1.91	0.0058
	0.204	0.0050	2.07E-04	0.0005	2.03E-04	90.00	39.19	0.0045
	0.206	0.0044	2.93E-04	-0.0018	2.52E-04	57.69	6.93	0.0062
T037	0.208	0.0053	1.27E-04	0.0013	1.11E-04	90.01	75.18	0.0040
	0.1925	0.0038	1.67E-04	-0.0007	2.33E-04	89.96	35.57	0.0045
	0.204	0.0033	2.49E-04	-0.0004	2.43E-04	18.40	6.67	0.0037
	0.22	0.0049	2.45E-04	0.0029	4.58E-04	200.00	100.16	0.0020
T039	0.126	0.0028	2.25E-05	-0.0005	1.62E-04	40.00	13.54	0.0033
	0.108	0.0024	3.13E-05	-0.0010	2.69E-05	49.11	1.75	0.0034
	0.1075	1.49E-06	1.02E-04	-0.0028	1.01E-04	7.33	0.28	0.0028
	0.053	0.0005	2.51E-05	-0.0020	2.42E-05	37.11	0.61	0.0025
	0.052	0.0018	3.63E-05	-0.0011	3.30E-05	76.67	2.96	0.0029
T040	0.088	2.16E-06	7.52E-05	-0.0018	7.39E-05	12.02	0.50	0.0019
	0.072	0.0021	3.69E-05	-0.0012	3.83E-04	200.00	85.91	0.0032
	0.08	0.0022	3.21E-05	-0.0014	2.95E-05	107.69	3.21	0.0036
	0.08	0.0018	2.34E-05	-0.0003	9.24E-05	99.99	40.71	0.0021
	0.088	0.0019	6.24E-05	-0.0004	5.87E-05	58.58	7.94	0.0022
T041	0.08	0.0019	5.42E-05	-0.0007	5.33E-05	14.41	0.88	0.0027
	0.074	0.0027	3.50E-05	-0.0008	3.32E-05	99.98	8.31	0.0035
	0.074	0.0025	2.79E-05	-0.0002	8.27E-05	100.00	48.73	0.0027
	0.062	0.0018	3.07E-05	-0.0017	2.94E-05	36.52	0.74	0.0035
	0.069	1.97E-06	5.23E-04	-0.0020	5.21E-04	2.55	0.63	0.0020
	0.056	0.0015	8.31E-05	-0.0003	8.15E-05	15.79	3.86	0.0018
	0.058	0.0021	8.94E-05	0.0004	8.71E-05	29.45	12.19	0.0017
T042	0.09	0.0028	5.54E-05	0.0004	4.46E-05	80.01	39.25	0.0024
	0.088	0.0019	1.81E-04	-0.0008	1.80E-04	8.75	1.73	0.0027
	0.0825	0.0022	3.33E-05	-0.0016	3.14E-05	68.73	1.91	0.0039
	0.09	0.0022	7.74E-05	-0.0008	7.19E-05	60.43	5.91	0.0030
	0.0725	0.0017	8.57E-05	-0.0008	7.76E-05	35.53	4.02	0.0025
	0.0825	0.0017	1.21E-04	-0.0009	1.18E-04	17.10	2.20	0.0027
	0.078	0.0021	4.78E-05	-0.0007	4.69E-05	49.99	4.68	0.0027
	0.082	0.0028	7.13E-05	-0.0015	6.76E-05	100.01	6.73	0.0043
T044	0.19	0.0039	4.75E-05	-1.63E-05	2.21E-05	30.00	41.96	0.0039
	0.17	0.0050	1.42E-04	0.0004	1.32E-04	50.10	10.31	0.0046
	0.171	0.0034	6.38E-05	0.0011	5.46E-05	68.89	15.19	0.0023
	0.1725	0.0050	1.64E-04	0.0004	1.61E-04	49.98	10.92	0.0046
T045	0.12	0.0034	1.60E-04	0.0009	1.47E-04	30.02	15.12	0.0026
	0.1225	0.0030	8.69E-05	-0.0024	8.17E-05	34.37	1.34	0.0054
	0.1325	0.0044	1.62E-04	0.0010	1.41E-04	130.01	102.86	0.0034

Table D.4: Rate-and-state friction parameters using Slip Law for triaxial experiments, α=0

Sample Number	σ_{eff} [+/- std] (MPa)	Temp [+/- std] (^{o}C)	μ [min, max]	V_0 (μm/s)	V_1 (μm/s)	a	a std	b	b std	Dc (μm)	Dc std (μm)	a-b
T035	165.87	106.86	0.11	1.414	14.14	0.0029	6.89E-05	-0.0010	5.97E-05	100.00	12.47	0.0040
	[6.64]	[3.88]	[0.09, 0.17]	1.414	4.243	0.0034	1.52E-04	-0.0015	1.09E-04	90.00	24.80	0.0049
				4.243	42.43	0.0027	1.29E-04	6.35E-05	1.16E-04	80.00	254.59	0.0026
				1.414	14.14	0.0034	7.79E-05	-0.0002	6.67E-05	100.00	53.13	0.0036
				14.14	42.43	0.0029	2.67E-04	-0.0011	2.02E-04	100.00	58.81	0.0040
T036	125.48	73.50	0.22	1.414	14.14	0.0043	6.04E-05	-0.0010	5.20E-05	105.39	12.07	0.0053
	[7.11]	[3.52]	[0.18, 0.25]	1.414	4.243	0.0039	8.59E-05	-0.0013	6.68E-05	94.99	11.63	0.0053
				4.243	42.43	0.0027	1.03E-04	-0.0032	8.72E-05	133.66	8.78	0.0059
				1.414	14.14	0.0036	7.50E-05	-0.0011	6.40E-05	101.62	14.62	0.0047
				14.14	42.43	0.0033	2.56E-04	-0.0029	2.07E-04	110.49	19.10	0.0062
T037	72.36	47.54	0.21	1.414	14.14	0.0042	1.16E-04	0.0002	1.03E-04	100.00	107.65	0.0040
	[2.67]	[3.13]	[0.17, 0.35]	1.414	4.243	0.0030	1.60E-04	-0.0015	1.69E-04	183.32	67.16	0.0044
				4.243	42.43	0.0024	2.55E-04	-0.0013	2.36E-04	72.45	23.16	0.0037
				14.14	141.4	0.0041	2.47E-04	0.0016	2.15E-04	200.00	78.99	0.0024
T039	152.08	20	0.11	1.414	14.14	0.0023	2.90E-05	-0.0008	3.16E-05	68.68	8.62	0.0031
	[14.86]	[NA]	[0.05, 0.15]	1.414	4.243	0.0022	2.88E-05	-0.0014	2.41E-05	100.00	5.42	0.0035
				4.243	42.43	3.08E-05	1.04E-04	-0.0028	1.03E-04	14.13	0.70	0.0029
				1.414	14.14	2.50E-05	3.24E-05	-0.0024	3.11E-05	50.00	1.05	0.0024
				14.14	141.4	0.0015	4.15E-05	-0.0014	3.71E-05	127.71	6.33	0.0029
T040	156.01	73.34	0.08	1.414	14.14	6.32E-06	7.86E-05	-0.0019	8.20E-05	18.96	0.75	0.0019
	[5.35]	[3.80]	[0.07, 0.12]	1.414	4.243	0.0019	3.96E-05	-0.0010	1.08E-04	200.01	47.95	0.0029
				4.243	42.43	0.0019	3.46E-05	-0.0018	2.98E-05	247.56	12.45	0.0037
				1.414	14.14	0.0012	6.10E-05	-0.0008	5.81E-05	36.32	4.13	0.0019
				14.14	141.4	0.0016	7.92E-05	-0.0007	7.16E-05	100.00	20.65	0.0022
T041	104.30	20	0.08	1.414	14.14	0.0017	6.10E-05	-0.0009	5.96E-05	26.13	2.31	0.0027
	[6.80]	[NA]	[0.06, 0.12]	1.414	4.243	0.0025	3.68E-05	-0.0011	3.41E-05	154.88	16.45	0.0035
				4.243	42.43	0.0021	5.00E-05	-0.0005	4.59E-05	100.00	18.27	0.0026
				1.414	14.14	0.0016	3.34E-05	-0.0019	3.11E-05	69.71	1.91	0.0035
				14.14	141.4	0.0018	5.41E-05	-0.0003	4.77E-05	100.00	39.35	0.0020
				4.243	42.43	0.0014	1.02E-04	-0.0004	9.90E-05	27.14	9.90	0.0018
				14.14	141.4	0.0020	8.93E-05	0.0002	8.65E-05	50.00	26.23	0.0017
T042	60.40	20	0.10	1.414	4.243	0.0026	5.66E-05	0.0002	4.72E-05	80.00	45.59	0.0024
	[4.25]	[NA]	[0.08, 0.18]	4.243	42.43	0.0016	2.11E-04	-0.0011	2.08E-04	15.40	4.19	0.0027
				1.414	14.14	0.0019	3.65E-05	-0.0020	3.20E-05	145.39	6.22	0.0039
				14.14	141.4	0.0017	9.24E-05	-0.0013	8.30E-05	100.00	13.15	0.0030
				1.414	4.243	0.0016	8.52E-05	-0.0010	7.59E-05	53.69	7.44	0.0026
				4.243	42.43	0.0012	1.64E-04	-0.0015	1.60E-04	22.42	3.62	0.0026
				1.414	14.14	0.0019	5.24E-05	-0.0009	4.87E-05	123.54	20.38	0.0028
				14.14	141.4	0.0025	7.60E-05	-0.0020	7.54E-05	253.62	30.15	0.0045
T044	68.00	48.00	0.18	1.414	14.14	0.0042	6.47E-05	0.0009	6.09E-05	40.37	4.23	0.0033
	[3.58]	[3.36]	[0.16, 0.28]	1.414	4.243	0.0042	5.63E-05	-0.0005	4.30E-05	97.69	18.48	0.0047
				4.243	42.43	0.0028	5.81E-05	0.0006	5.02E-05	116.50	32.94	0.0023
				1.414	14.14	0.0036	5.32E-05	-0.0011	4.90E-05	71.81	5.25	0.0047
T045	26.15	20	0.14	4.243	42.43	0.0030	1.39E-04	0.0004	1.24E-04	52.36	30.69	0.0026
	[0.84]	[NA]	[0.08, 0.22]	1.414	14.14	0.0024	9.12E-05	-0.0031	8.03E-05	74.22	4.45	0.0055
0	0	0		14.14	141.4	0.0038	1.75E-04	0.0003	1.56E-04	130.01	141.43	0.0035

Table D.5: Continuation of Table D.4, α=μ_{ss}

Sample Number	α	a	a std	b	b std	Dc (μm)	Dc std (μm)	a-b
T035	0.118	0.0034	7.35E-05	-0.0006	6.25E-05	100.00	13.15	0.0040
	0.101	0.0039	1.62E-04	-0.0011	1.21E-04	90.00	26.87	0.0049
	0.106	0.0030	1.46E-04	0.0004	1.32E-04	70.00	227.10	0.0026
	0.11	0.0038	8.27E-05	0.0002	6.99E-05	100.00	51.48	0.0036
	0.106	0.0033	2.88E-04	-0.0008	2.19E-04	100.00	64.00	0.0041
T036	0.235	0.0056	7.90E-05	0.0003	6.89E-05	80.00	9.12	0.0053
	0.232	0.0051	1.13E-04	-0.0002	9.09E-05	70.00	8.41	0.0052
	0.234	0.0035	1.33E-04	-0.0024	1.14E-04	102.72	6.74	0.0059
	0.204	0.0045	9.09E-05	-0.0002	7.62E-05	90.00	13.70	0.0047
	0.206	0.0042	3.19E-04	-0.0020	2.59E-04	90.00	15.74	0.0063
T037	0.208	0.0052	1.38E-04	0.0013	1.22E-04	90.00	89.17	0.0040
	0.1925	0.0035	2.22E-04	-0.0007	1.68E-04	90.01	23.85	0.0042
	0.204	0.0030	3.20E-04	-0.0007	2.98E-04	57.70	18.44	0.0037
	0.22	0.0052	2.98E-04	0.0029	2.66E-04	200.00	92.06	0.0023
T039	0.126	0.0026	3.31E-05	-0.0005	3.27E-05	60.05	7.53	0.0031
	0.108	0.0025	3.14E-05	-0.0011	2.66E-05	100.00	5.89	0.0036
	0.1075	1.52E-05	1.05E-04	-0.0029	1.07E-04	13.95	0.57	0.0029
	0.053	0.0002	3.06E-05	-0.0023	2.90E-05	58.96	1.23	0.0025
	0.052	0.0016	4.38E-05	-0.0014	3.92E-05	121.11	6.00	0.0029
T040	0.088	2.46E-06	9.60E-05	-0.0019	8.65E-05	17.18	1.19	0.0019
	0.072	0.0020	4.22E-05	-0.0009	1.26E-04	200.00	51.21	0.0030
	0.08	0.0021	3.76E-05	-0.0016	3.18E-05	227.81	11.46	0.0037
	0.08	0.0013	6.63E-05	-0.0007	6.33E-05	33.42	3.81	0.0019
	0.088	0.0017	8.33E-05	-0.0005	7.46E-05	100.00	21.14	0.0022
T041	0.08	0.0019	6.62E-05	-0.0008	6.47E-05	24.09	2.13	0.0027
	0.074	0.0027	3.97E-05	-0.0009	3.53E-05	143.52	15.25	0.0035
	0.074	0.0023	5.22E-05	-0.0003	4.75E-05	100.00	18.84	0.0026
	0.062	0.0017	3.56E-05	-0.0018	3.32E-05	65.41	1.79	0.0035
	0.069	3.96E-06	4.24E-04	-0.0020	4.22E-04	5.31	1.27	0.0020
	0.056	0.0015	1.08E-04	-0.0003	1.05E-04	25.68	9.37	0.0018
	0.058	0.0021	9.19E-05	0.0004	8.89E-05	50.00	26.78	0.0017
T042	0.09	0.0028	6.02E-05	0.0004	4.95E-05	80.00	45.02	0.0024
	0.088	0.0017	2.31E-04	-0.0010	2.27E-04	14.08	3.83	0.0027
	0.0825	0.0021	3.97E-05	-0.0019	3.45E-05	133.41	5.70	0.0039
	0.09	0.0020	9.80E-05	-0.0011	8.69E-05	100.00	13.61	0.0030
	0.0725	0.0017	9.29E-05	-0.0009	8.32E-05	48.46	6.69	0.0025
	0.0825	0.0013	1.79E-04	-0.0014	1.75E-04	20.57	3.32	0.0026
	0.078	0.0020	5.69E-05	-0.0008	5.14E-05	113.88	18.78	0.0028
	0.082	0.0027	8.27E-05	-0.0018	7.81E-05	232.97	27.71	0.0045
T044	0.19	0.0051	7.94E-05	0.0019	7.53E-05	32.91	3.45	0.0033
	0.17	0.0050	6.84E-05	0.0003	5.39E-05	79.36	14.84	0.0047
	0.171	0.0034	7.02E-05	0.0011	5.81E-05	95.82	26.93	0.0023
	0.1725	0.0043	6.43E-05	-0.0004	5.97E-05	59.41	4.34	0.0047
T045	0.12	0.0035	2.02E-04	0.0009	1.90E-04	30.00	17.72	0.0026
	0.1225	0.0027	1.04E-04	-0.0027	9.15E-05	65.15	3.90	0.0055
0	0.1325	0.0044	1.93E-04	0.0009	1.68E-04	130.00	136.18	0.0034